High-Rayleigh-Number Thermal Convection of Compressed Gases in Inclined Rectangular Enclosures of Varied Aspect Ratios

A DISSERTATION
SUBMITTED TO THE FACULTY OF THE
UNIVERSITY OF MINNESOTA
BY

Umesh Madanan

IN PARTIAL FULFILLMENT OF THE REQUIREMENTS
FOR THE DEGREE OF DOCTOR OF PHILOSOPHY

Richard J. Goldstein, Advisor

August, 2019

ACKNOWLEDGEMENT

I would like to thank my advisor, Professor Richard Goldstein, for his continued guidance and support throughout my doctoral studies. I appreciate and value his patience in affording me with the flexibility to develop my research at my own pace, and offering timely counsel when required, while simultaneously also providing me with opportunities to explore and evolve my teaching capabilities. I also deeply appreciate his foresight in offering me with an opportunity to work on different topics, thus, helping me get familiarized with a diverse range of topics within heat transfer. I am very grateful to my committee members, Prof. Terrence Simon, Prof. Shri Ramaswamy, and Dr. Vinod Srinivasan, for their constructive thoughts, conversations, and criticisms. My special thanks to Prof. Terrence Simon for his suggestions and guidelines while editing my thesis in its initial stages and his mentorship and support during the course of my teaching fellowship. Also, many thanks to Dr. Vinod Srinivasan for his help with the preliminary setting up for my experiments. I would also like to thank Prof. Joseph Nichols for agreeing to serve as my preliminary defense committee member.

I would also like to acknowledge the past and present members of the Heat Transfer Laboratory at the University of Minnesota Twin Cities for their assistance at various stages in my research. I would like to especially thank Dr. Sangjo Han and Dr. Amy Fleischer for their vital role in helping me set up the laboratory equipment for my research. I greatly appreciate their valuable inputs. Sincere thanks to my co-authors Dr. Kaustubh Kulkarni, Rajat Mittal, and Francesco Papa, for allowing me a chance to contribute to their work.

To the CSE shop members, Pat Nelson, Ron Boystrom, Bob Jones, and Mike Jensen, my sincere thanks for their patience and assistance in building my experimental setup. Special thanks to Pat Nelson for fabricating all the experimental test cells. I would also like to thank Ray Muno and Paul Markfort for their help and support with all the IT troubles, especially for their assistance in the installation of GPIB controls for my experiments. Heartfelt thanks to Richard Maharaj for his invaluable help with setting up my new lab and fixing various concerns that cropped up in the lab during this period. I would also like to thank him for permitting me the service of his student helpers, Nikolas King and Derek Huston, in torquing/untorquing the pressure vessel. Sincere thanks to Pam Wilson for helping me smoothly transition my lab space to a new location

and promptly allocating the funds required to replace equipment misplaced during this move. Special thanks to Paul Krueger for his timely support with the numerous facilities management related requests. My sincere thanks to Gail Johansen and John Gardner for always answering the inordinate number of questions I came up with without protest.

To my fellow graduate students who helped me along the way with discussions and new ideas, Dr. Mahmood Alqefl, Dr. Brandon Shadakofsky, Sankarganesh Muthukrishanan, Ian Wright, Dr. John Gorman, Manish Sachdeva, and so many more, thank you. Special thanks to Santosh Kumar Sankar for his help with the flow visualization experiment.

I would also like to thank my parents for their never-ending support, understanding, and encouragement during the past few years. Lastly, but most importantly, I would like to thank my wife for setting aside her career goals to support me during this challenging period in my life. Graduate student life would have been lonely and difficult without you. This thesis is as much yours as it is mine!

Dedicated to my wonderful wife, Aruna, and my parents

ABSTRACT

In the present study, heat transfer measurements and flow visualization are carried out for high-Rayleigh-number thermal convection in horizontal and tilted rectangular enclosures. The heat transfer measurements are performed for a wide range of Rayleigh numbers ($1.85 \times 10^6 \leq Ra \leq 1.04 \times 10^{11}$) using enclosures of different aspect ratios (AR = 1, 3, 6, and 10) and angles of inclination (ϕ = 0°, 30°, 60°, 90°, 120°, and 150°). Here, high Rayleigh numbers are achieved using compressed nitrogen and argon. Another set of experiments is conducted using sidewalls made of three materials having different thermal conductivities (Styrofoam, Plexiglas, and high-density polyethylene) to assess the effect of sidewall conductance heat loss on the horizontal enclosure free convection. Additionally, a z-type shadowgraph visualization is employed at angles of inclination between 0° and 90° to characterize the buoyant flow and validate the observed heat transfer trends.

Firstly, the effect of sidewall conductance heat loss on Nusselt number is examined by performing nearly identical sets of experiments using horizontal cubical enclosures with sidewalls made of three different materials. The results from these experiments reveal a higher difference (ΔNu) between the sidewall-uncorrected Nusselt number (Nu_{net}) and the sidewall-corrected Nusselt number (Nu_c) than that obtained when using a traditional empty-cell gradient assumption. Thus, a semi-analytical model is proposed to estimate the sidewall-corrected Nusselt number, given the corresponding uncorrected values, which is found to predict this experimentally observed difference in Nusselt numbers to within 11% (when $Wn \geq \mathcal{O}(1)$). Another empirical model is also proposed to estimate the sidewall-corrected Nusselt numbers for smaller wall numbers (or, $Wn \to 0$) and the predicted ΔNu values for this case are found to be within 1.5% of the corresponding experimental data. Additionally, the Nusselt numbers for an ideal zero-thermal-conductivity sidewalls case are also estimated by extrapolating the corresponding Nu_{net} values obtained from the experiments. Further experiments in the present study are conducted after taking into consideration this effect of the sidewall conductance heat loss and using a sidewall material of low wall number (Styrofoam).

Another set of experiments is carried out to determine the correlating equations for Nusselt number, computed from steady-state electrical power input and temperature measurements, in terms of the studied variables for the horizontal and tilted enclosures. For the horizontal enclosure problem, this correlation is found to closely follow the classical $\frac{1}{3}^{rd}$ scaling relation between Nusselt number and Rayleigh number. For the tilted enclosure problem, a set of single-parameter ($Nu = f(Ra)$) and two-parameter ($Nu = f(Ra, AR)$) correlating equations are proposed to estimate the average Nusselt number at any of the investigated angles of inclination. The proposed correlations are found to predict the experimental values with reasonable accuracy.

The effect of aspect ratio on Nusselt number is assessed by performing experiments

with varied aspect ratios at a fixed Rayleigh number. For inclined enclosures, at any angle of inclination and a given Rayleigh number, Nusselt number is observed to follow a decreasing trend with an increase in the aspect ratio. Moreover, this decreasing trend is observed to gradually amplify as the angle of inclination is increased, with a negligible effect at an angle of inclination of 0° (or, for the horizontal enclosure problem) and a prominent effect at an angle of inclination of 90° (or, for the vertical enclosure problem).

The effect of angle of inclination on Nusselt number is also examined by performing experiments with varied aspect ratios and Rayleigh numbers. Nusselt number is found to decrease with an increase in the angle of inclination and this decreasing trend remains qualitatively the same for all the studied aspect ratios and Rayleigh numbers. There is a substantial drop observed in the Nu values between the angles of inclination 0° and 90°, whereas, in general, this drop is found to be minimal between the angles of inclination 90° and 150°. For any given aspect ratio, this variation in the Nu values is observed to become more prominent as the Rayleigh number increases.

The flow visualization studies for the horizontal enclosure problem indicate the presence of thermal plumes together with a large scale flow. These thermal plume eruptions are found to move across the central region (or, core) of the enclosure toward the opposing active wall. The frequency of the thermal plume eruptions and the velocity of the large scale flow are observed to increase with an increase in the Rayleigh number. For tilted enclosures, mixing within the core region is found to decrease as the angle of inclination is increased. Thus, for the vertical enclosure problem, the most prominent feature is an unperturbed core, with traveling wave-like structures over the boundary layers on the hot and cold vertical walls. In addition, the buoyant flow velocity is observed to decrease with an increase in the angle of inclination.

TABLE OF CONTENTS

LIST OF TABLES

LIST OF FIGURES

NOMENCLATURE

a	Constant in SPRT calibration (see Eqn. 3.3)
A	Arbitrary constant (see Table 2.2)
AR	Aspect ratio = L/H
c	Arbitrary constant (see Eqn. 4.4)
c_1, c_2	Arbitrary constants (see Eqn. 2.4)
c_p	Specific heat at constant pressure $[J/kgK]$
C	Pre-factor in the Nusselt number correlation
e_{tc}	Thermocouple voltage $[mV]$
f	Focal length $[m]$ (see Fig. 3.1)
F_B	Buoyant force $[N]$
F_{ij}	View factor for radiation heat loss calculations
F_V	Viscous force $[N]$
g	Acceleration due to gravity $[m/s^2]$
G_i	Irradiation on surface i $[W/m^2]$
Gr	Grashof number = $\frac{g\beta\Delta TH^3}{\nu^2}$
H	Spacing between the hot and cold plates $[m]$
h	Average heat transfer coefficient in the test cell $[W/m^2 - K]$
I_g	Current passing through the guard heater $[A]$
I_i	Current flowing through the i^{th} Kapton heater $[A]$
J_i	Radiosity of surface i $[W/m^2]$
k	Thermal conductivity $[W/m - K]$
k_f	Thermal conductivity of fluid $[W/m - K]$
k_p	Thermal conductivity of Plexiglas $[W/m - K]$
L	Extent of the square hot (or, cold) plate $[m]$

L_c Characteristic length of the fin problem $[m]$ (see Section 4.1)

m Exponent of AR in the two-parameter Nusselt number correlation

MW Molecular weight of the operating fluid (see Eqn. 3.1)

m^2 Fin parameter $[m^{-2}]$ (see Section 4.1)

n Exponent of Ra in the $Nu - Ra$ correlation

Nu Average Nusselt number = hH/k_f

Nu_c Sidewall-corrected Nusselt number (see Eqn. 4.3)

Nu_{net} Nusselt number based on q_{net} (see Eqn. 4.6)

Nu_∞ Nusselt number with plates of infinite thermal conductivity (see Eqn. 2.1)

p Pressure $[bar]$

P Arbitrary thermo-physical property (see Section 2.1.5)

Pr Prandtl number = ν/α

q'' Average heat flux $[W/m^2]$

q_{conv} Convective heat transfer in the enclosure $[W]$

q_{corr} Net input power (corrected for all heat losses) $[W]$ (see Eqn. 4.5)

q_e Edge heat loss $[W]$ (see Eqn. A.25)

q_{fin} Fin heat transfer $[W]$ (see Eqn. 4.5)

q_g Guard heat loss $[W]$ (see Eqn. A.11)

q_h Heat transfer from the heater in the direction of the hot plate $[W]$ (see Eqn. A.4)

q_{inp} Total heater power input $[W]$ (see Eqn. A.1)

q_{net} Net input power (corrected for all heat losses except sidewall conductance heat loss) $[W]$ (see Eqn. A.2)

q_r Radiation heat loss $[W]$ (see Eqn. A.22)

q_s Surface heat loss $[W]$ (see Eqn. A.28)

q_{sw} Sidewall conductance heat loss $[W]$ (see Fig. 4.4)

R Thermal diffusion resistance $[K/W]$ (see Eqn. A.5)

R^2 Coefficient of determination

$\overline{R}$ Specific gas constant $[J/kgK]$ (see Eqn. 3.1)

Ra Rayleigh number = $\frac{g\beta\Delta TH^3}{\nu\alpha}$

Ra_c Critical Rayleigh number

Sc Schmidt number

Sh Average Sherwood number

t Time $[s]$

t_B Balsa wood insulation thickness $[m]$

t_h Hot plate thickness $[m]$

t_w Thickness of the sidewalls $[m]$

T Temperature $[K]$

T_{amb} External fluid temperature within the pressure vessel $[K]$ (see Eqn. A.28)

$\overline{T}_{B,out}$ Average outer surface temperature of the balsa wood insulation $[K]$ (see Eqn. A.25)

T_c Temperature of cold plate $[K]$

T_g Guard plate surface temperature $[K]$

T_h Temperature of hot plate $[K]$

T_{heater} Heater surface temperature $[K]$ (see Eqn. A.4)

T_m Mean or bulk temperature = 0.5 (T_h + T_c) $[K]$

u Velocity $[m/s]$

$\vec{V}$ Velocity vector $[m/s]$ (see Eqn. 1.1)

V_g Voltage of the guard heater $[V]$

V_i Voltage of the i^{th} Kapton heater $[V]$

Wn Wall number = $\frac{4k_w t_w}{ARHk_f}$ (see Section 4.1)

X Fin height $[m]$ (see Eqn. 4.4)

X_p Ratio of the thermal resistance of the fluid to that of the plate (see Eqn. 2.2)

Greek Symbols

α Thermal diffusivity $[m^2/s]$

β Volumetric thermal expansion coefficient $[K^{-1}]$

δ_u Thickness of viscous boundary layer $[m]$

δ_θ Boundary layer thickness at the hot-end = $\frac{H}{2Nu}$ $[m]$

ΔNu Difference between Nu_{net} and Nu_c (see Eqn. 4.7)

ΔT Temperature difference = $(T_h - T_c)$ $[K]$

$\Delta\rho$ Density excess $[kg/m^3]$

ε_{Ag} Emissivity of polished silver surface on the hot and cold plates

ε_i Emissivity of the surface i

ε_u Viscous dissipation rate $[m^2/s^3]$

ε_θ Thermal energy dissipation rate $[m^2/s^3]$

$\theta*$ Non-dimensional temperature excess = $\frac{T-T_c}{T_h-T_c}$ (see Eqn. 1.7)

θ Temperature excess = $(T - T_m)$ $[K]$ (see Eqn. 4.1)

θ_h Temperature excess at the hot-end = $(T_h - T_m)$ $[K]$ (see Eqn. 4.7)

μ Dynamic viscosity $[Pa \cdot s]$

ν Momentum diffusivity $[m^2/s]$

ρ Density of the operating fluid $[kg/m^3]$

σ Stefan-Boltzmann constant ($5.67 \times 10^{-8} W/m^2K^4$)

τ_d Diffusion time scale (s)

τ_c Convection time scale (s)

ϕ Angle of inclination

ϕ_c Critical angle

∇ Nabla operator

Subscripts

B Balsa wood

c Cold

ch Characteristic

f Convecting fluid

e Edge

eff Effective

exp Experimental

g Guard

h Hot

ha Heater adhesive

k Kapton

m Mean

p Plate (hot or cold)

ph Phenolic

st Styrofoam sidewall

tp Triple point

w Sidewall

CHAPTER 1
Introduction

1.1 Motivation

Free convection is one of the prevalent modes of heat transfer in nature. It occurs whenever an object in a body force field (or, more commonly, the gravitational field) is hotter or cooler than its quiescent surroundings, thereby, producing density gradients in the surrounding fluid. The immediate consequence is a buoyant force which induces convection currents due to rising hot low-density (lighter) fluid and falling cold high-density (denser) fluid. This process happens continuously and, thus, establishes the free convective heat transfer with an associated flow pattern.

Among the numerous free convective heat transfer research, free convective heat transfer within enclosures having differentially heated isothermal walls has been of particular interest to researchers and is a heavily studied topic. This is mostly due to its natural occurrence in many real-world engineering systems, such as double-glazed windows, solar energy flat-plate collectors, nuclear reactors, and building enclosures. Furthermore, it is also of significant interest to researchers in various fields, such as meteorology (atmospheric flows), geophysics (creeping buoyancy driven flow of magma in the Earth's mantle), and astrophysics (bulk movement of plasma in the outer layer of stellar bodies). Most of these applications can be simulated in a laboratory setting with a horizontal enclosure (having a temperature gradient that is anti-parallel with the gravity vector), a vertical enclosure (where the temperature gradient is orthogonal to the gravity vector), or a tilted enclosure. Modeling any of the aforementioned applications can be

achieved using rectangular enclosures, comprised of two active walls (across which a temperature gradient exists) and four other adiabatic walls (or, sidewalls) to confine the fluid within. Scrutinizing the existing literature for free convective heat transfer within enclosures (see Chapter 2), a few noteworthy observations can be drawn.

Due to its simplicity and easily controllable experimental parameters, experimental free convection at very high Rayleigh numbers (or, turbulent free convection) is a great tool to study turbulence. For horizontal enclosures (or, the Rayleigh-Bénard convection; Bénard, 1901 and Rayleigh, 1916), heat transfer and flow pattern characterization at low, moderate, and high (and very high) Rayleigh numbers have been well documented in the literature. However, the experimental literature for tilted enclosure free convection at very high Rayleigh numbers, with the exception of vertical enclosures, is too scarce. This is especially true for a $Pr \approx 0.7$ fluid (or, that for argon, air, and many diatomic gases), where the experimental free convective heat transfer studies are limited to a maximum Rayleigh number of $\sim 10^7$. Interestingly, as Hideo (1984) has argued, the Earth's surface is rarely aligned with its geopotential lines. Thus, in addition to the various applications for tilted enclosures, strictly speaking, all the aforementioned practical situations are also to be examined as free convection across tilted enclosures. Although, there have been many numerical studies conducted for tilted enclosure free convection at high Rayleigh numbers, the unavailability of experimental data for the same can hinder the validation of the various turbulence models used in these studies. This underlines the need to systematically analyze the tilted enclosure heat transfer at high Rayleigh numbers.

Another significant observation inferred from the literature is that, in most cases, the sidewalls of the enclosures are either assumed to be perfectly insulating or having a linear temperature profile within (i.e., a pure conduction assumption wherein the internal enclosure convection is neglected). In actuality, due to the internal free convection and the boundary layer formation, the temperature profile within the sidewall material is non-linear with a steeper temperature gradient near the hot- and cold-ends, thus, rendering the above assumptions incorrect. These incorrect assumptions can lead

to discrepancies when estimating the rate of convective heat transport between the hot and the cold active walls (and, in turn, on the average Nusselt number (Nu), interpreted as the dimensionless heat transfer coefficient of the free convective enclosure problem). Hence, it is necessary to experimentally verify this effect of sidewall conductance heat loss on Nusselt number, which has not yet been accomplished.

Furthermore, visualization of flow patterns in tilted enclosure free convection is limited to lower Rayleigh numbers ($\leq 10^6$), mainly to analyze the instabilities in laminar free convection. Extending the visualization of flow patterns to include higher Rayleigh numbers ($Ra > 10^6$) will help our understanding of the mechanism behind the transition to turbulence and the turbulent free convection.

These observations and inferences from the literature and the scaling analysis performed in the following section form the basis of this dissertation and the subsequent experimental design.

1.2 Scaling analysis

A scaling analysis is performed to identify the significant dimensionless parameters for a tilted enclosure problem, which is the first step toward designing the experiments for the present study.

Consider a rectangular enclosure, as shown in Figure 1.1, the hot-end of which (with a uniform surface temperature of T_h) is tilted at an angle of ϕ from the horizontal. Here, T_c denotes the cold-end uniform surface temperature, H is the spacing between the hot and cold plates, and L is the extent of the hot- or cold-end square plates.

One can write the governing equations for this case as follows:

(i) Continuity equation:

$$\nabla \cdot \vec{V} = 0 \tag{1.1}$$

(ii) Momentum equation:

$$\frac{\partial \vec{V}}{\partial t} + \vec{V} \cdot \nabla \vec{V} + \frac{1}{\rho} \nabla p = \vec{g} \frac{\Delta \rho}{\rho} + \nu \nabla^2 \vec{V} \tag{1.2}$$

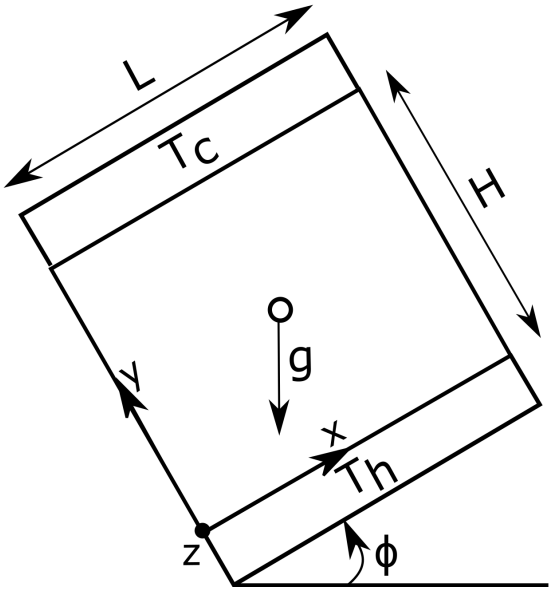

Fig. 1.1 Schematic of tilted enclosure for scaling analysis

where, $\vec{g} = g\sin\phi\hat{i} + g\cos\phi\hat{j} + 0\hat{k}$

(iii) Energy equation:

$$\frac{\partial T}{\partial t} + \vec{V}\cdot\nabla T = \alpha\nabla^2 T \tag{1.3}$$

where, $\vec{V}$ is the velocity vector, ρ is the density of the fluid confined between the plates, p is pressure, ν is the kinematic viscosity, α is the thermal diffusivity, and T is the temperature.

To non-dimensionalize Equations 1.1 - 1.3, characteristic scales for velocity, time, length, pressure, and temperature need to be identified. They are as follows:

$$\left.\begin{array}{l} \text{Velocity, } V_{ch} \simeq \dfrac{\alpha}{H} \\ \text{Time, } t_{ch} \simeq \dfrac{H}{V_{ch}} = \dfrac{H^2}{\alpha} \\ \text{Length, } L_{ch} \simeq \text{L or H, depending on the direction (L for x and z, H for y)} \\ \text{Temperature excess, } \Delta T_{ch} \simeq T_h - T_c \\ \text{Pressure, } p_{ch} \simeq \rho V_{ch}^2 = \dfrac{\rho\alpha^2}{H^2} \end{array}\right\} \tag{1.4}$$

Here, the velocity scale is chosen as the diffusion velocity.

Using Equation 1.4 in Equation 1.2 along with the Oberbeck-Boussinesq approxi-

mation (i.e., density invariant of temperature and pressure, except for the $\Delta\rho$ that appears in the buoyancy term, which is given by: $\frac{\Delta\rho}{\rho} = -\beta\Delta T$), we get:

$$\frac{\alpha^2}{H^3}\frac{\partial\vec{V}^*}{\partial t^*} + \frac{\alpha^2}{H^2 L_{ch}}\vec{V}^*\nabla^*\vec{V}^* + \frac{\alpha^2}{H^2 L_{ch}}\nabla^* p^* = -\vec{g}\beta\left(T_h - T_c\right)\theta + \frac{\nu\alpha}{L_{ch}^2 H}\nabla^{*^2}\vec{V}^* \quad (1.5)$$

Simplifying, Equation 1.5 becomes:

$$\frac{\partial\vec{V}^*}{\partial t^*} + \frac{H}{L_{ch}}\vec{V}^*\nabla^*\vec{V}^* + \frac{H}{L_{ch}}\nabla^* p^* = \frac{-g\beta\left(T_h - T_c\right)H^3}{\nu\alpha}\cdot\frac{\nu}{\alpha}\cdot\frac{\theta\vec{g}}{g} + \frac{\nu}{\alpha}\left(\frac{H}{L_{ch}}\right)^2\nabla^{*^2}\vec{V}^* \quad (1.6)$$

Similarly, Equation 1.3 becomes:

$$\frac{\partial\theta^*}{\partial t^*} + \frac{H}{L_{ch}}\vec{V}^*\nabla^*\theta^* = \left(\frac{H}{L_{ch}}\right)^2\nabla^{*^2}\theta^* \quad (1.7)$$

In Equation 1.5-1.7, '*' represents the corresponding non-dimensional variables, with 'θ^*' denoting the non-dimensional temperature excess (i.e., $\theta^* = \frac{T-T_c}{T_h-T_c}$). Also, one can note that Equation 1.6 and Equation 1.7 are coupled.

From this scaling analysis, or from the non-dimensional momentum (Equation 1.6) and energy (Equation 1.7) equations, one can infer that the significant dimensionless groups for a tilted enclosure free convective heat transfer problem are aspect ratio, Rayleigh number, Prandtl number, and angle of inclination. These parameters can be defined as follows:

$$\text{Aspect ratio } (AR) = \frac{L_{ch}}{H}$$

$$\text{Rayleigh number } (Ra) = \frac{g\beta\left(T_h - T_c\right)H^3}{\nu\alpha}$$

$$\text{Prandtl number } (Pr) = \frac{\nu}{\alpha}$$

$$\text{Angle of inclination} = \phi$$

Considering q'' to be the heat flux (assumed steady) due to free convection from the hot plate to the cold plate and ΔT to be the difference in temperature between the plates, one can define an average heat transfer coefficient for this problem as $h = q''/\Delta T$. Then, the average Nusselt number (Nu), which is the non-dimensional form of the heat transfer coefficient, can be defined as $Nu = hH/k_f$. Thus, the average Nusselt number (Nu) can be interpreted as $f(Ra, AR, Pr, \phi)$

1.3 Objectives

Based on the observations and inferences from the literature and the scaling analysis detailed in the previous section, the following objectives are considered in the present study:

1. To quantify the effect of thermal conductance of sidewalls on Nusselt number for free convection in horizontal enclosures by performing nearly identical sets of experiments with three different sidewall materials for Rayleigh numbers in the range $2.68 \times 10^6 \leq Ra \leq 1.16 \times 10^9$ and to propose a semi-analytical model, based on the idea of extended surfaces, to estimate the sidewall-corrected Nusselt numbers

2. To determine the dependence of Nusselt number on the angle of inclination for a fixed Rayleigh number by performing a set of nineteen experiments, covering 6 decades of Rayleigh numbers (1.85×10^6 to 1.04×10^{11}), for each of the six investigated angles of inclination ($0°$, $30°$, $60°$, $90°$, $120°$, and $150°$)

3. To assess the effect of aspect ratio on Nusselt number by conducting supplementary experiments with varied aspect ratios ($1, 3, 6,$ and 10) and angles of inclination ($0°$, $30°$, $60°$, and $90°$) at a fixed Rayleigh number ($Ra = 4.4 \times 10^7$)

4. To propose $Nu - Ra$ (or, $Nu = f(Ra, AR)$) correlations for all the investigated angles of inclination that is valid for the studied range of Rayleigh numbers (1.85×10^6 to 1.04×10^{11}) and aspect ratios ($1, 3, 6,$ and 10)

5. To visualize and characterize the flow patterns for high-Rayleigh-number ($\geq 10^6$)

free convection in horizontal, vertical, and tilted enclosures using a z-type shadowgraph technique.

CHAPTER 2
Literature Review

Free convection across a fluid layer confined between two differentially heated parallel isothermal plates is of great significance to many scientific and engineering applications. When the temperature gradient is anti-parallel to the body force field (which, in most common applications is the acceleration due to gravity), as is the case for a horizontal enclosure heated from below, convection (or, specifically, bulk fluid motion) occurs only if the density gradient is above a certain value. In contrast, when the temperature gradient is orthogonal to the gravitational vector, as is the case for a vertical enclosure, fluid motion is always present. But, for a differentially heated enclosure inclined at an angle (ϕ) with the horizontal, the flow and heat transfer characteristics are distinct and complex, and may even assume some behavior of horizontal or vertical enclosures based on the value of the angle of inclination. Thus, due to their distinct behavior, the literature review has been split into three separate sections. Section 2.1 reviews the literature for the horizontal enclosure problem, Section 2.2 examines the literature pertaining to the vertical enclosure problem, and Section 2.3 discusses the literature for the inclined enclosure problem.

2.1 Horizontal enclosure

Bénard (1901) and Rayleigh (1916) are the pioneers in research pertaining to free convection across a horizontal fluid layer. Bénard has observed some flow patterns when a thin layer of sperm whale oil is heated from below. Rayleigh has used basic fluid flow and energy equations to propose a theoretical explanation for Bénard's results and,

thus, established the existence of a critical density gradient, below which the bulk fluid motion is absent (or, in other words, the heat transport across a fluid layer is purely due to thermal diffusion or conduction). When the density gradient exceeds this critical value, the consequent buoyant force dominates the viscous stabilizing force to set up fluid motion. Here, the net result of buoyant and viscous forces is responsible for convection.

The time scale of the thermal diffusion (τ_d) across a horizontal fluid layer of height, H, can be defined as $\frac{H^2}{\alpha}$. The time scale of convection for a fluid element of size, H, can be determined by assuming an equilibrium between the buoyant force ($F_B = \Delta\rho H^3 g$) and the viscous force ($F_V = \mu H u$) and, thus, equality of the two forces. This yields a velocity scale, $u \sim \frac{\Delta\rho H^2 g}{\mu}$, and a time scale, $\tau_c \sim \frac{H}{u} \sim \frac{\mu}{\Delta\rho H g}$. By assuming a linear relation for the density deficit with the temperature difference across the fluid layer $\left(\frac{\Delta\rho}{\rho} = -\beta\Delta T\right)$ (refer to the Oberbeck-Boussinesq approximation in Section 2.1.5), one gets a non-dimensional parameter, called the Rayleigh number, given by $Ra = \frac{g\beta\Delta T H^3}{\nu\alpha}$. Thus, Rayleigh number can be defined as the ratio of the time scales of thermal diffusion and convection. Hence, one can conclude that there exists a critical Rayleigh number (Ra_c), below which the heat transport is purely due to thermal diffusion. As the Rayleigh number increases, the dominance of buoyant forces over the viscous forces also strengthens. This leads to changes in the flow patterns and, subsequently, in the flow regimes for the free convection problem.

A treatise by Chandrasekhar (2013) provides a comprehensive analysis of the process of arriving at the critical Rayleigh numbers for convection in a horizontal layer. Linear stability theory has also been found to work well for predicting the onset of convection. The value of this critical Rayleigh number, which has been verified experimentally and analytically, is ≈ 1708 for isothermal surfaces with no-slip.

As the Rayleigh number is increased beyond its critical value, according to Krishnamurti (1973), the flow patterns are in the form of two-dimensional rolls. Further increasing the Rayleigh number first causes a transition to a steady three-dimensional flow, then to a time-dependent flow, and, finally, to a turbulent flow. Krishnamurti

(1973) has also observed that these transitions are strongly dependent on Prandtl number (Pr), with a direct transition from two-dimensional flow to time-dependent flow when $Pr \leq 5$. These transitions have also been extensively documented by Malkus (1954), Willis and Deardorff (1967), Brown (1973), and Chu and Goldstein (1973).

Since the current study focuses mainly on turbulent free convection, the discussion in the following sections will be limited to moderate- and high-Rayleigh-number studies. Hence, the low-Rayleigh-number convection, which has been extensively studied both analytically and experimentally and is the subject of a number of reviews (Brindley, 1967; Palm, 1975; Bergé and Dubois, 1984), will not be pursued further.

2.1.1 Flow structures and visualization studies

High-Rayleigh-number (or, turbulent) Rayleigh-Bénard convection is characterized by a large scale flow, i.e., a well-defined and nearly coherent circulating roll, spanning the height of the convection cell and superimposed on the turbulent background. This large scale flow is driven by the warm and cold thermal plumes emitted from the unstable thermal boundary layers near the top and bottom plates, respectively. The eruption of these thermal plumes, and their transport across the central region, and the formation of the large scale flow have been first reported by Chu and Goldstein (1973). A representative image depicting the transport of such a thermal is given in Figure 2.1. A pictorial representation of the large scale flow, the plumes, and the boundary layers is given by Figure 2.2a. A shadowgraph of the same at $Ra = 6.8 \times 10^8$ ($Pr = 596$ and $AR = 1$) is shown in Figure 2.2b.

An interesting characteristic of the large scale flow is its irregular and occasional cessations, i.e., a momentary vanishing of the entire circulation flow followed by a randomly established new direction (Sreenivasan et al., 2002; Brown and Ahlers, 2006; Xi and Xia, 2007). This phenomenon is called a cessation if the flow direction is unaltered and a reversal if the flow direction has changed.

Wang et al. (2018) have communicated that the intermittent eruptions of thermal plumes disrupt the large scale flow so that its rotation is reset after each eruption event, with an equal probability for the large scale flow to be in either clockwise or counter-

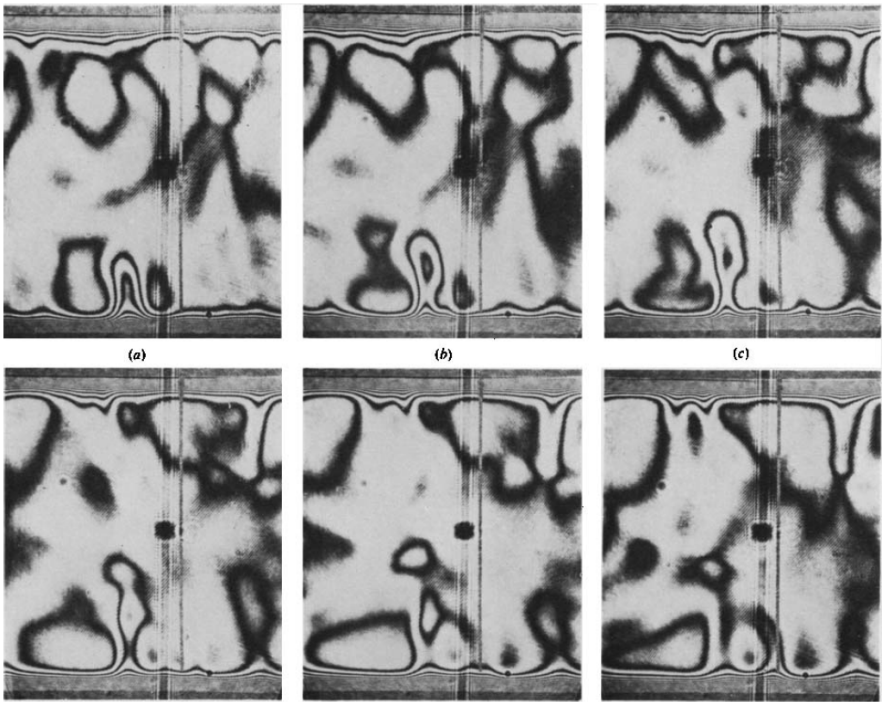

Fig. 2.1 Release of a thermal plume and its transport at $Ra = 2.23 \times 10^6$ (Chu and Goldstein, 1973)

clockwise direction. Fleischer and Goldstein (2002) have observed that these thermal plumes are uniformly emitted from multiple random locations of the hot and cold plates. At very high Rayleigh numbers ($Ra \sim 10^{10}$), these plumes penetrated through the horizontal large scale flow near the plates and reached the core of the enclosure while the bulk of the core remained primarily homogeneous. They have further reported that as the Rayleigh number is increased beyond 10^{11}, frequent horizontal bursts (characterized by a sudden random horizontal fluid burst from each direction) sweep these plumes toward the sidewalls. These horizontal bursts then force the vertically moving plumes into swirls and eddies. The plume eruption, velocity and intensity of the large scale flow, and burst frequency have also been observed to increase as the Rayleigh number is increased.

Ahlers et al. (2009a) have reported that the large scale flow has a fixed and predominant orientation along the diagonal when using rectangular enclosures. Furthermore, when the aspect ratio is altered from unity, there is a high possibility of the large scale flow splitting into multiple rolls.

Interestingly, according to Chu and Goldstein (1973), their experiments using water

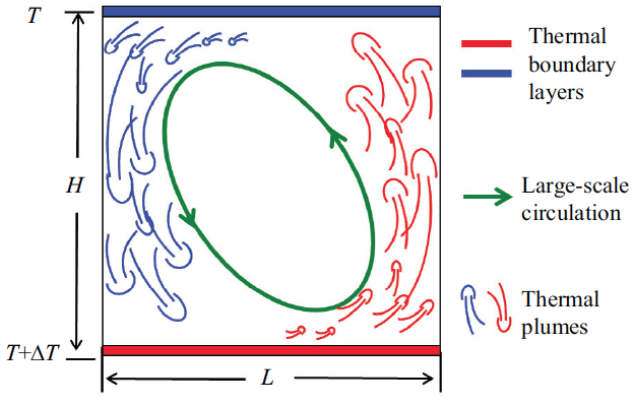

(a) A schematic drawing of turbulent Rayleigh-Bénard convection that shows the major coherent structures in the system: thermal plumes and the large scale flow, as well as the boundary layers at the top and bottom plates (Xia, 2013)

(b) Shadowgraph visualization of rising and falling plumes at $Ra = 6.8 \times 10^8$, $Pr = 596$ (dipropylene glycol) in an $AR = 1$ cell (Shang et al., 2003)

Fig. 2.2 Salient flow structures in turbulent Rayleigh-Bénard convection

as the convecting fluid for Rayleigh numbers beyond 4×10^6 have shown that, despite all these, the central region of the enclosure (or, the core) is found to maintain the mean temperature (T_m, which is the average of the hot- and cold-end temperatures). Hence, most of the temperature drop is expected to occur only within a few boundary layer distances from the hot and cold isothermal plates.

Cioni et al. (1996) have performed experiments with rectangular enclosures, using water as the working fluid, to examine the effect of large scale flow on heat transport (in other words, on the Nusselt number). They have utilized two similar test cells, with one having several vertically positioned screens to weaken the large scale flow, to compare the heat transfer rates and flow patterns for each of the cases. They have observed considerably weak large scale flow in the test cell having vertical screens, but the heat transfer rates for both test cells are found to be identical. This suggests that heat transport is determined primarily by the conductance and the instability of the thermal boundary layers, which are not significantly affected by the large scale flow. The thermal plumes find their own way to exchange energy in the absence of (or, in presence of) a weak large scale flow. This shows the insensitivity of Nusselt number to the large scale flow.

Further details on the flow structures in turbulent Rayleigh-Bénard convection can

be found in Ahlers et al. (2009a) and Xia (2013). Ahlers et al. (2009a) have also emphasized the importance of experimentally exploring flow structures in rectangular enclosures of large aspect ratios ($AR > 4$), which has hardly been attempted.

2.1.2 Classical theories and scaling arguments

Priestley (1959) is one of the earliest physicists to come up with a theoretical scaling for free convection. Priestley has used similarity and dimensional analysis to propose that, at high Rayleigh numbers, when the fluid layers are bounded by two differentially heated surfaces, the two boundary layers do not communicate. Thus, one can infer that the heat flux should be independent of the fluid layer thickness. The classical $\frac{1}{3}^{rd}$ scaling, or power-law, relation ($Nu \sim Ra^{1/3}$), is formulated on the basis of this assumption.

Consider q" to be the heat flux (assumed steady) due to free convection from the hot bottom surface to the cold top surface, and ΔT to be the difference in temperature between these two surfaces. One can define the average heat transfer coefficient for the Rayleigh-Bénard convection problem as $h = \frac{q"}{\Delta T}$. Hence, the average Nusselt number, which is the non-dimensional form of this heat transfer coefficient, can be defined as $Nu = \frac{hH}{k_f}$. Given that the boundary layers at the bottom and top plates develop independently and are not coupled in any manner, this immediately yields a scaling relation of $Nu \sim Ra^{1/3}$.

But, Kraichnan (1962) has postulated that, at some point, the boundary layers become coupled due to the large scale flow (often, also termed as the mean flow), which interacts with the top and bottom boundary layers. According to Kraichnan (1962), when the turbulent transport above the boundary layer becomes the dominant mechanism, the heat flux increases and becomes independent of the molecular viscosity and the thermal conductivity. This situation can be analytically true only when Nusselt number scales as $Nu^2 \sim RaPr$ or $Nu \sim (RaPr)^{1/2}$. Thus, Kraichnan's analysis predicts a shift in the exponent of Rayleigh number in the $Nu - Ra$ correlation from $\frac{1}{3}$ to $\frac{1}{2}$. This regime, having very high Rayleigh numbers and a $\frac{1}{2}$ power-law, is termed as the ultimate (or, asymptotic) regime. Ahlers et al. (2012) have used the Grossmann-Lohse

model (Grossmann and Lohse, 2000; see Section 2.1.3 for details) and determined the Rayleigh number (for AR = 1 and $Pr \approx 1$) for transitioning to this ultimate regime to be $\sim 10^{14}$. Since the highest value of Rayleigh number for the present study is 10^{11}, investigations focusing on the existence of the ultimate regime will not be discussed further.

2.1.3 Dissipation based regime-specific scaling arguments

According to Shraiman and Siggia (1990) and Siggia (1994), two significant quantities that play an important role in the heat transport process of the turbulent Rayleigh-Bénard convection are kinetic energy dissipation rate and thermal energy dissipation rate, which are respectively identified as:

$$\text{Kinetic energy dissipation rate:} \varepsilon_{u(\boldsymbol{x},t)} = \frac{1}{2}\nu \sum_{ij} \left[\frac{\partial u_{j(\boldsymbol{x},t)}}{\partial x_i} + \frac{\partial u_{i(\boldsymbol{x},t)}}{\partial x_j} \right]^2$$

$$\text{Thermal energy dissipation rate:} \varepsilon_{\theta(\boldsymbol{x},t)} = \alpha \sum_{i} \left[\frac{\partial \theta_{(\boldsymbol{x},t)}}{\partial x_i} \right]^2$$

It is to be noted that $\varepsilon_{u(\boldsymbol{x},t)}$ and $\varepsilon_{\theta(\boldsymbol{x},t)}$ represent direct dissipation of the turbulence kinetic energy and thermal energy due to the breaking down of eddies into smaller and smaller eddies by virtue of the fluid viscosity and thermal diffusivity. Thus, they can be determined by knowing the gradients of the turbulent velocity $(u(\boldsymbol{x},t))$ and temperature $(\theta(\boldsymbol{x},t))$ fields.

Also, Shraiman and Siggia (1990) and Siggia (1994) have presented the exact relations for the ensemble (or, space-time) averaged energy dissipation rates for Rayleigh-Bénard convection as:

$$\varepsilon_u = \frac{\nu^3}{H^4}(Nu - 1)RaPr^{-2}$$

$$\varepsilon_\theta = \alpha \left(\frac{\Delta T}{H} \right)^2 Nu$$

Grossmann and Lohse (2000) have proposed a unifying theory, based on ε_u and ε_θ, to explain the different plausible power-law relations by separating ε_u and ε_θ into their individual contributions by the bulk in the isothermal core (due to the mean flow within the enclosure) and boundary layers near the hot/cold walls. Based on the relative dominance in the contributions of bulk, or boundary layers, to the kinetic and thermal energy dissipation rates, they have categorized the Rayleigh-Bénard convection problem into four distinct regimes, as shown in Table 2.1. Here, δ_u and δ_θ represent the momentum and thermal boundary layer thicknesses, respectively, the relative growth of which is determined by the Prandtl number. Grossmann and Lohse (2000) have also presented these results in a regime-based map, as shown in Figure 2.3, and have hypothesized the possibility of having a linear combination of scaling relations for data points that are spread across two neighboring regimes.

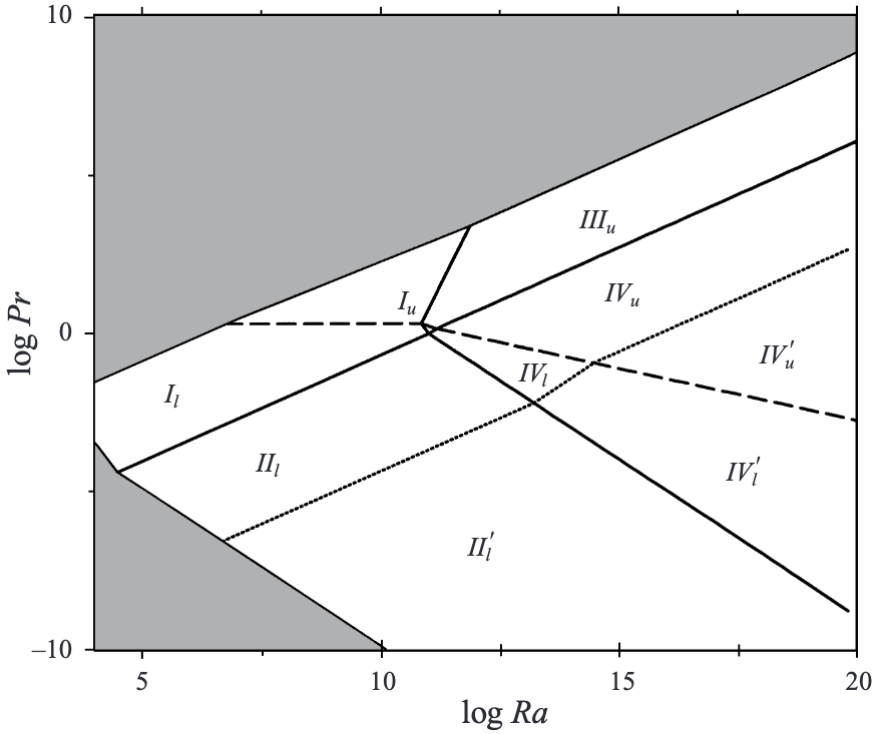

Fig. 2.3 Regime-based map by Grossmann and Lohse (2000)

2.1.4 Moderate- to high-Rayleigh-number heat transfer studies

There have been many experimental investigations conducted for studying various aspects of the turbulent Rayleigh-Bénard convection. The common experimental tech-

Table 2.1 Regime-specific scaling relation from Grossmann and Lohse (2000)

Regime	Dominance of	Boundary Layer	Nu
I_l	$\epsilon_{u,BL}, \epsilon_{\theta,BL}$	$\delta_u < \delta_\theta$	$0.27Ra^{1/4}Pr^{1/8}$
I_u		$\delta_u > \delta_\theta$	$0.33Ra^{1/4}Pr^{-1/12}$
II_l	$\epsilon_{u,bulk}, \epsilon_{\theta,BL}$	$\delta_u < \delta_\theta$	$0.97Ra^{1/5}Pr^{1/5}$
II_u		$\delta_u > \delta_\theta$	$\sim Ra^{1/5}$
III_l	$\epsilon_{u,BL}, \epsilon_{\theta,bulk}$	$\delta_u < \delta_\theta$	$6.43 \times 10^{-6}Ra^{2/3}Pr^{1/3}$
III_u		$\delta_u > \delta_\theta$	$3.43 \times 10^{-3}Ra^{3/7}Pr^{-1/7}$
IV_l	$\epsilon_{u,bulk}, \epsilon_{\theta,bulk}$	$\delta_u < \delta_\theta$	$4.43 \times 10^{-4}Ra^{1/2}Pr^{1/2}$
IV_u		$\delta_u > \delta_\theta$	$0.038Ra^{1/3}$

niques for achieving very high Rayleigh numbers are: (i) using compressed gases, wherein high Rayleigh numbers are realized by virtue of increases in the fluid density due to high pressures (Fleischer and Goldstein, 2002; Srinivasan, 2007; Madanan and Goldstein, 2019a), (ii) using cryogenic fluids (mostly, cryogenic helium at a temperature of $\approx 5K$), where very high Rayleigh numbers are attained due to the higher coefficient of thermal expansion ($\beta \approx \frac{1}{T_m}$, where the mean temperature, T_m, is much lower than in a typical ambient condition experiment) and very low viscosity and thermal conductivity (Heslot et al., 1987; Castaing et al., 1989; Chavanne et al., 2001; Roche et al. (2001b, 2002, 2010); Niemela et al. (2000, 2001); Niemela and Sreenivasan (2003, 2006, 2010)), and (iii) using very large convection test cells and/or using high-Prandtl-number fluids (Ahlers and Xu, 2001; Xu et al., 2000; Xia et al., 2002). Some select entries from the literature (mainly experimental) for Rayleigh numbers in the range $10^6 \leq Ra \leq 10^{12}$ are listed in Table 2.2.

One noteworthy observation from the experimental literature is the substantial variation in the exponent of Rayleigh number in the $Nu - Ra$ relation. Though, an increase in the value of the local exponent with an increase in the Rayleigh number is probable, one would expect to observe identical exponents for the same range of Rayleigh numbers. But, as can be observed from the literature tabulated in Table 2.2, this is not the case. Several investigators, like Goldstein and Tokuda (1980), Goldstein et al. (1990), and Niemela and Sreenivasan (2006), have observed a $\frac{1}{3}^{rd}$ scaling relationship through their experiments in the range $10^8 < Ra < 10^{12}$. Some other researchers (Fleischer and Goldstein, 2002; Nikolaenko et al., 2005; Srinivasan, 2007) have also obtained an exponent very close to $\frac{1}{3}$ for a similar range of Rayleigh numbers, which

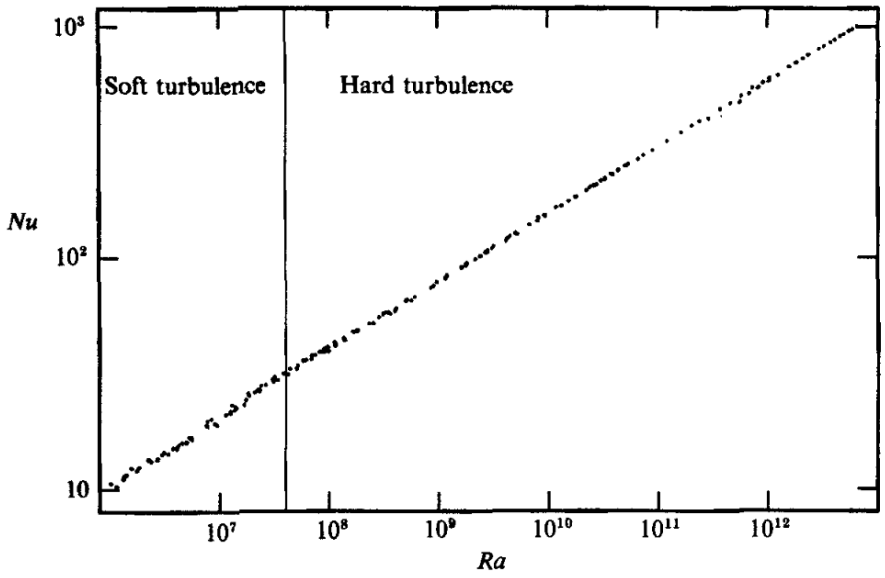

Fig. 2.4 Soft vs. hard turbulence, with a transition at 4×10^7 (Castaing et al., 1989)

also indicates a possibility of the classical scaling relation. In contrast, many studies for moderate Rayleigh numbers have reported a scaling relationship ($Nu \sim Ra^{2/7}$) that differs from this classical scaling relationship (Castaing et al., 1989; Wu and Libchaber, 1992; Belmonte et al., 1994; Ciliberto et al., 1996; Urban et al., 2014). Niemela et al. (2000) and Niemela and Sreenivasan (2003) have proposed yet another scaling argument ($Nu \sim Ra^{0.31}$) based on their experimental study using cryogenic helium over a wide range of Rayleigh numbers ($10^6 \leq Ra \leq 10^{17}$). A similar scaling relation has also been recently communicated by Chong and Xia (2016) from their numerical studies for $3 \times 10^4 \leq Ra \leq 10^{11}$. This discrepancy, and the potential cause of the same, will be discussed in Section 2.1.4.4. Various other reasons that may alter the experimental Nusselt number are discussed in Sections 2.1.4.1 through 2.1.5.

Another interesting communication has been made by Heslot et al. (1987), who have observed an exponent of $\frac{2}{7}$ for Rayleigh number in the $Nu - Ra$ relation for high Ra values ($4 \times 10^7 \leq Ra \leq 6 \times 10^{12}$) and a higher exponent of $\frac{1}{3}$ for lower Ra values ($5 \times 10^5 \leq Ra \leq 4 \times 10^7$). Although both of these Ra ranges correspond to the turbulent regime, the scaling relation is different. Heslot et al. (1987) have prefered to distinguish them as soft turbulence ($\frac{1}{3}$ exponent) and hard turbulence ($\frac{2}{7}$ exponent), because both regimes are turbulent, yet distinct.

Computational modeling for the Rayleigh-Bénard convection has been mostly carried out using Direct Numerical Simulations (DNS). Several advantages of this method over experimental methods are: (i) it does not require probes to make local or global quantity measurements, (ii) the boundary conditions can be set at will to match those for an ideal Rayleigh-Bénard convection scenario (isothermal hot and cold plates and adiabatic sidewalls), and (iii) fluid properties (for example, Prandtl number) and the texture of the hot and cold walls can be chosen as desired. The disadvantages of DNS simulations are mainly the computational time (CPU hours $\propto Ra^{3/2} \ln Ra$), which increases with an increase in Rayleigh number, and the spatial resolution requirements (very fine resolution in the boundary layers) at very high Rayleigh numbers, which may get sacrificed.

Kerr (1996) is one of the earliest to perform 3D simulations of the Rayleigh-Bénard convection ($Ra = 2 \times 10^7$, $Pr = 0.7$) and has reported a $Nu - Ra$ scaling relation of $Nu \sim Ra^{0.28}$. Benzi et al. (1998) have also obtained an effective exponent of ≈ 0.28 for the Rayleigh number based on their DNS simulations using a lattice Boltzman method for a fixed Rayleigh number of 3.5×10^7.

Verzicco and Camussi (1997, 2003) have used DNS based on a finite difference scheme to solve for the flow and heat transfer in a cylindrical Rayleigh-Bénard cell of $AR = \frac{1}{2}$ ($2 \times 10^6 \leq Ra \leq 2 \times 10^{11}$ and $Pr = 0.7$). They have reported that the single-roll large scale flow is observed to split into a double-roll large scale flow (with one roll over the other). Amati et al. (2005) have extended the values of Rayleigh number in the DNS simulations of Verzicco and Camussi (1997, 2003) to 2×10^{14} and have reported a $Nu - Ra^{1/3}$ scaling relation.

Stevens et al. (2011) have performed DNS for cylindrical Rayleigh-Bénard cells of varied aspect ratios and different Prandtl numbers and a Rayleigh number of 2×10^{12}. They have communicated a $Nu - Ra^{1/3}$ scaling relation and a negligible dependence of Prandtl number in the heat transfer behavior.

Many other investigators have employed DNS based on finite volume schemes to study various other aspects of the Rayleigh-Bénard convection. Shishkina and Wagner

(2006, 2007, 2008) have studied the role of thermal plumes and the organization of the large scale flow in the Rayleigh-Bénard convection. Verzicco (2002, 2004) has also extensively examined the effect of sidewall thermal conductance (see Section 2.1.4.4) and finite thermal conductivity of the hot and cold plates (see Section 2.1.4.2) on experimentally estimated Nusselt numbers.

A comprehensive review of turbulent Rayleigh-Bénard convection has been provided by Siggia (1994), Ahlers et al. (2009a), and Chillá and Schumacher (2012).

2.1.4.1 Effect of aspect ratio on Nusselt number

The effect of aspect ratio and, thus, the effect of the large scale flow in the core, on Nusselt number has been probed by many investigators. Most investigators have reported slight to no discernible effect of aspect ratio on Nusselt number.

Deardorff and Willis (1965) have reported that the Nusselt number becomes asymptotic when aspect ratio is increased to values greater than 2. Goldstein et al. (1987) have examined the effect of aspect ratio at a fixed Rayleigh number of 4.8×10^{10} by performing electrochemical mass transfer experiments with varied aspect ratios in the range $1.4 \leq AR \leq 18$ and have reported no discernible effect of aspect ratio on Nusselt number.

Xu et al. (2000) have also performed experiments for varied aspect ratios ($0.5 \leq AR \leq 12.8$) at a fixed Rayleigh number to verify the isolated effect of aspect ratio on Nusselt number. They have observed that the Nu values decrease slightly as the aspect ratio is increased. Interestingly, they have found the scaling exponent in the $Nu - Ra$ relation to be a constant and the pre-factor to be responsible for this change in Nusselt number with varied aspect ratios at a fixed Rayleigh number.

Wu and Libchaber (1992) have observed a strong dependence of Nusselt number on aspect ratio, with the pre-factor showing a 30% increase when the aspect ratio is changed from 0.5 to 1. Nikolaenko et al. (2005) have later attributed this variation to the improper correction of the sidewall conductance heat loss and the finite thermal conductivity of the hot and cold plates (see Sections 2.1.4.4 and 2.1.4.2). They have also observed the sidewall corrected Nu values to be independent of AR when $AR \geq 0.43$.

Sun et al. (2005), after examining $AR = 0.67, 1, 2, 5, 10,$ and 20 at a fixed Rayleigh number, have reported that the corrected Nu values are smaller for larger aspect ratios, but this observed difference in the Nu values between the smallest and the largest aspect ratio is only minimal. Beyond $AR = 10$, they have found the Nusselt number to be independent of aspect ratio. A similar weak dependence of Nusselt number on aspect ratio has been reported by the recent investigations of Zhou et al. (2012) and Madanan and Goldstein (2019a), based on their experiments with rectangular test cells of varied aspect ratios at a fixed Rayleigh number and Prandtl number.

Since the large scale flow in the core is clearly altered by the aspect ratio, especially below and above an aspect ratio of unity, this weak dependence of Nusselt number on aspect ratio clearly also supports the claims of Ahlers et al. (2009a) that the Nusselt number is insensitive to the nature of the large scale flow at the core.

Theoretical studies to understand the effect of aspect ratio on Nusselt number are limited to the studies conducted by Grossmann and Lohse (2003) and Ching and Tam (2006). Ching and Tam (2006) have proposed a pre-factor correlation in terms of aspect ratio, with an observed decrease in this pre-factor as the aspect ratio is increased.

2.1.4.2 Effect of finite plate thermal conductivity on Nusselt number

As discussed by Verzicco (2004), to maintain isothermal surfaces on the inner surfaces, which are in contact with the convecting fluid, of hot and cold plates, the thermal conductivity of the plates should be very large compared to that of the working fluid. Though this situation may be satisfied for low Rayleigh numbers, the apparent thermal conductivity of the convecting fluid for very high Rayleigh numbers can be large due to turbulence and may become comparable to that of the plate. Thus, a careful analysis is required to compare the thermal conductivity of the plate and the effective thermal conductivity of the fluid to devise a model to correct the measured Nu values in the case of comparable thermal conductivities.

Although some investigators (Chaumat et al., 2002; Hunt et al., 2003) have pursued this challenge, the first useful solution has been suggested by Verzicco (2004). Verzicco (2004) has performed DNS of a Rayleigh-Bénard cell, taking into account the presence

of sidewalls and has suggested a correction for the measured Nu values in terms of ratio of the effective thermal resistances of the fluid and the plate. He has related the Nusselt number for infinitely conducting plates (Nu_∞) and the measured Nusselt number as:

$$\frac{Nu_\infty}{Nu} = \frac{1}{F(X_p)} \tag{2.1}$$

where X_p is the ratio of the effective thermal resistance of the fluid to that of the plate given by:

$$X_p = \frac{R_{th,eff,fluid}}{R_{plate}} = \frac{\left(\frac{H}{k_f Nu}\right)}{\left(\frac{t_h}{k_p}\right)} = \frac{1}{Nu}\left(\frac{Hk_p}{t_h k_f}\right) \tag{2.2}$$

And $F(X_p)$, a fitted function of X_p, is given by:

$$F(X_p) = 1 - \exp\left(-\left(X_p/4\right)^{1/3}\right)\frac{X_p}{X_p - 2} \tag{2.3}$$

Brown et al. (2005) have experimentally approached the same problem with two cylindrical cells, made of aluminum and copper plates respectively, and have observed that the $F(X_p)$ suggested by Verzicco (2004) does not fit very well with their experimental data. They have modified this functional form, as shown in Equation 2.4, to yield better results.

$$F(X_p) = 1 - \exp\left(-c_1 X_p^{c_2}\right) \tag{2.4}$$

where $c_1 = 0.275$ and $c_2 = 0.39$.

The finite thermal conductivity of the plates is typically a serious problem for the Rayleigh-Bénard convection when liquid metals are used as the convecting fluid ($\frac{k_p}{k_f}$ is of the order of 1 to 10). Since this thermal conductivity ratio is larger or of the order of margnitude of 10^4 for experiments with compressed gases, the corresponding X_p values are very large. Thus, unless the Nusselt number is a very high number, these experiments produce only negligible corrections ($F(X_p) \approx 1$).

2.1.4.3 Effect of Prandtl number on Nusselt number

Experimental investigations have been carried out by various researchers to scrutinize the effect of Prandtl number on Nusselt number at a fixed Rayleigh number.

Ahlers (2000) and Xia et al. (2002) have performed experiments using various organic fluids ($4 \leq Pr \leq 1350$) at two fixed Rayleigh numbers (1.78×10^7 and 1.78×10^9) and high Prandtl numbers ($Pr \gg 1$) to examine this effect. They have both observed a gradual decline in the Nu values as the Prandtl number is increased, which is best described by $Nu \propto Pr^{-0.03}$ for the investigated range of Prandtl numbers.

Goldstein and Tokuda (1980) and Goldstein et al. (1990) have examined the Rayleigh-Bénard convection using water ($Pr = 6.6$) and an electrochemical solution (Sc ($\approx Pr$) $\approx$ 2750) and have communicated scaling relations of $Nu = 0.0556Ra^{1/3}$ and $Nu = 0.0659Ra^{1/3}$, respectively. Forcing a Pr^m factor into these correlations yields an m value of -0.028, which, interestingly, is comparable to the -0.03 exponent observed by Ahlers (2000) and Xia et al. (2002).

For low Prandtl numbers ($Pr \ll 1$), many investigators have conducted experiments using either mercury ($Pr \approx 0.025$) (Rossby, 1969; Naert et al., 1997; Cioni et al., 1997; Glazier et al., 1999) or liquid sodium ($Pr \approx 0.005$) (Horanyi et al., 1999).

Ahlers et al. (2009a) have plotted these results, together with their results for air ($Pr \approx 0.7$) and water ($4 \leq Pr \leq 7$). They have observed a steep increase in the Nu values with increasing Prandtl numbers up to $Pr \approx 0.5$, but the Nu values have been found to be independent of Prandtl number for $Pr \gtrsim 1$. A similar observation has also been communicated by Roche et al. (2002), based on their experiments with cryogenic helium ($0.7 \leq Pr \leq 21$).

Also, the effect of Prandtl number on Nusselt number has been analytically predicted by Grossmann and Lohse (2000) for various Ra and Pr values (Refer to Table 2.1).

2.1.4.4 Effect of sidewall conductance on Nusselt number

One of the common approaches to correct for the heat loss through the sidewalls is the empty-cell gradient method. In this method, the sidewall conductance is estimated

by assuming that there is no convection within the test cell or, in other words, the test cell is considered to be an empty-cell having a stagnant fluid. By this assumption, the temperature distribution within the sidewalls can be considered linear, i.e., having a Linear Temperature Profile (LTP), or that for pure conduction.

According to Ahlers (2000), this approach is inadequate when using sidewall materials having thermal conductivities an order of magnitude higher than that of the convecting fluid (for example, Plexiglas or high-density polyethylene sidewalls with compressed gases or stainless steel sidewalls with cryogenic helium) for smaller Rayleigh numbers ($Ra < 10^9$). This yields Nu values that are unreasonably higher than the values that would exist if the sidewalls were perfectly adiabatic. This is because thermal contact between the convecting fluid and the sidewalls in the thin boundary layer regions close to the hot and cold plates imposes a much higher temperature gradient in the sidewalls than given by a conveniently estimated empty-cell gradient.

Ahlers (2000) and Roche et al. (2001a) have both proposed approximate models to correct for the effect of sidewall conductance heat loss on Nusselt number. Ahlers (2000), using his model together with a sidewall material of thermal conductivity approximately 20 times that of the convecting fluid, has observed a 10% correction for $Ra = 4 \times 10^9$ and a 6% correction for $Ra \simeq 10^{11}$. Roche et al. (2001a) have proposed a simple semi-analytical model to estimate this sidewall effect based on wall number (Wn), which they have defined as the ratio of thermal diffusion resistance of the stagnant fluid to that of the sidewalls.

Later, Verzicco (2002), based on his DNS of a Rayleigh-Bénard convection test cell of $AR = \frac{1}{2}$, has reported that the previously proposed corrections by Ahlers (2000) and Roche et al. (2001a) under-predict the sidewall conductance heat loss. Thus, the experimentally calculated Nu values at low Rayleigh numbers, obtained after correcting for the sidewall conductance heat loss (using Ahlers, 2000 or Roche et al., 2001a), are found to be higher than those predicted by his numerical simulations performed for perfectly insulating sidewalls.

In addition, all of these studies have communicated that this effect of sidewall con-

ductance heat loss gradually diminishes as Rayleigh number is increased beyond 10^9.

2.1.5 Very-high-Rayleigh-number experiments and the Oberbeck-Boussinesq approximation

The most important approximation employed for the investigation of the Rayleigh-Bénard convection is the Oberbeck-Boussinesq approximation. This approximation assumes the fluid properties, except for the density difference in the buoyancy term, to be constant, i.e., they show no variation with pressure or temperature. The density difference ($\Delta\rho$) in the buoyancy term is considered to be a linear function of temperature difference (ΔT), as given in Equation 2.5.

$$\frac{\Delta\rho}{\rho} = -\beta\Delta T \tag{2.5}$$

The immediate consequence of this approximation is a perfect top-bottom symmetry. This symmetry may be broken due to non-uniform fluid properties within the convection cell such as when the temperature difference is too high, the pressure is near the critical pressure of the fluid, or the cell is too tall. All of these are common in experimental settings where the goal is to attain very high Rayleigh numbers. These deviations are called non-Oberbeck-Boussinesq (NOB) effects. Wu and Libchaber (1991) have observed that under the non-Oberbeck-Boussinesq (NOB) condition, the temperature at the core region (or, the bulk), away from the hot and cold plates, show a visible shift when compared to the arithmetic mean of the hot and cold plate surface temperatures. They have proposed a measure to quantify this effect in terms of the ratio of temperature drops in the hot and cold boundary layers, which is given by:

$$\frac{\Delta T_c}{\Delta T_h} = \left(\frac{\beta_h \nu_c \alpha_c}{\beta_c \nu_h \alpha_h}\right)^{1/3} \frac{\alpha_h}{\alpha_c} \tag{2.6}$$

Ideally, this ratio would be unity and any deviation from unity would be identified as a departure from the Oberbeck-Boussinesq approximation.

Gray and Giorgini (1976) have proposed a condition ($\beta\Delta T \lesssim 0.2$) for adhering to

the Oberbeck-Boussinesq approximation.

Niemela and Sreenivasan (2003) have also put forward a method to assess adherence to the Oberbeck-Boussinesq approximation using the measure of fractional deviations $\left(\frac{P_c - P_h}{P_m}\right)$ for the thermo-physical properties relevant to the problem (P). Here, the subscripts c, h, and m stand for cold, hot, and mean, respectively. They have also suggested that the three measures to confirm the validity of the Oberbeck-Boussinesq approximation (given by Gray and Giorgini (1976), Wu and Libchaber (1991), and Niemela and Sreenivasan (2003)) are basically equivalent.

A possible consequence of not adhering to the Oberbeck-Boussinesq approximation can be an increase in the Nu values and, therefore, an increase in the exponent of Rayleigh number in the $Nu - Ra$ relation. For instance, one can compare the results of Niemela and Sreenivasan (2006) and Roche et al. (2001b, 2002). Niemela and Sreenivasan (2006) ($\beta \Delta T \lesssim 0.2$), with an aspect ratio of 4 and, thereby, introducing a weak mean flow, have observed that the exponent of Rayleigh number asymptotes at a value of $\frac{1}{3}$ even for $Ra \sim 2 \times 10^{13}$, whereas experiments by Roche et al. (2001b, 2002) have suggested the possibility of achieving an asymptotic regime only when the Rayleigh number is increased beyond 10^{13}, with an observed increase in the local exponent for $Ra > 2 \times 10^{11}$. Since Niemela and Sreenivasan (2006) adhere to the Oberbeck-Boussinesq approximation and show no increase in local exponent beyond a value of $\frac{1}{3}$, the results of Roche et al. (2001b, 2002) may most likely be due to a weak adherence to the Oberbeck-Boussinesq condition.

Table 2.2 Moderate Ra results from the literature for horizontal enclosures

Authors	Ra Range	Nu-Ra scaling	Pr	AR	Fluid
Goldstein and Chu (1969)	6×10^5 - 1.2×10^8	$Nu = 0.123Ra^{0.294}$	0.71	1	Air
Garon and Goldstein (1973)	1.3×10^7 - 3.3×10^9	$Nu = 0.130Ra^{0.293}$	6.5	2.5, 4.5	Water
Goldstein and Tokuda (1980)	10^8 - 10^{11}	$Nu = 0.0556Ra^{1/3}$	6.5	0.6 - 4.5	Water
Castaing et al. (1989)	10^7 - 10^{12}	$Nu = 0.23Ra^{0.282}$	0.6 - 1.5	0.5 - 1	Cryogenic He
Goldstein et al. (1990)	10^9 - 10^{12}	$Sh = 0.0659Ra^{1/3}$	2750	0.86 - 6	Electrochemical
Wu and Libchaber (1992)	10^9 - 10^{12}	$Nu \sim Ra^{2/7}$	0.64 - 1	1 - 6.7	Cryogenic He
Belmonte et al. (1994)	10^5 - 10^{11}	$Nu = 0.22Ra^{0.285}$	0.7	1	He, N_2, SF_6
Ciliberto et al. (1996)	10^6 - 10^{11}	$Nu = 0.19Ra^{0.29}$	3	0.25, 1, 1.5	Water
Xu et al. (2000)	10^5 - 10^{10}	$Nu = ARa^b$ $0.277 < b < 0.3$ (b increases with Ra)	4.0	0.5 - 12.8	Acetone
Niemela et al. (2000)	10^6 - 10^{12}	$Nu = 0.124Ra^{0.309}$	0.7 - 12	0.5	Cryogenic He
Grossmann and Lohse (2000)	-	various regime-based scaling relations *	-	-	-
Chavanne et al. (2001)	3.6×10^4 - 1×10^{11}	$Nu = 0.188Ra^{2/7}$	0.66 - 36	0.5	Cryogenic He
Fleischer and Goldstein (2002)	1×10^9 - 1.7×10^{12}	$Nu = 0.071Ra^{0.328}$	0.69 - 0.74	0.99 - 2.96	N_2, Ar
Xia et al. (2002)	2×10^7 - 3×10^{10}	$Nu = 0.14Ra^{0.297}Pr^{-0.03}$	4 - 1350	1	Water 1-Pentanol Triethylene glycol Dipropylene glycol
Niemela and Sreenivasan (2003)	6×10^6 - 1×10^{11}	$Nu \sim Ra^{0.31}$	0.7 - 13.4	1	Cryogenic He
Nikolaenko et al. (2005)	7×10^7 - 1×10^{12}	$Nu = 0.0797Ra^{0.3222}$	4.4	0.43, 0.67, 0.98	Water
Niemela and Sreenivasan (2006)	1.1×10^8 - 2.9×10^{12}	$Nu = 0.088Ra^{0.32}$	0.7 - 14.7	4	Cryogenic He
Srinivasan (2007)	2×10^9 - 3×10^{12}	$Nu = 0.063Ra^{0.336}$	0.685 - 0.796	0.6 - 2	N_2, Ar, Kr
Bailon-Cuba et al. (2010)	10^7 - 10^9	$0.165Ra^{0.287}$ at 10^7 $0.118Ra^{0.305}$ at 10^9	0.7	0.5 - 12	- (DNS)
Urban et al. (2014)	10^6 - 10^{15}	$Nu \sim Ra^{2/7}$ when $7.2 \times 10^6 < Ra < 10^{11}$	0.68 - 11.29	1	Cryogenic He
Chong and Xia (2016)	3×10^4 1×10^{11}	$Nu - 1 = 0.106Ra^{0.308}$ when $10^6 < Ra < 10^{10}$	4.38	$\frac{1}{128}$ - 1	- (DNS)

* Refer to Table 2.1 for $Nu - Ra$ scaling relations by Grossmann and Lohse (2000)

2.2 Vertical enclosure

The characteristics of a vertical enclosure are quite different from those of a horizontal enclosure. One such contrasting feature is that in a vertical enclosure, fluid motion is always present. Batchelor (1954) has named this fluid motion as "base flow". Eckert and Carlson (1961) have reported that, despite this base flow, the heat transfer between the hot and cold plates is still purely due to conduction when the driving potential (ΔT) is small. The only exception to this is near the corners of the enclosure where the base flow turns.

Convection occurs when the driving potential is increased. This leads to formation of laminar boundary layers on the vertical active walls, with upward motion along the hot vertical walls and downward motion along the cold vertical walls. When the density gradient (or, the temperature gradient) or the height of the enclosure is sufficiently large, the laminar boundary layer becomes unstable and transitions to a turbulent boundary layer.

This transition between laminar and turbulent boundary layers reveals another difference in the characteristics of the vertical enclosure when compared with the horizontal enclosure, i.e., their flow transition behavior. Unlike flow transition in horizontal enclosures, where the entire flow field undergoes simultaneous transition, in vertical enclosures, the turbulent boundary layer begins at a certain vertical distance from the bottom-most corner when the Rayleigh number (based on the vertical distance) exceeds a critical value. If the Rayleigh number is based on the spacing between the hot and cold isothermal plates, as is the case for the present study, this transition Rayleigh number depends on the aspect ratio, as can be seen from Figure 2.5 (Chenoweth and Paolucci, 1986).

The various flow regimes in a vertical enclosure, as depicted in Figure 2.5, have been extensively studied by Elder (1965a, 1965b). A general review of free convection in vertical enclosures has been provided by Catton (1978), Yang (1987), and Raithby and Hollands (1998).

Table 2.3 Some significant experimental, numerical and analytical literature for vertical enclosure free convection

Authors	Ra Range	$Nu(Ra, AR)$ scaling	Pr	AR	Fluid
Eckert and Carlson (1961)	10^4 - 10^7	$Nu = 0.132Ra^{0.3}AR^{-0.1}$	0.71	2 - 47	Air
Dropkin and Somerscales (1965)	5×10^4 - 7.17×10^8	$Nu = 0.049Ra^{1/3}Pr^{0.074}$	0.02 - 11, 560	4.41 - 16.56	Mercury, Water, Silicone oil
MacGregor and Emery (1969)	10^6 - 10^9	$Nu = 0.046Ra^{1/3}$	1 - 20	10 - 40	Air, water, ethanol and castor oil
Jannot and Mazeas (1973)	7×10^4 - 7×10^{10}	$Nu = 0.082Ra^{1/3}$	0.75	3.5 - 100	N_2, CO_2
Raithby et al. (1977)	turbulent	$Nu = 0.29C_tRa^{1/3}$ $C_t = \left[0.15, 0.14Pr^{0.084}\right]_{max}$	Any	$AR > 5$	Arbitrary
Seki et al. (1978a)	$Ra > 1.86 \times 10^7$ (turbulent)	$Nu = 0.039Ra^{1/3}$	1 - 4	5 - 47.5	Freon
Wirtz and Tseng (1980)	10^6 - 9×10^7	$Nu = 1 + \left[\left[\left(\frac{\widetilde{Ra}AR^4}{362880}\right)^2\right]^{-n} + \left[0.623\widetilde{Ra}\right]^{-n}\right]^{-1/n}$ $\widetilde{Ra} = Ra \cdot \frac{Pr}{Pr+0.2}$	0.2, 0.733, 6.82, and 100	0.2 - 1	Numerical
Elsherbiny et al. (1982a)	10^3 - 10^8	$Nu_1 = 0.0605Ra^{1/3}$ $Nu_2 = \left[1 + \frac{0.104Ra^{0.293}}{\left(1+\left(\frac{6310}{Ra}\right)^{1.36}\right)^3}\right]^{1/3}$ $Nu_3 = 0.242\left(\frac{Ra}{AR}\right)^{0.272}$ $Nu = [Nu_1, Nu_2, Nu_3]_{max}$	0.7	5 - 110	Air
Markatos and Pericleous (1984)	10^6 - 10^{12}	$Nu = 0.082Ra^{0.329}$ or $Nu = 0.072Ra^{1/3}AR^{-1/9}$	0.71	1	Air
Goldstein et al. (1987)	2×10^8 - 1.6×10^{12}	$Nu = 0.0498Ra^{0.312}$ or $Nu = 0.2486Ra^{0.258}AR^{-0.155}$	$S_c \approx 2750$	1.8 - 36	$CuSO_4$ - H_2SO_4 - Water solution
Henkes et al. (1989)	10^9 - 10^{15}	$Nu = 0.047Ra^{1/3}$	0.71 or 7.0	1	Air, Water (numerical, $k - \varepsilon$ turbulence model)
Kuyper et al. (1993)	$Ra \geq 10^8$	$Nu = 0.05Ra^{0.341}$	0.7	1	Air
Hsieh and Wang (1994)	$RaAR^3 > 1.4 \times 10^7$	$Nu = 0.133Ra^{0.301}AR^{-0.192}Pr^{0.053}$	0.7, 6, and 464	3, 5, 10	Air, Water, Silicone oil
Barakos et al. (1994)	10^8 - 10^{11}	$Nu = 0.065Ra^{0.333}$	0.71	1	Air (numerical, $k - \varepsilon$ turbulence model)
Wright (1996)	$Ra > 5 \times 10^4$	$Nu = 0.0674Ra^{1/3}$	$\simeq 0.71$	≥ 40	Air
Bairi et al. (2007)	10^3 - 10^8	$Nu = 0.147Ra^{0.287}$	0.7	0.75 and 1.5	Air
Altaç and Uğurlubilek (2016)	10^8 - 10^{13}	$Nu = a\left(1 + b\exp\left(-c\left(\frac{Ra}{Ra_0}\right)^m\right)\right)Ra^n$ $a = 0.089605$ $b = 0.361711$ $c = 5.85635$ $m = 0.3893$ $n = 0.305$ $Ra_0 = 5 \times 10^{10}$	0.71	1 -10	Air

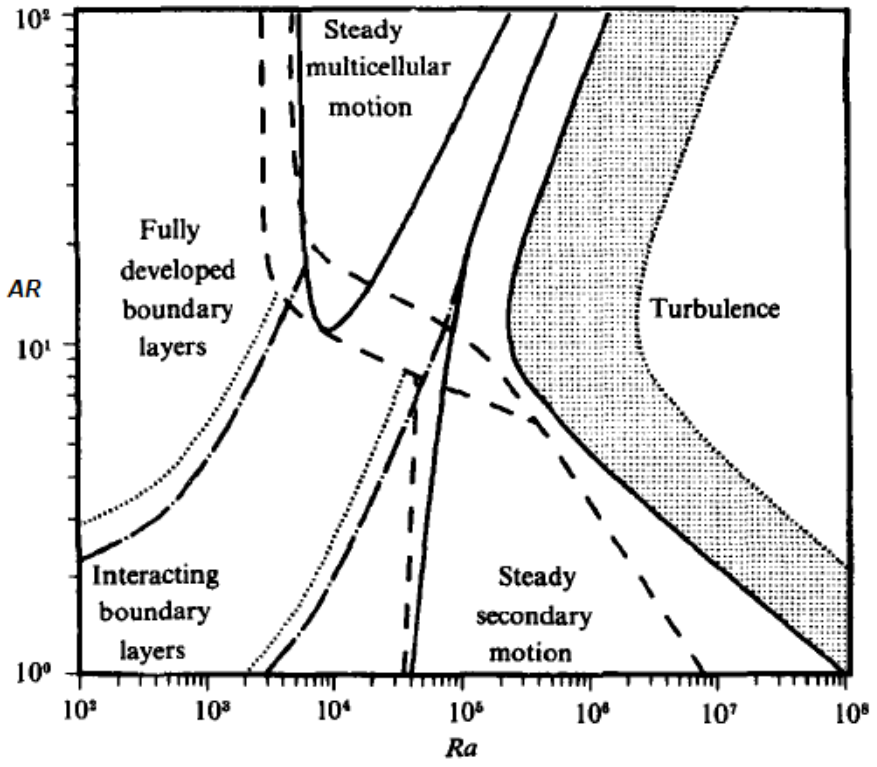

Fig. 2.5 Transition to turbulence: effect of AR and Ra (Chenoweth and Paolucci, 1986)

2.2.1 Moderate- to high-Rayleigh-number heat transfer studies

Analyzing the literature pertaining to free convective heat transfer in vertical enclosures and taking a closer look at its most significant results (see Table 2.3) reveal that when the Rayleigh number is sufficiently high ($\geq 10^6$), with a narrow, tall vertical enclosure ($AR \geq 10$), most studies (with the exception of Goldstein et al., 1987) have reported a $Nu \sim Ra^{1/3}$ relationship. Goldstein et al. (1987) have reported a $Nu \sim Ra^{1/4}$ scaling relation, even when their range of investigated Rayleigh number is very high, with a maximum Ra value of $\sim 10^{12}$. The reason for this may be that their studies, which use an electrochemical solution with a large Schmidt number (or, Pr in the analogous heat transfer domain), yield a laminar Grashof number ($Gr = Ra/Pr$) even at the highest investigated Rayleigh numbers.

2.2.1.1 Effect of aspect ratio on Nusselt number

Unlike in horizontal enclosures, aspect ratio is expected to play a significant role in deciding the free convective heat transport between the two active vertical plates and,

hence, in determining the Nusselt number for vertical enclosures. As communicated by Eckert and Carlson (1961) and Schinkel and Hoogendoorn (1983), this is primarily due to a vertical density stratification present at large Rayleigh numbers. Eckert and Carlson (1961) have observed that fluid temperatures of the central region in horizontal planes are uniform for high Rayleigh numbers ($Ra > 10^6$). However, the fluid temperature increases in the positive vertical direction. Thus, the density of the fluid, is different (or, decreases) at each of the vertical positions, which leads to a vertical density stratification.

Jakob (1946) is the first to propose a power-law relation of the form $Nu = CRa^n AR^m$ to account for the effect of aspect ratio on Nusselt number. Since then, many investigators (Wirtz and Tseng, 1980; Elsherbiny et al., 1982a; Markatos and Pericleous, 1984; Goldstein et al., 1987; Hsieh and Wang, 1994) have attemptted to determine the value of "m". But, most of them have reported differing values for this exponent at high Rayleigh numbers (see Table 2.3).

Numerous other moderate- to high-Rayleigh-number studies have indicated no effect of aspect ratio on Nusselt number, as can be inferred from Table 2.3. But, interestingly, most of these studies have a coupling between Rayleigh number and aspect ratio (or, in other words, Rayleigh number and aspect ratio are not independent). This is because an increase in the Rayleigh number is achieved by changing (or, increasing) the spacing between the active plates, which has a direct consequence on the value of aspect ratio.

2.2.1.2 Effect of Prandtl number on Nusselt number

The effect of Prandtl number on Nusselt number has been studied by several investigators (Dropkin and Somerscales, 1965; MacGregor and Emery, 1969; Seki et al., 1978a; Wirtz and Tseng, 1980; Hsieh and Wang, 1994).

Dropkin and Somerscales (1965) have observed a $Pr^{0.074}$ dependence on Nusselt number based on their experiments with varied Prandtl numbers (0.02 - $11,560$). More recently, Hsieh and Wang (1994) have observed a similar, yet weaker, dependence of Nusselt number on Prandtl number ($Nu \propto Pr^{0.053}$) when they conducted experiments

with air, water, and silicone oil.

However, Wirtz and Tseng (1980) have proposed replacing Rayleigh number with $\left(\frac{RaPr}{Pr+0.2}\right)$ in their correlation to take into account the effect of Prandtl number on Nusselt number and have found the correction valid for a wide range of Prandtl numbers ($0.2 \leq Pr \leq 100$).

Some studies have shown no Prandtl number dependence on Nusselt number when Rayleigh numbers are sufficiently high ($Ra > 10^6$). MacGregor and Emery (1969) and Seki et al. (1978a), for instance, have found a dependence of Nusselt number on Prandtl number when $Ra < 10^6$ (or, for the laminar regime), but have observed no influence of Prandtl number on Nusselt number from their experiments with varied Prandtl numbers in the range $1 \leq Pr \leq 20$ and $1 \leq Pr \leq 4$, respectively, when $Ra > 10^6$.

2.2.2 Visualization studies in vertical enclosures

Most of the visualization studies for vertical rectangular enclosures are limited to the laminar boundary layer regime and for enclosures with very high aspect ratios. Two significant studies are those by Elder (1965a) and Eckert and Carlson (1961).

Elder (1965a) is one of the first to investigate the flow and temperature fields in tall vertical rectangular enclosures (with AR values up to 60) using medicinal parafin and silicone oil ($Pr \approx 1000$) as the working fluids. He has utilized aluminum powder suspended in the fluid for flow visualization and type-T thermocouples for temperature measurements. When $Ra \approx 10^5$ and $AR = 19$, he has observed a development of regular cellular patterns, which he has attributed to strengthening of the base flow. These cellular patterns, which he has termed "secondary flow", become superimposed on the base flow, as shown in Figure 2.6. He has also reported that the sense of rotation of this secondary flow is the same as that of the base flow. When the Rayleigh number is increased further, the amplitude of the secondary flow is observed to become large enough to generate steady cellular motion in the weak shear regions between the two secondary flow cells, which he has termed as "tertiary flow". He has also reported that the temperature field in the core region, which is far removed from the active vertical walls, maintains a uniform temperature at a particular vertical position, with an

observed increase in this temperature upon moving upward (or, vertical temperature stratification).

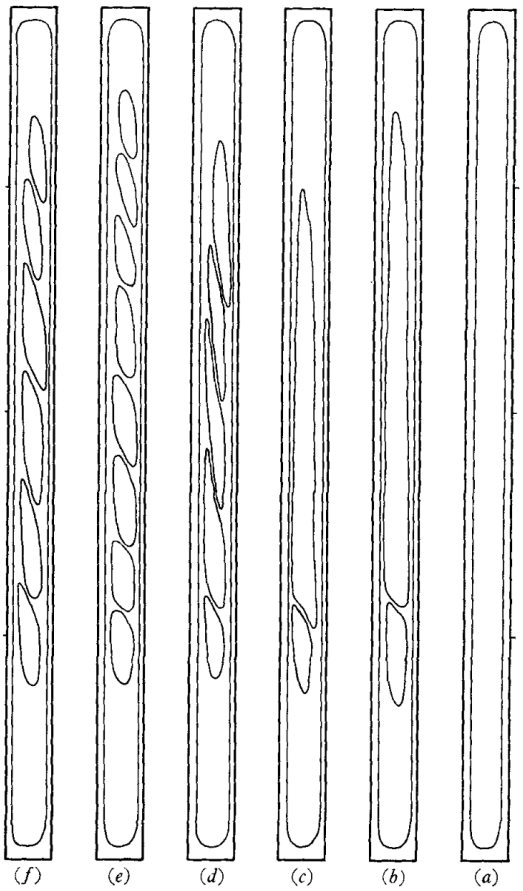

Fig. 2.6 Secondary flow at various Rayleigh numbers for a fixed aspect ratio of 19: (a) 3×10^5; (b) 3.6×10^5; (c) 4×10^5; (d) 4.9×10^5; (e) 5.8×10^5; (f) 6.8×10^5 (Elder, 1965a)

With the aid of a Mach-Zehnder interferometer, Eckert and Carlson (1961) have confirmed this vertical temperature stratification, wherein the temperature is uniform on horizontal planes and increases in the positive vertical direction. They have reported that this will be true only for a regime in which Rayleigh number is greater than 10^6 (and $AR \leq 100$), which they call the boundary layer regime. One sample interferogram from their study showing this regime is Figure 2.7.

Visualization studies, experimental or numerical, in vertical enclosure free convection with very high Rayleigh numbers (or, within the turbulent regime) are scarce. Elder (1965b) has investigated tall vertical enclosures ($AR = 10 - 30$) filled with water ($Pr \approx 7$) for Rayleigh numbers greater than 10^6. He has employed dye in water to study the transition to turbulence and has shown differences in the flow structures due

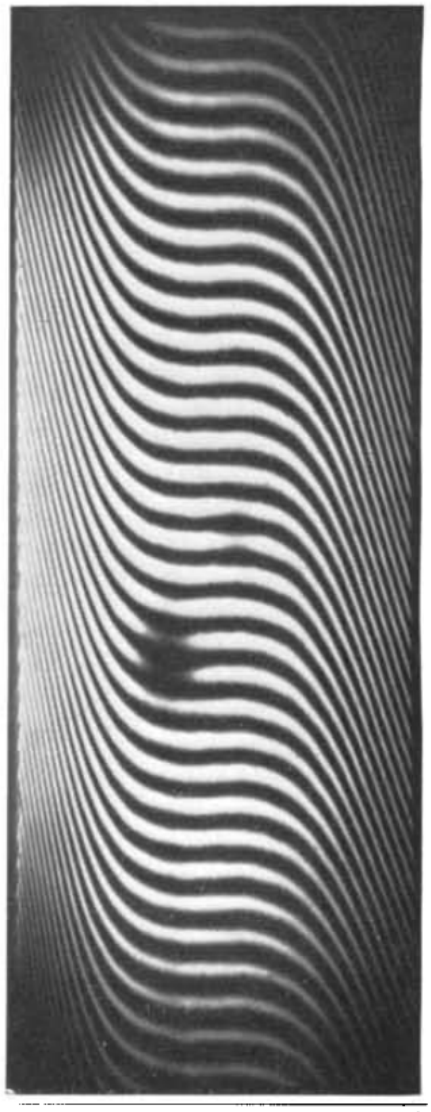

Fig. 2.7 Interferogram of free convection in a tall rectangular enclosure showing vertical temperature stratification (Eckert and Carlson, 1961)

to turbulence. He has reported the presence of travelling wave-like motions, as shown in Figure 2.8, near the hot and cold vertical plates when $Ra > 8 \times 10^8 \sqrt{(Pr/AR)}$. Similar results have also been communicated by Seki et al. (1986).

Also, Bohn et al. (1984) have performed visualization studies using dye in deionized water with $Ra \sim 10^{10}$ and $AR = 1$. They have observed transition to turbulence, as indicated by waviness in the boundary layer (similar to that observed by Elder, 1965b), near the top (bottom) $\frac{1}{3}^{rd}$ of the heated (cooled) vertical plates.

Kuyper et al. (1993) have numerically investigated free convection in a cubical vertical enclosure for $10^4 \leq Ra \leq 10^{11}$ and $Pr \approx 0.7$. They have also performed a de-

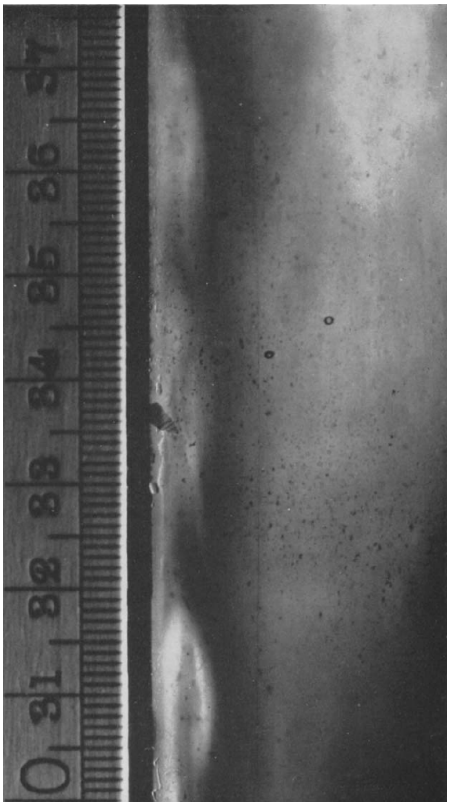

Fig. 2.8 Detailed view of wall wave-fronts obtained for $Ra = 2.2 \times 10^7$ and $AR = 9$ (Elder, 1965b)

tailed analysis for the turbulent regime ($Ra \approx 10^{10}$) using the standard $k - \varepsilon$ turbulence model. Their results show that, even at very high Rayleigh numbers, the temperature distribution in a large part of the enclosure's central region is extremely stratified, with the majority of the temperature drop occuring in a thin boundary layer adjacent to the hot/cold vertical plates, as shown in Figure 2.9. Similar results have also been communicated for high Rayleigh numbers by many other numerical analysts (Yedder and Bilgen, 1995; Bairi et al., 2007; Williamson et al., 2016).

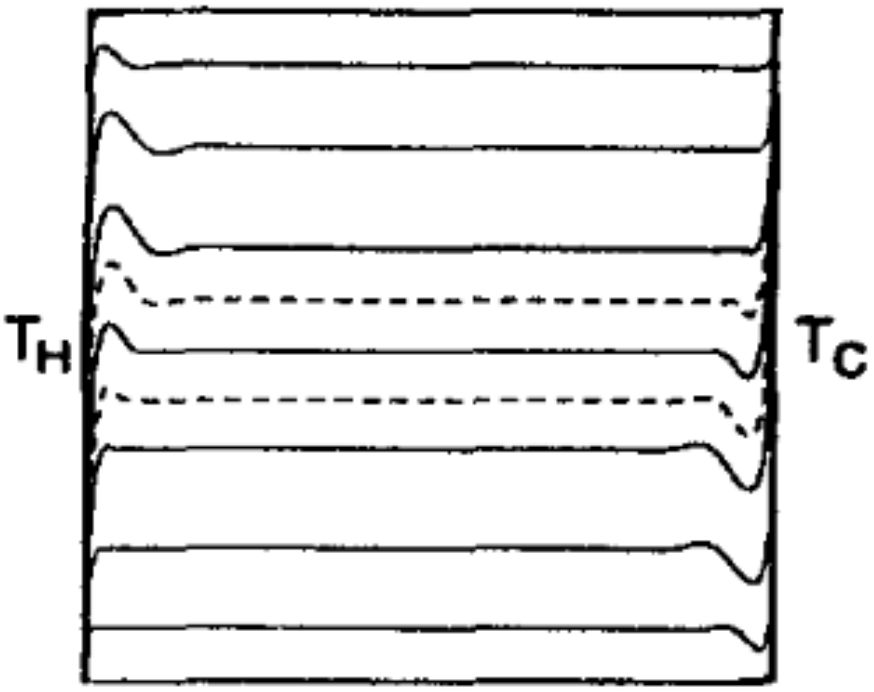

Fig. 2.9 Temperature distribution for $Ra = 10^{10}$ and $AR = 1$ showing vertical temperature stratification (Kuyper et al., 1993)

2.3 Inclined enclosure

Flow and heat transfer characteristics become complex when an enclosure is tilted. There have been numerous experimental, numerical, and theoretical investigations for low- to moderate-Rayleigh-number free convection in tilted enclosures, with many of them often proposing correlating equations for Nusselt number in terms of the studied variables (Table 2.4). But, unfortunately, the data available for high-Rayleigh-number free convection in tilted enclosures are scarce. This is especially the case for $Pr \approx 0.71$, for which there are no experimental data reported beyond a Rayleigh number of 10^7. Hence, discussions on inlcined enclosures in the following sections is limited to low- and moderate-Rayleigh-number (laminar) free convection studies.

2.3.1 Visualization studies: low to moderate Rayleigh numbers

Hart (1971) has systematically studied flow patterns in tilted enclosures with nominal aspect ratios of 25 and 36 by introducing small thin flakes of ground fish-scales into

the convecting fluid (water). He has reported instabilities in the form of longitudinal rolls (i.e., rolls with their axes parallel to the up-slope direction of the inclination) for angles of tilting between 0° and 80°. For near-vertical angles (i.e., 80° - 100°), he has observed transverse rolls (i.e., rolls with their axes parallel to the cross-slope direction of inclination) super-imposed on the base flow. Hideo (1984) has also observed similar flow patterns (longitudinal rolls at lower inclination angles and transverse rolls at nearly vertical angles) through his experiments with inclined rectangular enclosures that cover a wide range of Rayleigh numbers ($1.2 \times 10^3 \leq Ra \leq 2 \times 10^6$) and aspect ratios ($5 \leq AR \leq 83$). He has used air as the working fluid and has introduced cigar-smoke for visualization. Qualitatively similar observations have also been communicated by Goldstein and Wang (1984) and Shadid and Goldstein (1990) through their investigations using an interferometric technique and temperature-sensitive liquid crystals, respectively. Visualized results of these flow patterns and their qualitative interpretations are shown in Figure 2.10.

The main differences among the numerous flow pattern studies for tilted enclosures lie in the values of the angle of inclination at which instabilities change form from longitudinal rolls to transverse rolls, typically called critical angle (ϕ_c) or transition angle (Hart, 1971; Ozoe et al., 1975; Arnold et al., 1976; Hideo, 1984; Goldstein and Wang, 1984; Shadid and Goldstein, 1990). Goldstein and Wang (1984), who have observed this transition at 57.5° for a nominal aspect ratio of 9.25, have attributed the difference in aspect ratio to be the main cause for this variation of reported critical angles. Goldstein et al. (1987) have provided further clarification and have communicated that the value of this critical angle is a weak function of aspect ratio when $AR > 10$ and a strong function when $AR \leq 10$. Arnold et al. (1976) and Goldstein and Wang (1984) have studied the effect of aspect ratio on the critical angle and have communicated an increase in the critical angle when the aspect ratio is increased for $AR \geq 1$.

However, Linthorst et al. (1981) have observed an absence of transverse rolls for vertical enclosures for small to moderate aspect ratios ($AR \leq 7$) and $5 \times 10^3 \leq Ra \leq 2.5 \times 10^5$ and have observed secondary flows inside a base flow (similar to the observa-

tions of Elder (1965b); see Section 2.2.2).

The effects of Prandtl number on critical angle are yet to be studied.

2.3.2 Heat transfer studies: low to moderate Rayleigh numbers

Heat transfer results for inclined enclosures at low to moderate Rayleigh numbers have been documented by many investigators. Some of the significant literature are listed in Table 2.4.

A majority of the heat transfer studies for inclined enclosures is focused on the effect of angle of inclination, aspect ratio, and Rayleigh number on average Nusselt number. One of the major findings from these studies is the strong interlacing effect of angle of inclination and aspect ratio, especially for small aspect ratios ($AR \leq 10$), on the average Nusselt number (Goldstein et al., 1987). Another common noteworthy observation from these studies is the presence of a local minimum in the average Nusselt number for angles of inclination approximately equal to the critical angle, as shown in Figure 2.11 (Arnold et al.,1974; Ozoe et al., 1975; Hamady et al., 1989; Kuyper et al., 1993; Chang, 2014). Most investigators have attributed this characteristic local minimum to be a consequence of the transition between the two modes of instabilities (or, flow patterns), characterized by longitudinal rolls and transverse rolls. Interestingly, some other investigators have not reported the presence of this local minimum (Elsherbiny et al., 1982a; Elsherbiny et al., 1982b; Schinkel and Hoogendoorn, 1985), even for a similar range of Rayleigh numbers.

The majority of earlier work in this area is focused on recommending a simple scaling relation to predict the average Nusselt number for inclined enclosures by relating it to correlations of either horizontal or vertical enclosure problems.

Clever (1973) has proposed a $Nu - Ra\cos\phi$ scaling relation that combines Ra and ϕ into a single parameter by replacing g with $g \bullet \cos\phi$ in the definition of Rayleigh number. Based on their experimental data for $0^\circ \leq \phi \leq \phi_c$, many researchers have confirmed this scaling relation.

Ayyaswamy and Catton (1973) have proposed a $\sin\phi$ scaling for nearly vertical angles ($\phi \approx 90^\circ \pm 30^\circ$), valid only in the boundary layer regime. According to them,

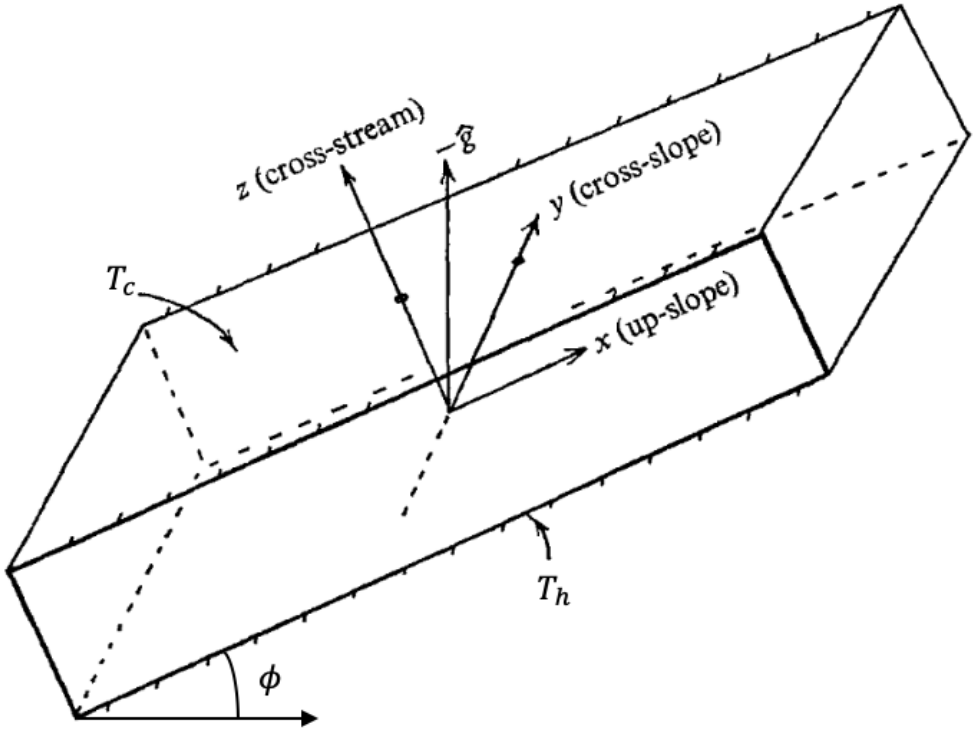

(a) A schematic drawing of a tilted enclosure showing the up-slope and cross-slope directions (Hart, 1971)

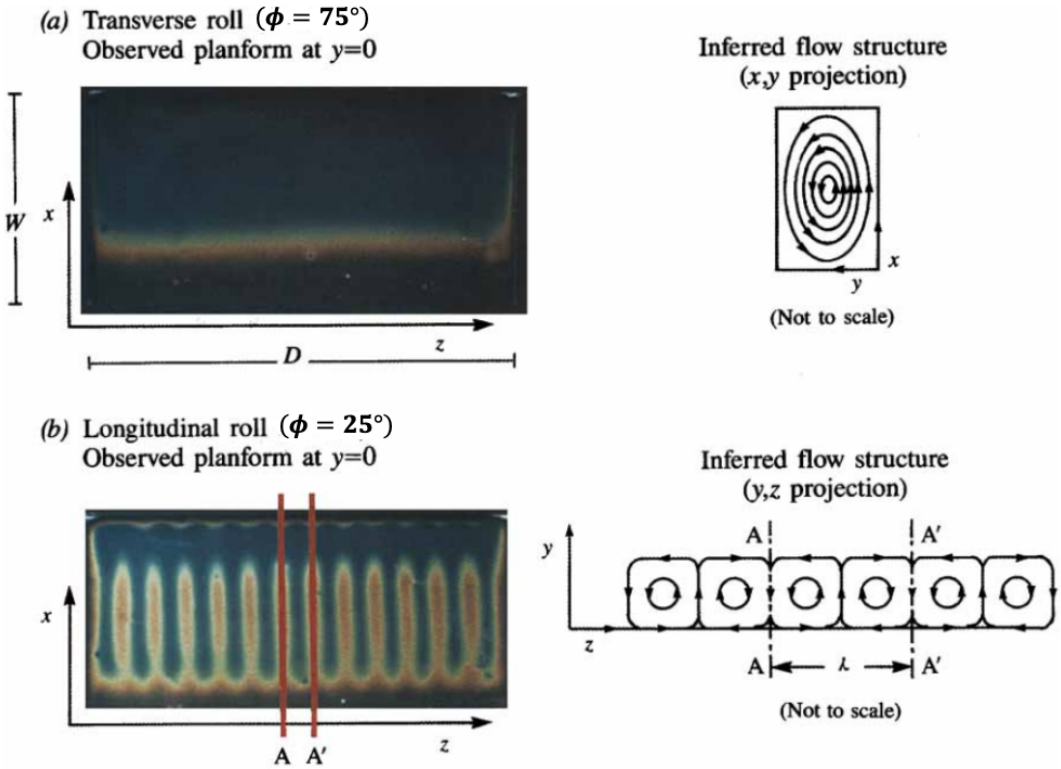

(b) Two different types of instabilities: (a) transverse rolls and (b) longitudinal rolls (Shadid and Goldstein, 1990)

Fig. 2.10 Longitudinal rolls and transverse rolls in low- to moderate-Rayleigh-number free convection in tilted enclosures

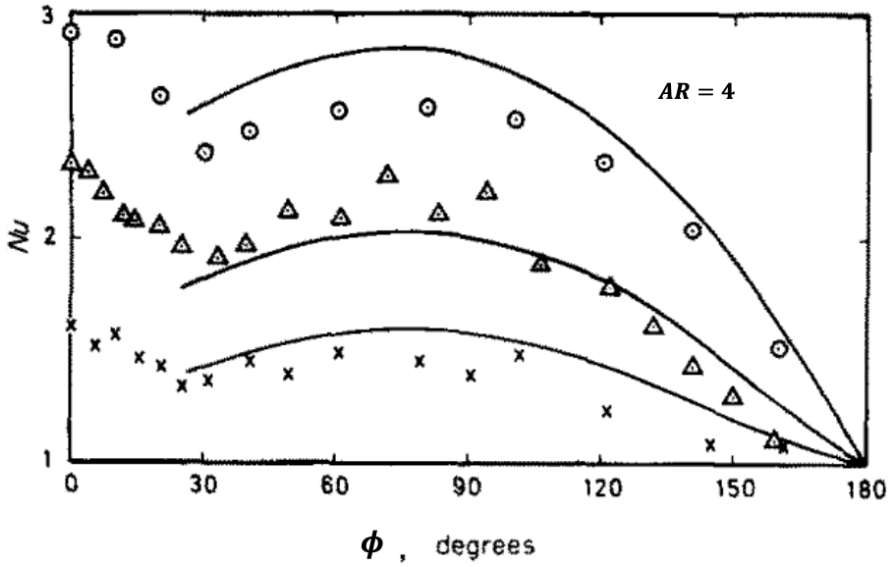

Fig. 2.11 Heat transfer results using silicon oil ($Pr \approx 4000$) in a tilted enclosure of $AR = 4$ showing a Nusselt number local minima at $\approx 30°$ ($\odot : Ra = 1.68 \times 10^4$, $\triangle : Ra = 6.2 \times 10^3$, $\times : Ra = 3.05 \times 10^3$) (Ozoe et al., 1975)

the following two conditions must be fulfilled for free convection in a tilted enclosure to be in the boundary layer regime: (i) $Ra(AR)^3 \sin\phi \gg 10^4$ and (ii) $AR \gg \cot\phi$.

Arnold et al. (1974) have proposed a scaling relation of the form $Nu_{(\phi)} = 1 + [Nu_{(90°)} - 1]\sin\phi$ for $10^3 \leq Ra \leq 10^6$. This scaling relation gives good estimates for the average Nusselt number when $90° < \phi < 180°$ (or, for the heated from above scenario).

It is to be noted that all of the aforementioned studies are limited to low and moderate Rayleigh numbers. Transition to a turbulent regime occurs at high Rayleigh numbers, the value of which, according to Arnold et al. (1974), depends on the aspect ratio and the angle of inclination. Hideo (1984) has proposed conditions of the fully-turbulent regime in terms of Ra and ϕ based on his tilted enclosure experiments, which cover a wide range of aspect ratios ($AR = 5 - 83$) and for a $Pr \approx 0.71$. These conditions are: (i) $Ra\cos\phi > 4 \times 10^5$ (for $\phi < 60°$) and (ii) $Ra\sin\phi > 1.2 \times 10^6$ (for $\phi : 60° - 120°$).

Tilted enclosure experimental studies for high Rayleigh numbers are limited to Goldstein et al. (1987) and Dropkin and Somerscales (1965), as can be seen from Table 2.4. Goldstein et al. (1987) have utilized the heat and mass transfer analogy (Nusselt, 1930; Chilton and Colburn, 1934) to transform their mass transfer results (in terms of

Sh, Sc) before interpreting the corresponding heat transfer analogues (Nu, Pr). Interestingly, since both Goldstein et al. (1987) and Dropkin and Somerscales (1965) have used very high Pr (or, Sc) fluids to achieve high Rayleigh numbers, the corresponding values of Grashof number ($Gr = Ra/Pr$) are smaller, thus limiting the flow regime to either laminar or transitional.

There are also a few numerical studies which take into account slightly higher Rayleigh numbers (Kuyper et al., 1993; Bairi et al., 2007; Williamson et al., 2016).

Kuyper et al. (1993) have performed 2-D numerical simulations of free convection in an inclined square cavity filled with air ($Pr \approx 0.71$) for $10^4 \leq Ra \leq 10^{11}$ and have proposed $Nu - Ra$ power-law relations for $\phi = 45°$ and $\phi = 90°$ in the laminar and turbulent regimes. They have employed the standard $k - \varepsilon$ model for simulating turbulent natural convection, which is assumed to exist for Rayleigh numbers beyond 10^8.

Bairi et al. (2007) have carried out numerical studies using a finite volume method and have proposed correlating equations for Nu in terms of Ra for all the investigated orientations. They have also provided thermal and flow maps of the convecting fluid ($Pr = 0.71$) for several angles of inclination ($\phi = 0°$ to $360°$) and a wide range of Rayleigh numbers ($10^3 \leq Ra \leq 10^8$).

Williamson et al. (2016) have presented 2-D numerical solutions for natural convection flow in inclined square enclosures ($AR = 1$) with differentially heated and cooled opposing walls and two other adiabatic walls. They have reported thermal and flow maps of the convecting fluid for $10^4 \leq Ra \leq 10^8$ and $Pr = 7$. They have noted that when the enclosure is tilted, boundary layers that form on the heated/cooled walls discharge plumes onto the inclined adiabatic surfaces, which are then entrained by the far side boundary layers. This is different from a vertical enclosure case, wherein the boundary layers discharge fluid into diffuse intrusions adjacent to the upper and lower adiabatic boundaries, which then travel across the cavity and are entrained by the opposing natural convection boundary layer. They have also observed the velocity of the discharged plumes in the inclined enclosure case to be higher than that for the diffuse

intrusions. Thus, one may postulate this to be responsible for the higher heat transfer rate in the inclined enclosure cases ($0^\circ < \phi < 90^\circ$) when compared to the vertical enclosure cases.

A more detailed review of the heat transfer studies for tilted enclosures can be found in Catton (1978), Goldstein et al. (1987), and Raithby and Hollands (1998).

2.3.2.1 Effect of Prandtl number on Nusselt number

The effect of Prandtl number on Nusselt number is not well researched. Dropkin and Somerscales (1965) have observed a $Pr^{0.074}$ dependence on Nusselt number from their experiments with varied Prandtl numbers (0.02 - $11,560$). However, Arnold et al. (1976) have used fluids that cover a wide range of Prandtl numbers ($Pr \approx 4.5$ (water) to $Pr \approx 2000$ (silicon oil)) and have reported no discernible effect of Prandtl number on the measured heat transfer.

2.3.2.2 Effect of aspect ratio on Nusselt number

Very few investigators have attempted to find the isolated effects of aspect ratio on Nusselt number. According to Goldstein et al. (1987), based on their high-Rayleigh-number electrochemical mass transfer experiments, the effect of aspect ratio on Nusselt number is found to increase as the enclosure is tilted, with a negligible effect for an angle of inclination of 0° (or, a horizontal enclosure case) and a maximum effect for 90° (or, a vertical enclosure case).

Table 2.4 Some significant experimental, numerical, and analytical literature on tilted enclosure free convection

Authors, Year	Ra Range	Nu-Ra scaling	Pr	AR	ϕ	Fluid
Dropkin and Somerscales (1965)	5×10^4 - 7.17×10^8	$Nu = CRa^{1/3}Pr^{0.074}$ ϕ C 0° 0.069 30° 0.065 45° 0.059 60° 0.057 90° 0.049	0.02 - 11, 560	4.41 - 16.56	0° - 90°	Mercury, Water, Silicone oil
Clever (1973)	$3 \times 10^3 \leq Ra\cos\phi \leq 4 \times 10^5$	$Nu = C(Ra\cos\phi)^n$	–	–	$\phi < 70^\circ$	Any fluid
Ayyaswamy and Catton (1973)	$Ra(AR)^3 \sin\phi \gg 10^4$	$Nu_{(\phi=70^\circ-120^\circ)} = Nu_{(90^\circ)} \sin^{1/4}\phi$	-	$AR \gg cot\phi$	70° - 120°	-
Arnold et al. (1974)	10^3 - 10^6	$Nu_{(\phi)} = 1 + [Nu_{(90^\circ)} - 1]\sin\phi$: $90^\circ \leq \phi \leq 180^\circ$	4.5, 500, 2000	6	0° - 180°	Water, silicone oil
Ozoe et al. (1975)	3×10^3 - 10^5	$Nu_{(\phi<\phi_c)} = 0.109\,(Ra\cos\phi)^{1/3}$	0.71, 3880 – 4870	0.966 - 15.5	0° - 150°	Air, silicone oil
Arnold et al. (1976)	10^3 - 10^6	$Nu_{(\phi)} = C_1(Ra\cos\phi)^{0.29} : \phi < 60^\circ$ $Nu_{(\phi)} = Nu_{(\phi=90^\circ)} \sin^{1/4}\phi : 60^\circ \leq \phi \leq 120^\circ$	4.5 - 2000	1, 3, 6, 12	0° - 180°	Water, 200cs silicone oil
Hideo (1984)	1.2×10^3 - 2×10^6	$Nu = 0.0785(Ra\cos\phi)^{0.330}$ $\phi < 60^\circ$ (when $Ra\cos\phi > 4 \times 10^5$) $Nu = 0.271(Ra\cos\phi)^{0.250}$ $0^\circ < \phi < 60^\circ$ (when $5 \times 10^3 \leq Ra\sin\phi \leq 1.2 \times 10^6$)	0.71	5 - 83	0° - 180°	Air
Goldstein et al. (1987)	2×10^8 - 1.6×10^{12}	$Sh = 0.066(Ra\cos\phi)^{1/3} : 0^\circ \leq \phi \leq 75^\circ$	$Sc \approx 2750$	1.8 - 36	0° - 150°	Cupric Sulfate - Sulphuric acid solution
Kuyper et al. (1993)	10^4 - 10^{11}	$Nu = 0.231Ra^{0.258} : Ra \leq 10^8, \phi = 45^\circ$ $Nu = 0.171Ra^{0.282} : Ra \leq 10^8, \phi = 90^\circ$ $Nu = 0.069Ra^{0.332} : Ra > 10^8, \phi = 45^\circ$ $Nu = 0.050Ra^{0.341} : Ra > 10^8, \phi = 90^\circ$	0.71	1	0° - 180°	Air
Elsherbiny (1996)	1×10^2 - 2×10^6	$Nu_{(120^\circ)} = \left[1 + \left(0.0566Ra^{0.332}\right)^{4.76}\right]^{1/4.76}$ $Nu_{(180^\circ)} = \left[1 + \left(0.212Ra^{0.136}\right)^{11}\right]^{1/11}$ $Nu_{(\phi)} = Nu_{(180^\circ)} + \frac{180-\phi}{60}\left[Nu_{(120^\circ)} - Nu_{(180^\circ)}\right]$: $120^\circ \leq \phi \leq 180^\circ$	0.71	20, 80	0° - 180°	Air
Bairi et al. (2007)	10^3 - 10^8	$Nu = 0.133Ra^{0.304} : \phi = 0^\circ$ $Nu = 0.130Ra^{0.305} : \phi = 45^\circ$ $Nu = 0.147Ra^{0.287} : \phi = 90^\circ$	0.71	0.75, 1.5	0° - 360°	Air
Chang (2014)	10^3- 10^6	$Nu = 0.189Ra^{0.26}AR^{0.11} : \phi = 0^\circ$ $Nu = 0.223Ra^{0.26}AR^{-0.11} : \phi = 90^\circ$	0.71	1, 2, 4, 8	0° - 180°	Air
Williamson et al. (2016)	10^4- 10^8	$Nu \sim \left[\left(\frac{2\sin\phi+\cos\phi}{\sin\phi+\cos\phi}\right)\cos\phi\right]^{1/4}$	7	1	0° - 90°	-

CHAPTER 3

Experiments

3.1 Experimental theory

High Rayleigh numbers are achieved by pressurizing the working fluid inside a pressure vessel. Assuming the working fluid to be an ideal gas, $Ra(= \frac{g\beta\Delta T H^3}{\nu\alpha})$ can be written as:

$$Ra = \frac{p^2 g c_p \Delta T H^3 (MW)^2}{\bar{R}^2 T_m^3 \mu k_f} \tag{3.1}$$

where, $\nu = \frac{\mu_m}{\rho_m}$, $\alpha = \frac{k_{f_m}}{\rho_m C_{p_m}}$, $\rho_m = \frac{p}{RT_m}$, $\beta = \frac{1}{T_m(K)}$, and $\bar{R} = \frac{R}{MW}$. Here, the subscript, 'm', is used to indicate that these thermo-physical properties are gathered at the mean temperature, T_m. As can be inferred from Equation 3.1, Rayleigh number is proportional to the square of the operating pressure, which means that if the operating pressure is doubled, Rayleigh number is quadrupled. Since at high pressures, the kinematic viscosity and thermal diffusivity become small due to a higher fluid density, it becomes possible to achieve higher Rayleigh numbers.

Although many liquids have very low thermal diffusivities and kinematic viscosities due to their high densities, their incompressibility makes it difficult to achieve a wide range of Rayleigh numbers without changing the dimensions of the enclosure. Hence, gases are a better choice compared to liquids. While selecting a gas as the working fluid, utmost care must be taken to ensure that the critical point of the gas is

far-removed from the operating conditions, which are defined by very high pressures and close to room temperature. This is because, when the operating conditions are very close to the critical point, even a minute difference in the temperature between the hot and cold plates can induce a significant difference in the thermo-physical property values, which will thereby lead to a violation of the Oberbeck-Boussinesq approximation (Gray and Giorgini, 1976). Taking all these factors into consideration, in the present work, nitrogen and argon are used as the working fluids because in addition to them being inert, non-toxic, nonflammable, and easy to handle, accurate thermo-physical data at very high pressures (Lemmon et al., 2003) are available for them.

Another noteworthy observation from Equation 3.1 is that a higher Rayleigh number can also be achieved by introducing a working fluid of higher molecular weight (MW), given that the operating conditions, defined by the pressure (p), mean temperature (T_m), and temperature difference (ΔT), remain the same. Hence, argon, which has approximately 1.5 times the molecular weight of nitrogen, is used to extend the Rayleigh number values to the highest investigated decade.

3.2 Experimental apparatus

3.2.1 Convection cell

3.2.1.1 Hot plate assembly

The convection test cell is made up of three major components; a hot plate assembly, a cold plate assembly, and four adiabatic sidewalls, together forming an enclosure to confine the fluid.

The hot plate assembly has a sandwich design with four square plates ($0.15\,m \times 0.15\,m$) of different materials and thicknesses, as shown in Figure 3.1. The inner plate in contact with the working fluid, is made of copper ($k = 400\,W/m - K$) and is sufficiently thick ($12.7\,mm$) to smooth out any possible temperature gradients. Twenty-six independently controlled polyamide (*Kapton*) heaters (*KHLV series, Omega Engineering*), sandwiched between this inner copper plate and an insulating phenolic plate

($6.4\,mm$ thick, $k = 0.07\,W/m - K$) following it, are used to achieve a uniform temperature on the inner surface (facing the fluid) of the copper plate. A thin copper plate (or guard plate), $6.4\,mm$ in thickness ($k = 400\,W/m - K$), follows the phenolic plate. A single large polyamide heater ($0.15\,m \times 0.15\,m$, ***KH-606 series, Omega Engineering***), fixed between the guard plate and the phenolic plate, minimizes the outward heat flow from the inner copper plate toward the guard plate by maintaining a temperature nearly equal to that of the isothermal inner copper plate. Five thermocouples, embedded within this guard plate, monitor its temperature and help quantify the outward conduction heat loss caused due to the temperature gradient between the inner copper plate and the guard plate. Another insulating layer, made of $9.5\,mm$ phenolic plate, serves as the outermost layer in this sandwich design. To eliminate contact resistance, thermal paste is applied at the interface of each of the plates in this sandwich design.

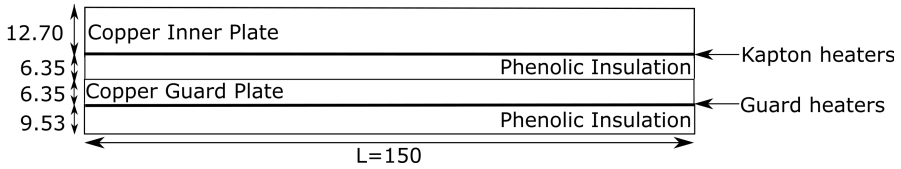

Fig. 3.1 Sandwich design of the hot-end (all dimensions are in mm)

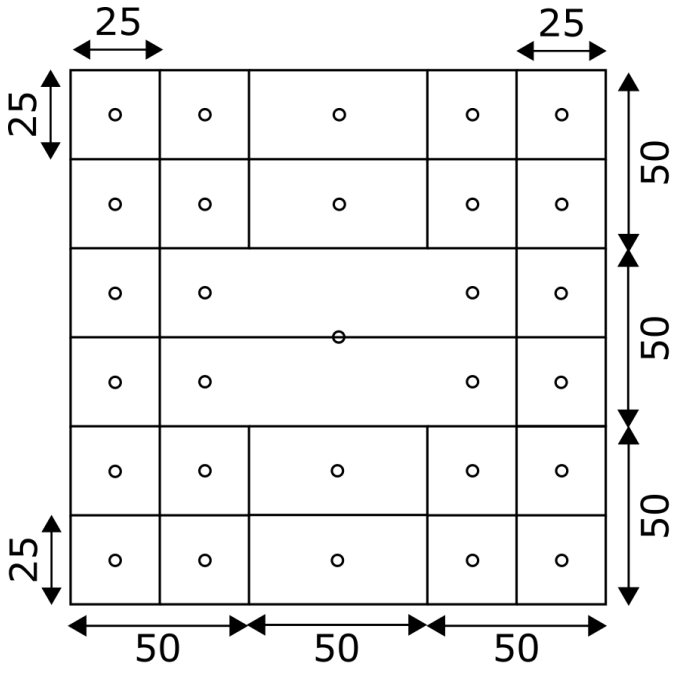

Fig. 3.2 Top view of the inner hot plate showing the heater (square and rectangular boxes) design and thermocouple (circular dots) locations (all dimensions are in mm)

Figure 3.2 portrays the arrangement of the aforementioned twenty-six independently controlled heaters on the inner copper plate. One dimension of all the heaters is always fixed to $25\,mm$, the smallest practically available size for square/rectangular *Kapton* heaters (*KHLV series, Omega Engineering*), to have a better control over the surface temperature uniformity. This is because when the test cell is vertical, i.e., temperature gradient is orthogonal to the gravity vector, the hot plate assembly (or, the hot-end) will act like a thick vertical hot plate that is surrounded by quiescent gas at a cooler ambient temperature. The free convection boundary layer developing on it will have an increasing thickness as we move from bottom to top. As a consequence, the free convective heat loss from the hot plate will be uneven along the height of the plate and, thus, demands an uneven heating from top-to-bottom to maintain its surface isothermal (with more heater power required at the bottom than at the top). This can be achieved by covering the entire height of the plate with small heaters ($25\,mm$ in width).

It can also be noted from Figure 3.2 that each of the four corners of the plate is provided with small heaters ($25\,mm \times 25\,mm$). This is to ensure that the heat loss from the corners are compensated appropriately, without having to alter the temperature of the entire plate or the larger area at the center of the plate. The heaters fixed close to the center of the plate are designed to be relatively longer. From Figure 3.2, it can also be noted that the inner copper plate has twenty-nine thermocouples embedded to monitor the temperature uniformity.

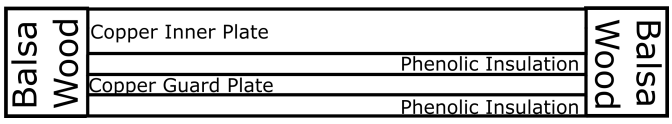

Fig. 3.3 Hot-end assembly

This entire hot plate assembly is snug-fit into a $25.4\,mm$ thick balsa wood box ($k = 0.035\,W/m - K$), as shown in Figure 3.3. This helps to reduce edge heat loss from the hot-end. Four thermocouples, one on each side of the outer surface of the balsa wood box, measure its outer surface temperature, the average value of which is used to compute the edge heat loss.

3.2.1.2 Cold plate assembly

The cold plate assembly (or the cold end) is comprised of two square plates ($0.185\,m \times 0.185\,m$) made of copper. The inner plate (facing the convecting fluid) has an integral heat exchanger with square double spirals that provide channels for cooling water circulation, as shown in Figure 3.4a. This heat exchanger design promotes a uniform surface temperature at the cold-end. The thickness of the inner heat exchanger plate that separates the circulating cooling water and the working (convecting) fluid is designed with the intention of achieving a Biot number (based on thickness) much smaller than 0.1, to provide a very good temperature uniformity all over the surface facing the convecting fluid. This is verified by inserting six thermocouples into the inner copper plate. The outer plate, as shown in Figure 3.4b, acts as a cover plate. This outer cover plate has an inlet port and an outlet port for the circulating cooling water to enter and leave the cold end, respectively. These two plates are assembled together using thirty-two threaded fasteners. An o-ring, coated with vacuum grease, is used as the sealant between the two plates. This assembly is leak-tested for vacuum before introducing it to the cooling water circuit.

The inner surface, facing the convecting fluid within the enclosure, of both the hot and cold plate assemblies are coated with mirror-polished silver ($\varepsilon_{Ag} \approx 0.025$) to minimize radiation heat loss.

3.2.1.3 Adiabatic sidewalls

Four sheets (each with identical dimensions and $6\,mm$ thickness) of the same material are used to fabricate a four-walled box (open at the top and bottom) that encloses the working fluid between the hot and cold plate assemblies. Four holes of $3\,mm$ diameter are provided on each of the sidewalls for pressure equalization. For all the experimental runs, except for the visualization studies, the sidewall surfaces are wrapped in a thick layer of glass wool to reduce surface heat loss.

Sidewalls of three different thermal conductivities are employed for the first part of the present study, the results from which are used to quantify the effect of sidewall conductance heat loss on free convective heat transfer in horizontal enclosures.

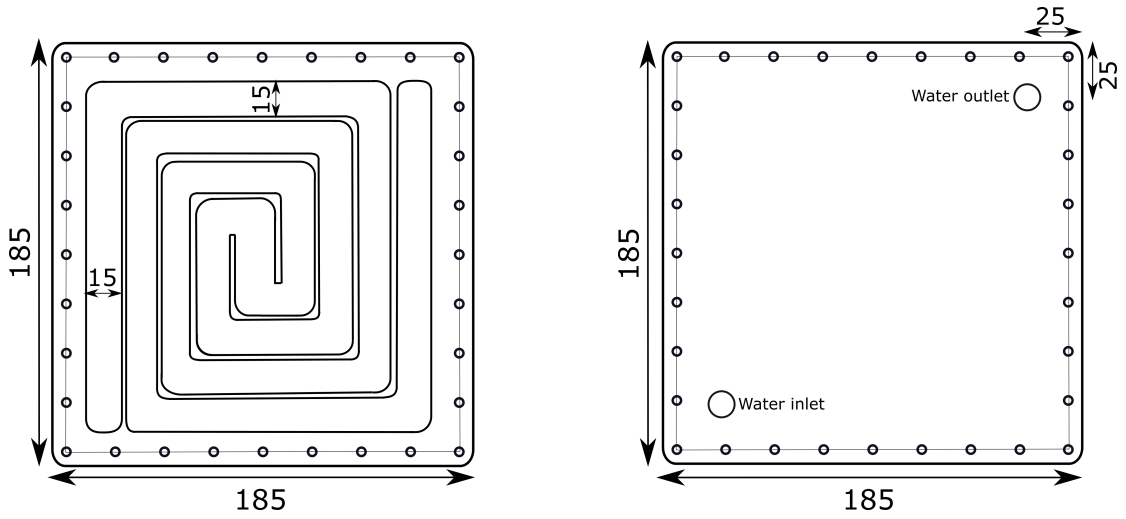

(a) Inner plate with heat exchanger **(b)** Outer plate

Fig. 3.4 Design of cold plate assembly (all dimensions are in mm)

The three sidewall materials are Styrofoam ($k = 0.033\,W/m - K$), Plexiglas ($k = 0.195\,W/m - K$), and high-density polyethylene ($k = 0.48\,W/m - K$). It is to be noted that each of the three selected materials has a low thermal conductivity, which helps reduce the conduction heat loss, and, thereby, validate the assumption of adiabatic sidewalls. Since this part of the study is limited to an aspect ratio of unity, the internal dimensions of the box are kept as $0.15\,m \times 0.15\,m \times 0.15\,m$.

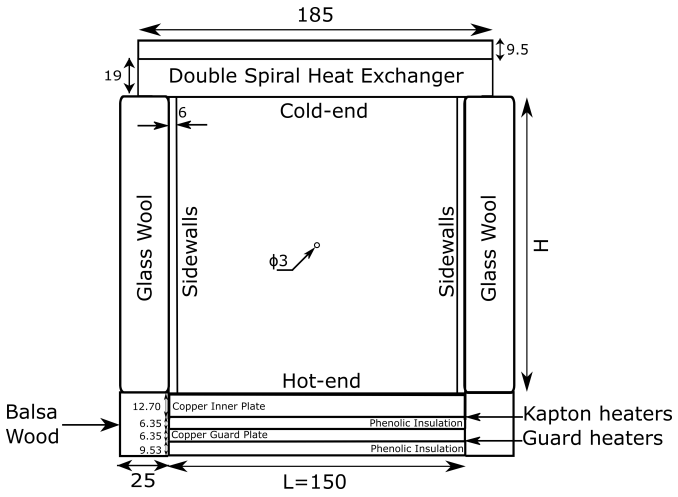

Fig. 3.5 Test cell schematic

For the rest of the experiments in this study, except for the visualization experiments (conducted using the Plexiglas sidewalls), the only sidewall material used is Styrofoam, due to its extremely low thermal conductivity. The internal dimensions of the Styrofoam

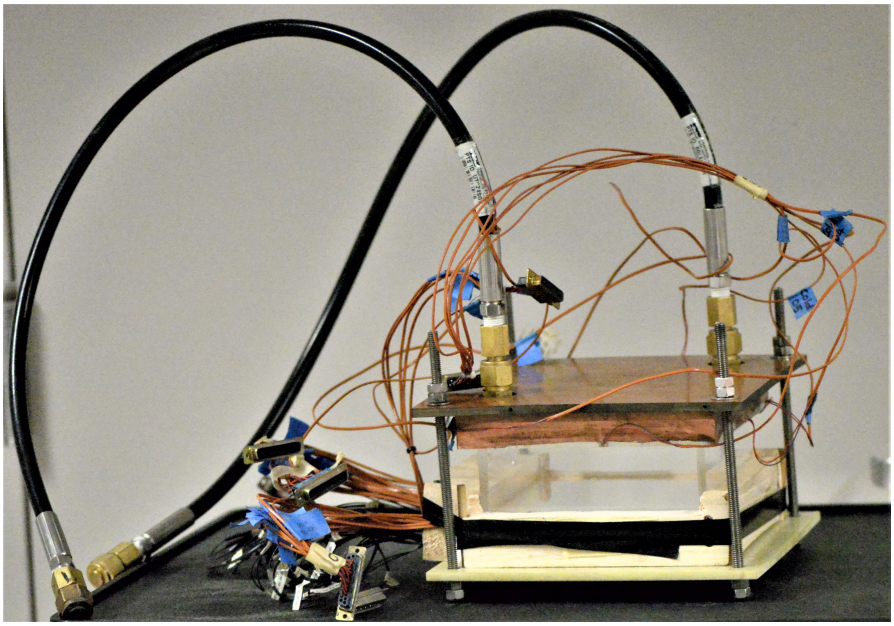

Fig. 3.6 Picture of the test cell (Plexiglas sidewalls, $AR = 3$)

box are maintained as $0.15\,m \times 0.15\,m \times H\,m$ (refer to Figure 3.5 for the dimension, H) to achieve varied aspect ratios.

A complete assembly of the convection test cell can be found in Figures 3.5 and 3.6. This test cell assembly is placed inside a pressure vessel on a thick garolite plate to reduce conduction heat loss to the pressure vessel wall.

3.2.2 Pressure vessel

A pressure vessel, shown in Figure 3.7, is used to compress the working fluid to pressures as high as $92\,bars$. It is made from $22.2\,mm$ thick rolled steel plate and is circular in cross-section, with an inner diameter of $565\,mm$ and an outer diameter of $608\,mm$. The top flange of the pressure vessel is $940\,mm$ in diameter and $100\,mm$ thick, with a similar mating flange closing the vessel securely with 24 stud bolts (each of diameter $47.6\,mm$) and matching nuts. A 5:1 torque multiplier is used to apply a torque value of $1810\,Nm$ and bolt the pressure vessel down. The *ASME* bolting sequence (ASME, 1999) is followed when the torquing is performed. A gasket made from stainless steel and graphite is sandwiched between the flanges to seal the pressure vessel. This gasket needs to be replaced with a new one every time the pressure vessel stud bolts are untorqued. The pressure vessel has two view ports, each $140\,mm$ in diameter as shown

in Figure 3.7, made with heat-treated Pyrex glass of $32\,mm$ thickness. They are fixed using a torque wrench to a torque value of $605\,Nm$. The inner walls of the pressure vessel is coated with *Plasite-7122 (VOC)* paint (by *Carboline*), which does not emit any contaminating gases under vacuum or high pressure. The thermocouple and heater wires are routed out of the pressure vessel via high pressure sealant glands (by *Conax Technologies*) located at the bottom of the pressure vessel, as shown in Figure 3.8.

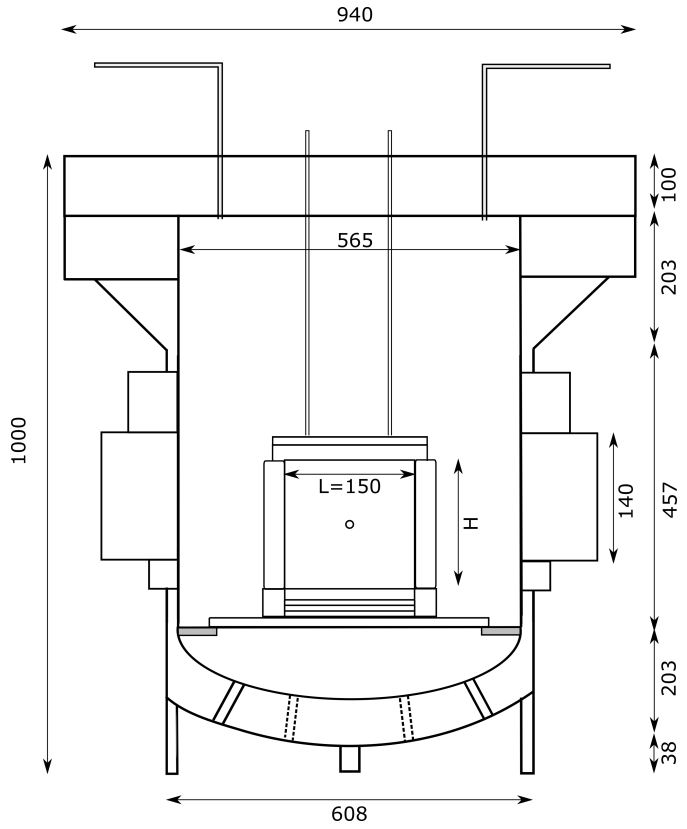

Fig. 3.7 Pressure vessel with test cell (all dimensions are in mm)

3.2.3 Supporting equipment

As shown by the dashed-lines in Figure 3.10, the cooling water circuit is comprised of the cold plate assembly, a pair of flexible tubing (*Parker Hannifin*) that can withstand very high external pressures without collapsing, thick copper tubes, a helical copper coil placed inside a *Thermo Scientific Neslab RTE 10* water bath circulator, a brass rotary vane pump (*PROCON* pump) driven by a $\frac{1}{2}$ HP split-phase *Carbonator* pump motor, and tube fittings (including some *Swagelok* compression fittings).

Before filling the pressure vessel with the operating gas, a duo-seal vacuum pump

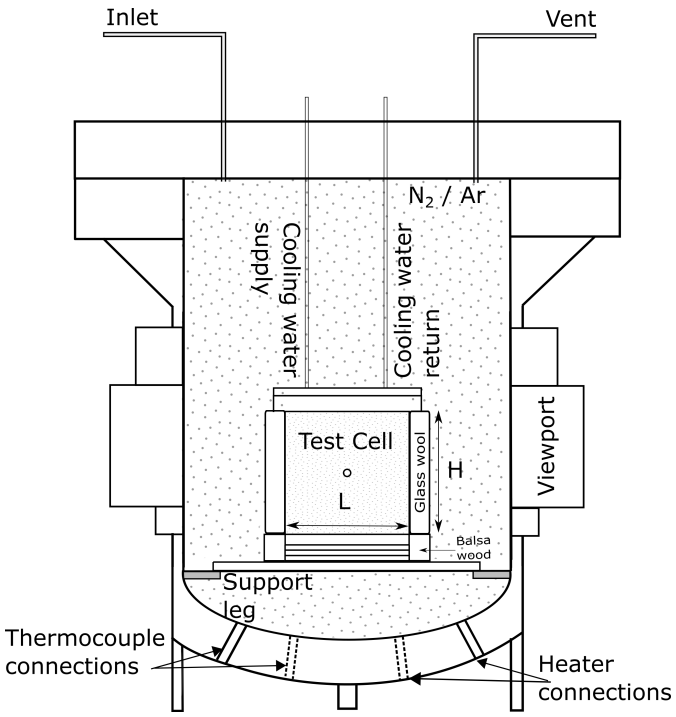

Fig. 3.8 Pressure vessel with test cell: horizontal enclosure (no wedge)

(*Model 1399, Welch Vacuum*) is used to evacuate the pressure vessel, as shown by the dotted-lines in Figure 3.10. High-purity grade (99.998%) N_2 and Ar gas cylinders (*Matheson Gas*) are used to pressurize the pressure vessel. Stainless steel tubes with an outer diameter of $\frac{1}{4}$" (0.049" thickness) are employed with *Swagelok* compression fittings to avoid any potential leaks while supplying compressed gas to the pressure vessel. To inspect for any potential leaks after torquing down the pressure vessel, and pressurizing it to the desired value, soap solution is sprayed over each of the fittings and the high pressure sealant glands. If a minor leak is detected and its location cannot be identified by the soap solution method, the gas cylinder valve is kept slightly open to maintain the working pressure during the entire span of the experiment. Table 3.1 can be used as a reference for choosing the right valve combinations to perform the experimental run itself or for various experimental procedures such as pressurizing, relieving, and evacuating the pressure vessel.

Additional equipment is required for the flow-field visualization portion of the present study. A z-type shadowgraph technique (as shown in Figure 3.11) is employed for this purpose, which uses two parabolic mirrors (each with a focal length of 30"), an LED

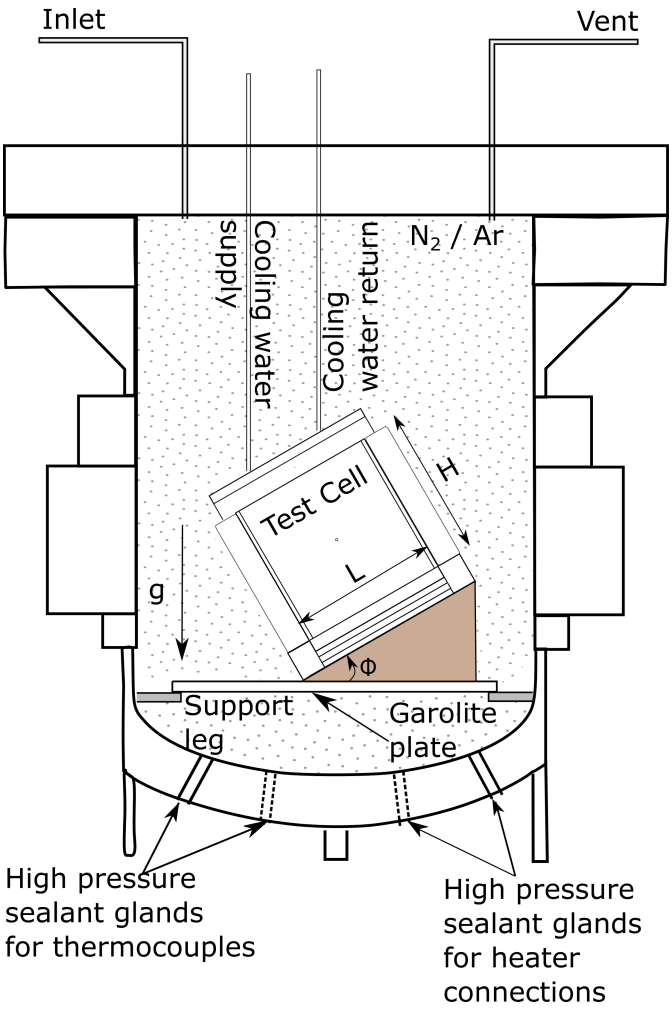

Fig. 3.9 Pressure vessel with test cell: tilted enclosure

light source (*LPS* from *iLA 5150 GmbH*), a condenser lens, a pin hole, and a DSLR Camera (*Nikon D610*).

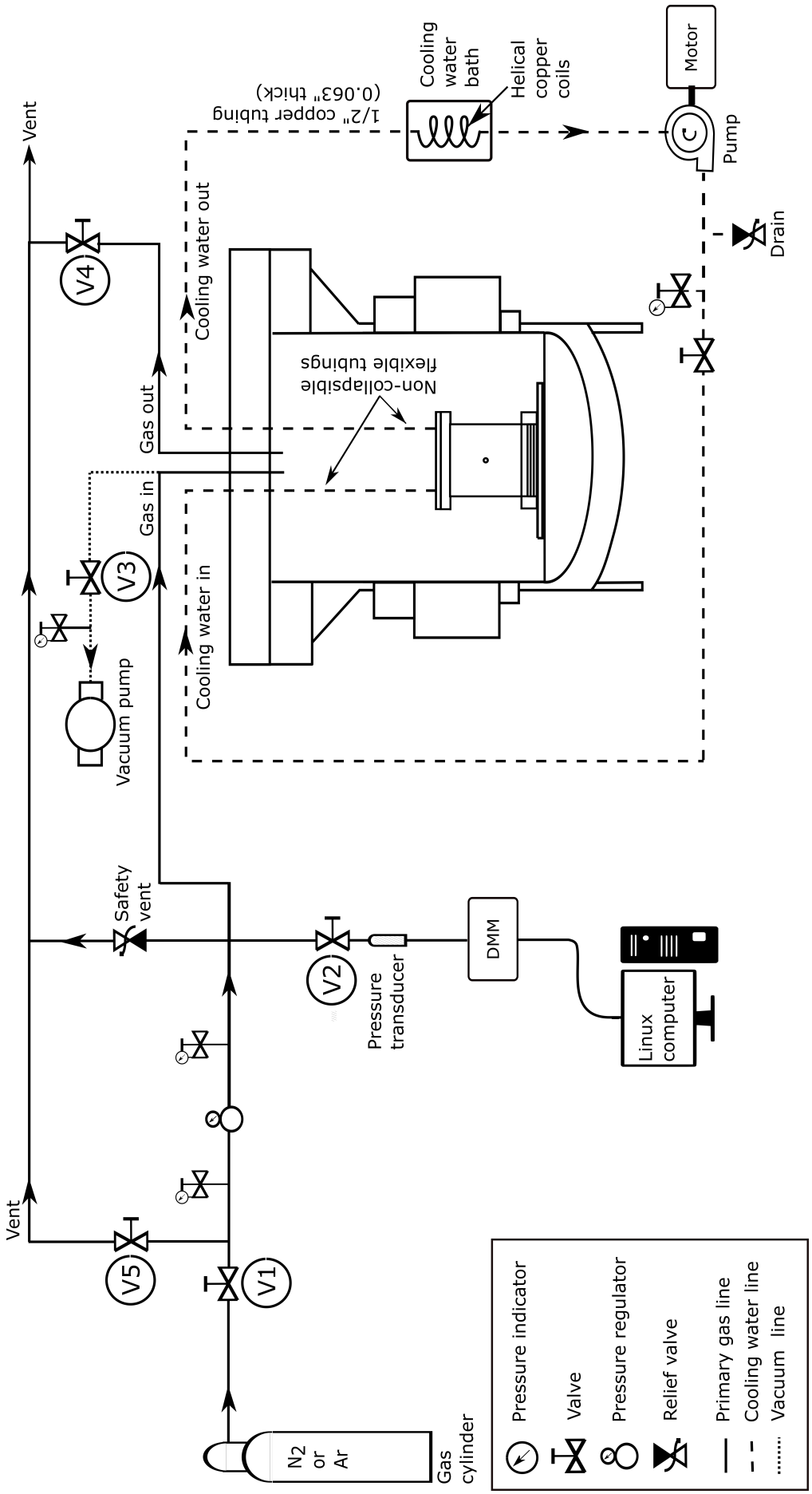

Fig. 3.10 Line diagram of the fluid flow circuit

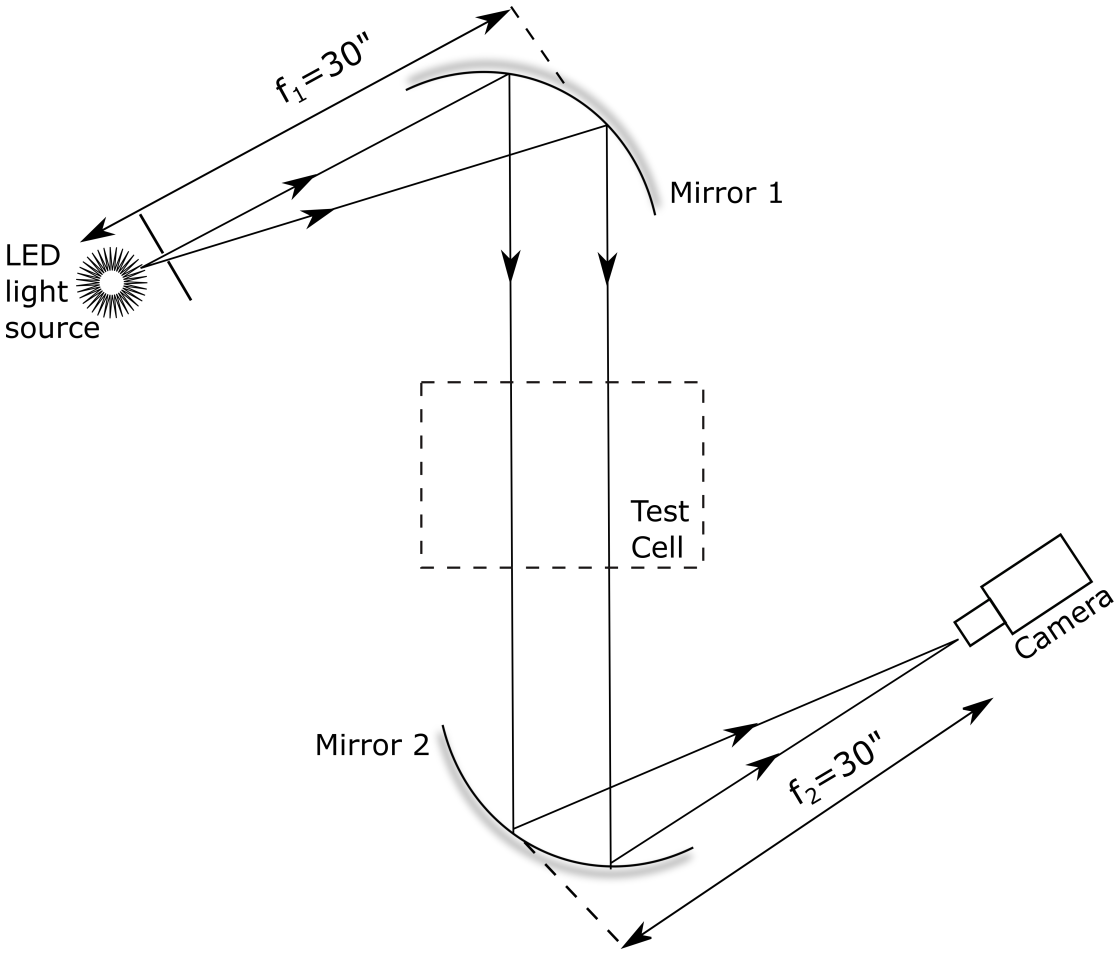

Fig. 3.11 Schematic of the z-type shadowgraph technique

3.3 Instrumentation

3.3.1 Voltage and current measurements

Three *Keithley Model 2000* $6\frac{1}{2}$ digital multimeters (DMM), having a 0.02% 90 day accuracy, are used in the present study. One of the *Keithley Model 2000* DMMs is used to measure the difference in thermocouple voltage (EMF) for each of the 45 thermocouples used in this study and to measure the output voltage of the pressure transducer. To switch between the EMF and pressure transducer channels, an 80 channel *Keithley Model 7001 Switch System* digital multiplexer (MUX) is used.

The voltage and current measurements for each of the 26 *Kapton* heaters are taken using two independent measuring systems, each comprised of a *Keithley Model 2000* DMM and a switch system. The switch system consists of a switch controller (*Fluke 2205A*) and a scanner (*Keithley Model 705*). These measurements are then used to estimate the total power input into the convection test cell.

3.3.2 Temperature measurements

Temperature measurements are made with calibrated 30 gage type-E thermocouples. These thermocouples are made by using an in-house spot-welding machine. To achieve a clean and robust thermocouple junction (spherical-type bead formed between two thermocouple wires), the spot-welding is done in an inert atmosphere, created by passing argon gas over the thermocouple wires that are to be joined and by using a current setting of $\approx 10\,A$ on the spot-welding machine. The thermocouple calibration procedure, as detailed in Section 3.4.1, results in an uncertainty of $\pm 0.01K$.

3.3.3 Pressure measurements

A factory calibrated pressure transducer *(PX309-3KG5V, OMEGA Engineering)*, powered by a *PSR-24L* DC power supply unit, is used to monitor the operating pressure inside the pressure vessel. This pressure transducer, having a stated static accuracy of 0.25% (User manual for *PX309 series pressure transducers, OMEGA Engineering*), produces a DC voltage in the range of $0-5\,V$ for any pressure in the range $0-3000\,psig$

Table 3.1 Valve logic for various processes during setting up and execution of the experiments

Process	V_1	V_2	V_3	V_4	V_5
Pressurizing	1	1	0	0	0
Experimental run	0	1	0	0	0
Venting	0	1	0	1	0
Evacuating	0	0	1	0	0

(or, $0 - 208\,bar$) with a linear relation. For a particular experimental run, this DC voltage output is measured and converted to the corresponding pressure by using this linear relation. It must be noted that this pressure is a gauge pressure and has to be converted to absolute pressure before using it for any calculations. This conversion is done by measuring the ambient pressure value (obtained from *http://www.enet.umn.edu/auto-generated/pressure/*) and adding it to the estimated gauge pressure.

3.3.4 Power supply units

The twenty-six independently controlled *Kapton* heaters are powered by an in-house Digital Power Supply (DPS) unit (for details, refer to Han, 2004). This DPS has computer controlled digital potentiometers and chipsets to help change the voltage supplied to each of the *Kapton* heaters using the temperature measurements from the thermocouples, shown in Figure 3.2, as feedback. A Proportional Integral (PI) control technique is employed to achieve voltage change through this feedback system and maintain a uniform surface temperature at the hot-end. A *Hewlett-Packard HP66104A* power supply unit is used to power the single heater fixed between the guard plate and the phenolic plate, the voltage and current measurements for which can be taken directly from the power supply unit.

3.3.5 Data acquisition and control

A data acquisition program is written in *C* and run on a *Linux* machine. All the instrumentation make use of the *IEEE-488* bus specification (or, General Purpose Interface Bus, i.e., GPIB) for inter-device communication during the course of an experimental run, including the data acquisition phase. Since the *Linux* computer does not have a GPIB port, a *National Instruments* USB to GPIB adapter is used for this purpose.

3.4 Experimental procedures

3.4.1 Thermocouple calibration

The thermocouples are calibrated against a Standard Platinum Resistance Thermometer (SPRT) in a well-controlled constant temperature water bath, manufactured by *Rosemount Inc*. The calibration procedure is comprised of two steps, i.e., (i) calibrating the SPRT itself against standard reference temperatures and (ii) calibrating the thermocouples against the temperature indicated by the SPRT for a range of temperatures, which, ideally, should cover the operating temperatures of all the primary experiments to avoid any extrapolation errors.

3.4.1.1 Calibration of SPRT against reference temperatures

Triple point of water and transition temperature of anhydrous sodium sulfate are selected as the reference temperatures in the present work.

A *Jarrett - Isotech* made triple point cell is employed to realize the triple point of water ($0.01°C$, $611.657\,Pa$). The triple point cell is immersed in an ice bath for a sufficiently long time to pre-chill the cell before the preparations begin. The first layer of ice is formed by slowly adding dry ice (frozen carbon dioxide) into the well of the triple point cell after pouring isopropyl alcohol to the half-way mark of the well. A thicker layer of ice sheath is built by repeating this procedure and adding more isopropyl alcohol (above the meniscus of the water in the cell) and dry ice. Special care is taken to avoid the formation of an ice bridge near the water meniscus (or, the ice-water-vapor interface) and the ice sheath touching the inner surface of the borosilicate glass, as either of these situations will not only spoil the realization of the triple point of water but also break the triple point cell itself. The first situation can be avoided by warming the outer surface of triple point cell, near to the meniscus, with hands. To check for the second situation, and to see the amount of ice sheath that has formed around the well, the triple point cell is placed in a clear beaker filled with distilled water. This will cancel out any refraction of light due to the water in the triple point cell and help to visualize the actual size of the ice sheath. When the size of ice sheath around the well reaches $75 - 80\%$

of the cell size (measured from the outer surface of the well to the outer surface of the triple point cell), a warm rod (with a diameter approximately equal to the diameter of the triple point well) is placed into the well to purge any leftover isopropyl alcohol and free the ice sheath from the well (the ice sheath should spin freely around the well). The triple point cell is then allowed to relax to the triple point temperature of water, by placing it in an ice bath for several hours, as the initial temperature of the cell can be as much as $1\ mK$ off the true value (White et al., 2007).

Magin et al. (1981) have summarized the use of hydrate transition temperatures as a reference point for temperature measurements. From Figure 3.12, it can be inferred that solutions greater than 33.2% sodium sulfate by weight, when cooled from at least $40°C$, undergo a stable hydrate transition at $33.373°C$. Here, since the solution is heated above $40°C$, the form of the salt (hydrate or anhydrous) used becomes irrelevant (see Figure 3.12). Therefore, in the present work, anhydrous sodium sulfate is selected, instead of the hydrated salts used by Magin et al. (1981), since it is easily available and economical. Also, since the transition temperature reported by Magin et al. (1981) is based on *IPTS-68*, it needs to be converted to *ITS-90* by following the method suggested by Fellmuth (2012) before performing any calculations for the calibration procedure. This conversion results in a change in the transition temperature, from the reported $32.373°C$ to $32.365°C$, with an additional uncertainty of $1\ mK$.

Since the phase change process is an exothermic reaction, liberating thermal energy, the solution temperature remains stable for several hours. The procedure followed to achieve this transition temperature reference point is as listed below:

1. A solution prepared with sodium sulfate and distilled water is heated to at least $40°C$, as any temperature below this value poses a difficulty in yielding a stable transition temperature
2. One of the most important things to check is the percentage composition by weight of sodium sulfate in the solution. This is verified to be greater than 33.2% by ensuring that there is enough anhydrous sodium sulfate precipitation in the solution even at temperatures as high as $40°C$ (see Figure 3.12)

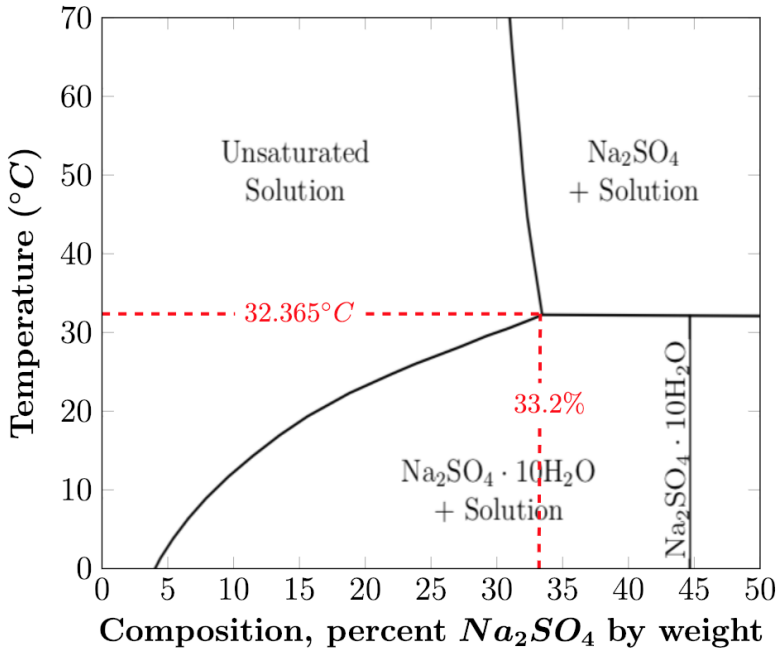

Fig. 3.12 Phase diagram for $Na_2SO_4 : H_2O$ showing the transition temperature (Magin et al., 1981)

3. When the temperature of the solution reaches a few tenth of a degree Celsius below the transition temperature, the phase change is triggered by adding hydrated sodium sulfate (prepared by thoroughly mixing the anhydrous sodium sulfate with distilled water at room temperature)

A four-wire resistance measurement technique is employed to measure the platinum resistance at the triple point of water (R_{tp}) and sodium sulfate transition temperature ($R_{Na_2SO_4}$). The hydrate transition temperatures and the measured resistances (by the SPRT) from more than 300 measurements are used to find the constants R_{tp} and a, defined by the *ITS-90*, as outlined in Preston-Thomas (1990).

$$W = \frac{R_{Na_2SO_4}}{R_{tp}} \tag{3.2}$$

$$W - W_r = a(W - 1) \tag{3.3}$$

$$W_r = C_0 + \sum_{i=1}^{9} C_i \left[\frac{T - 754.15}{481}\right]^i \tag{3.4}$$

Table 3.2 The values of the coefficient C_i (Preston-Thomas, 1990)

C_i	Value
C_0	2.78157254
C_1	1.64650916
C_2	−0.1371439
C_3	−0.00649767
C_4	−0.00234444
C_5	0.00511868
C_6	0.00187982
C_7	−0.00204472
C_8	−0.00046122
C_9	0.00045724

where the values for the constant C_i are listed in Table 3.2.

When the calibration is performed, the measured resistance values are found to be $25.556\,\Omega$ and $28.838\,\Omega$, respectively. The value of a, estimated using Equations 3.2 - 3.4, along with the measured resistance values, and the sodium sulfate transition temperature, is found to be 3.43×10^{-5}. Moreover, the temperature coefficient of resistance for the SPRT is estimated to be $0.003969\,\Omega/\Omega \bullet {}^{\circ}C$, which is higher than the minimum value of $0.003925\,\Omega/\Omega \bullet {}^{\circ}C$ imposed by Preston-Thomas (1975) for accurate calibrations.

Now, the temperature of the platinum resistance thermometer from the measured resistance values can be estimated by following the method put forward by Preston-Thomas (1990) and is given by Equation 3.5 and Table 3.3.

$$T - T_{tp} = D_0 + \sum_{i=1}^{9} D_i \left[\frac{W_r - 2.64}{1.64}\right]^i \tag{3.5}$$

3.4.1.2 Calibration of thermocouples against SPRT temperature

In the second step of the temperature calibration, the thermocouples are calibrated against the SPRT indicated temperatures, given by Equation 3.5. Out of the 45 thermocouples used, only a set of five randomly selected thermocouples are utilized for calibration, assuming that the selected set represents the distribution of the whole set. These thermocouples are then immersed in long glass vials filled with engine oil (to avoid getting exposed to any non-uniform temperature distribution) before placing them

Table 3.3 The values of the coefficient D_i (Preston-Thomas, 1990)

D_i	Value
D_0	439.932854
D_1	472.41802
D_2	37.684494
D_3	7.472018
D_4	2.92828
D_5	0.005184
D_6	-0.963864
D_7	-0.188732
D_8	0.191203
D_9	0.049025

into the controlled water bath. After placing the SPRT and thermocouple vials into the controlled water bath, multiple readings (thermocouple EMFs and SPRT resistances) are recorded at the same temperature for each of the 13 different temperature settings (in the range of $4.71°C$ - $73.16°C$). The resulting averaged voltage data (in mV) for each of the five thermocouples are plotted against the SPRT indicated temperature (in $°C$) to establish a suitable polynomial least square fit, as given by Equation 3.6, which serves as the calibration curve for the thermocouple temperature measurements. The results are plotted in Figure 3.13. The goodness of the fit, measured in terms of an R^2 value, is nearly unity, which suggests that Equation 3.6 is an appropriate model for predicting temperature from the thermocouple voltage measurements.

$$T = 0.2288 + 16.981e_{tc} - 0.2091e_{tc}^2 \tag{3.6}$$

3.4.2 Primary experiments

Before starting an experimental run, a standard operating procedure is followed to ensure a successful execution and to minimize the lead time of the experiment. The steps to be followed in this procedure are as follows:

1. The cooling water bath is turned on at least an hour before beginning the experiment to get the cooling water temperature down to the desired value. The desired value of the bath is dictated by the cold-plate temperature for a particular experiment. On some rare occasions, the temperature of the cooling water bath is kept

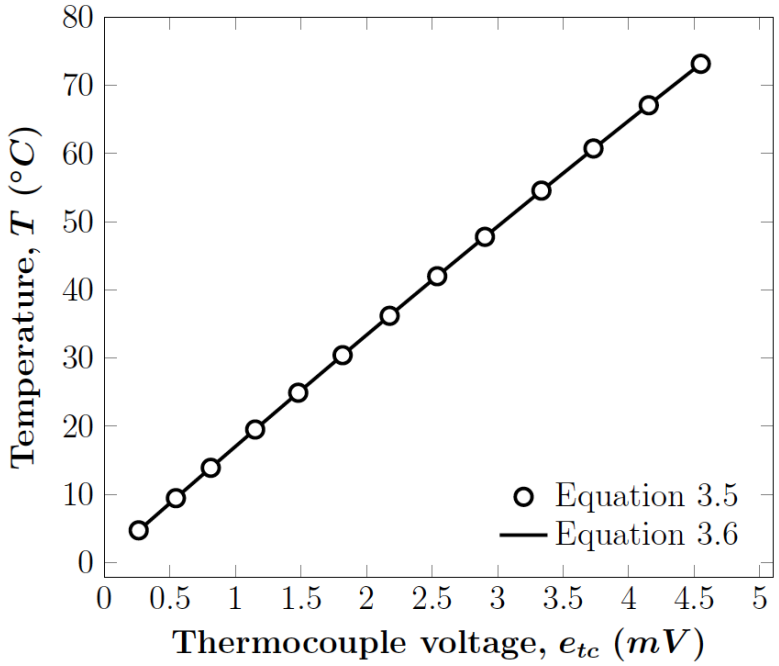

Fig. 3.13 Thermocouple calibration curve

a few tenth of a degree Celsius lower than the desired cold-end temperature to compensate for the heating of the water pump.

2. The pressure inside the pressure vessel is monitored with the help of a pressure transducer and the supply from the gas cylinder is cut off after reaching the desired value.

3. The reference junction for the thermocouples, i.e., an ice bath, is formed by mixing crushed ice and water. Care must be taken to have much more ice than water in order to obtain an ideal ice bath with a reference temperature of $0°C$

4. Temperature readings from each of the employed thermocouples are examined to confirm that there are no faulty thermocouples and/or all the thermocouple connections are intact

5. Finally, the water pump and the power supply units are turned on before starting the data acquisition and control code.

Typically, a steady-state is achieved in $7 - 8$ hours and the steady-state data is recorded for a sufficiently long time (approximately an hour). Representative plots of relevant measured quantities with respect to time after reaching steady-state is given in

Figure 3.14. The ice bath is replaced once, after approximately 4 hours from the start of the experiment. The pressure and temperature (of the thermocouples) are continuously monitored. Before turning the experiment off, the heater voltage and current readings are recorded, in addition to the temperatures of the hot plate, cold plate, guard plate, balsa wood outer surface, the fluid temperature inside the pressure vessel, and pressure.

3.4.3 List of experiments

A set of nineteen experiments, covering 6 decades of Rayleigh numbers (1.85×10^6 to 1.04×10^{11}), is performed for each of the six investigated angles of inclination ($0°$, $30°$, $60°$, $90°$, $120°$, and $150°$), as listed in Table 3.4. For achieving various tilting angles for the enclosure, two wedges of internal angles $30°$ and $60°$, as shown in Figure 3.9, are used. Apart from the 19 experiments designed to check the $Nu - Ra$ scaling relation, two sets of experiments (marked with ^{a} and ^{b} in Table 3.4) are performed, at fixed Rayleigh numbers, to verify the effect of aspect ratio on Nusselt number.

For achieving any of the Rayleigh numbers listed in Table 3.4, proper care is taken while setting the hot plate and cold-plate temperatures to achieve a temperature difference that does not violate the Oberbeck-Boussinesq approximation, i.e., $\beta\Delta T \leq 0.2$ (Gray and Giorgini, 1976) and a mean temperature close to the temperature inside the pressure vessel ($\approx 22\,°C$), which helps to reduce the heat loss from the sidewall surfaces.

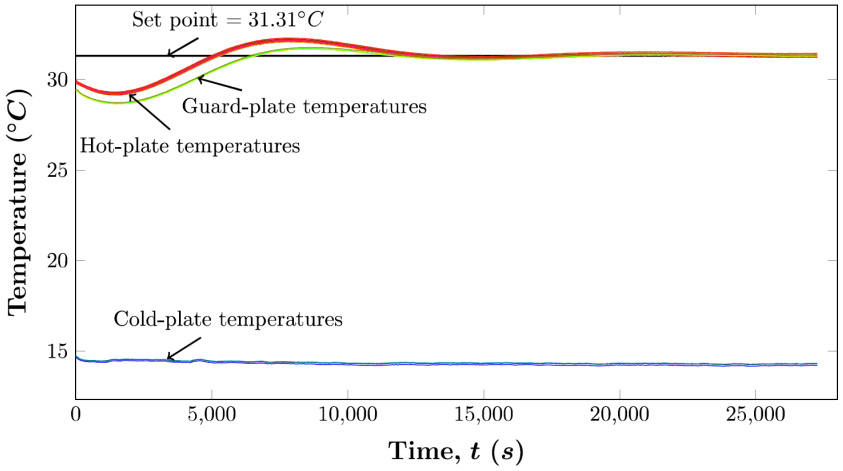

(a) Temperatures

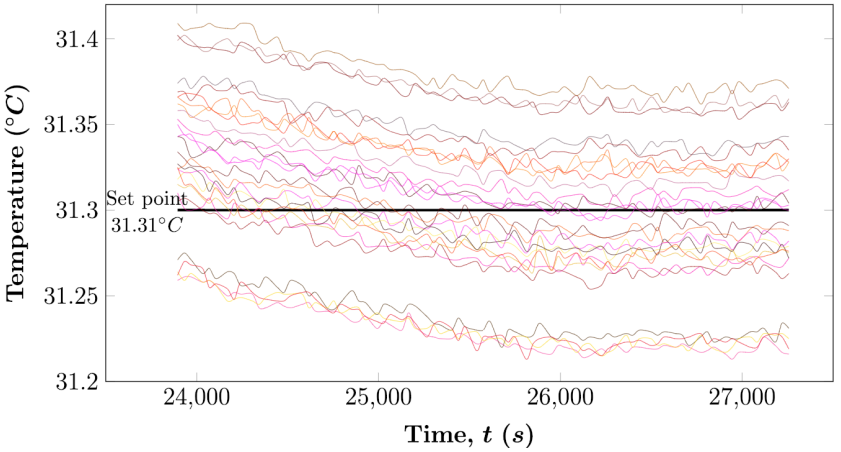

(b) Steady state hot-plate temperatures

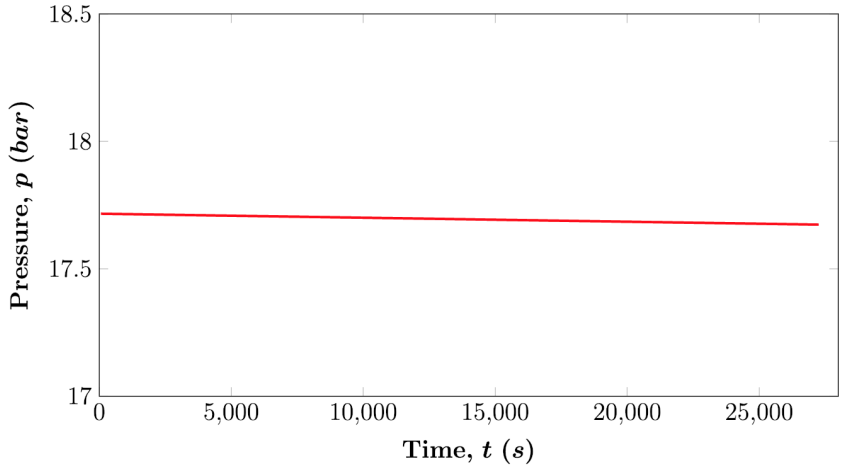

(c) Pressure

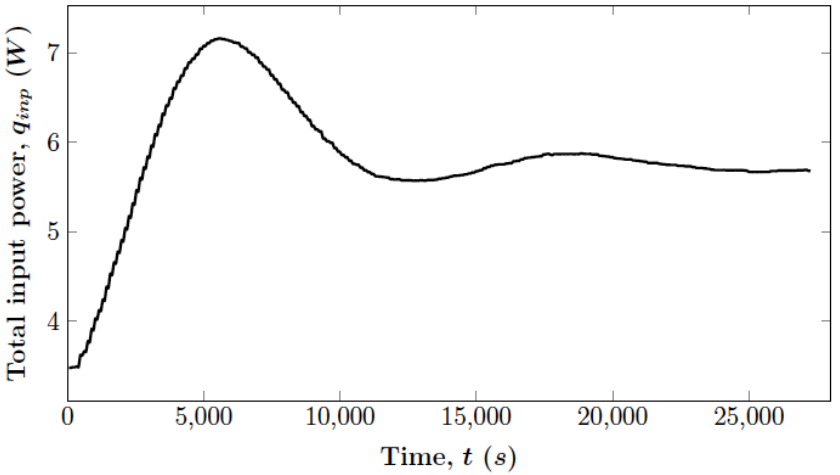

(d) Input power

Fig. 3.14 Representative time history plots of the monitored parameters

Table 3.4 Complete set of experiments

Run No.	Pressure (bar)	T_m ($^\circ C$)	Fluid	$\Delta T(K)$	Ra	AR
1	17.67	22.80	N_2	17.03	1.85×10^6	10
2	32.83	21.96	N_2	8.11	3.25×10^6	10
3	40.03	22.22	N_2	9.25	6.14×10^6	10
4	50.00	22.29	N_2	7.04	8.77×10^6	10
5	70.03	22.29	N_2	4.99	1.05×10^7	10
6	62.8	22.14	N_2	9.09	1.28×10^7	10
7	34.78	22.03	N_2	19.91	3.98×10^7	6
8	46.17	22.38	N_2	17.97	6.33×10^7	6
9	58.81	22.08	N_2	17.01	9.76×10^7	6
10	29.87	23.00	N_2	24.98	2.89×10^8	3
11	53.27	22.23	N_2	20.97	7.90×10^8	3
12^a	69.01	22.29	N_2	16.03	1.00×10^9	3
$12A^a$	58.6	22.05	N_2	21.96	1.00×10^9	1
13	79.64	22.05	N_2	21.96	1.82×10^9	3
14	24.97	21.99	N_2	17.96	3.96×10^9	1
15	65.32	22.04	N_2	6.06	9.23×10^9	1
16	67.32	21.87	N_2	9.97	1.62×10^{10}	1
17	79.64	22.05	N_2	21.96	4.92×10^{10}	1
18	89.88	22.08	Ar	18.98	7.60×10^{10}	1
19	89.93	22.35	Ar	25.92	1.04×10^{11}	1
A^b	79.38	22.2	N_2	19.96	4.40×10^7	10
B^b	35.43	22.11	N_2	20.94	4.40×10^7	6
C^b	14.97	22.01	N_2	15.56	4.40×10^7	3
D^b	3.03	22.31	N_2	14.53	4.40×10^7	1

^{a,b} Experiments at fixed Ra to examine the effect of AR on Nu

3.5 Data reduction

Nusselt number is computed based on the net convective heat transfer rate (Equation 3.7), which is estimated from the total power input to the bottom plate heaters after carefully correcting for all possible heat losses. These losses, typically $2-5\%$ of the total input power, include:

1. Guard heat loss: heat loss from the inner hot plate to the guard plate
2. Edge heat loss: heat loss from the hot plate assembly to the balsa wood box
3. Sidewall conductance heat loss: conduction heat loss through the sidewall material due to the temperature gradient between the hot plate and the cold plate.
4. Surface heat loss: heat loss from the sidewall surface to the fluid outside the test cell
5. Radiation heat loss: Net heat exchange between the hot plate and other internal surfaces of the enclosure.

Rayleigh numbers are computed by using the fluid properties estimated at the mean temperature and the measured temperature difference between the hot and cold plates.

The uncertainties, calculated using the method of error propagation (Equation 3.8), associated with Nusselt number and Rayleigh number are estimated to be modest, within $\pm\, 8.1\,\%$ and $\pm\, 3.7\,\%$ respectively.

$$Nu = \frac{q_{net}}{L^2 \Delta T}\frac{H}{k_f} = \frac{q_{net}}{AR \cdot L \cdot \Delta T \cdot k_f} \tag{3.7}$$

For a parameter (R) that depends on multiple independent variables (V_i), the associated uncertainty (U_R) is (Kline and Mcclintock,1953):

$$U_R = \left[\sum_{i=1}^{n}\left(\frac{\partial R}{\partial V_i}U_{Vi}\right)^2\right]^{\frac{1}{2}} \tag{3.8}$$

where U_{Vi} is the uncertainty associated with an independent variable.

Detailed data analysis, including relevant equations, uncertainty analysis, and sample calculations are provided in the appendices (see Appendices A through C).

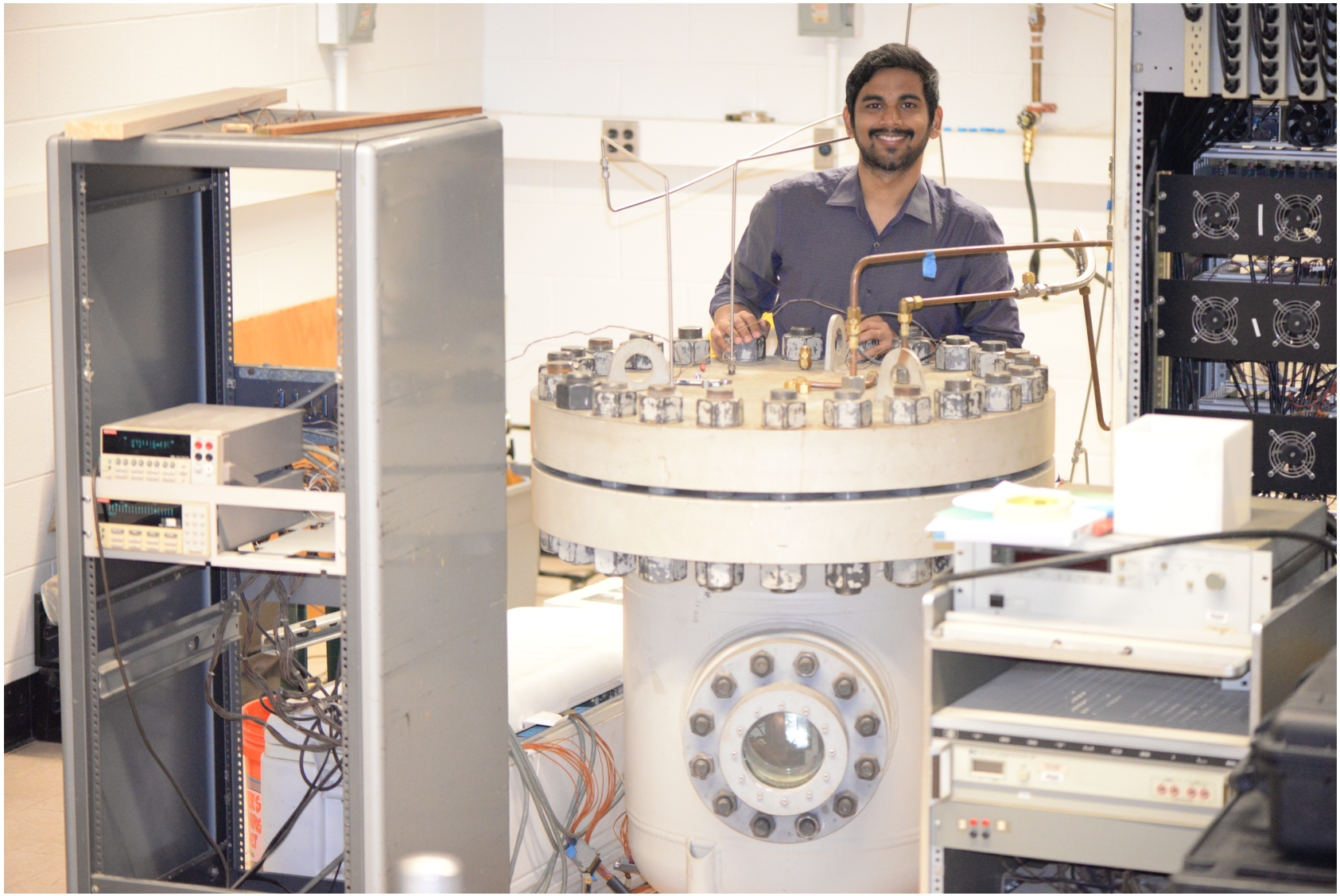

Fig. 3.15 Author with the test equipment

CHAPTER 4

Horizontal Enclosures: Effect of Sidewall Conductance

As can be inferred from the literature (see Chapter 2, Section 2.1.4), the presence of sidewalls with finite thermal conductivity imposes a serious challenge when experimentally estimating the Nu values for the horizontal enclosure problem (Rayleigh-Bénard convection problem), especially when the thermal conductivity of the sidewall material is of the same order, or of an order of magnitude higher, than that of the convecting fluid (Ahlers, 2000; Roche et al., 2001a; Verzicco, 2002; Niemela and Sreenivasan, 2003).

Although it is ideal to use a sidewall material with very low thermal conductivity, some situations, such as using Plexiglas sidewalls ($k_w = 0.195\,W/mK$) for visualization of flow patterns within an enclosure for compressed gas experiments ($k_f = 0.028\,W/mK$) or using stainless steel sidewalls ($k_w = 0.2\,W/mK$) to confine cryogenic helium ($k_f = 0.01\,W/mK$), demand the use of sidewall materials with a thermal conductivity higher than that of the convecting fluid. In such cases, it is essential to correct for the sidewall conductance heat loss before estimating the experimental Nu values.

One of the commonly followed approaches to estimate this sidewall conductance heat loss is the empty-cell gradient method. For this method, the sidewall conductance is estimated by assuming that there is no convection within the test cell or, in other words, the test cell is considered to be an empty-cell or having a stagnant fluid within. Thus, by this assumption, the temperature distribution within the sidewalls can be con-

sidered linear or that for a pure conduction situation. According to Ahlers (2000), this approach is found to be inadequate when using sidewalls with high thermal conductivities and for smaller Rayleigh numbers ($Ra < 10^9$), and yields Nu values unreasonably higher than the values that would exist if the sidewalls were perfectly adiabatic. This is because the thermal contact between the convecting fluid and the sidewalls in the thin boundary layer regions close to the hot and cold plates imposes a much higher temperature gradient in the sidewalls than a conveniently estimated empty-cell gradient. Hence, an empty-cell temperature gradient assumption is expected to yield lower estimates for the sidewall conductance heat loss and, thus, higher Nu values. A serious consequence of this is the change in exponent of Ra in the $Nu - Ra$ relation, for the same range of Ra values, between the cases where the sidewall conductance is appropriately corrected and where it is either ignored or corrected using the empty-cell gradient method (Madanan and Goldstein, 2018 and 2019c). Figure 4.1 shows this difference in the exponent of Rayleigh number (or, in the slope of the log-log $Nu - Ra$ plot) between the two cases, i.e., when the sidewall conductance is estimated using a non-linear temperature gradient (Niemela and Sreenivasan, 2006; where the data are sidewall-corrected using the model proposed by Roche et al., 2001a) and when it is either neglected or modeled conveniently using an empty-cell gradient assumption (Belmonte et al., 1994; Ciliberto et al., 1996). From Figure 4.1 it is evident that the exponent of Rayleigh number is lower for the case where the sidewall conductance is either neglected or modeled using an empty-cell gradient assumption.

Thus, a semi-analytical model is proposed, based on the idea of extended surfaces, to estimate the sidewall-corrected Nusselt number.

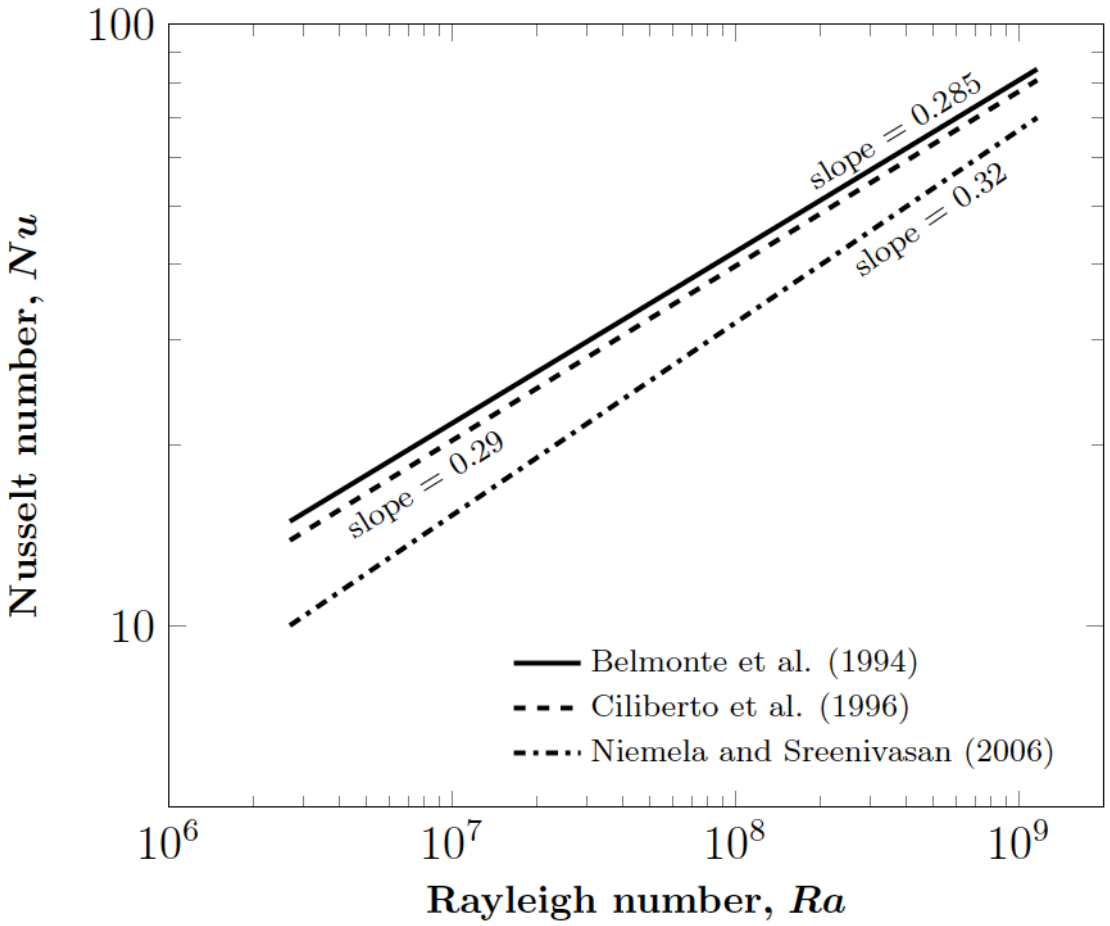

Fig. 4.1 Difference in the exponent of Ra: sidewall correction using different approaches

4.1 The model

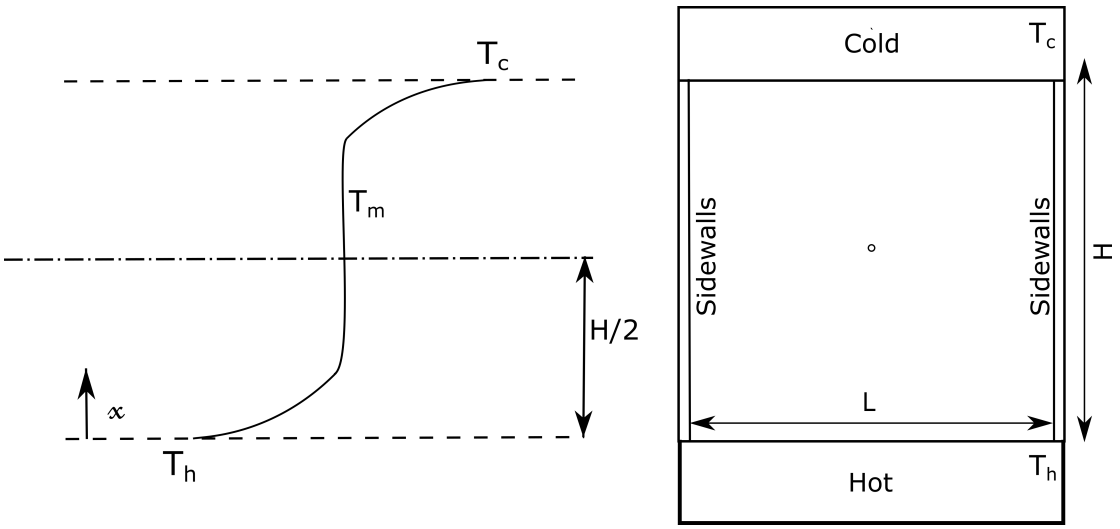

Fig. 4.2 Temperature profile in the sidewall

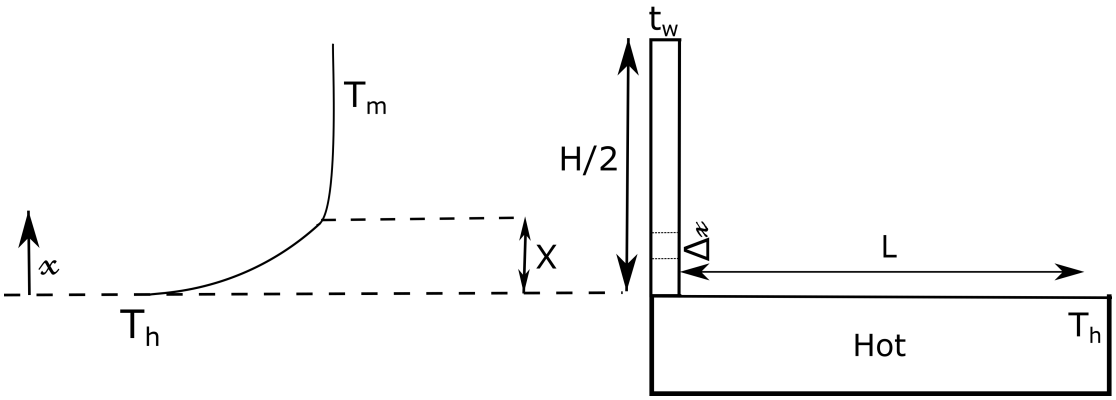

Fig. 4.3 Fin height selection based on the sidewall temperature profile

From the symmetry of the Rayleigh-Bénard problem, the temperature within the sidewall is expected to follow an inverted mirror image symmetry about the horizontal mid-plane at $x = H/2$, as shown in Figure 4.2. Thus, only the bottom half of the enclosure is considered for the analysis, and the temperature profile is expected to be as shown on the left hand side in Figure 4.3. One can assume that, up to a certain height (X), the temperature of the sidewalls is higher than that of the convecting fluid due to its higher thermal conductivity, as shown in Figure 4.3. The temperature profile within the sidewalls is dictated by convection-driven-conduction due to the presence of natural convection within the enclosure. Here, the outer surface of the sidewalls is

assumed to be perfectly insulating. Hence, X can be assumed to be proportional to the characteristic length, L_c, of the convection-driven-conduction problem (or, the fin problem).

To estimate the characteristic length, L_c, of the fin problem, a control volume along the sidewall (shown in Figure 4.3) is considered. Now, one can write:

$$k_w t_w L \Delta x \frac{d^2\theta}{dx^2} - hL\Delta x\theta = 0 \tag{4.1}$$

where $\theta = (T - T_m)$. Since the outer surface of the sidewalls is assumed to be perfectly insulating, this fin is subjected to only internal convection and the perimeter in the fin problem is assumed to be L.

Here, T_m is the mean temperature. According to Chu and Goldstein (1973), based on their experiments using water as the convecting fluid, for Rayleigh numbers beyond 4×10^6, the core region of the enclosure is found to maintain this mean temperature. Hence, most of the temperature drop is expected to occur within a few boundary layer distances from the hot or cold plates. Furthermore, analyzing only the bottom half of the enclosure from Figure 4.3, it can be inferred that there is hardly any heat transfer present between the sidewalls and the convecting fluid after a distance of X from the hot-end. While writing Equation 4.1, the average heat transfer coefficient along the fin height is assumed to be equal to that for the Rayleigh-Bénard convection problem.

Simplifying Equation 4.1 yields:

$$\frac{d^2\theta}{dx^2} - \frac{h\theta}{k_w t_w} = 0 \tag{4.2}$$

And writing h in terms of Nusselt number yields:

$$\frac{d^2\theta}{dx^2} - \frac{Nu_c k_f \theta}{H k_w t_w} = 0 \tag{4.3}$$

The following inferences can be made from Equation 4.3:

- the fin parameter is given by $m^2 = \frac{Nu_c k_f}{H t_w k_w}$

- the characteristic length of the problem, $L_c = \frac{1}{m} = \sqrt{\frac{Ht_w k_w}{Nu_c k_f}}$
- the temperature profile within the sidewalls is exponential

Now, since X is assumed to be proportional to the characteristic length, L_c, one can write:

$$X = cL_c = c\sqrt{\frac{k_w t_w H}{Nu_c k_f}} \tag{4.4}$$

where c is an arbitrary constant.

Consider q_{net} to be the heat input to the hot-end, computed after carefully correcting for all possible heat losses except for the sidewall conductance heat loss. To find the sidewall-corrected net heat input, q_{corr}, one needs to subtract the fin heat transfer from the net heat input (q_{net}). Since the temperature difference between the sidewalls and the fluid is expected to die out after X, this fin heat transfer must be estimated for a fin with a height X and an adiabatic tip.

$$q_{corr} = q_{net} - q_{fin} \tag{4.5}$$

This can be written in terms of Nusselt number as:

$$Nu_c = Nu_{net} - \Delta Nu \tag{4.6}$$

where ΔNu (or, the discrepancy in the experimental Nusselt number due to the presence of sidewalls having finite thermal conductivity) is estimated from q_{fin} and is given by:

$$\Delta Nu = \frac{q_{fin} H}{2L^2 \theta_h k_f} \tag{4.7}$$

Substituting the expression of the fin heat transfer for a fin of height, X, having an adiabatic tip, we get:

$$\Delta Nu = \frac{\left[4k_w t_w L\sqrt{\frac{Nu_c k_f}{Ht_w k_w}}\theta_h \tanh\left[\sqrt{\frac{Nu_c k_f}{Ht_w k_w}}c\sqrt{\frac{k_w t_w H}{Nu_c k_f}}\right]\right]H}{2L^2\theta_h k_f} \tag{4.8}$$

Simplifying this gives:

$$\Delta Nu = \frac{2}{AR}\sqrt{\frac{Nu_c t_w k_w}{Hk_f}}\tanh c \tag{4.9}$$

By substituting Equation 4.6 in Equation 4.9, we get:

$$Nu_{net} = Nu_c\left[1 + \frac{2}{AR}\sqrt{\frac{k_w t_w}{Nu_c k_f H}}\tanh c\right] \tag{4.10}$$

or

$$Nu_c = \frac{Nu_{net}}{\left[1 + \frac{2}{AR}\sqrt{\frac{k_w t_w}{Nu_c k_f H}}\tanh c\right]} \tag{4.11}$$

Introducing wall number, Wn $(= \frac{4k_w t_w}{ARHk_f})$, as suggested by Roche et al. (2001a), this equation can be rewritten as:

$$Nu_c = \frac{Nu_{net}}{\left[1 + \sqrt{\frac{Wn}{Nu_c AR}}\tanh c\right]} \tag{4.12}$$

$$\Delta Nu = Nu_{net} - Nu_c = \sqrt{\frac{WnNu_c}{AR}}\tanh c \tag{4.13}$$

where, Wn is the ratio of thermal diffusion resistance of the stagnant fluid to that of the sidewalls. In Equation 4.12, the value of 'c' is unknown and must be determined experimentally. Equation 4.12 also clearly indicates that sidewall correction is a function of this wall number. This means that the sidewall conductance is not merely a function of the ratio of the thermal conductivities of the sidewall and the convecting fluid $\left(\frac{k_w}{k_f}\right)$, but also depends on the thickness of the sidewall itself and the aspect ratio of the enclosure.

Table 4.1 Experimental conditions for assessing the effect of sidewall conductance ($H = L = 0.15\,m$, $AR = 1$, and $\Delta T \approx 8\,K$)

Experiment	Pressure (bar)	Ra	Fluid
1	1.00	2.68×10^6	N_2
2	1.58	6.67×10^6	N_2
3	2.07	1.15×10^7	N_2
4	4.54	5.52×10^7	N_2
5	6.05	9.82×10^7	N_2
6	9.02	2.23×10^8	N_2
7	15.01	6.18×10^8	N_2
8	20.54	1.16×10^9	N_2

4.2 Experiments

Experiments are performed with a cubical convection test cell of dimension $0.15\,m$ (i.e., $AR = 1$) placed inside a pressure vessel which can compress the fluid (nitrogen) to high pressures. Three sidewall materials are used for this part of the present study, i.e., Styrofoam ($k_w = 0.033\,W/m \cdot K$), Plexiglas ($k_w = 0.195\,W/m \cdot K$), and high-density polyethylene (HDPE) ($k_w = 0.49\,W/m \cdot K$), which yield wall numbers (Wn) of 0.18, 1.09, and 2.74, respectively. Three sets of experiments, having eight sub-experiments each (refer to Table 4.1) are carried out with each of the three different sidewall materials. The corresponding experiments for each of these sidewall materials are performed by fixing the operating conditions (p, T_m, and ΔT) as shown in Table 4.1. Rayleigh numbers of the order of 10^6 - 10^9 are achieved by compressing nitrogen to pressures as high as $20\,bars$ with an imposed $\Delta T \approx 8\,K$. Achieving nearly the exact same Rayleigh number among the corresponding experiments with each of the three sidewall materials is found to be a challenging task when using nearly identical operating conditions. Hence, the estimated Nu values for each of the three cases are scaled using the local exponent of Rayleigh number to ensure that they all correspond to the same Rayleigh number.

The net power input (q_{net}) to the convection test cell is computed by subtracting all the carefully accounted losses, except for the sidewall conductance heat loss (q_{sw}), from the total power input. As shown in Figure 4.4, the accounted losses include: (1) outward heat loss from the hot plate in the direction opposite to the convecting fluid

(q_g), (2) edge heat loss from the hot plate assembly through the balsa wood insulation that runs all around the periphery of the hot-end (q_e), (3) surface heat loss from the sidewall outer surfaces (q_s), and (4) radiation heat loss from the hot surface (q_r).

Using q_{net}, the Nu_{net} values, for each of the operating conditions listed in Table 4.1 and all the three investigated sidewall cases, can be estimated as:

$$Nu_{net} = \frac{q_{net} H}{\Delta T L^2 k_f} \tag{4.14}$$

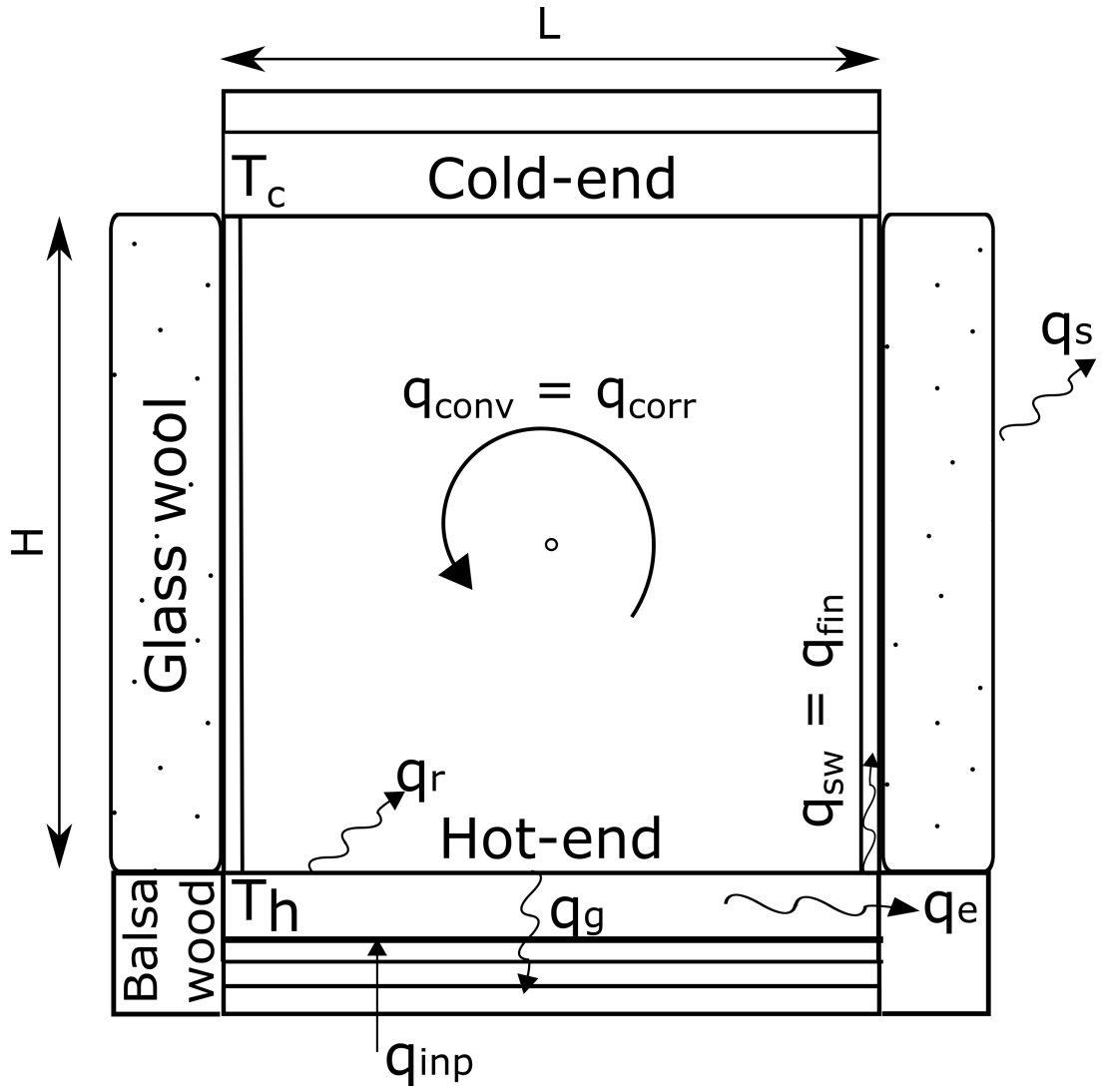

Fig. 4.4 Schematic of the test cell depicting various heat losses

4.3 The corrected Nusselt numbers and value of c

Figure 4.5 shows the Nu_{net} values, normalized with $Ra^{0.31}$, plotted against Wn. Here, an exponent of 0.31 is chosen based on the results from two studies corresponding to the investigated range of Rayleigh numbers, i.e., the sidewall-corrected results of Verzicco (2002) and the experiments by Goldstein and Tokuda (1980) using water as the convecting fluid, wherein the effect of sidewalls may be ignored due to the higher thermal conductivity of the convecting fluid. This plot is utilized to extrapolate and estimate the Nu_{net} value for an ideal zero-thermal-conductivity sidewall case or, in other words, Nu_c. It can be inferred from the plot that the spread in the normalized Nu_{net} values increases with an increase in Wn. For the HDPE sidewall (or, a higher Wn value case), the lowest $\left(\frac{Nu_{net}}{Ra^{0.31}}\right)$ corresponds to the highest investigated Rayleigh number. This indicates that the effect of sidewall conductance decreases as the Rayleigh number is increased. From the trendline equations estimated for the data points in Figure 4.5, it can be concluded that $Nu_c \approx 0.0965Ra^{0.31}$. Furthermore, when the absolute Nu_{net} values are plotted against Wn and utilized to extrapolate and estimate the Nu_c values, the estimated values yield a relation of the form: $Nu_c \approx 0.0881Ra^{0.315}$.

In Figure 4.6, the difference between the Nu_{net} and Nu_c values (or, ΔNu) is plotted against Wn. The dotted line in the plot corresponds to the ΔNu values estimated based on a traditional empty-cell temperature gradient assumption. The experimentally measured ΔNu values are found to be higher than those estimated using a traditional empty-cell gradient assumption, with the experiments, oftentimes, yielding values up to six times the corresponding empty-cell corrections. Another noteworthy observation is that the slope $\left(\frac{d\Delta Nu}{dWn}\right)$ of the curve reduces as Wn is increased. This possibly indicates that for very large Wn values (i.e., when the sidewalls can be assumed to be "perfectly conducting"), the experimental ΔNu values may be approaching the empty-cell temperature gradient estimates.

Figure 4.7 shows a comparison of the experimental and predicted ΔNu values for the Plexiglas and HDPE sidewall cases. Equation 4.13 is used for predicting the ΔNu values. The constant 'c' in Equation 4.13 needs to be estimated, which can be achieved

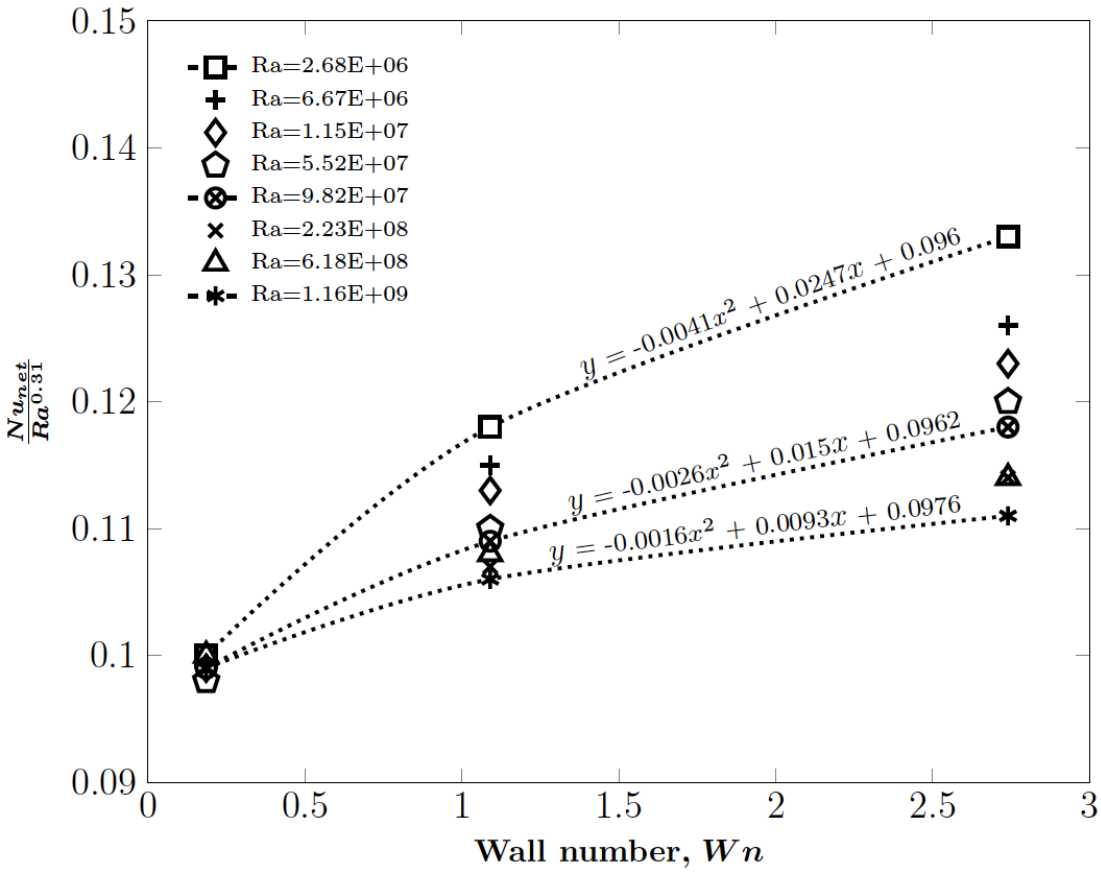

Fig. 4.5 Normalized Nu vs. wall number for extrapolation

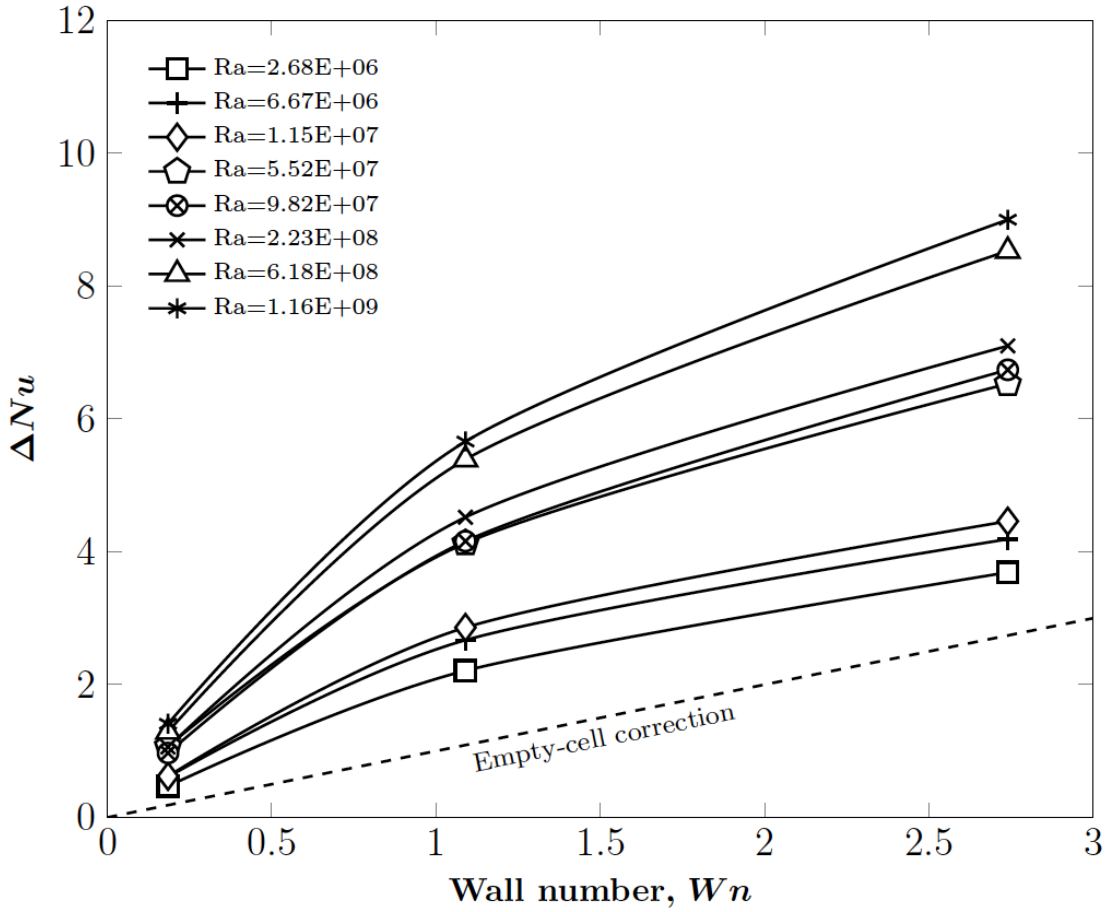

Fig. 4.6 Difference between net and corrected Nu values

by utilizing the experimental Nu_{net} values and their corresponding Nu_c values. The values of 'c' estimated for the Plexiglas sidewall case are observed to be a very weak function of Rayleigh number. Hence, these values of 'c' are averaged to ≈ 0.925. This value of 'c' is then used to predict the ΔNu values for the HDPE case. These ΔNu predictions are found to agree to within 11% of the experimental ΔNu values for the investigated range of Ra values, thus, validating the generality of the value of 'c' for the investigated range of parameters. Hence, this value of 'c' is used for future computations.

For the case with Styrofoam sidewalls, or for smaller Wn values ($Wn \rightarrow 0$), Equation 4.12 is found to be inappropriate. This departure in the predictions from the experimental values may be due to the deviation from one of the aforementioned assumptions that the temperature of the sidewalls is higher than that of the convecting fluid. In this case, the temperature of the sidewalls is dictated by the fluid itself. Hence, an empirical relation (Equation 4.15) is developed using the present data, which is found to predict the experimental Nu_c values with very good accuracy (within 1.5%).

$$Nu_c = \frac{Nu_{net}}{[1 + Wn^2]} \tag{4.15}$$

In Figure 4.8, this same value of c ($= 0.925$) is used to predict the ΔNu values for Verzicco's (2002) direct numerical simulation studies ($AR = \frac{1}{2}$, $Wn = 0.919$, and $2 \times 10^6 \leq Ra \leq 2 \times 10^9$). The predicted ΔNu values are found to agree reasonably well (within 8%) with Verzicco's estimates for $Ra > 10^7$. Hence, Equation 4.12 with $c = 0.925$ (for $Wn \geq \mathcal{O}(1)$) and Equation 4.15 (for $Wn \rightarrow 0$) are recommended for estimating the sidewall conductance heat loss for $10^6 \leq Ra \leq 10^9$.

Figure 4.9 compares the experimental Nu_c values with the corresponding Nu_{net} values for each of the three sidewall materials by plotting them against Rayleigh number on a decadic log-log plot. One of the serious implications here is an appreciable difference in the slope of the log-log plot between Nusselt number and Rayleigh number (or, the exponent of Ra in the $Nu - Ra$ relation), with the slope for the HDPE sidewalls case being considerably lower when compared with that for the sidewall-corrected data.

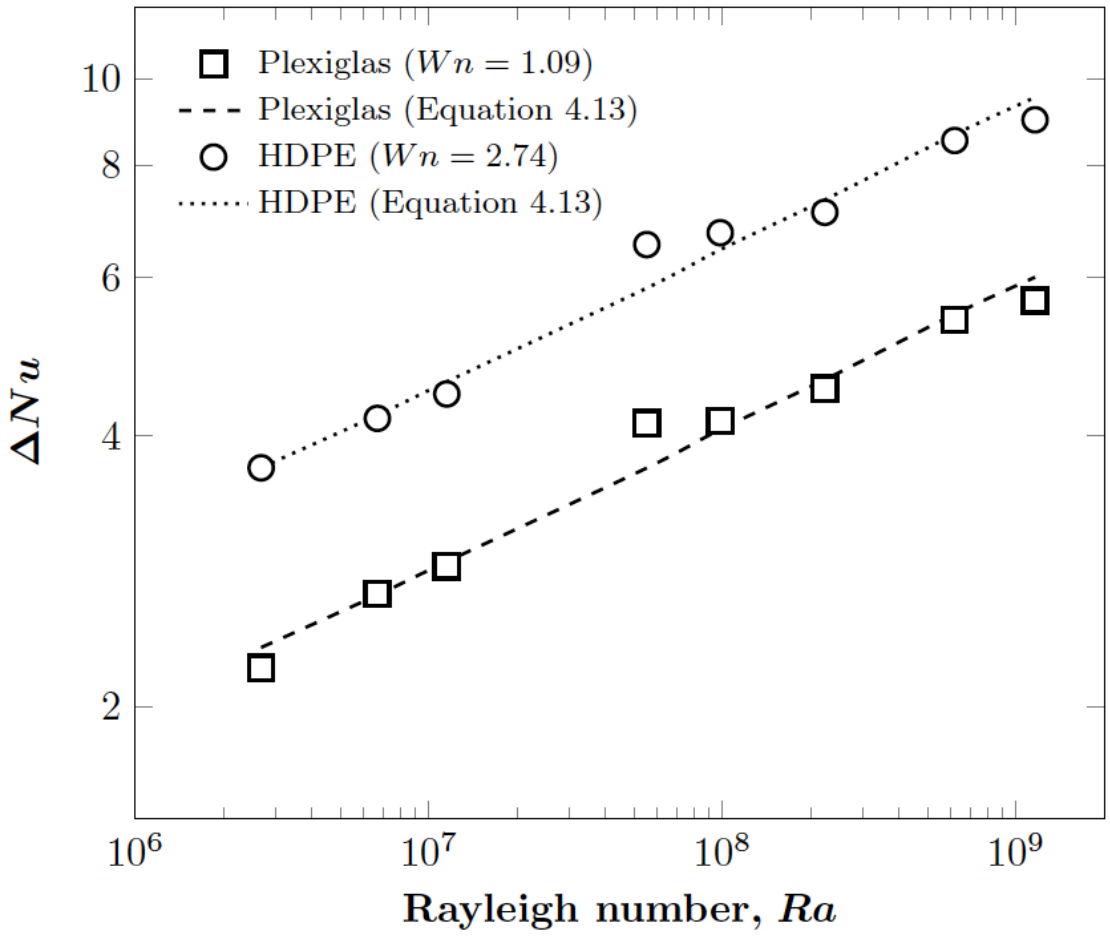

Fig. 4.7 ΔNu: experiment vs. prediction ($c = 0.925$)

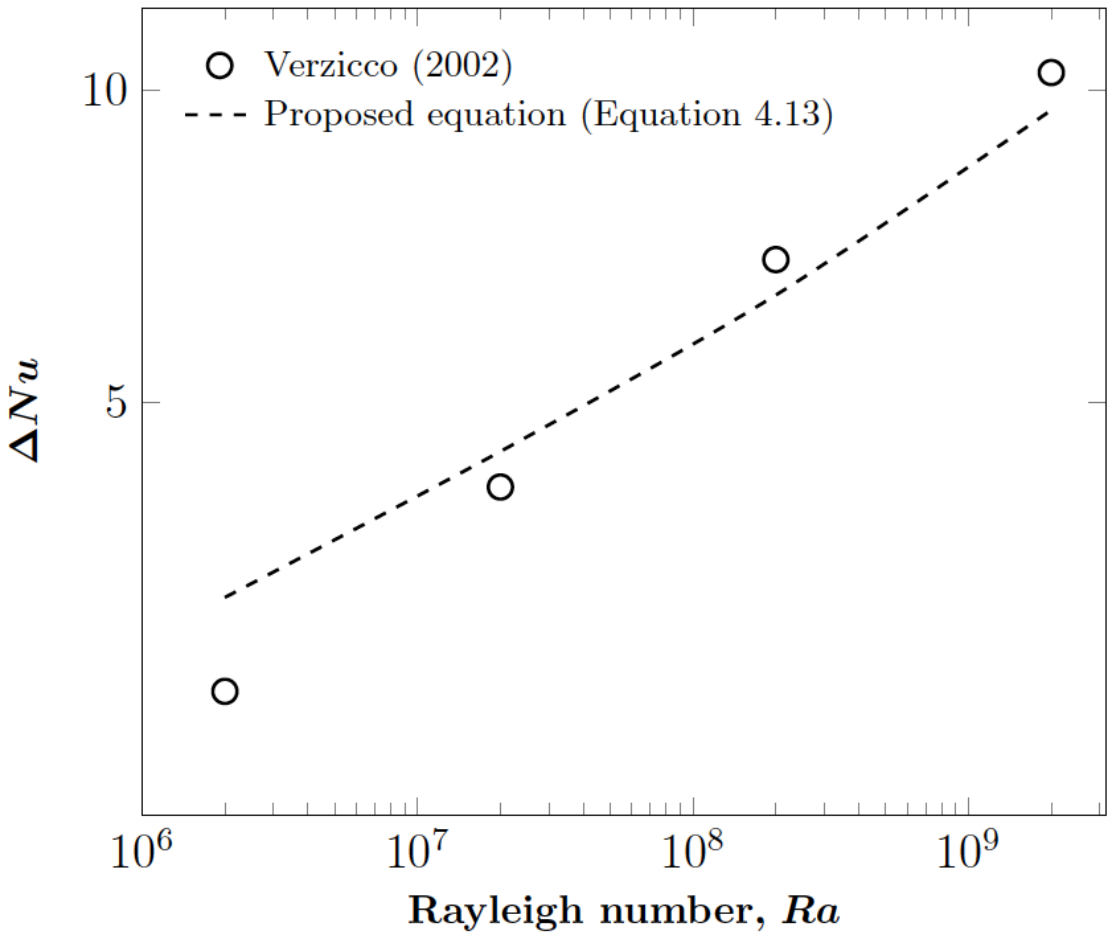

Fig. 4.8 Comparison with the literature: model ($c = 0.925$) vs. Verzicco (2002) ($Wn = 0.919$, $AR = \frac{1}{2}$)

One may refer to Madanan and Goldstein (2019c) for further details. This underscores the importance of properly modeling and correcting the sidewall conductance heat loss for the Rayleigh-Bénard convection studies, especially when $Ra \leq 10^9$.

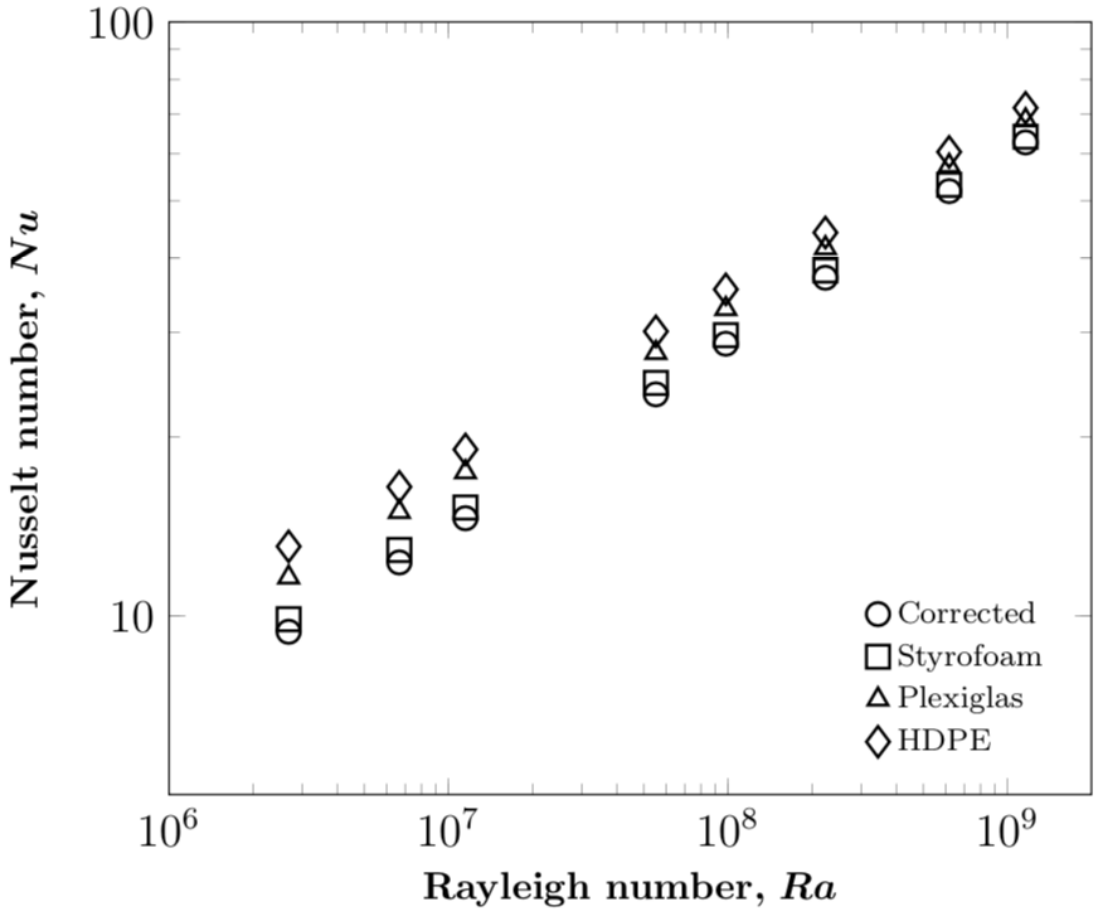

Fig. 4.9 Comparison of corrected (Nu_c) and net Nusselt number (Nu_{net}) values

CHAPTER 5
Horizontal Enclosures

5.1 Validity of data points

The complete set of experiments, with the operating conditions and the estimated Nusselt numbers, is listed in Table 5.1. As can be seen from Table 5.1, the fractional variation of density (or, $\beta\Delta T$) is found to be within ≈ 0.11, which is lower than the yardstick value proposed by Gray and Giorgini (1976) for adherence to the Oberbeck-Boussinesq approximation. To further examine the validity of the data points, fractional variations of the various thermo-physical properties are scrutinized. For any thermo-physical property (obtained from the *NIST Chemistry WebBook*; Lemmon et al., 2003), this fractional variation is computed by normalizing the difference in the property values estimated at the hot- and cold-plate temperatures with the respective values estimated at the mean temperature.

Figure 5.1 depicts the fractional variation of density, thermal conductivity, specific heat, and dynamic viscosity plotted against Rayleigh number for all the experimental data points. Similarly, the fractional variation of Prandtl number for all the experimental data points is plotted against Rayleigh number in Figure 5.2. It is evident from the two plots that the computed fractional variations for the entire range of investigated Rayleigh numbers are modest (and within 10%). Since the current study employs fluids (nitrogen and argon) that have very similar property values, except for their molecular weights, the fractional variation of Prandtl number and the thermo-physical properties between the two fluids is not expected to show a large variation when plotted against

Table 5.1 Horizontal enclosure experimental data

Run No.	Pressure (bar)	T_m ($^\circ C$)	$T_{amb}(^\circ C)$	Fluid	$\Delta T(K)$	Ra	AR	Pr	$\beta\Delta T$	$q_{inp}(W)$	Nu_{exp}
1	17.67	22.80	22.64	N_2	17.03	1.85×10^6	10	0.7335	0.0602	6.397	8.87
2	32.83	21.96	21.87	N_2	8.11	3.25×10^6	10	0.7421	0.0297	3.622	10.39
3	40.03	22.22	22.16	N_2	9.25	6.14×10^6	10	0.7454	0.0343	5.061	12.80
4	50.00	22.29	22.18	N_2	7.04	8.77×10^6	10	0.7494	0.0266	4.423	14.33
5	70.03	22.29	22.22	N_2	4.99	1.05×10^7	10	0.7568	0.0195	3.022	14.83
6	62.8	22.14	22.08	N_2	9.09	1.28×10^7	10	0.7542	0.0351	6.251	15.93
7	34.78	22.03	22.00	N_2	19.91	3.98×10^7	6	0.7431	0.0733	10.831	21.78
8	46.17	22.38	22.27	N_2	17.97	6.33×10^7	6	0.7479	0.0675	11.146	24.22
9	58.81	22.08	21.98	N_2	17.01	9.76×10^7	6	0.7528	0.0654	13.230	29.71
10	29.87	23.00	22.89	N_2	24.98	2.89×10^8	3	0.7404	0.0907	12.167	41.33
11	53.27	22.23	22.14	N_2	20.97	7.90×10^8	3	0.7507	0.0799	15.489	57.32
12^a	69.01	22.29	22.23	N_2	16.03	1.00×10^9	3	0.7564	0.0626	13.251	62.14
$12A^a$	58.6	22.05	21.89	N_2	21.96	1.00×10^9	1	0.7528	0.0845	5.946	62.52
13	79.64	22.05	21.97	N_2	21.96	1.82×10^9	3	0.7603	0.0872	24.148	78.11
14	24.97	21.99	21.87	N_2	17.96	3.96×10^9	1	0.7380	0.0647	7.132	96.78
15	65.32	22.04	21.89	N_2	6.06	9.23×10^9	1	0.7552	0.0235	3.587	133.22
16	67.32	21.87	21.79	N_2	9.97	1.62×10^{10}	1	0.7560	0.0389	7.112	161.55
17	79.64	22.05	21.97	N_2	21.96	4.92×10^{10}	1	0.7603	0.0872	21.760	219.19
18	89.88	22.08	21.96	Ar	18.98	7.60×10^{10}	1	0.7408	0.0821	16.047	256.12
19	89.93	22.35	22.27	Ar	25.92	1.04×10^{11}	1	0.7406	0.1123	24.862	291.12
A^b	79.38	22.2	22.03	N_2	19.96	4.40×10^7	10	0.7601	0.0791	19.960	22.08
B^b	35.43	22.11	21.87	N_2	20.94	4.40×10^7	6	0.7433	0.0772	11.625	22.19
C^b	14.97	22.01	21.77	N_2	15.56	4.40×10^7	3	0.7319	0.0547	4.220	22.27
D^b	3.03	22.31	22.13	N_2	14.53	4.40×10^7	1	0.7226	0.0496	1.302	22.41

^{a,b} Experiments at fixed Ra to examine the effect of AR on Nu

Rayleigh number.

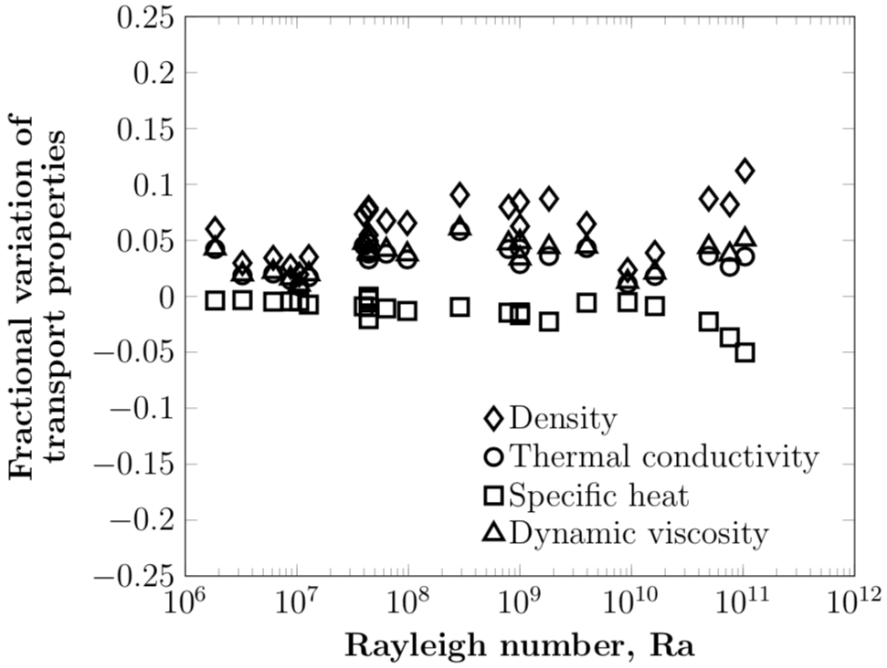

Fig. 5.1 Fractional variation of transport properties for the complete data set

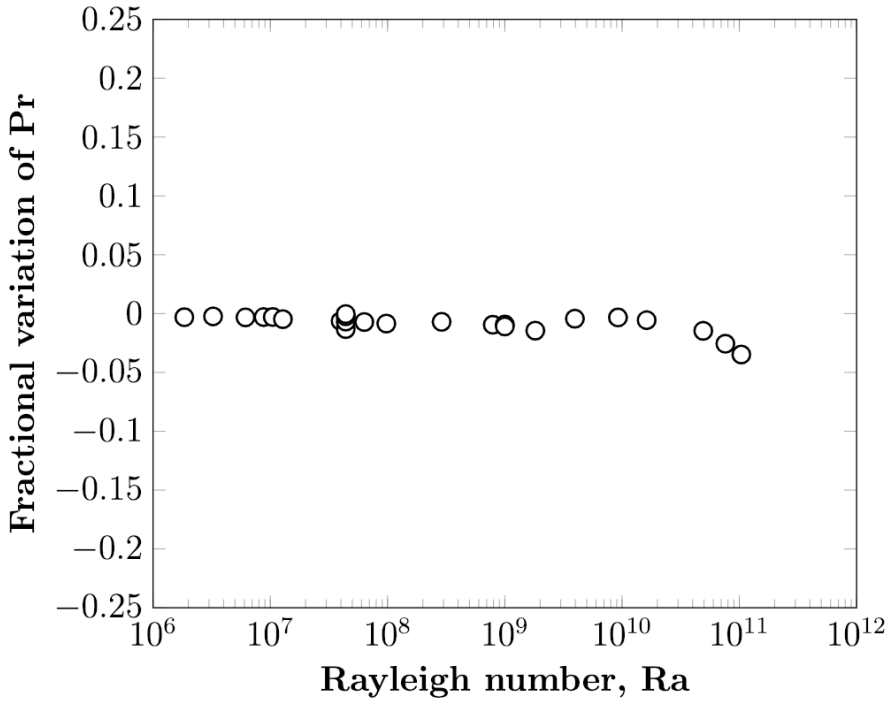

Fig. 5.2 Fractional variation of Prandtl number for the complete data set

5.2 Experiments

The primary set of experiments consists of heat transfer measurements taken for 19 data points for various Rayleigh numbers ($1.85 \times 10^6 \leq Ra \leq 1.04 \times 10^{11}$) and different aspect ratios ($AR = 1, 3, 6,$ and 10). In these experiments, a higher Rayleigh number is achieved by increasing the working pressure, increasing the temperature difference between the hot and cold plates, or increasing the spacing between the hot and cold plates (i.e., decreasing the aspect ratio). Thus, it is difficult to ascertain the individual effects of aspect ratio and Rayleigh number on Nusselt number from the primary experiments.

Hence, two supplementary sets of experiments are also conducted, each for a fixed value of Rayleigh number (as shown by ^{a} and ^{b} in Table 5.1) to isolate the effect of aspect ratio on Nusselt number. Within a particular set of supplementary experiments, achieving almost the exact same Rayleigh number with different operating conditions is found to be a challenging task. In such cases, the obtained Nu values are scaled using an appropriate exponent to ensure that they all correspond to the same Rayleigh number.

5.3 $Nu - Ra$ scaling

Experimental Nu values are plotted against Ra values on a decadic log-log plot, as shown in Figure 5.3. The best fit for the entire set of 19 data points (i.e., for $1.85 \times 10^6 \leq Ra \leq 1.04 \times 10^{11}$ and $Pr \approx 0.74$) is found to be:

$$Nu = 0.067 Ra^{0.330} \tag{5.1}$$

The exponent of this best fit is very close to that of the classical $\frac{1}{3}^{rd}$ scaling relation and is within the experimental uncertainty. Two noteworthy observations from this scaling relation are: (i) the exponent of Rayleigh number in the proposed scaling relation is considerably different than the often reported exponent of $\frac{2}{7}$ (Castaing et al., 1989; Wu and Libchaber, 1992; Belmonte et al., 1994; Ciliberto et al., 1996; Urban et al., 2014) and (ii) even at the highest investigated decade of Ra values, the scaling exponent of Ra is found to be nearly equal to $\frac{1}{3}$ and there is no indication of a transition to a higher exponent, unlike the findings reported by many researchers (Ahlers et al., 2012; Chavanne et al., 2001; He et al., 2012a, 2012b).

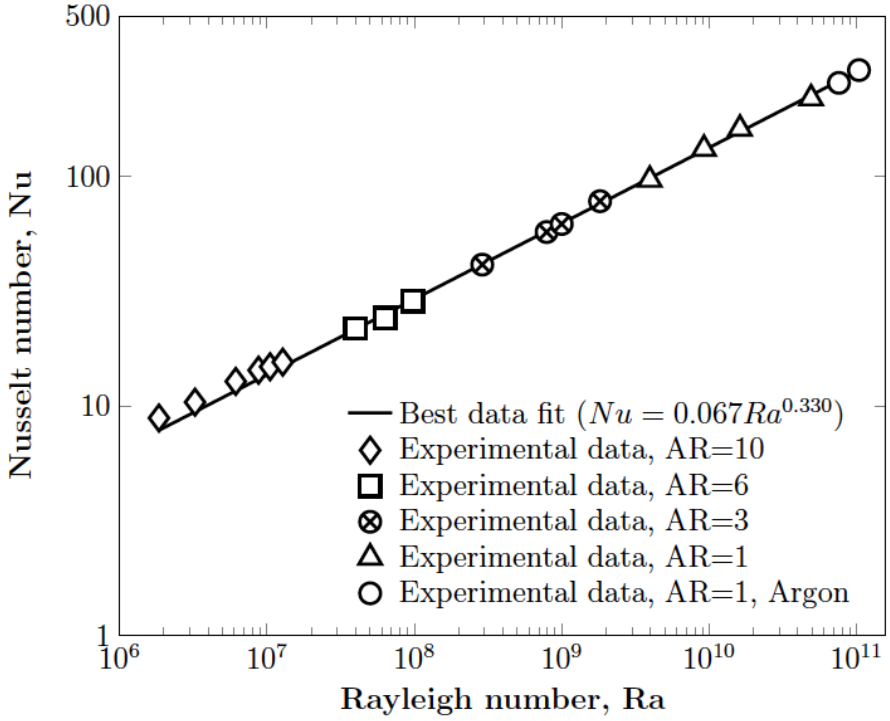

Fig. 5.3 $Nu - Ra$: decadic log-log plot of data points

Figure 5.4 shows the classical $\frac{1}{3}^{rd}$ scaling relation overlaid on the complete set of data for comparison and Figure 5.5 shows the scatter of the experimental data when a $Nu \sim Ra^{1/3}$ is enforced. This scatter is well within 2 standard deviation ($\approx \pm 11\%$) on either side of the mean (≈ 0.0645). Hence, for the entire range of investigated Rayleigh numbers and a $Pr \approx 0.74$, this data set yields an approximate yet reasonably accurate fit of:

$$Nu = 0.0645 Ra^{1/3} \tag{5.2}$$

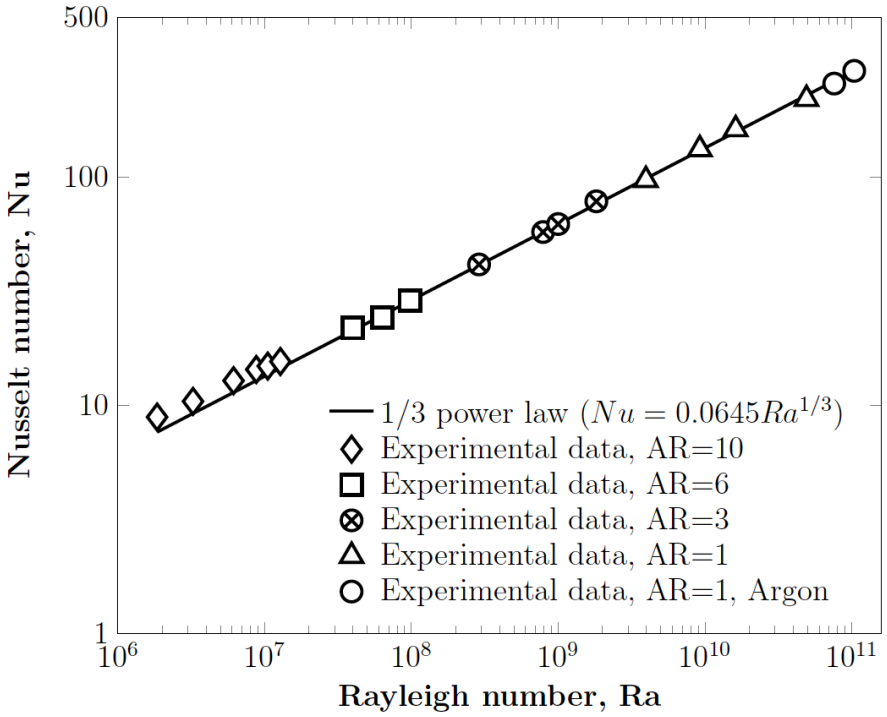

Fig. 5.4 $Nu - Ra$ classical scaling: decadic log-log plot of data points

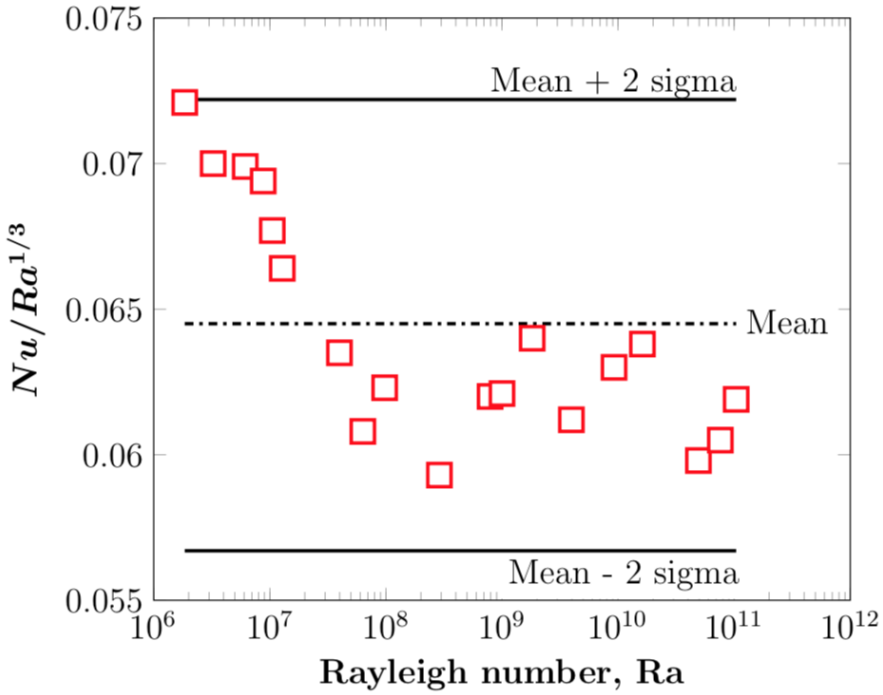

Fig. 5.5 $Nu - Ra^{1/3}$ fit of the primary data points

5.4 Effect of aspect ratio on Nu

Two sets of experiments (marked ^{a} and ^{b} in Table 5.1) are performed to verify the effect of aspect ratio on Nusselt number. To analyze this effect, Nusselt number, normalized with Nusselt number for the highest aspect ratio (in that particular set), is plotted against aspect ratio, as shown in Figure 5.6. Hence, Nusselt number is normalized using $Nu_{AR=3}$ for the first set of experiments (^{a} in Table 5.1) and $Nu_{AR=10}$ for the second set (^{b} in Table 5.1).

The first set of experiments (^{a} in Table 5.1) is carried out for $Ra = 4.40 \times 10^7$ and covers all aspect ratios. The second set of experiments for $Ra = 1.0 \times 10^9$ is limited to two aspect ratios (AR = 1 and 3) since achieving this Rayleigh number for aspect ratios 6 and 10 is not possible due to the constraints imposed by the pressure vessel capabilities. The variation in the Nu values between the lowest and highest aspect ratios for the first set of experiments is found to be negligible and within 1.5%. An identical trend is observed for the second set of experiments. Goldstein et al. (1987), with their electrochemical mass transfer experiments at a fixed Rayleigh number of 4.8×10^{10}, have also observed a similar negligible effect of aspect ratio on Nusselt number, with

a 1.5% variation in the Nu values when the aspect ratio is varied from 1.4 to 18. Xu et al. (2000), Funfschilling et al. (2005), Zhou et al. (2012), and Madanan and Goldstein (2019a) have also communicated a negligible effect of aspect ratio on Nusselt number for a similar range of Rayleigh numbers. Although this effect is negligible, the Nu values are observed to decrease slightly with an increase in the aspect ratio (as shown in Figure 5.6).

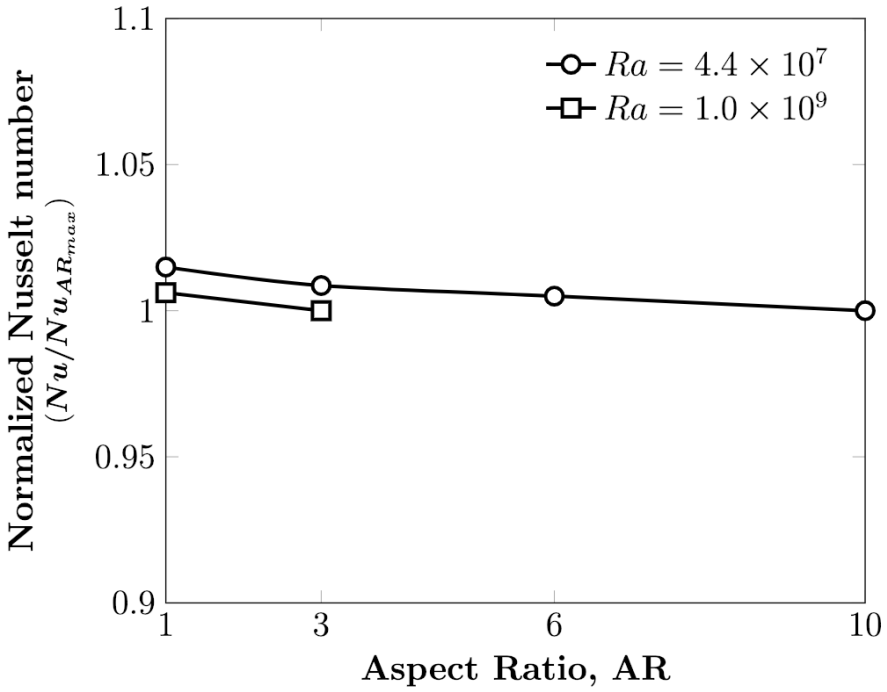

Fig. 5.6 Effect of aspect ratio on Nusselt number

5.5 $Nu - Ra$ scaling: comparison with the literature

The experimental Nu values are compared with the Nu values predicted using select $Nu - Ra$ correlations from the existing literature, chosen based on different criteria outlined in the following paragraphs, and plotted on a decadic log-log plot, as depicted in Figures 5.8 through 5.18.

Since, according to Ahlers et al. (2009a), Nusselt number is a weak function of Prandtl number when $Pr \gtrsim 1$, the first set of studies chosen for comparison are Goldstein and Chu (1969), Goldstein and Tokuda (1980), and Goldstein et al. (1990), previous experimental studies conducted in the same laboratory as the present study but

using different working fluids. Goldstein and Chu (1969) have used air as the working fluid and their data are limited to the lower range of Rayleigh numbers ($6 \times 10^5 \leq Ra \leq 1.2 \times 10^8$). The maximum deviation of the current data from that of Goldstein and Chu (1969) is found to be 5.6%. The data of Goldstein and Tokuda (1980) and Goldstein et al. (1990) overlap with the present study in the range $10^9 \leq Ra \leq 10^{11}$, with the present data falling between the values predicted by them. The data of Goldstein and Tokuda (1980) (with water as the working fluid, $Pr \approx 6.5$) are found to under-predict the Nu values by as high as 13% and that of Goldstein et al. (1990) (with an electro-chemical solution as the working fluid, $Pr\ (Sc) \approx 2750$) over-predict the Nu values by up to 10%, as depicted by Figures 5.8 and 5.9.

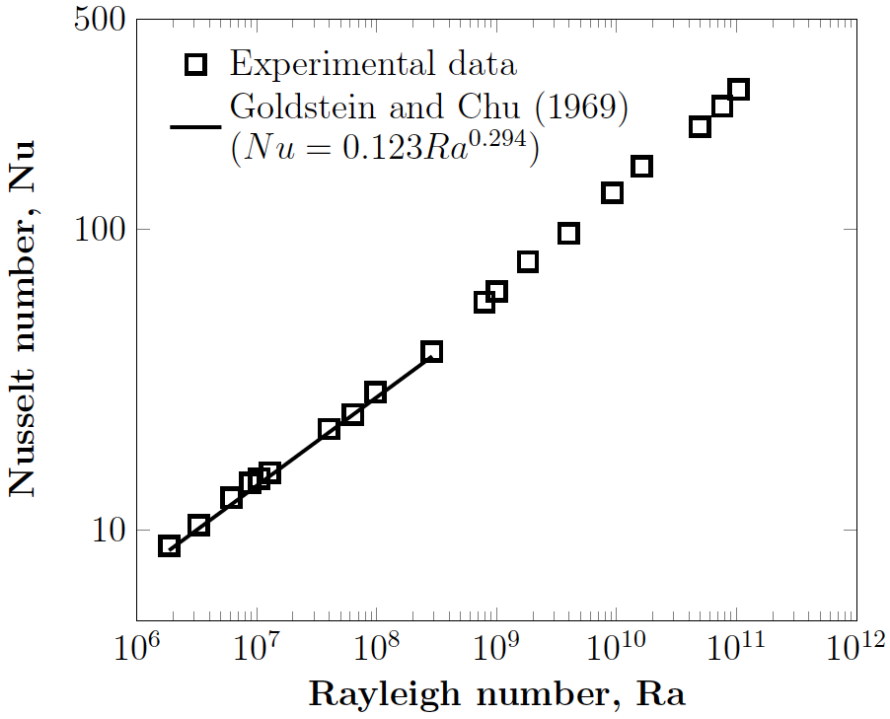

Fig. 5.7 Nu vs. Ra on a log-log plot: data vs. Goldstein and Chu (1969)

The second set of comparisons uses two other experimental investigations conducted in the same laboratory (Fleischer and Goldstein, 2002; Srinivasan, 2007) using similar working fluids as the present study (compressed nitrogen, argon, and krypton) (refer to Figures 5.10 and 5.11). However, these experiments are performed only for $10^9 \leq Ra \leq 10^{12}$ and $0.6 \leq AR \leq 3$. The maximum deviation of the current data from Fleischer and Goldstein (2002) in the region with overlapping Ra values is found

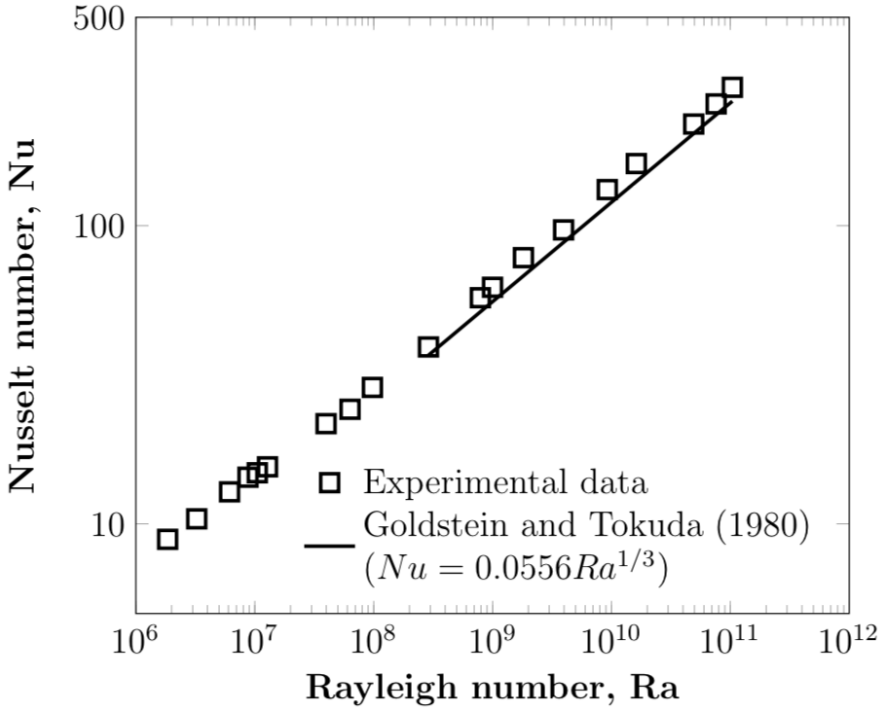

Fig. 5.8 Nu vs. Ra on a log-log plot: data vs. Goldstein and Tokuda (1980)

to be 3.64%, whereas for Srinivasan (2007), this is observed to be 12.46%. Moreover, the $\frac{1}{3}$ fit of Fleischer and Goldstein (2002) yields a relation $Nu = 0.0616Ra^{1/3}$, which is very similar to that of the present study.

The present study is also compared with a few select literature that suggests a $\frac{2}{7}$ scaling relation (Castaing et al., 1989; Belmonte et al., 1994; Ciliberto et al., 1996), as shown by Figures 5.12, 5.13, and 5.14. Here, the values obtained from the literature show a clear over-prediction for the lower range of Ra values ($10^6 \leq Ra \leq 10^9$).

Four other studies used for comparison are Niemela et al. (2000), Niemela and Sreenivasan (2006), Waleffe et al. (2015), and Chong and Xia (2016), who have proposed an exponent higher than $\frac{2}{7}$ but lower than the classical $\frac{1}{3}^{rd}$ scaling (i.e., $Nu \sim Ra^{0.31}$). The experimental data, especially for lower Ra values, are observed to match very well with Niemela and Sreenivasan (2006), showing a deviation of only 6.3%. The other three comparisons show an over-prediction of the Nu values for the lower range of Ra values, which is qualitatively similar to the trend observed for the comparison between the present study and the literature suggesting a $\frac{2}{7}$ scaling relation.

Comparing the experimental and literature-predicted Nu values, one can observe a

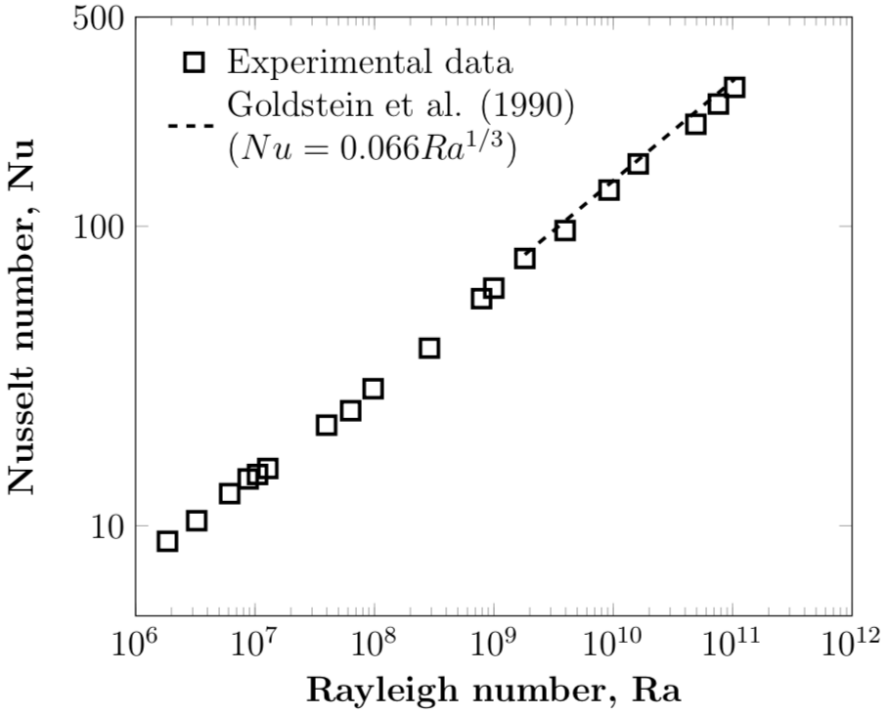

Fig. 5.9 Nu vs. Ra on a log-log plot: data vs. Goldstein et al. (1990)

considerable variation at lower Ra values, which gradually converge to match as the Ra values go beyond 10^9. This is certainly true for Castaing et al. (1989), Belmonte et al. (1994), and Ciliberto et al. (1996), who have proposed considerably lower exponents for the same range of Ra values. Niemela and Sreenivasan (2006), who have taken into account the effect of sidewall conductance on Nusselt number, have presented a distinctly higher slope (or, the exponent of Ra in the scaling relation) compared to the other literature covering the lower range of Rayleigh numbers. The lower exponent of Ra in the scaling relation observed in the literature can be explained by revisiting Figure 3.9 (refer to Chapter 3), where we notice that the Nu values for the case with HDPE sidewalls (or, for an improperly modeled sidewall conductance scenario) are discernibly higher for the lower range of investigated Ra values. This can contribute to a lower slope in the $Nu - Ra$ log-log plot, thereby yielding a lower exponent for Ra in the scaling relation.

Figure 5.19 shows the experimental data points overlaid on the Grossmann-Lohse regime-specific map (Grossmann and Lohse, 2000) to verify how the scaling relation obtained from the present experimental study compares with those proposed by Gross-

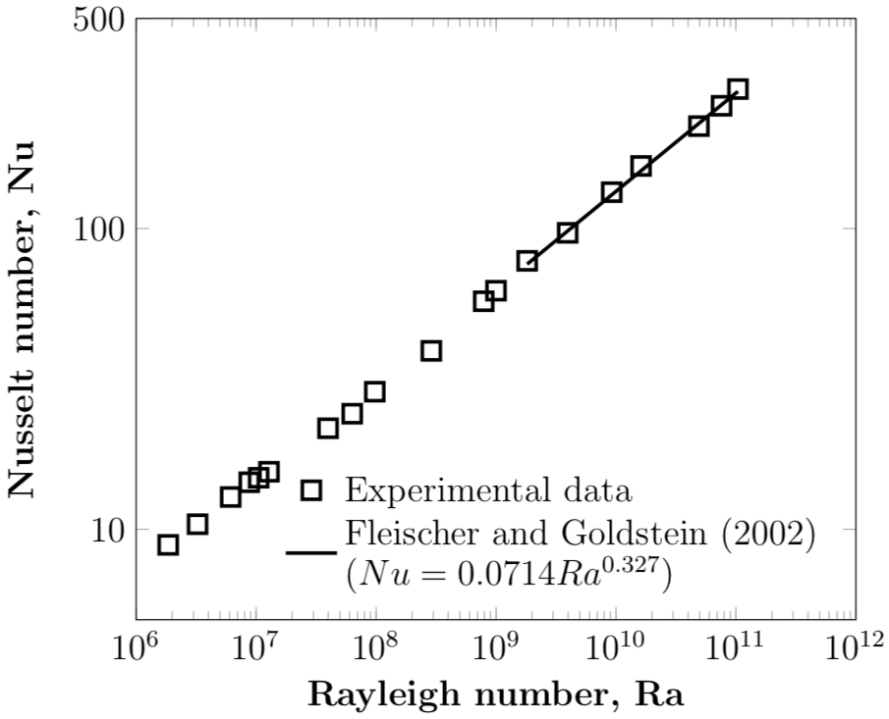

Fig. 5.10 Nu vs. Ra on a log-log plot: data vs. Fleischer and Goldstein (2002)

mann and Lohse (2000) for the same range of Rayleigh numbers and $Pr \approx 0.71$. The data points from the present study are in the I_l and IV_l regimes of the map, which, according to Grossmann and Lohse (2000), yields scaling relations of $Nu \sim Ra^{1/4}$ and $Nu \sim Ra^{1/2}$ respectively. Interestingly, the present data indicate a scaling relation of $Nu \sim Ra^{1/3}$, which may be interpreted as a linear combination of $Nu \sim Ra^{1/4}$ and $Nu \sim Ra^{1/2}$. Using a linear combination of the suggested scaling relations for I_l and IV_l regimes of the Grossmann-Lohse regime-specific map (Grossmann and Lohse, 2000) to predict the Nusselt number ($Nu = 0.27Ra^{1/4}Pr^{1/8} + 4.43 \times 10^{-4}Ra^{1/2}Pr^{1/2}$) yields Nu values within 10% of the experimental Nu values obtained from the present study (when $Ra > 2 \times 10^7$).

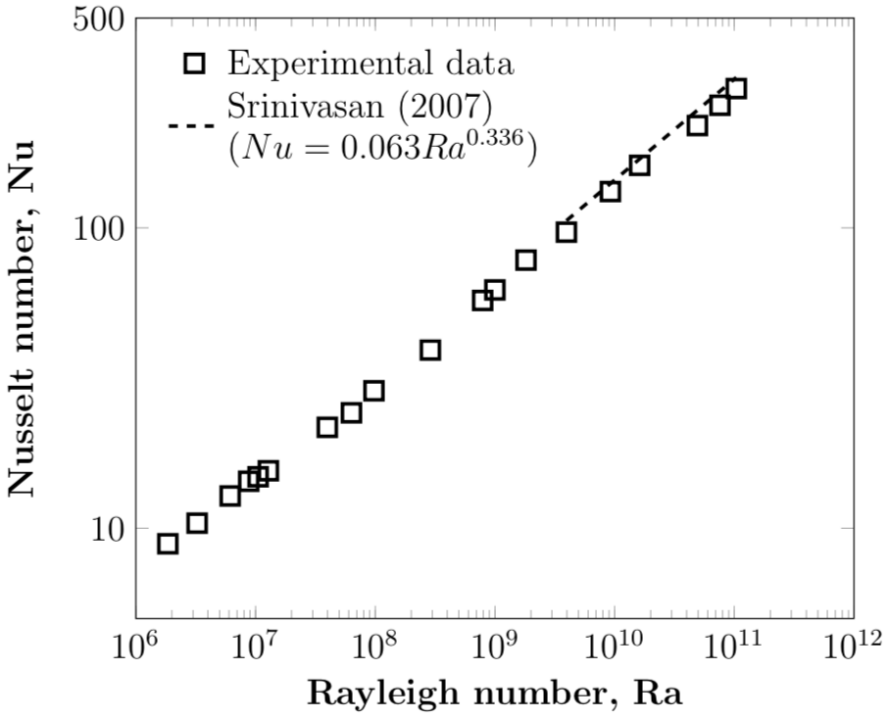

Fig. 5.11 Nu vs. Ra on a log-log plot: data vs. Srinivasan (2007)

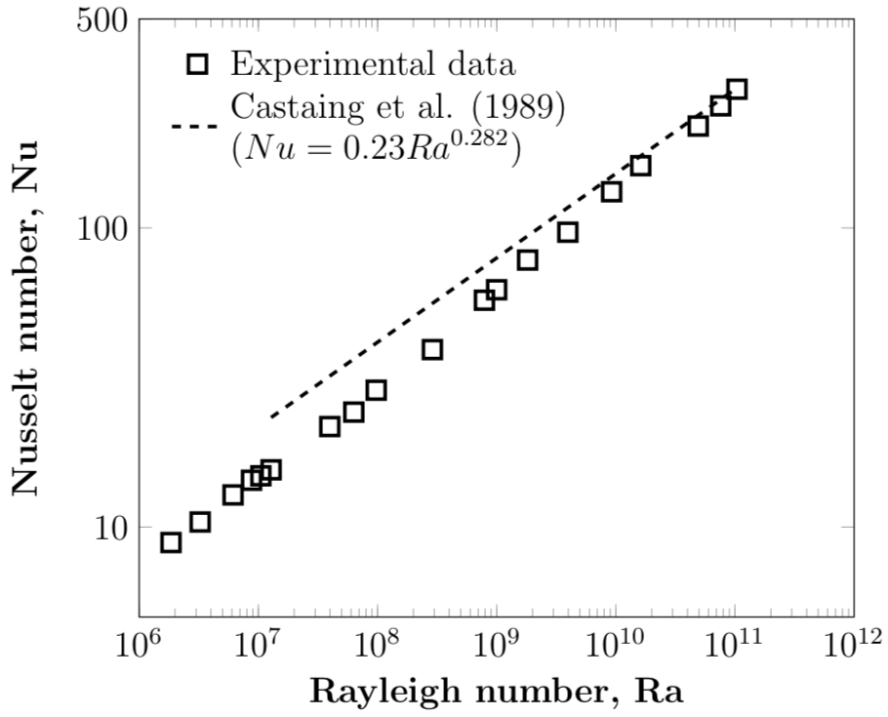

Fig. 5.12 Nu vs. Ra on a log-log plot: data vs. Castaing et al. (1989)

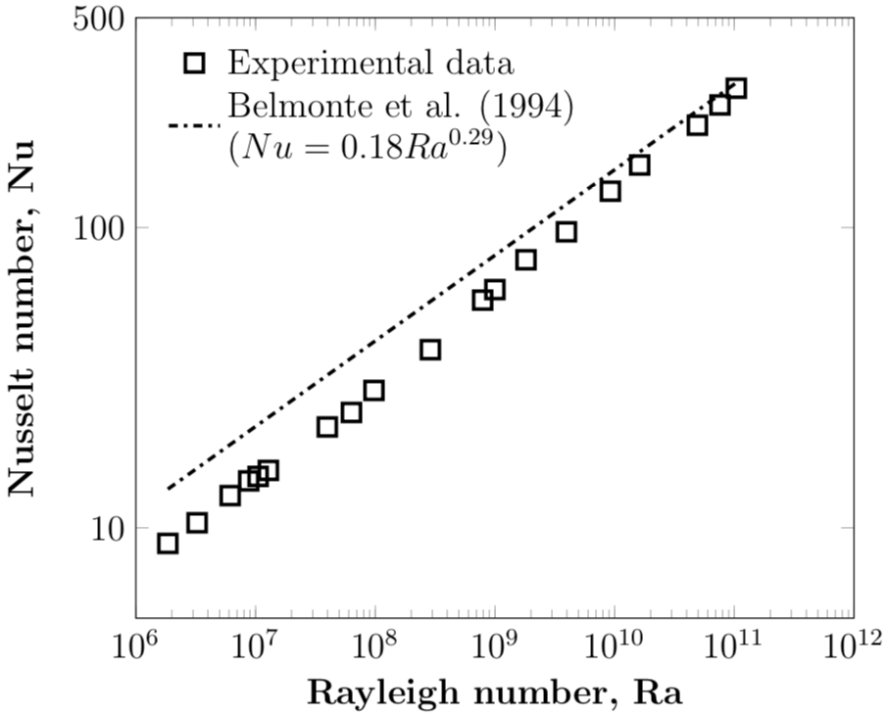

Fig. 5.13 Nu vs. Ra on a log-log plot: data vs. Belmonte et al. (1994)

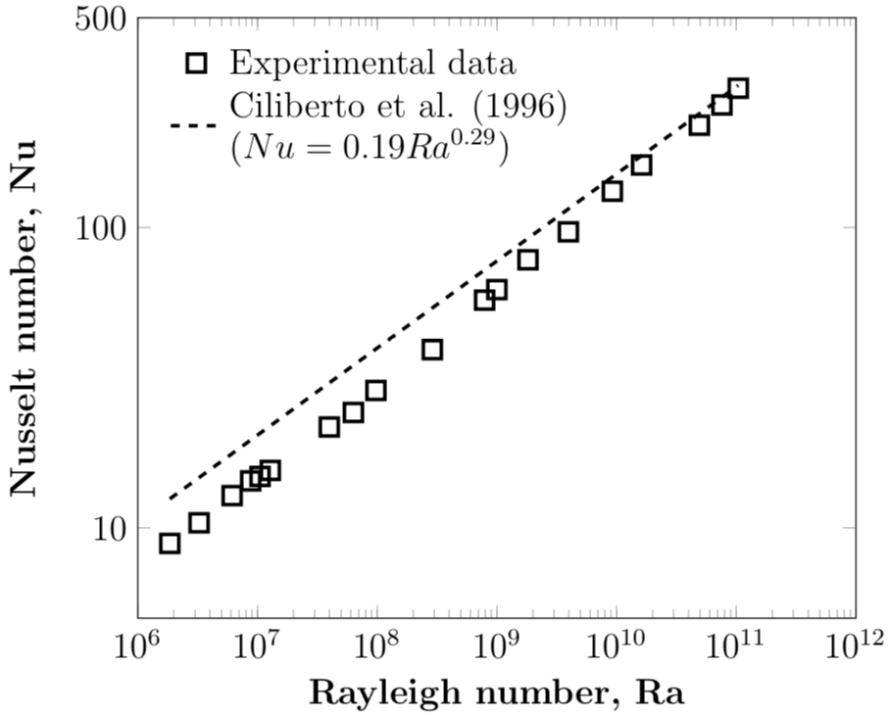

Fig. 5.14 Nu vs. Ra on a log-log plot: data vs. Ciliberto et al. (1996)

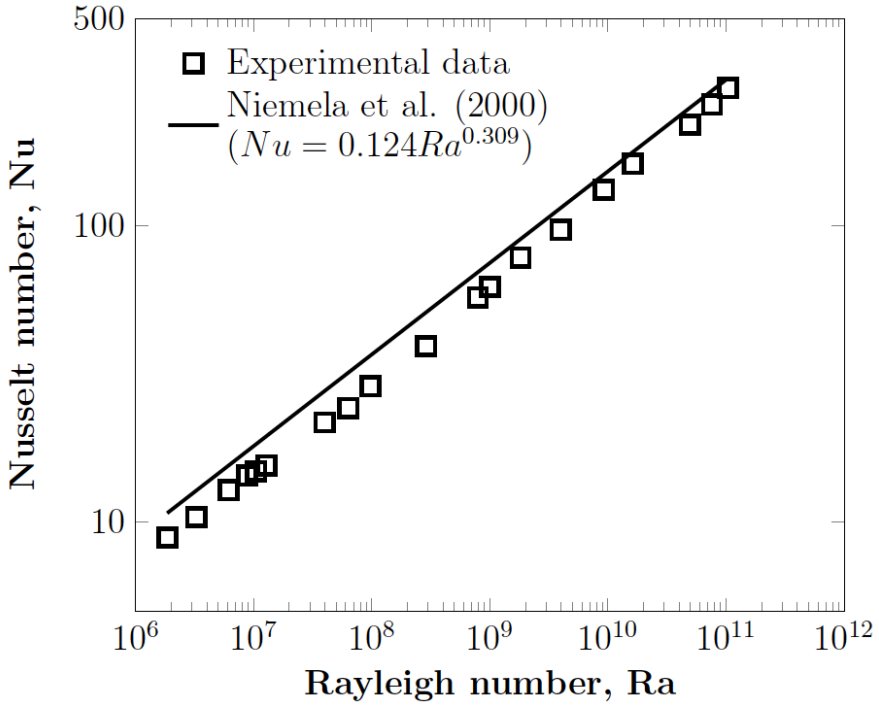

Fig. 5.15 Nu vs. Ra on a log-log plot: data vs. Niemela et al. (2000)

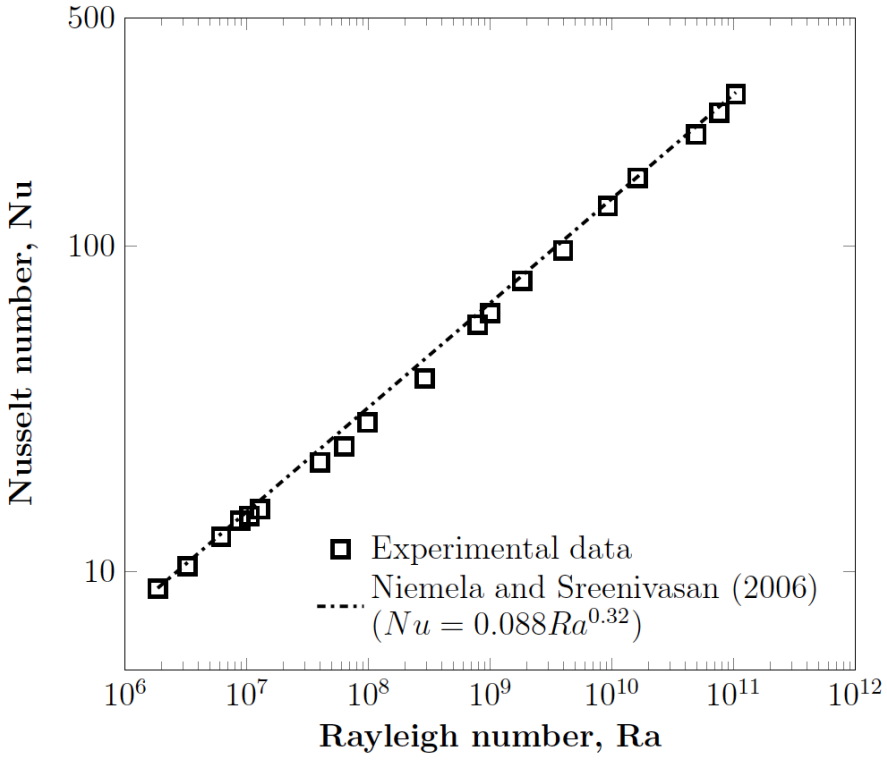

Fig. 5.16 Nu vs. Ra on a log-log plot: data vs. Niemela and Sreenivasan (2006)

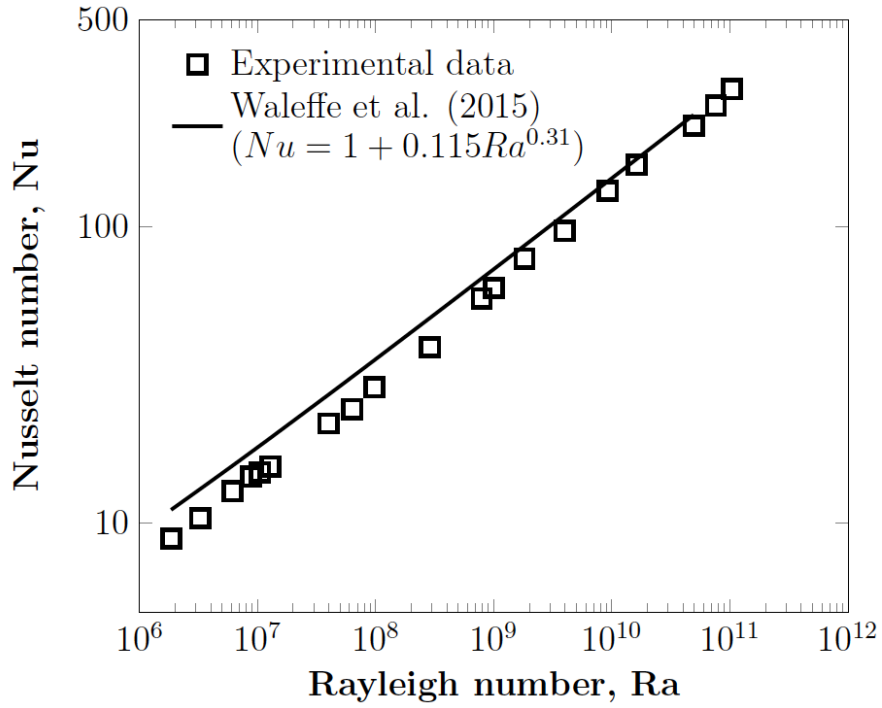

Fig. 5.17 Nu vs. Ra on a log-log plot: data vs. Waleffe et al. (2015)

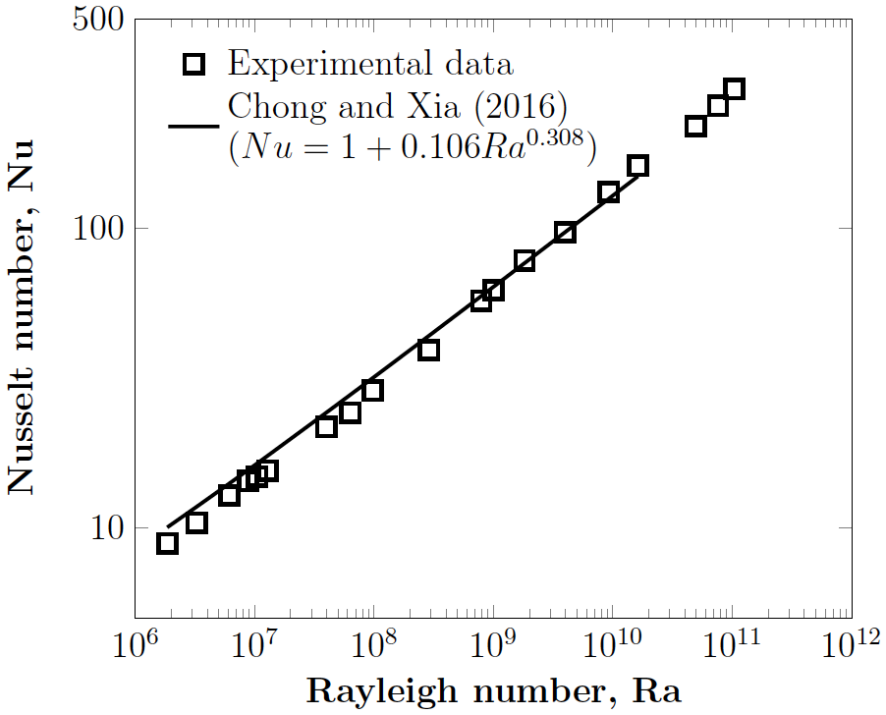

Fig. 5.18 Nu vs. Ra on a log-log plot: data vs. Chong and Xia (2016)

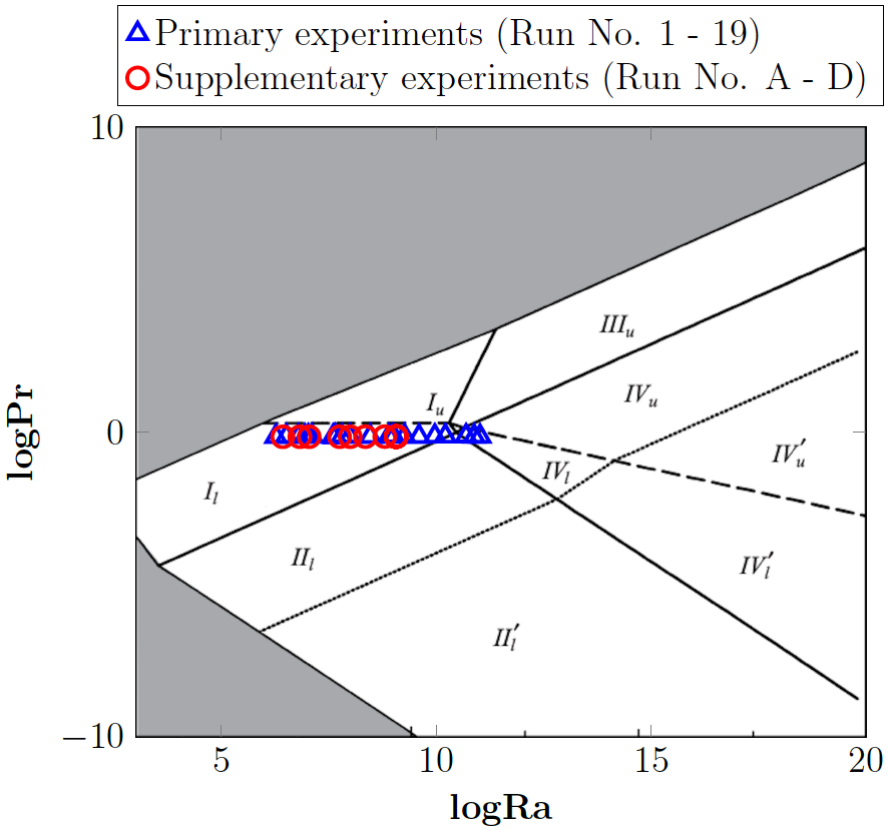

Fig. 5.19 Experimental data points on Grossmann-Lohse map (Grossmann and Lohse, 2000)

5.6 Effect of Prandtl number on Nusselt number

The current study employs fluids (nitrogen and argon) with near identical Pr values ($Pr \simeq 0.7$) which may be treated as $Pr \approx 1$. Furthermore, according to Ahlers et al. (2009a) and Roche et al. (2002), Nusselt number is found to be independent of Prandtl number when $Pr \approx 1$. Therefore, though it is difficult to ascertain the effect of Prandtl number on Nusselt number from the present experimental data, strictly speaking, even if one uses a broader range of Pr values close to unity (or, 1 ± 0.3), the results may still show only a negligible variation in Nusselt number.

5.7 Effect of finite thermal conductivity of hot plate on Nusselt number

According to Verzicco (2004), another important factor that can change the Nu values is the finite thermal conductivity of the hot or cold plates. When the input heat flux is high, the finite thermal conductivity of the plates can significantly alter the uniform surface temperature condition due to the fact that thermal convection leads to a much higher effective fluid thermal conductivity. Verzicco (2004) has performed Direct Numerical Simulations (DNS) of a Rayleigh-Bénard cell to suggest a correction for the measured Nu values in terms of the ratio of the effective thermal resistance of the fluid to that of the plate. He has related the ideal Nu values that would exist for an infinitely conducting plate (Nu_∞) to the measured Nusselt number as:

$$\frac{Nu_\infty}{Nu} = \frac{1}{F(X_p)} \tag{5.3}$$

Brown et al. (2005) have approached the same problem experimentally and have proposed a simple functional form for the correction factor suggested by Verzicco (2004), $F(X_p)$, as given by:

$$F(X_p) = 1 - \exp\left(-c_1 X_p^{c_2}\right) \tag{5.4}$$

with $c_1 = 0.275$ and $c_2 = 0.39$ (see Section 2.1.4.2 for details).

For the present study, this effect is analyzed by comparing the experimentally estimated Nu values with the Nu_∞ values, obtained using the simplified correction factor ($F(X_p)$) proposed by Brown et al. (2005), for all the investigated Rayleigh numbers. The correction factor estimated for the current study is found to be very close to unity, yielding a maximum value of $\approx 0.06\%$ for $(\frac{Nu_\infty}{Nu} - 1)$. This suggests that the effect of finite thermal conductivity of the hot or cold plates on Nusselt number can be assumed to be negligible for the present study. A plot showing the departure of Nu values from the ideal Nu_∞ values for each of the investigated Ra values is presented in Figure 5.20. According to Brown et al. (2005), these results are expected for a small test cell similar to the one used in the present study.

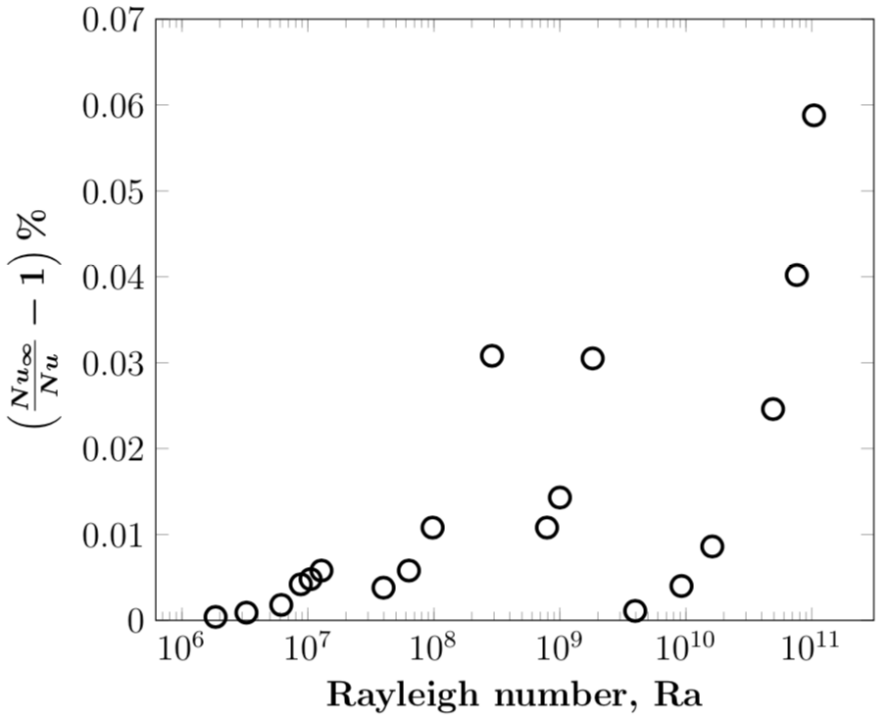

Fig. 5.20 Deviation of Nu values for an infinitely conducting hot plate from the experimentally observed Nu values using a copper hot plate

CHAPTER 6
Tilted Enclosures

6.1 Experiments

For tilted enclosures, in addition to Rayleigh number and aspect ratio, angle of tilting (or, inclination) of the test cell is also expected to play a significant role in deciding the total heat transfer between the hot and cold plates.

Thus, to deduce the effect of the angle of inclination, a set of nineteen experiments is performed for the range of Rayleigh numbers and aspect ratios listed in Table 6.1 for each of the six investigated angles of inclination. Since Rayleigh number is dependent on aspect ratio, a set of supplementary experiments is also conducted by varying the aspect ratio while keeping the Rayleigh number fixed (as identified by experiments A,B, C, and D in Table 6.1) to isolate and understand the effect of aspect ratio on Nusselt number. This set of supplementary experiments is limited to four of the more significant (having more real-world applications) angles of inclination ($\phi = 0°$, $30°$, $60°$, $90°$) among the investigated cases.

For each of the inclined enclosure experimental runs, the operating conditions are maintained nearly identical to those of the corresponding horizontal enclosure case (as detailed in Chapter 5) to ensure that the data points adhere to the Oberbeck-Boussinesq approximation and are valid. Achieving the exact same Rayleigh number with nearly identical operating conditions among different titled enclosure experimental runs is found to be a challenging task. In such cases, the obtained Nu values are scaled using an appropriate local exponent of Rayleigh number to ensure that they all correspond to

the same Rayleigh number. A similar procedure is carried out within a particular set of supplementary experiments, where achieving the exact same Rayleigh number with different operating conditions proves to be difficult.

Table 6.1 Primary experiments dataset: tilted enclosures

Run No.	Pressure (bar)	T_m ($^\circ C$)	Fluid	$\Delta T(K)$	Ra	$AR = L/H$	Nu_{exp}					
							0°	30°	60°	90°	120°	150°
1	17.67	22.80	N_2	17.03	1.85×10^6	10	8.87	7.02	6.66	5.90	4.73	4.22
2	32.83	21.96	N_2	8.11	3.25×10^6	10	10.39	8.32	7.63	7.03	6.24	5.86
3	40.03	22.22	N_2	9.25	6.14×10^6	10	12.80	10.01	9.25	8.77	7.85	7.03
4	50	22.29	N_2	7.04	8.77×10^6	10	14.33	12.01	10.99	9.66	8.17	7.65
5	70.03	22.29	N_2	4.99	1.05×10^7	10	14.83	12.64	11.87	10.23	8.67	7.94
6	62.8	22.14	N_2	9.09	1.28×10^7	10	15.93	13.77	12.76	10.63	9.02	8.43
7	34.78	22.03	N_2	19.91	3.98×10^7	6	21.78	18.64	16.31	14.99	12.92	11.67
8	46.17	22.38	N_2	17.97	6.33×10^7	6	24.22	22.72	20.99	17.98	16.26	14.72
9	58.81	22.08	N_2	17.01	9.76×10^7	6	29.71	27.67	25.23	20.99	18.23	16.93
10	29.87	23.00	N_2	24.98	2.89×10^8	3	41.33	36.23	34.27	31.00	25.65	22.47
11	53.27	22.23	N_2	20.97	7.90×10^8	3	57.32	54.67	49.26	43.11	35.23	32.17
12	69.01	22.29	N_2	16.03	1.00×10^9	3	62.14	58.93	54.19	45.44	39.82	37.23
13	79.64	22.05	N_2	21.96	1.82×10^9	3	78.11	76.22	69.99	55.87	49.22	46.32
14	24.97	21.99	N_2	17.96	3.96×10^9	1	96.78	88.77	83.19	70.49	63.29	52.11
15	65.32	22.04	N_2	6.06	9.23×10^9	1	133.22	124.55	113.15	95.88	79.44	73.67
16	67.32	21.87	N_2	9.97	1.62×10^{10}	1	161.55	152.77	141.38	117.00	101.26	92.33
17	79.64	22.05	N_2	21.96	4.92×10^{10}	1	219.19	207.81	195.67	162.23	146.47	139.23
18	89.88	22.08	Ar	18.98	7.60×10^{10}	1	256.12	239.23	228.11	191.23	178.11	162.34
19	89.93	22.35	Ar	25.92	1.04×10^{11}	1	291.12	283.11	269.23	211.11	201.88	189.11
A^a	79.38	22.2	N_2	19.96	4.40×10^7	10	22.08	18.43	15.61	14.11	-	-
B^a	35.43	22.11	N_2	20.94	4.40×10^7	6	22.19	19.20	16.77	15.76	-	-
C^a	14.97	22.01	N_2	15.56	4.40×10^7	3	22.27	19.73	17.88	16.99	-	-
D^a	3.03	22.31	N_2	14.53	4.40×10^7	1	22.41	20.45	19.01	18.42	-	-

[a] Experiments at fixed Ra to examine the effect of AR on Nu

6.2 Effect of angle of inclination on Nusselt number

Figures 6.1 - 6.4 depict the variation in the Nusselt number with different angles of inclination for each of the four examined aspect ratios. The dotted lines in these figures connect the Nu values corresponding to an angle of inclination of 150° to a Nusselt number of unity at an angle of inclination of 180°. Here, a Nusselt number of unity is a direct consequence of heat transfer due to pure conduction. This occurs at an angle of inclination of $\phi = 180^{\circ}$ (or, for the heated from above and cooled from below case) since the density gradient is stable, which leads to no bulk fluid motion within the enclosure.

A few noteworthy observations can be made by analyzing Figures 6.1 - 6.4. Firstly, the Nu values are observed to decrease with an increase in the angle of inclination and this decreasing trend remains qualitatively the same for all the studied aspect ratios. This monotonously decreasing trend in Nusselt number, which can be attributed to a reduction in buoyant force in the flow direction with an increase in the tilting angle, is comparable with that from some of the studied literature, i.e., Goldstein et al. (1987) for very high Rayleigh numbers ($Ra > 10^8$) and Elsherbiny et al. (1982a), Schinkel and Hoogendoorn (1985), and Elsherbiny (1996) for the lower range of Rayleigh numbers ($Ra \leq 10^6$). Furthermore, this variation in Nusselt number is observed to become more prominent as the Rayleigh number is increased, while maintaining the same aspect ratio. The decline or drop in the Nu values between the angles of inclination from 0° to 90° is found to be substantial, whereas, in general, it is minimal between the angles of inclination from 90° to 150°.

Another noteworthy observation made from Figures 6.1 - 6.4 is that Nusselt number does not achieve a local minimum between 0° and 90°, which indicates the absence of a critical angle of inclination for the investigated cases. A similar observation has been reported for very high Rayleigh numbers by Dropkin and Somerscales (1965) and Goldstein et al. (1987) based on their studies using very high Prandtl (or, Schmidt) number fluids.

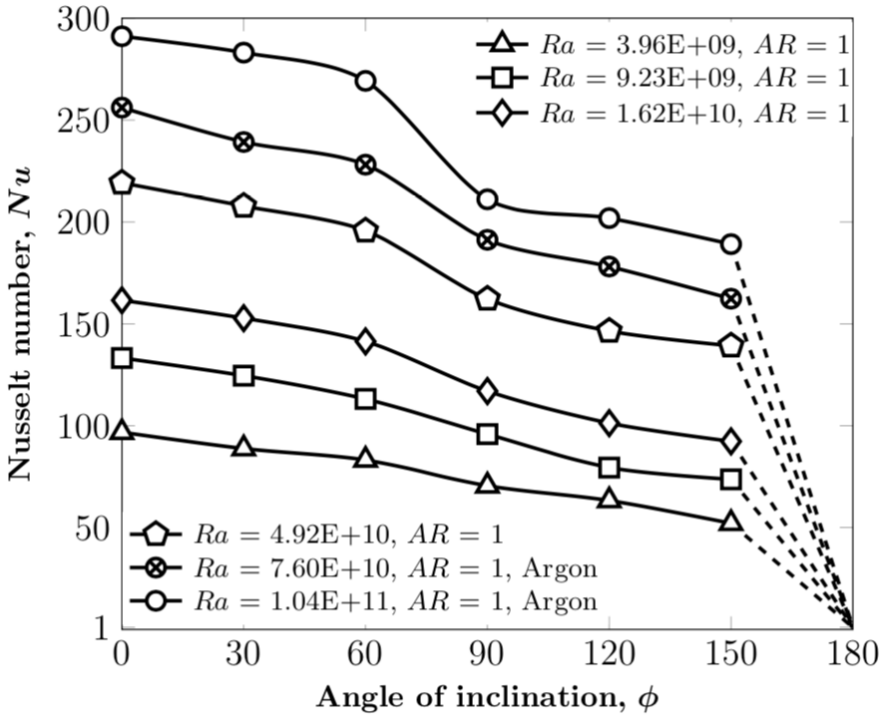

Fig. 6.1 Variation of average Nusselt number with angle of inclination ($AR = 1$)

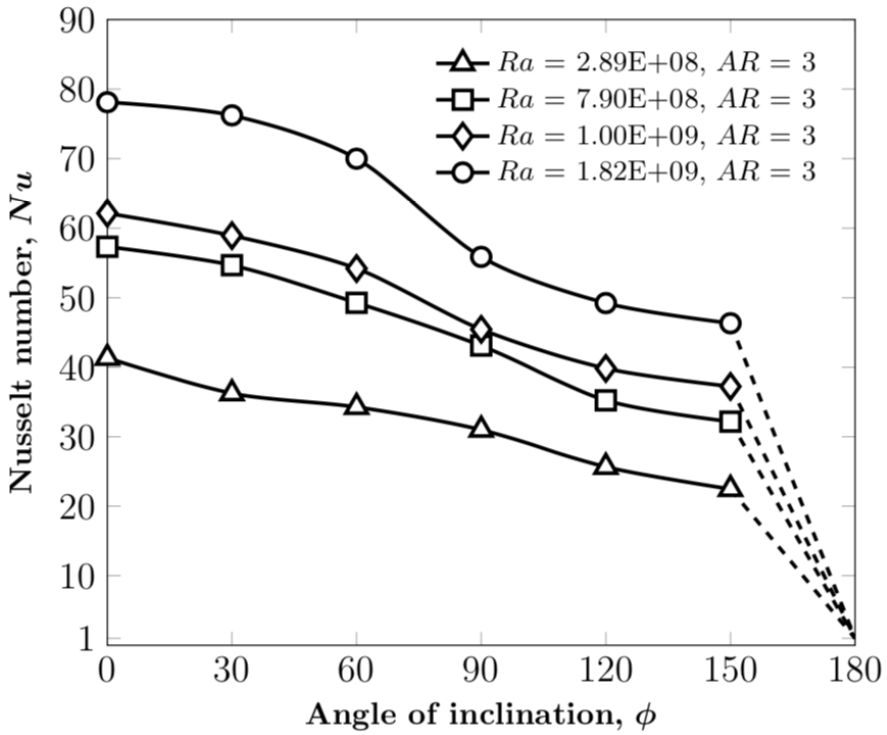

Fig. 6.2 Variation of average Nusselt number with angle of inclination ($AR = 3$)

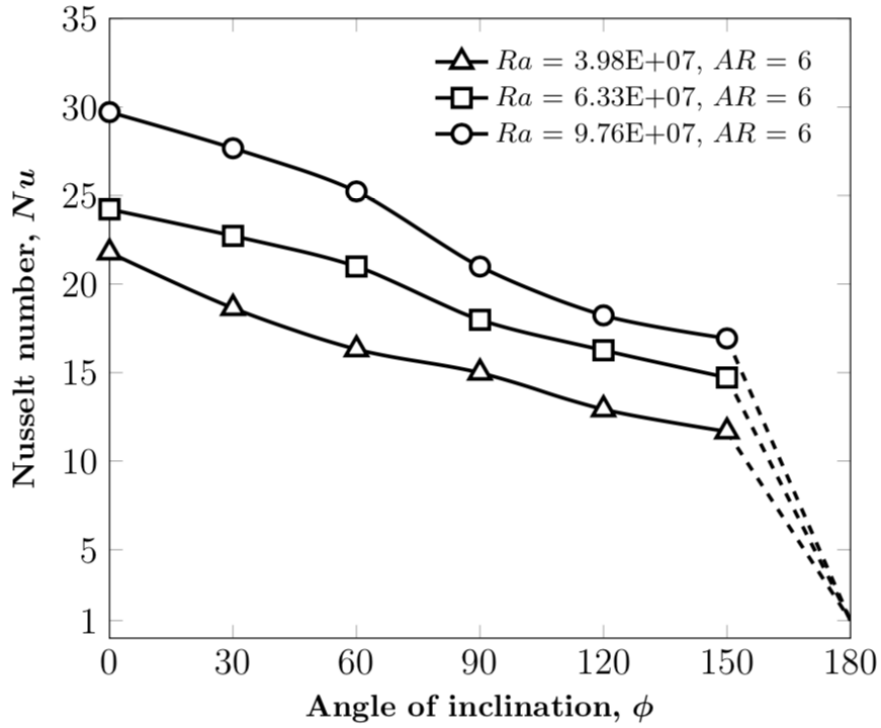

Fig. 6.3 Variation of average Nusselt number with angle of inclination ($AR = 6$)

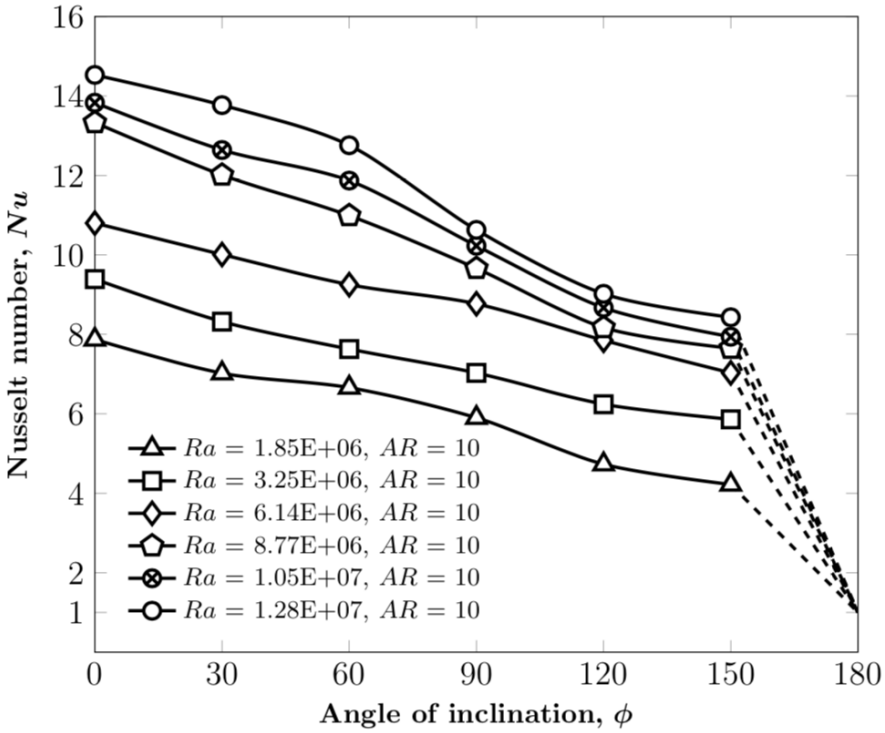

Fig. 6.4 Variation of average Nusselt number with angle of inclination ($AR = 10$)

6.3 Effect of aspect ratio on Nusselt number

Figures 6.5 and 6.6 present results from the supplementary experiments, with varied aspect ratios at a fixed Rayleigh number ($Ra = 4.4 \times 10^7$).

Figure 6.5 depicts normalized Nu values plotted against aspect ratio for the four investigated angles of inclination. The normalized Nu values are obtained by dividing the Nu values with that for $AR = 10$ for the same angle of inclination. It can be directly inferred from Figure 6.5 that the variation in Nusselt number is a mere 1.5% for the horizontal enclosure (Rayleigh-Bénard) case, whereas this difference is as high as 31% for the vertical enclosure case. Goldstein et al. (1987) have communicated similar effects of aspect ratio on Sherwood number (Sh) based on their electrochemical mass transfer experiments, which yield a $\approx 1.5 - 2\%$ variation for $\phi = 0°$ and $\approx 26\%$ variation at $\phi = 90°$ for a fixed Ra = 4.8×10^{10}. Their results are depicted in Figure 6.7. A recent publication by Madanan and Goldstein (2019b) reports similar trends from their heat transfer measurements.

Figure 6.6 portrays the variation of absolute Nu values against aspect ratio for different angles of inclination. For any angle of inclination, the Nu values are found to decrease with an increase in the aspect ratio. This may be attributed to the dampening of turbulence due to confinement (when the aspect ratio increases, the spacing between the hot and cold plates decreases), which, in turn, produces lower heat transfer rates and, thus, lower average Nusselt numbers. The decreasing trend of Nusselt number with aspect ratio gradually amplifies as the angle of inclination is increased, with negligible effect in the case of a horizontal enclosure ($\phi = 0°$) and a prominent effect in the case of a vertical enclosure ($\phi = 90°$).

The variation of Nusselt number with the angle of inclination for a fixed aspect ratio can be interpreted from Figure 6.8. The drop in the Nu values with an increase in the angle of inclination is found to be steeper as the aspect ratio increases. The Nu values obtained for all the studied aspect ratios are found to converge to a single value for an angle of inclination of $0°$, which clearly indicates the negligible effect of aspect ratio on Nusselt number in this case. Similar observations have also been communicated by Xu

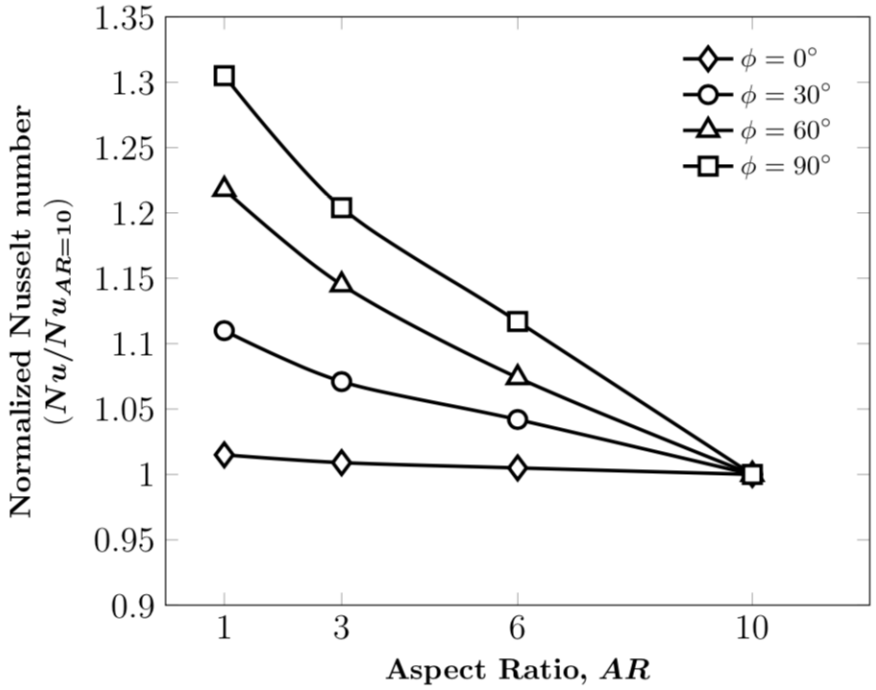

Fig. 6.5 Effect of aspect ratio on normalized Nusselt number for a fixed Rayleigh number ($Ra = 4.4 \times 10^7$)

et al. (2000), Funfschilling et al. (2005), Zhou et al. (2012), and Madanan and Goldstein (2019a) for a similar range of Rayleigh numbers.

The Nu values for the studied aspect ratios are observed to diverge as the angle of inclination is increased, attaining its maximum variation at an angle of inclination of $90°$. The maximum variation of Nu values for $\phi = 90°$ (among the four studied aspect ratios) can be attributed to vertical density stratification, as observed by Eckert and Carlson (1961). This density stratification makes the vertical dimension a significant parameter and, hence, aspect ratio (which is defined as the ratio of this vertical dimension and the spacing between the hot and cold plates) is expected to play an important role in the total heat transfer predictions. Thus, any angle of inclination between $0°$ and $90°$ is expected to have some density stratification due to its vertical component. This makes the Nu values vary with aspect ratio, with the effect of aspect ratio on Nusselt number amplifying gradually as ϕ is increased from $0°$ to $90°$.

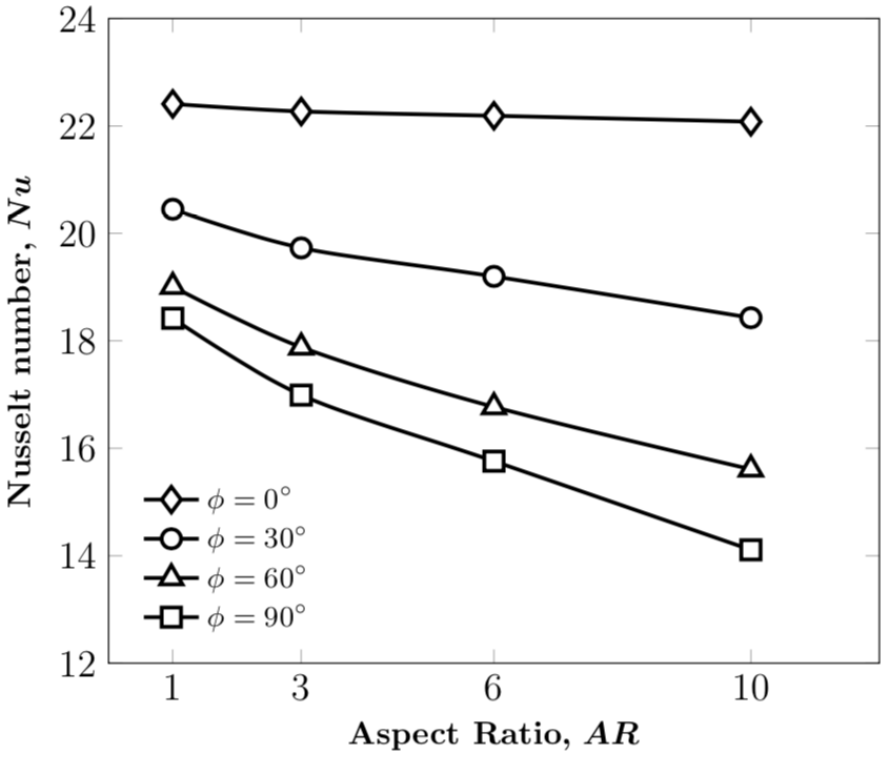

Fig. 6.6 Effect of aspect ratio on absolute Nusselt number for a fixed Rayleigh number ($Ra = 4.4 \times 10^7$)

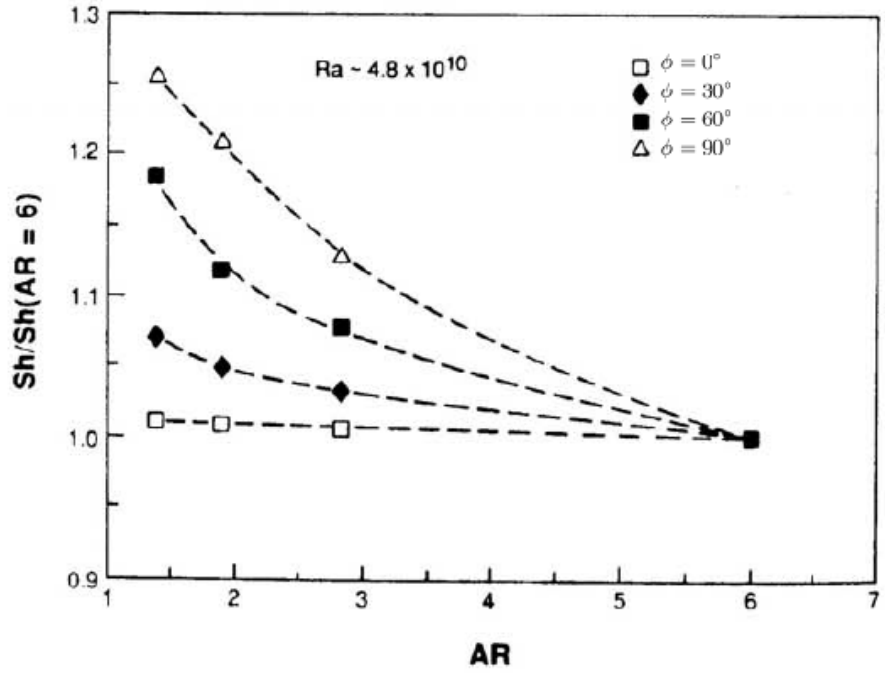

Fig. 6.7 Effect of aspect ratio on normalized Sherwood number for a fixed Rayleigh number (Goldstein et al., 1987)

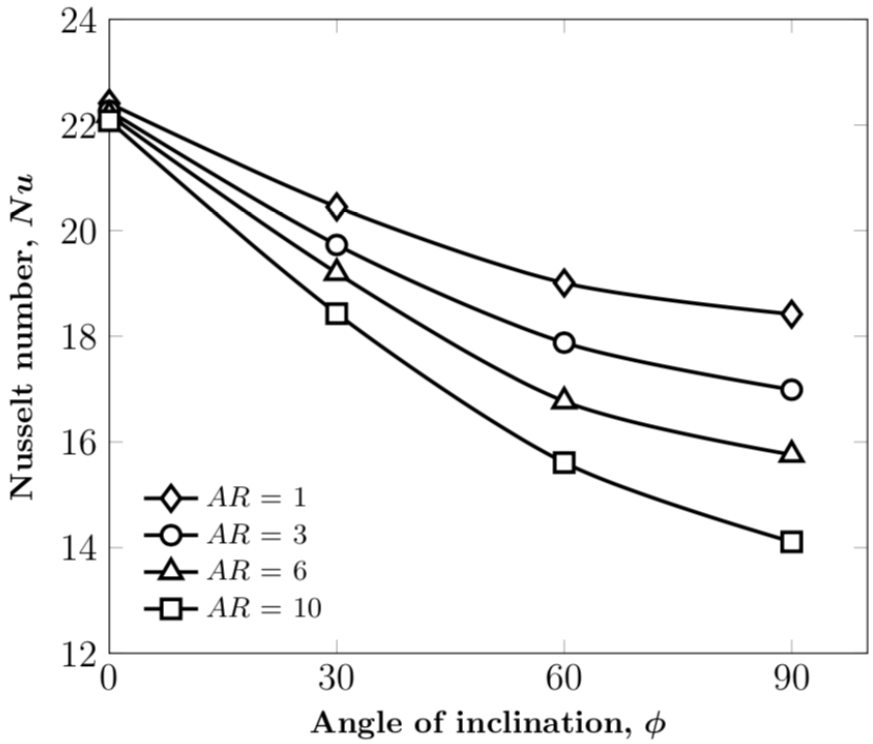

Fig. 6.8 Nusselt number vs. angle of inclination for a fixed Rayleigh number ($Ra = 4.4 \times 10^7$)

6.4 Nusselt number correlations

Figure 6.9 illustrates the $Nu - Ra$ relations for all the investigated angles of inclination on a decadic log-log plot. It is evident from the figure that the Nu values are higher for the $\phi = 0^\circ$ case and decrease as the angle of inclination is increased.

The Nusselt number correlations for each of the studied angles of inclination are developed using single-parameter ($Nu = CRa^n$) and two-parameter ($Nu = CRa^n AR^m$) regressions, as presented in Table 6.2. In the single-parameter regression, the Nu values are plotted against Rayleigh number on a decadic log-log plot (not taking into account the individual effect of aspect ratio), which yields a nearly straight line with a slope and an intercept. The pre-factor (C) and the exponent (n) in the single-parameter correlation are computed from the intercept $(= 10^{\text{intercept}})$ and the slope $(= n)$, respectively. For developing the two-parameter correlation (applicable only for $0^\circ \leq \phi \leq 90^\circ$; since the isolated effect of aspect ratio on Nusselt number is only studied for this range of ϕ in the present study), the Nu values are first plotted against aspect ratio (for a fixed $Ra = 4.4 \times 10^7$) to find the exponent (m) of aspect ratio (following a similar procedure as outlined earlier). Then, $\left(\frac{Nu}{AR^m}\right)$ is plotted against the investigated Rayleigh numbers on a decadic log-log plot to estimate the pre-factor (C) and exponent (n) of Rayleigh number for the two-parameter correlation.

A quick look at the correlations proposed using a single-parameter regression gives an impression that although the pre-factors of Rayleigh number are different, the exponent of Rayleigh number in all these correlations are very close to $\frac{1}{3}$. This is the classical scaling relation for a fully-turbulent regime when the heat flux (or, the heat transfer coefficient) is assumed to be independent of the characteristic length of the problem (or, H in the present study). Therefore, forced $\frac{1}{3}^{rd}$ scaling relations ($Nu = CRa^{1/3}$) are presented for each of the studied angles of inclination to facilitate easy comparison between the present study and the literature.

But, in reality, at any given angle of inclination, Nusselt number for a titled enclosure free convection problem is a function of both Rayleigh number and aspect ratio. Considering the effect of aspect ratio on Nusselt number, using a two-parameter cor-

Table 6.2 Proposed Nusselt number correlations for various angles of inclination

Angle of inclination (ϕ)	Single-parameter correlation ($Nu = CRa^n$)	Two-parameter correlation ($Nu = CRa^n AR^m$)	Classical $1/3$ scaling ($Nu = CRa^{1/3}$)
$0°$	$0.067Ra^{0.330}$	$0.0691Ra^{0.329}AR^{-0.006}$	$0.0645Ra^{1/3}$
$30°$	$0.054Ra^{0.337}$	$0.0687Ra^{0.327}AR^{-0.0377}$	$0.0578Ra^{1/3}$
$60°$	$0.049Ra^{0.338}$	$0.0759Ra^{0.320}AR^{-0.0704}$	$0.0535Ra^{1/3}$
$90°$	$0.050Ra^{0.329}$	$0.0898Ra^{0.305}AR^{-0.0921}$	$0.0459Ra^{1/3}$
$120°$	$0.039Ra^{0.335}$	–	$0.040Ra^{1/3}$
$150°$	$0.035Ra^{0.336}$	–	$0.0366Ra^{1/3}$

Valid for $1.85 \times 10^6 \leq Ra \leq 1.04 \times 10^{11}$ and $AR = 1 - 10$

relation, it can be noted that the exponent of Rayleigh number in the Nusselt number correlation gradually decreases with the angle of inclination. The value of this exponent drops from $\approx \frac{1}{3}$ for $\phi = 0°$ to ≈ 0.3 for $\phi = 90°$. This reduction in the value of exponent (n) may be attributed to the presence of mixed (both laminar and turbulent) boundary layers at angles of inclination $\phi > 0°$, thus, making a deviation from the fully turbulent condition all over the active (hot/cold) plates.

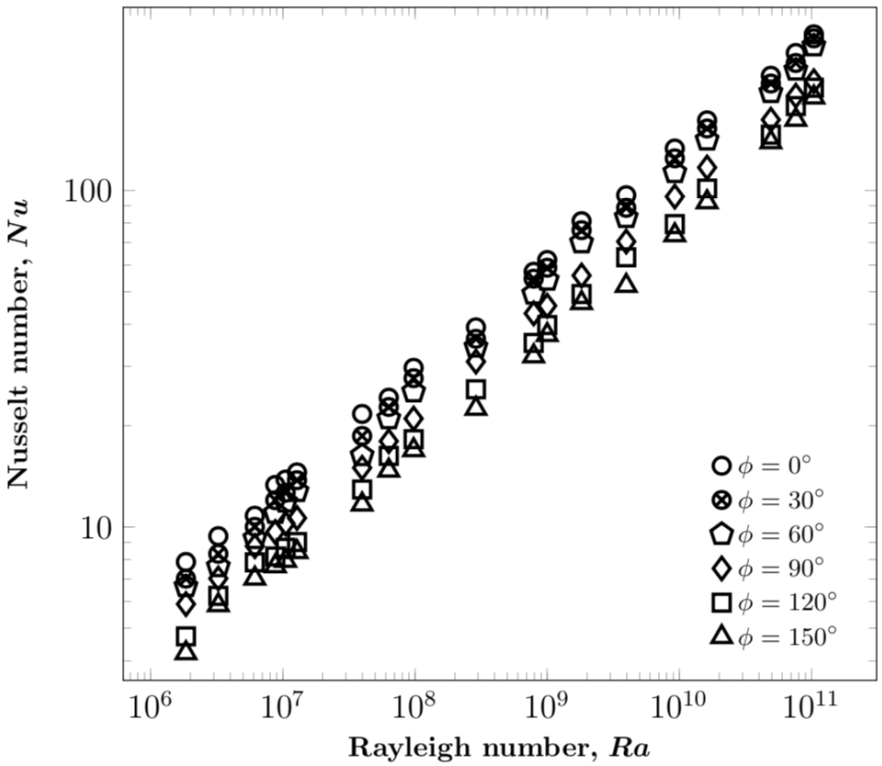

Fig. 6.9 Nusselt number versus Rayleigh number for various angles of inclination

Figures 6.10 - 6.15 depict the Nusselt number predictions obtained using both the single-parameter and the two-parameter (wherever applicable) correlations. In addi-

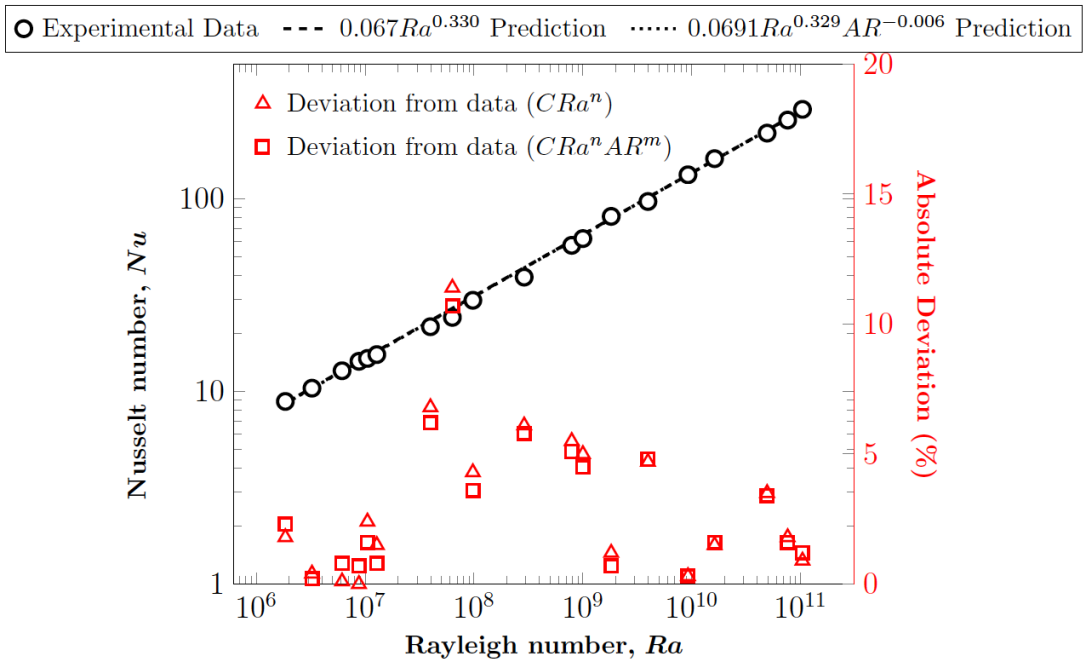

Fig. 6.10 Nusselt number versus Rayleigh number for $\phi = 0°$ on a log-log plot: data vs. predictions

tion, these figures also show the absolute deviation of the Nusselt number predictions from the single and two-parameter correlations with respect to the experimental data for each of the studied Rayleigh numbers and all the investigated angles of inclination on their secondary axis. Both the single-parameter and two-parameter correlations are found to yield reasonably accurate Nusselt number predictions when compared with the corresponding experimental values. In general, they are within 8% of the experimental values (a few exceptions show a slightly higher deviation, although, still within 11% of the experimental values).

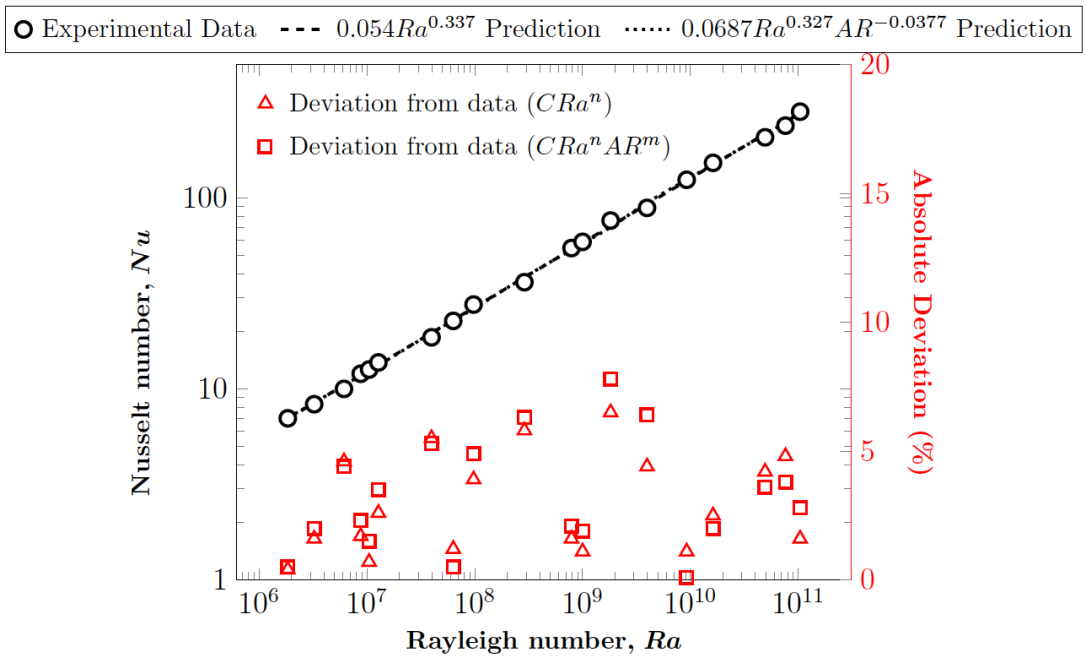

Fig. 6.11 Nusselt number versus Rayleigh number for $\phi = 30°$ on a log-log plot: data vs. predictions

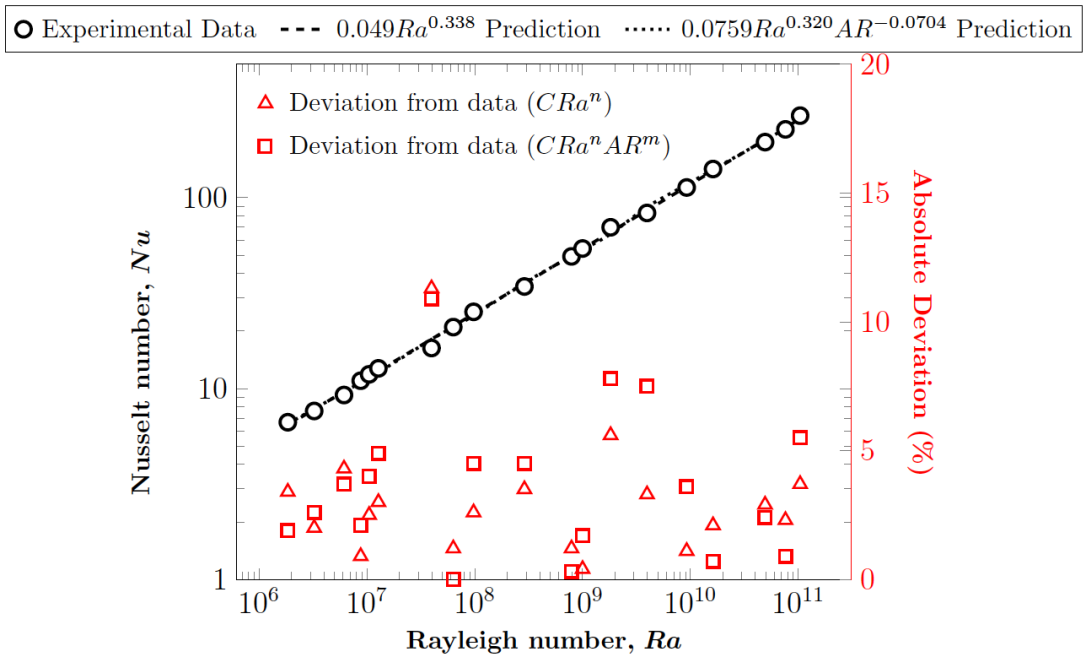

Fig. 6.12 Nusselt number versus Rayleigh number for $\phi = 60°$ on a log-log plot: data vs. predictions

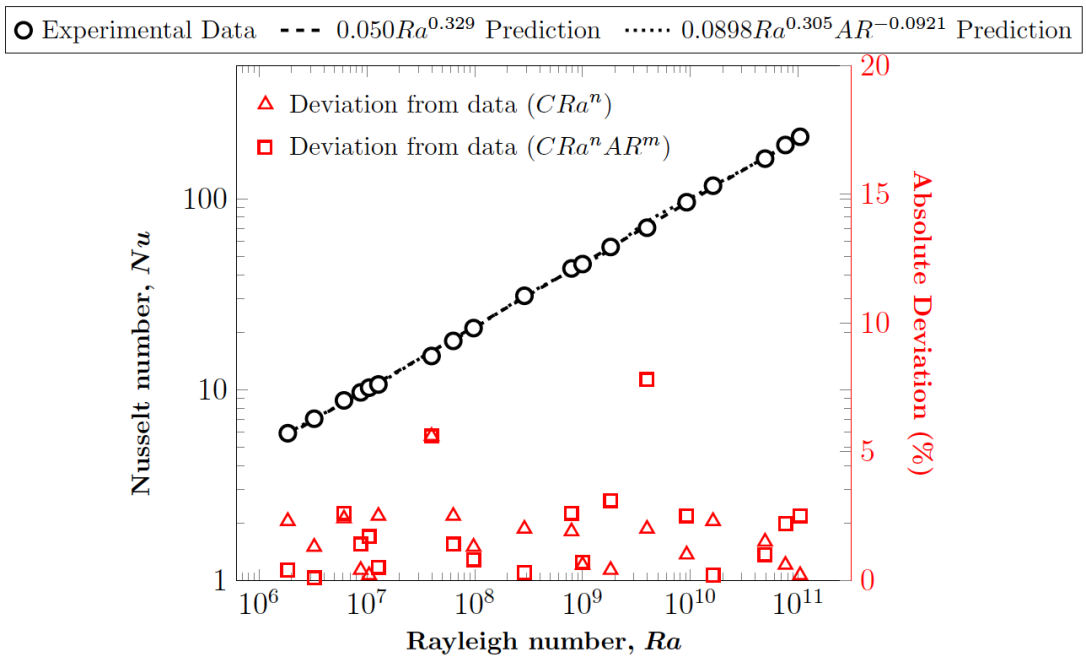

Fig. 6.13 Nusselt number versus Rayleigh number for $\phi = 90°$ on a log-log plot: data vs. predictions

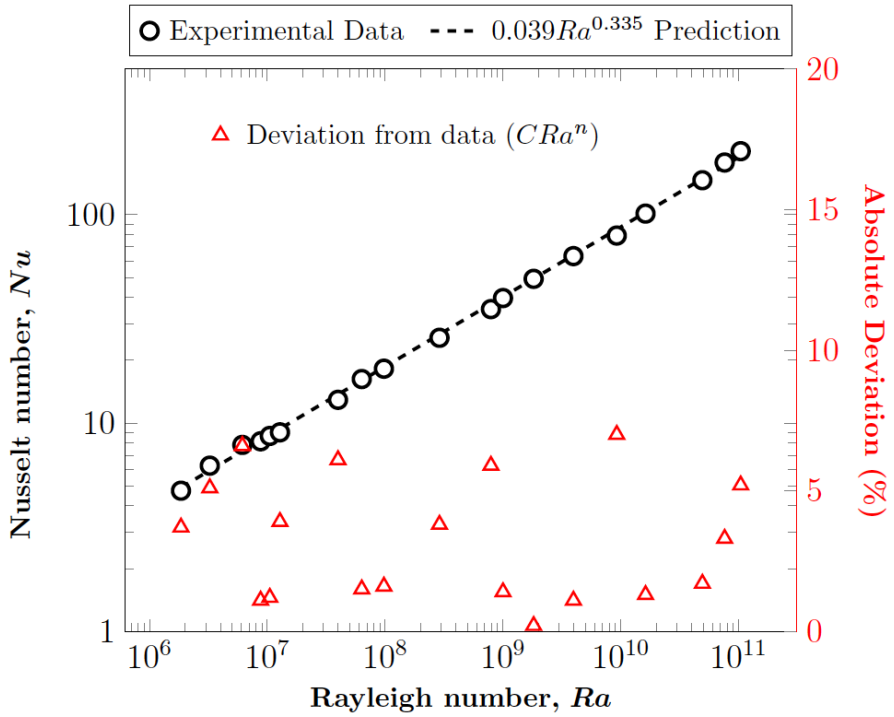

Fig. 6.14 Nusselt number versus Rayleigh number for $\phi = 120°$ on a log-log plot: data vs. predictions

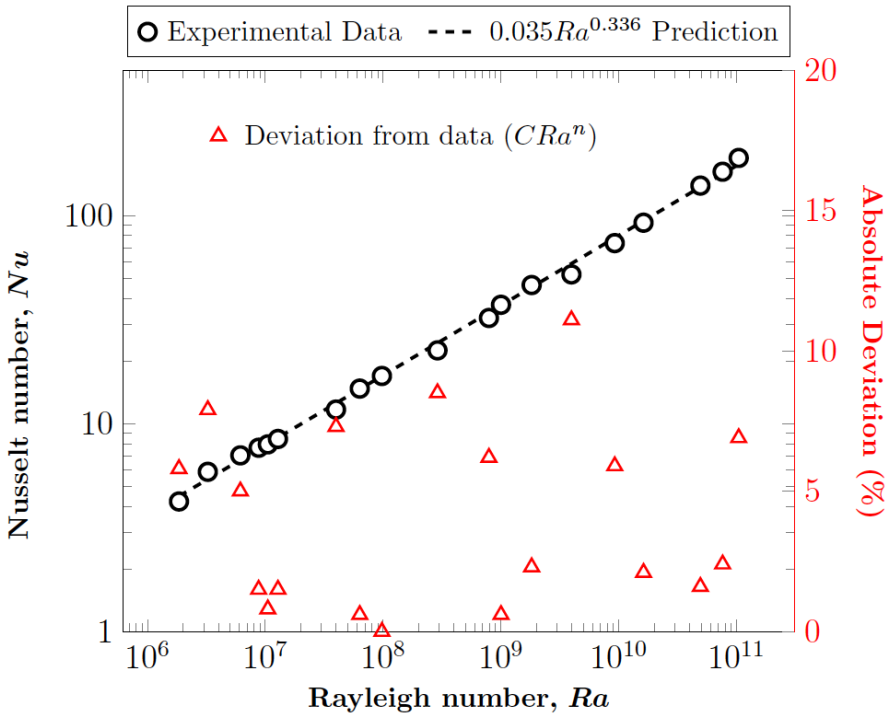

Fig. 6.15 Nusselt number versus Rayleigh number for $\phi = 150^\circ$ on a log-log plot: data vs. predictions

6.5 Comparison with the literature

The experimental data points for each of the investigated angles of inclination are compared with the literature, wherever available, as depicted in Figures 6.16 - 6.21.

Taking into account the fact that the uncertainties associated with the experimental Nu values themselves can be as high as $\pm 8.1\%$, the estimated Nu values for $\phi = 0^\circ$ match reasonably well with the literature (Fleischer and Goldstein, 2002; Niemela and Sreenivasan, 2006; Chong and Xia, 2016). This is especially true for Niemela and Sreenivasan (2006), whose results are found to agree very well with the present study, with a maximum observed absolute deviation of 6.3%.

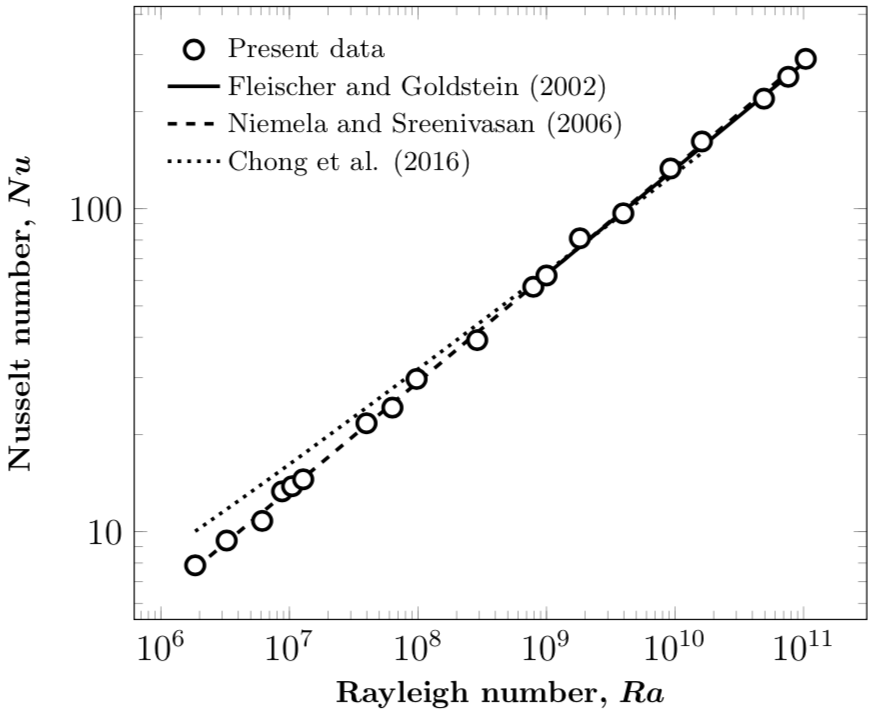

Fig. 6.16 Nusselt number versus Rayleigh number for $\phi = 0^\circ$ on a log-log plot: comparison with the literature

For angles of inclination of 30° and 60°, the experimental data are compared with the predictions of Dropkin and Somerscales (1965) and Goldstein et al. (1987), which are the only two references available for very high Rayleigh numbers at these angles of inclination. It is to be noted that the data for the lower range of Rayleigh numbers are compared with Dropkin and Somerscales (1965) and those for the upper range of Rayleigh numbers are compared with Goldstein et al. (1987), with an overlapping re-

gion in the range $2 \times 10^8 \leq Ra \leq 7.17 \times 10^8$. At $\phi = 30°$, they both under-predict the Nu values when compared with the present experimental data, with an observed maximum deviation of 15% with either of them. At an angle of inclination of $60°$, the data of Goldstein et al. (1987) are found to agree to within 9.5% of the present experimental data, whereas the results of Dropkin and Somerscales (1965) are found to over-predict the Nu values compared to the present study. This discrepancy between Dropkin and Somerscales (1965) and the present study can be explained by analyzing the correlations proposed for both, which reveals a steeper drop in the Nu values with an increase in the angle of inclination for the present study.

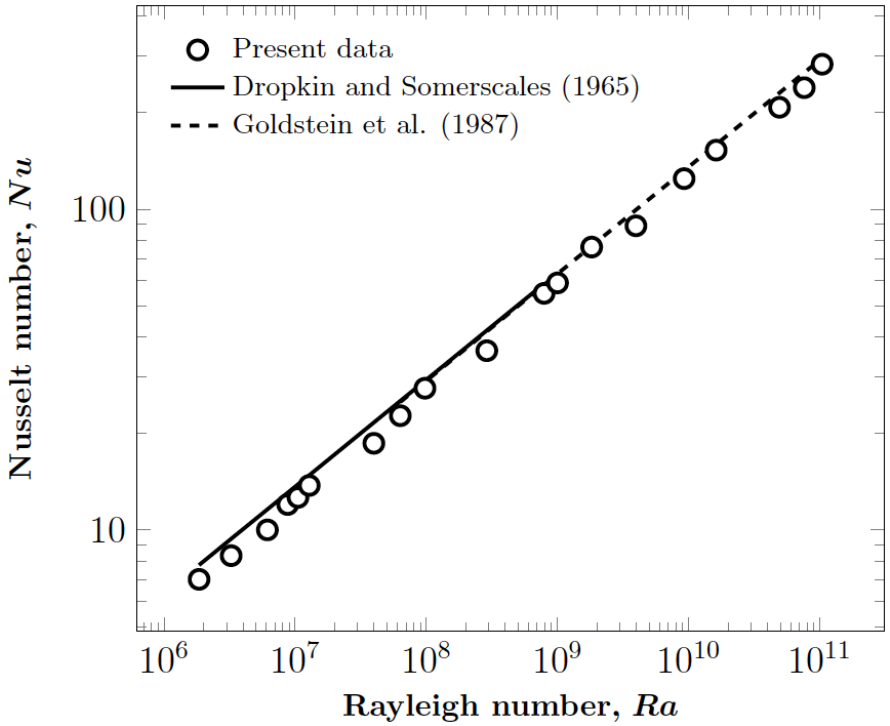

Fig. 6.17 Nusselt number versus Rayleigh number for $\phi = 30°$ on a log-log plot: comparison with the literature

In the present study, the Nu values are also plotted against $Ra\cos\phi$ (as shown in Figure 6.22) to examine the predictive capability of a $Nu - Ra\cos\phi$ scaling relation. As can be seen from this figure, the data points are observed to collapse and follow a similar relation for $0° \leq \phi \leq 60°$ when an $Ra\cos\phi$ scaling relation is enforced, whereas they are scattered when directly plotted against Rayleigh number for the same range of angles of inclination (as can be seen from Figure 6.9). Hence, a $Ra\cos\phi$

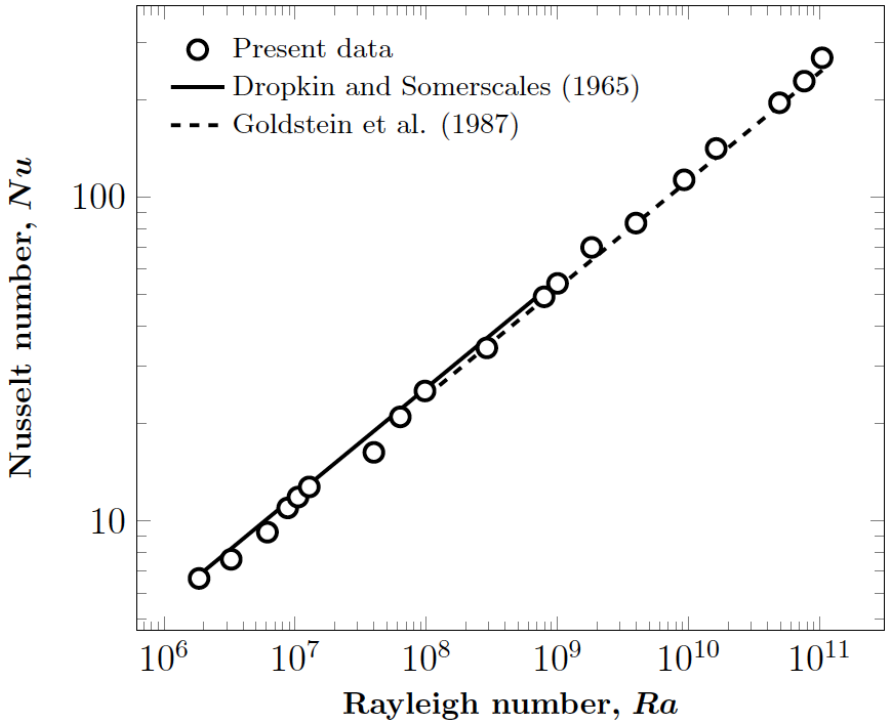

Fig. 6.18 Nusselt number versus Rayleigh number for $\phi = 60^\circ$ on a log-log plot: comparison with the literature

scaling relation is proposed by applying a simple regression, which is of the form:

$$Nu = 0.067\,(Ra\cos\phi)^{0.331} \tag{6.1}$$

The Nu values predicted using this $Ra\cos\phi$ scaling relation agree to within 11% of the experimental data. A similar observation has been reported by Goldstein et al. (1987), who have proposed a $Nu - Ra\cos\phi$ (or $g\cos\phi$) scaling relation based on their observations that the correlation with a $Ra\cos\phi$ scaling also work reasonably well in predicting their experimental Nu values.

For the vertical enclosure case (or, $\phi = 90^\circ$), the present data are compared with Elsherbiny et al. (1982b), Kuyper et al. (1993), and Bairi et al. (2007) and the Nusselt number predictions from this literature are found to over-predict when compared to the present data.

The experimental data for the angle of inclination of 90° is extrapolated to estimate those for $\phi = 120^\circ$ based on the $\sin^{1/4}\phi$ scaling relation proposed by Ayyaswamy and Catton (1973). These results are then compared with the experimental Nu values

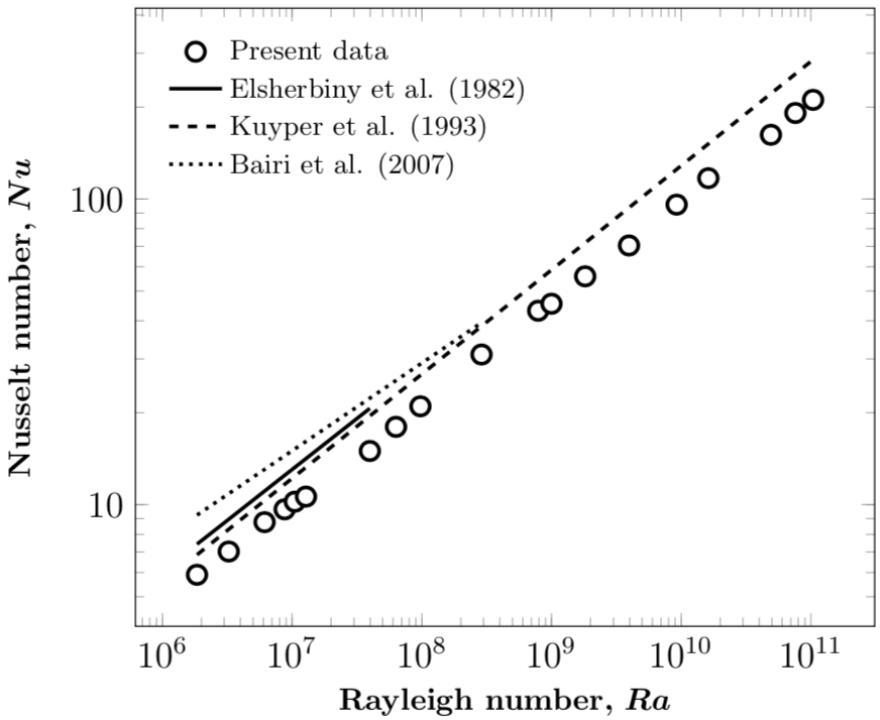

Fig. 6.19 Nusselt number versus Rayleigh number for $\phi = 90^\circ$ on a log-log plot: comparison with the literature

corresponding to $\phi = 120^\circ$ and found to differ by 12%.

The present experimental, or numerical, literature for the angles of inclination of 120° and 150° for very high Rayleigh numbers ($Ra > 10^7$) is too scarce to make any other useful comparisons and inferences.

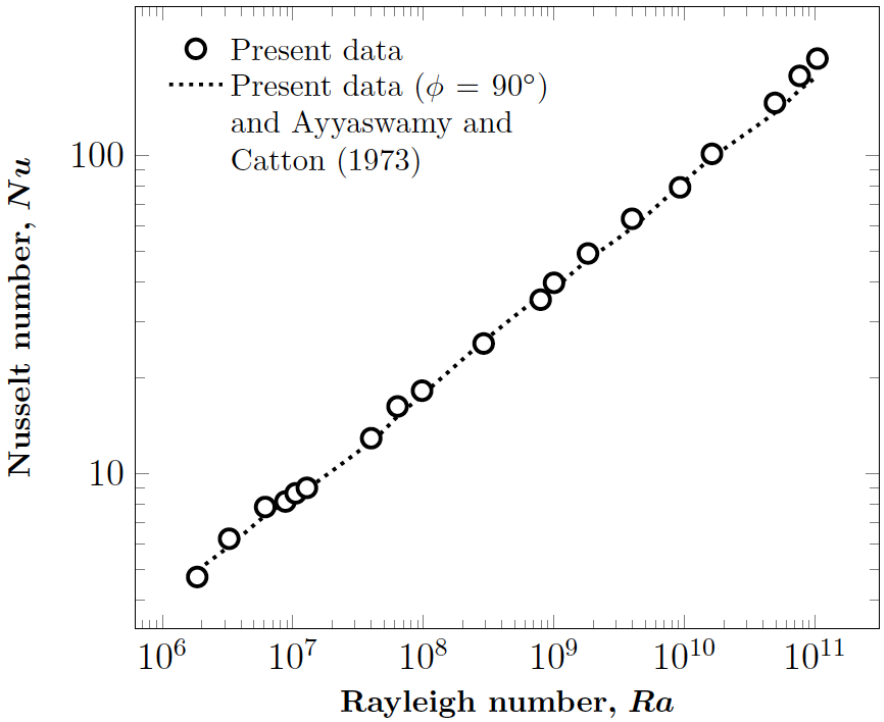

Fig. 6.20 Nusselt number versus Rayleigh number for $\phi = 120°$ on a log-log plot: comparison with the literature

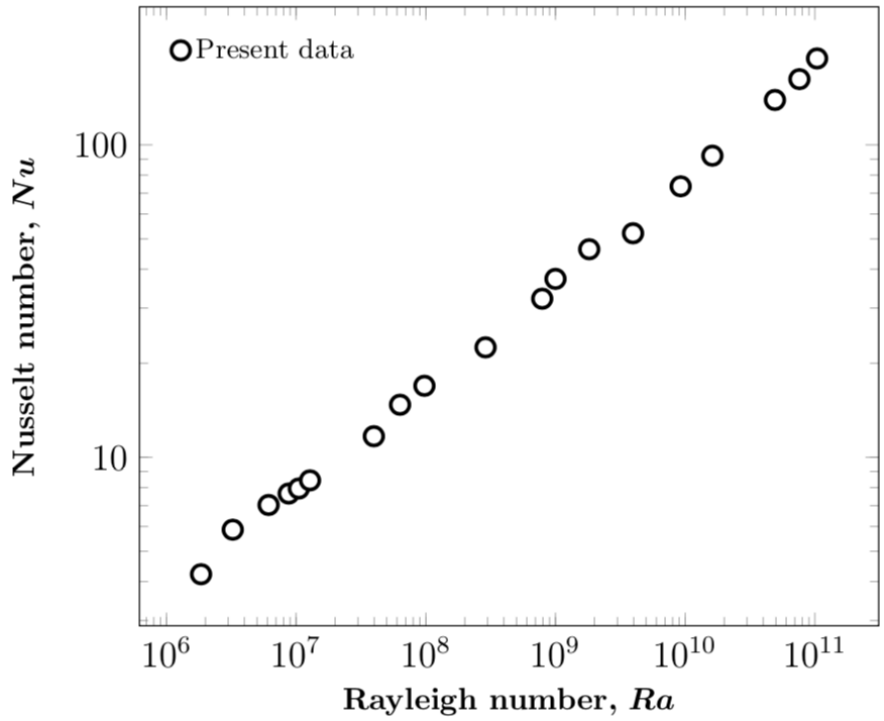

Fig. 6.21 Nusselt number versus Rayleigh number for $\phi = 150°$ on a log-log plot

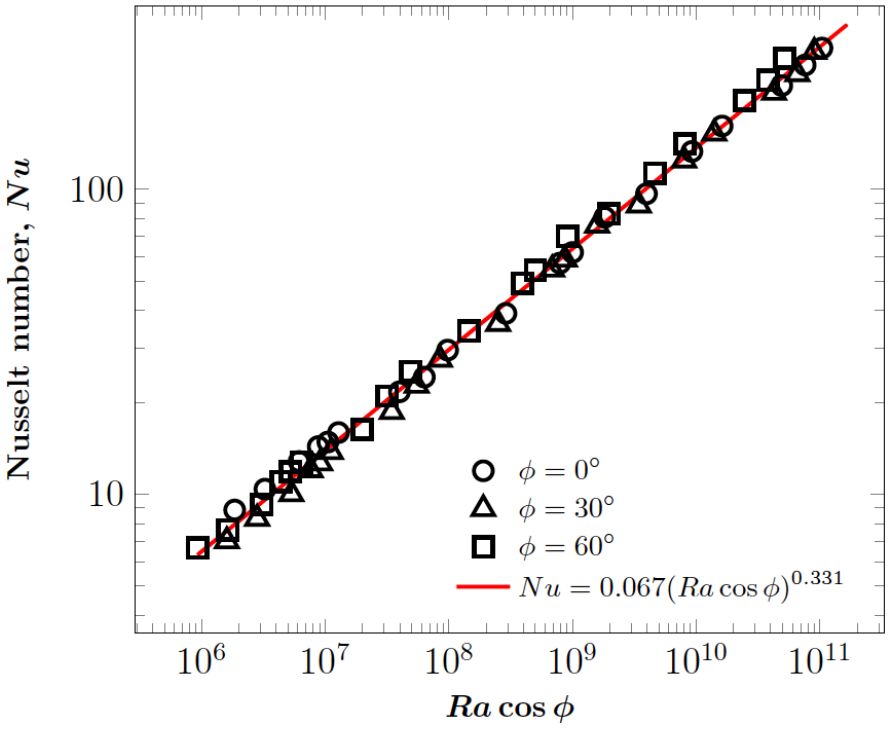

Fig. 6.22 $Nu - Ra\cos\phi$ scaling relation on a decadic log-log plot

CHAPTER 7
Flow Visualization

7.1 Method and limitations

Z-type shadowgraph technique, as shown in Figure 3.11 (see Chapter 3), is employed for visualization of buoyant flow. An LED light source that approximates a point source is placed one focal length away from the first parabolic mirror. The diverging light (or, the LED light source) becomes a beam of parallel light after reflecting from this mirror. This parallel beam of light then passes through the first optical port to the test cell (where it gets refracted by the density gradient in nitrogen) and then through the other optical port to reach the second parabolic mirror. This second mirror reflects the parallel beam of light, which then converges at a point one focal length away from the mirror. A camera is placed at this point to capture the fluid motion. Further details about this technique can be found in Settles (2012) and Goldstein (2017).

Visualization studies are performed for the experimental conditions and angles of inclination listed in Table 7.1. The visualization experiments are limited to four of the more significant angles of inclination ($\phi = 0°$, $30°$, $60°$, $90°$) among the investigated cases. These experiments are limited to an aspect ratio of 3, a value chosen based on the following two criteria: (i) a lower aspect ratio will make visualizing of both the hot-end and the cold-end impossible due to the restrictions imposed by the optical port dimension and (ii) a higher aspect ratio will result in substantially lower Rayleigh numbers, which does not fall under the scope of the present study.

Unfortunately, in the present study, this visualization technique produces blurred

images. This blurriness is thought to be due to the lower optical quality of the Pyrex glass window used for the optical ports rather than due to the weak density gradients near the active walls. Due to the dynamic nature of the flow, which stands out even when the background is hazy, the videos are found to be more useful in gaining insight about flow patterns. The videos are processed and analyzed to sharpen the quality and to interpret the flow field. Processing is performed using an open source image processing program, ImageJ®.

The steps involved in processing the videos are:

- The frames (≈ 200 per experimental condition) are extracted from the video file (*.mov*) using MATLAB® (see Appendix E)
- These frames, after their conversion to RGB format are imported to ImageJ® as an image sequence. The following steps are completed using the ImageJ® software:
    1. Frames are cropped to include only the field of interest
    2. The color channels are split to red (R), green (G), and blue (B) for each of the frames. Only the green component of the images is found to provide any intensity and, thus, the other color channels are discarded before further processing
    3. The average intensity of the frames is estimated using the "Z - projection" function, which is then subtracted from each of the frames using the "Image Calculator" function
    4. The resulting frames are then adjusted for optimum sharpness and contrast before finally exporting the file (as *.avi* or *.png*).

Table 7.1 Experimental conditions for the visualization studies ($AR = 3$, $\Delta T = 16K$, fluid $= N_2$)

Rayleigh number	$0°$	$30°$	$60°$	$90°$
3.13×10^6	✓	×	×	✓
1.27×10^7	✓	✓	✓	✓
2.87×10^7	✓	×	×	✓
5.13×10^7	✓	✓	✓	✓
1.17×10^8	✓	×	×	✓
2.09×10^8	✓	✓	✓	✓
3.28×10^8	✓	×	×	✓

7.2 Qualitative observations and inferences

For the horizontal enclosure case, flow visualization reveals a uniform eruption of thermal plumes from multiple random locations on the hot and cold surfaces, similar to the observations of Chu and Goldstein (1973), Fleischer and Goldstein (2002), and Wang et al. (2018). These thermal plumes are observed to be swept by a large scale flow. Though their motion is periodically interrupted by the sweeping large scale flow, the thermal plumes are still found to travel across the core region. The large scale flow is observed to pause or reverse in direction due to the release of the thermal plumes. This matches the reports of reversal and cessations in the literature (Sreenivasan et al., 2002; Brown and Ahlers, 2006; Xi and Xia, 2007; Wang et al., 2018). As the Rayleigh number increases, the frequency of the thermal plume emissions also increases, but the locations of these emission are still observed to be random. However, it must be noted that the flow visualization only captures all the thermal plumes on a single plane at which the imaging has happened. Thus, the observed uniform release of thermal plumes from an active surface may be a misinterpretation and there may be random locations on the plate surface where the thermal plume eruptions are more than the observed uniform counts. For example, at one instance, there may be more thermal plumes emitted from random locations at the right extreme of the hot plate, which can induce a counter-clockwise large scale flow. Eventually, the cooling fluid coming down on the left side would tend to enhance heat transfer there, giving rise to more thermals on that side, resulting in a clockwise flow. A similar argument could be made on cold plumes descending from the upper surface. Thus, the frequent reversal of the large scale

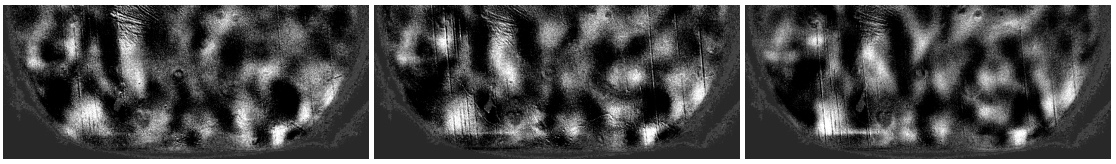

(a) Frame 1 **(b)** Frame 2 **(c)** Frame 3

(d) Frame 4 **(e)** Frame 5 **(f)** Frame 6

(g) Frame 7 **(h)** Frame 8 **(i)** Frame 9

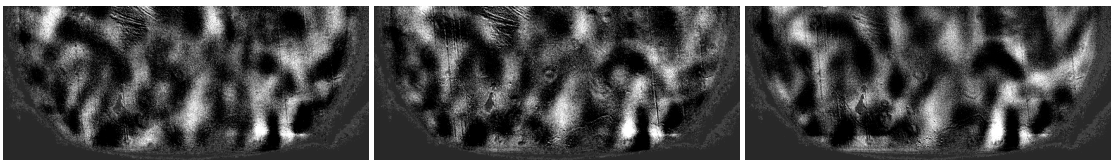

(j) Frame 10 **(k)** Frame 11 **(l)** Frame 12

Fig. 7.1 Thermal plume eruption from the hot surface shot at 10 frames per second: 12 continuous frames ($\phi = 0^\circ$ case, $Ra = 2.09 \times 10^8$)

flow may be interpreted as a consequence of a statistical fluctuation in the number of thermals on one side of the layer compared to the opposite side.

When the enclosure is inclined at an angle of 90° (the vertical enclosure), traveling wave-like structures are observed over the boundary layers that form on the active hot or cold vertical walls. Packets of fluid are discharged at frequent intervals along the boundary layers, which look similar to traveling waves superimposed on the boundary layers. Another observation is that these traveling wave-like structures, which according to Elder (1965b) are the characteristics of a turbulent flow, do not significantly disturb the core of the enclosure. Since this is so for the aspect ratio of 3 (having a small

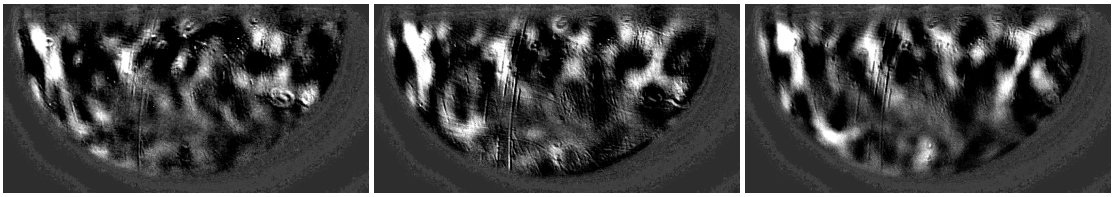

(a) Frame 1 **(b)** Frame 2 **(c)** Frame 3

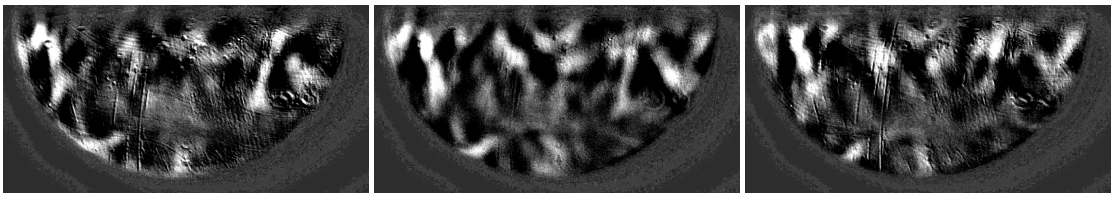

(d) Frame 4 **(e)** Frame 5 **(f)** Frame 6

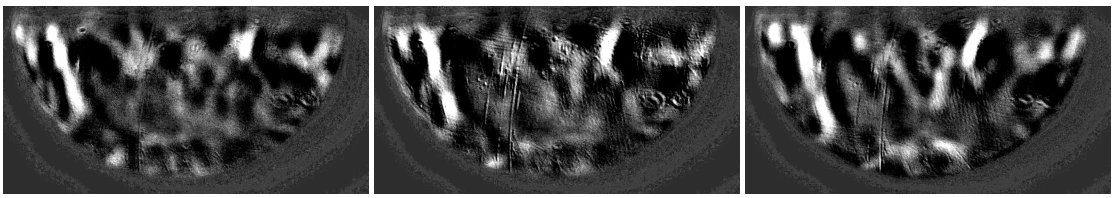

(g) Frame 7 **(h)** Frame 8 **(i)** Frame 9

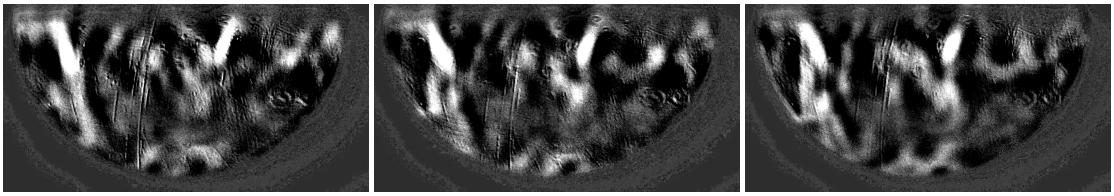

(j) Frame 10 **(k)** Frame 11 **(l)** Frame 12

Fig. 7.2 Thermal plume release from the cold surface shot at 10 frames per second: 12 continuous frames ($\phi = 0^\circ$ case, $Ra = 2.09 \times 10^8$)

spacing between the hot and cold plates), this may well be the reason for the undisturbed maximum vertical density (or, temperature) stratification reported by many investigators for the vertical enclosure case, even at moderate to very high Rayleigh numbers (Eckert and Carlson, 1961; Schinkel and Hoogendoorn, 1983; Kuyper et al., 1993; Yedder and Bilgen, 1995; Bairi et al., 2007; Williamson et al., 2016). This also explains why the effect of aspect ratio on Nusselt number is maximum for the vertical enclosure case.

When the enclosure is tilted at 30° or 60°, the observed characteristics are similar to those observed for a horizontal and vertical enclosure problem, respectively. However, unlike for the vertical enclosure problem, the inner core for the 60° enclosure problem is observed to experience a gentle perturbation due to the mixing of the turbulent flow and the ascending (or, descending) fluid parcels discharged by the boundary layers on the hot (or, cold) surfaces. But, for an angle of inclination of 30°, the flow pattern is nearly identical to the large scale flow observed in the horizontal enclosure problem. In this case, mixing in the core is observed to be more vigorous, probably resulting in a less stratified core, with its temperature being closer to the uniform mean temperature of T_m. This variation in the flow behavior is probably the reason behind the decreasing effect of aspect ratio on Nusselt number as the angle of inclination is decreased from 90° to 0°.

Another qualitative observation is the magnitude of buoyant velocity in the cases of different tilting angles. Interpreting a representative velocity is found to be challenging for the horizontal enclosure case because of frequent reversals and cessations. But, for the rest of the acute angle cases and for the vertical enclosure case, this interpretation is rather straight forward. The buoyant velocity is observed to decrease as the angle of inclination increases. This may be attributed to the decrease in buoyant force with inclination (or, in other words, due to the reduction in the apparent gravitational field with tilting). As the buoyancy-driven velocity of the fluid and the free convective heat transfer within the enclosure are directly related, this also explains why there is a reduction in heat transfer when the angle of inclination is increased.

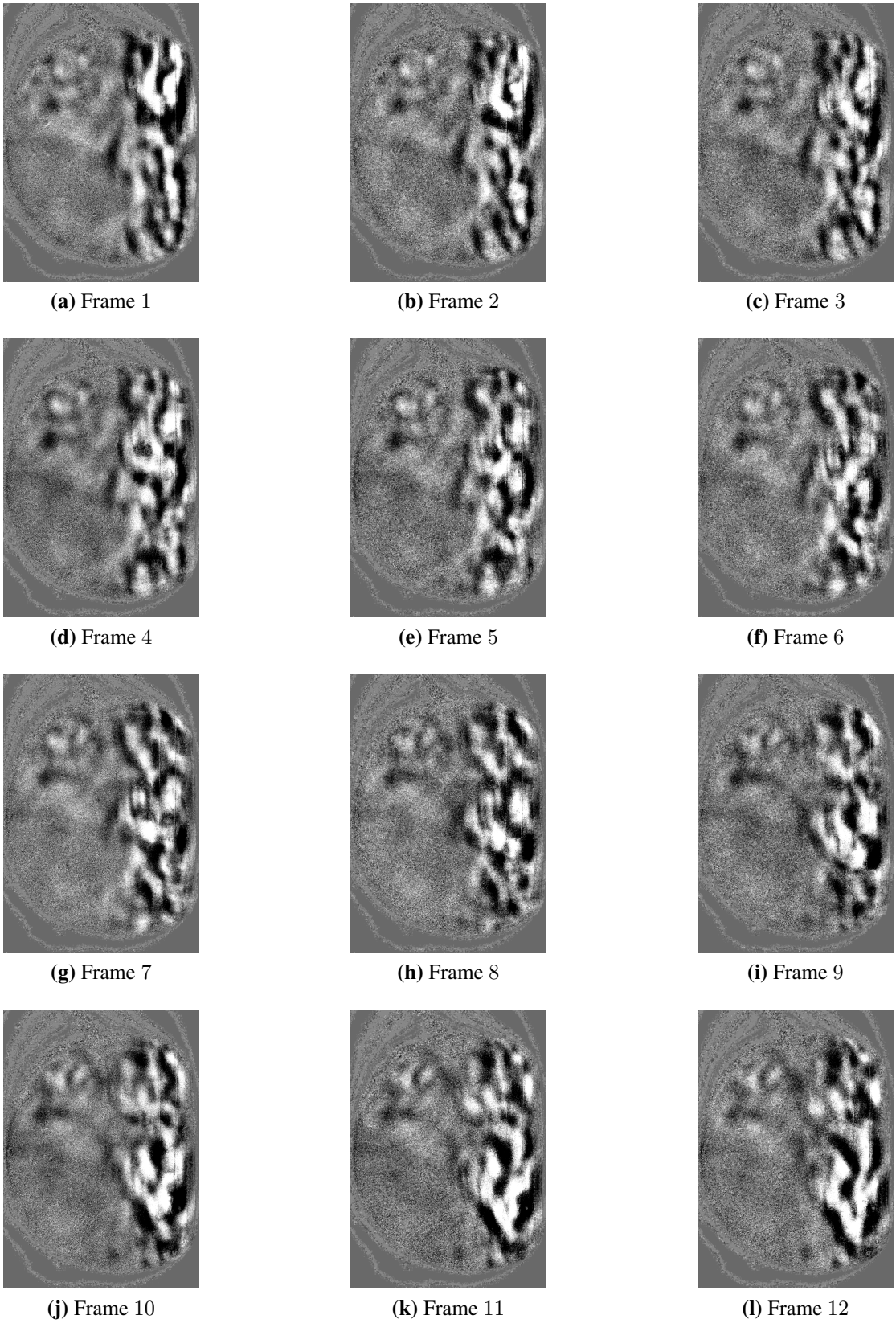

(a) Frame 1 **(b)** Frame 2 **(c)** Frame 3

(d) Frame 4 **(e)** Frame 5 **(f)** Frame 6

(g) Frame 7 **(h)** Frame 8 **(i)** Frame 9

(j) Frame 10 **(k)** Frame 11 **(l)** Frame 12

Fig. 7.3 Traveling wave-like structures superimposed on the boundary layer on cold vertical wall shot at 10 frames per second: 12 continuous frames ($\phi = 90^\circ$ case, $Ra = 2.09 \times 10^8$)

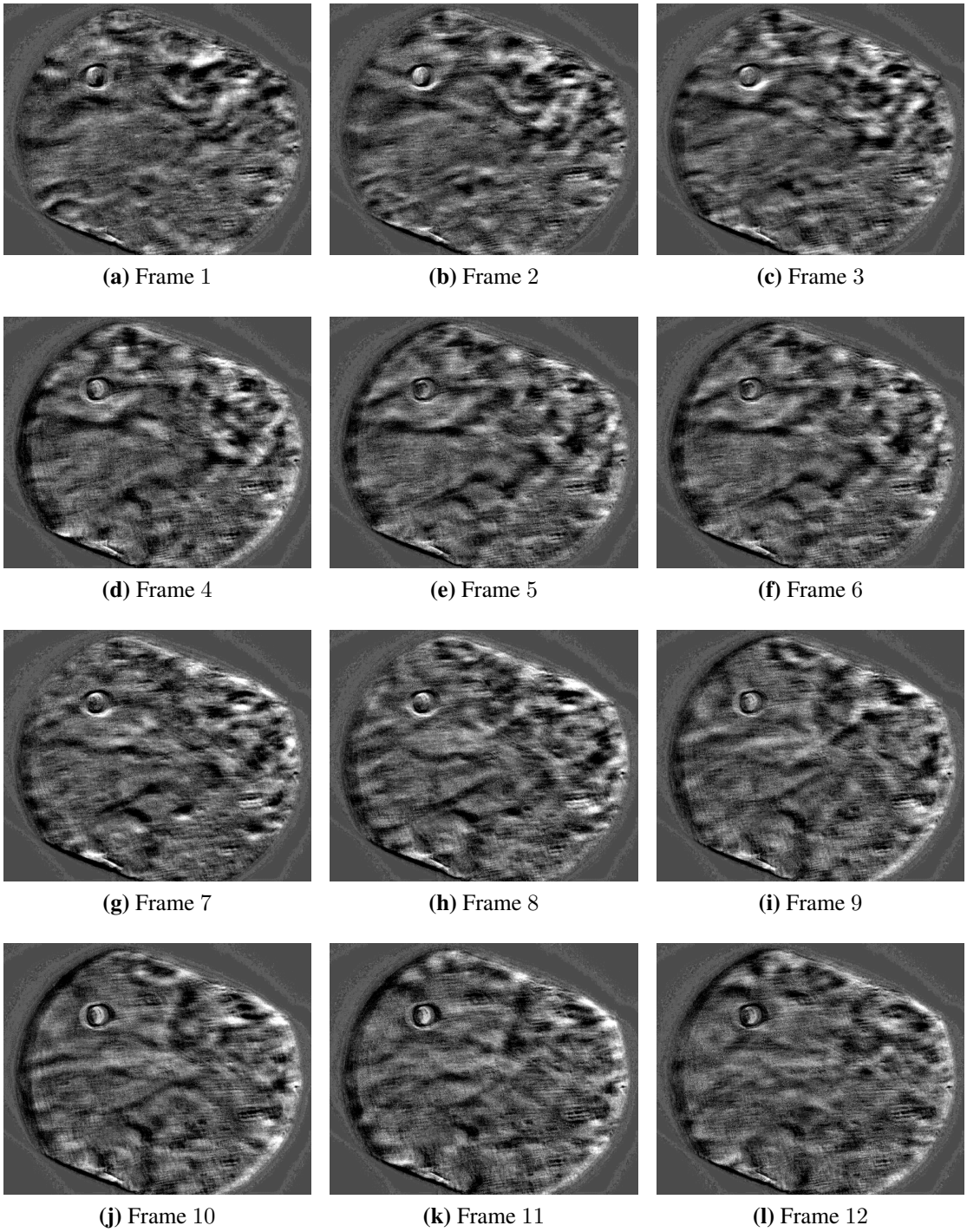

(a) Frame 1 **(b)** Frame 2 **(c)** Frame 3

(d) Frame 4 **(e)** Frame 5 **(f)** Frame 6

(g) Frame 7 **(h)** Frame 8 **(i)** Frame 9

(j) Frame 10 **(k)** Frame 11 **(l)** Frame 12

Fig. 7.4 Buoyant flow nearly identical to the large scale flow observed for 30° case shot at 10 frames per second: 12 continuous frames ($Ra = 2.09 \times 10^{8}$)

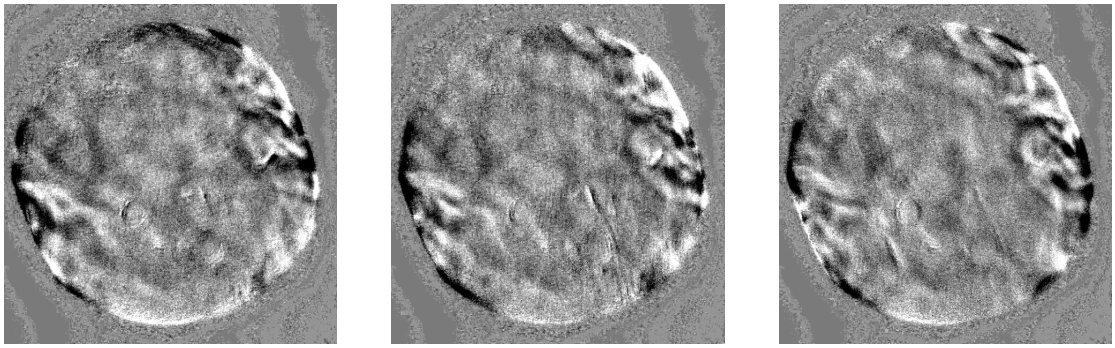

(a) Frame 1 **(b)** Frame 2 **(c)** Frame 3

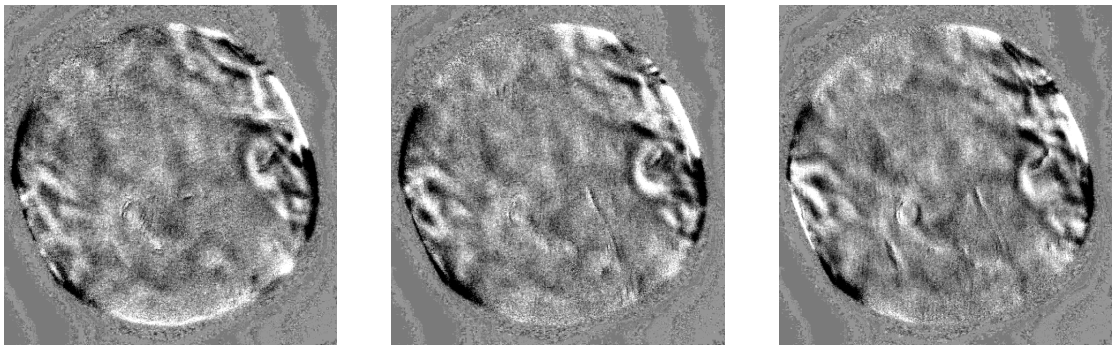

(d) Frame 4 **(e)** Frame 5 **(f)** Frame 6

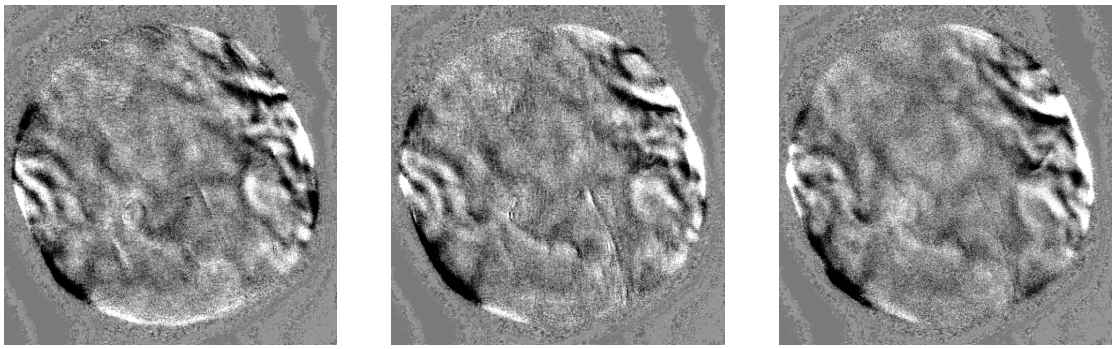

(g) Frame 7 **(h)** Frame 8 **(i)** Frame 9

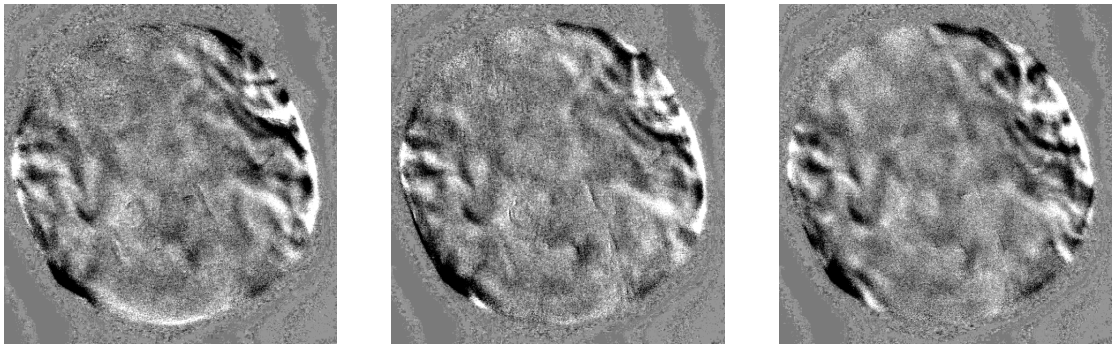

(j) Frame 10 **(k)** Frame 11 **(l)** Frame 12

Fig. 7.5 Visualized flow patterns for a 60° case shot at 10 frames per second: 12 continuous frames ($Ra = 2.09 \times 10^8$)

CHAPTER 8
Conclusion

High-Rayleigh-number free convection in inclined rectangular enclosures (with two differentially heated opposite walls) of different aspect ratios ($AR = 1$, 3, 6, and 10) is experimentally studied for various angles of inclination ($\phi = 0°$, 30°, 60°, 90°, 120°, and 150°) and a wide range of Rayleigh numbers (1.85×10^6 to 1.04×10^{11}). High Rayleigh numbers are achieved using compressed nitrogen and argon at pressures ranging from 3 to 90 bar and experimental Nusselt numbers (Nu) are computed from the steady state electrical power input and temperature measurements.

Chapter 4 reports the effect of sidewall conductance heat loss on the measured Nusselt number for the Rayleigh-Bénard (horizontal enclosure) convection by performing nearly identical sets of experiments with sidewalls of three different thermal conductivities (i.e., Styrofoam, Plexiglas, and high-density polyethylene) over three decades of Rayleigh numbers ($10^6 \leq Ra \leq 10^9$). The experimentally estimated Nu values, corrected for all the heat losses except for the sidewall conductance loss, from the three sets of experiments are utilized for extrapolating and estimating the Nu values for an ideal case with zero-thermal-conductivity sidewalls. This Nusselt number is found to follow the relation:

$$Nu_c \approx 0.0881 Ra^{0.315} \qquad \text{for } 2.68 \times 10^6 \leq Ra \leq 1.16 \times 10^9 \tag{8.1}$$

The experimentally measured difference (ΔNu) between the sidewall-uncorrected Nusselt number (Nu_{net}) and the sidewall-corrected Nusselt number (Nu_c) is found to be higher than that estimated using a traditional empty-cell gradient assumption,

with the experiments, often, yielding values up to 6 times the corresponding empty-cell gradient estimates. This discrepancy in the ΔNu values may be identified as the cause of the substantial variation in the exponent of Ra in the $Nu - Ra$ correlations observed in the literature for moderate to high Rayleigh numbers.

A semi-analytical model for $Wn \geq \mathcal{O}(1)$ (refer to Equation 8.2) and an empirical model for $Wn \rightarrow 0$ (refer to Equation 8.3) are proposed for estimating the sidewall-corrected Nusselt numbers for the investigated range of Rayleigh numbers ($10^6 \leq Ra \leq 10^9$). The ΔNu predictions obtained using the two models are found to agree reasonably well with the corresponding experimental data from the present study and results from the literature, with a maximum observed deviation of $\approx 11\%$ for the semi-analytical model and $\approx 1.5\%$ for the empirical model.

$$Nu_c = \frac{Nu_{net}}{\left[1 + \sqrt{\frac{Wn}{Nu_c AR}} \tanh c\right]} \qquad \text{with } c = 0.925 \tag{8.2}$$

$$Nu_c = \frac{Nu_{net}}{[1 + Wn^2]} \tag{8.3}$$

Taking into consideration the effect of the sidewall conductance heat loss, a simple $Nu - Ra$ scaling relation is proposed for the Rayleigh-Bénard convection in Chapter 5. The best fit to the entire data set in the investigated range of Rayleigh numbers is:

$$Nu = 0.067 Ra^{0.330} \tag{8.4}$$

Also, enforcing a $\frac{1}{3}^{rd}$ power law yields a scaling relation of the form:

$$Nu = 0.0645 Ra^{1/3} \tag{8.5}$$

The reasonably accurate predictions given by the $Nu \sim Ra^{1/3}$ scaling relation indicates that a scaling argument of $Nu \sim Ra^{2/7}$ for Rayleigh numbers in the range $1 \times 10^6 \leq Ra \leq 1 \times 10^{11}$ is less probable. The experimentally estimated Nusselt numbers are also compared against some significant literature pertaining to moderate

Rayleigh numbers and is found to match reasonably well with the previous studies for Rayleigh numbers beyond 10^9. One of the major contributors to the observed deviation in Nusselt numbers for $Ra \leq 10^9$ may be the improper modeling/correction of the sidewall conductance heat loss in the studied literature.

Chapter 6 focuses on high-Rayleigh-number free convection in tilted enclosures. A noteworthy observation from this study is that the Nusselt numbers are observed to monotonously decrease with an increase in the angle of inclination, which suggests the absence of a critical angle over the studied range of Rayleigh numbers. Another observation is that for all the studied aspect ratios and Rayleigh numbers, there is a substantial drop in the Nu values between angles of inclination from 0° to 90°, whereas this drop is found to be minimal for angles of inclination between 90° and 150°. Also, for any angle of inclination and a given Rayleigh number, Nusselt numbers are observed to follow a decreasing trend with an increase in aspect ratio. This decreasing trend gradually amplifies as the angle of inclination is increased, with a negligible effect for an angle of inclination of 0° and a prominent effect at an angle of inclination of 90°. This may be attributed to the effect of vertical density stratification reported in the literature for an orientation of 90°. Based on these results, sets of single-parameter ($Nu = f(Ra)$) and two-parameter ($Nu = f(Ra, AR)$) correlating equations are proposed to estimate the average Nusselt number at any of the investigated angles of inclination, as shown in Table 8.1. These results are also compared with the literature, especially for the angles of inclination of 0° and 90°, where literature is aplenty, and are found to agree well. Interestingly, an $Ra\cos\phi$ scaling relation for Nusselt number is also found to predict the experimental data within a reasonable accuracy for $0^\circ \leq \phi \leq 60^\circ$.

Finally, Chapter 7 deals with visualizing buoyant flow characteristics of horizontal and tilted enclosure problems ($0^\circ \leq \phi \leq 90^\circ$). For the horizontal enclosure problem, thermal plume eruptions are observed at multiple random locations on the hot and cold isothermal plates. A large scale flow with frequent cessations and reversals, caused by the erupting thermal plumes, is also found to exist. The velocity of this large scale flow and the frequencies of thermal plume releases are found to increase with in-

Table 8.1 Proposed Nusselt number correlations for various angles of inclination

Angle of inclination (ϕ)	Single-parameter correlation ($Nu = CRa^n$)	Two-parameter correlation ($Nu = CRa^n AR^m$)	Classical $1/3$ scaling ($Nu = CRa^{1/3}$)
0°	$0.067Ra^{0.330}$	$0.0691Ra^{0.329}AR^{-0.006}$	$0.0645Ra^{1/3}$
30°	$0.054Ra^{0.337}$	$0.0687Ra^{0.327}AR^{-0.0377}$	$0.0578Ra^{1/3}$
60°	$0.049Ra^{0.338}$	$0.0759Ra^{0.320}AR^{-0.0704}$	$0.0535Ra^{1/3}$
90°	$0.050Ra^{0.329}$	$0.0898Ra^{0.305}AR^{-0.0921}$	$0.0459Ra^{1/3}$
120°	$0.039Ra^{0.335}$	–	$0.040Ra^{1/3}$
150°	$0.035Ra^{0.336}$	–	$0.0366Ra^{1/3}$

Valid for $1.85 \times 10^6 \leq Ra \leq 1.04 \times 10^{11}$ and $AR = 1 - 10$

crease in Rayleigh number. For vertical enclosures, traveling wave-like structures are observed over the boundary layers that form on the hot and cold vertical walls. Also, the core of the enclosure is found to be unperturbed, even in the presence of these oscillatory boundary layers; which implies that vertical density (temperature) stratification is undisturbed. This unperturbed core region with the vertical density stratification may be the reason behind having the highest effect of aspect ratio on Nusselt number observed at this particular orientation. When the enclosure is tilted at 60°, the core is found to be gently disturbed by the turbulent flow and the ascending (or, descending) fluid parcels discharged by the boundary layers on the hot (or, cold) surfaces. But, for an angle of inclination of 30°, the mixing in the core is observed to be more vigorous, which probably results in a less stratified core. These explain the decrease in the effect of aspect ratio on Nusselt number with decreasing angles of inclination. Another noteworthy observation is the magnitude of buoyant velocity in the different tilted cases. The buoyant velocity is observed to decrease as the angle of inclination increases. As the buoyant velocity of the fluid and the free convective heat transfer within the enclosure are directly related, this explains why there is a reduction in the heat transfer when the angle of inclination is increased.

Bibliography

Ahlers, G. [2000], 'Effect of sidewall conductance on heat-transport measurements for turbulent Rayleigh-Bénard convection', *Physical Review E* **63**, 0153031–4.

Ahlers, G., Grossmann, S. and Lohse, D. [2009a], 'Heat transfer and large scale dynamics in turbulent Rayleigh-Bénard convection', *Reviews of Modern Physics* **81(2)**, 503.

Ahlers, G., He, X., Funfschilling, D. and Bodenschatz, E. [2012], 'Heat transport by turbulent Rayleigh-Bénard convection for $Pr \approx 0.8$ and $3 \times 10^{12} \lesssim Ra \lesssim 2 \times 10^{15}$: aspect ratio $\gamma = 0.50$', *New Journal of Physics* **14(10)**, 103012.

Ahlers, G. and Xu, X. [2001], 'Prandtl-number dependence of heat transport in turbulent Rayleigh-Bénard convection', *Physical Review Letters* **86(15)**, 3320.

Altaç, Z. and Uğurlubilek, N. [2016], 'Assessment of turbulence models in natural convection from two- and three-dimensional rectangular enclosures', *International Journal of Thermal Sciences* **107**, 237–246.

Amati, G., Koal, K., Massaioli, F., Sreenivasan, K. R. and Verzicco, R. [2005], 'Turbulent thermal convection at high Rayleigh numbers for a Boussinesq fluid of constant Prandtl number', *Physics of Fluids* **17(12)**, 121701.

Arnold, J. N., Bonaparte, P. N., Catton, I. and Edwards, D. K. [1974], Experimental investigation of natural convection in finite rectangular regions inclined at various angles from 0° to 180°, in Proceedings of 1974 HTFMI, Stanford U. Press, pp. 321–329.

Arnold, J. N., Catton, I. and Edwards, D. K. [1976], 'Experimental investigation of natural convection in inclined rectangular regions of differing aspect ratios', *Journal of Heat Transfer* **98(1)**, 67–71.

Ayyaswamy, P. and Catton, I. [1973], 'The boundary-layer regime for natural convection in a differentially heated, tilted rectangular cavity', *Journal of Heat Transfer* **95(4)**, 543–545.

Bailon-Cuba, J., Emran, M. S. and Schumacher, J. [2010], 'Aspect ratio dependence of heat transfer and large-scale flow in turbulent convection', *Journal of Fluid Mechanics* **655**, 152–173.

Bairi, A., Laraqi, N. and de Maria, J. G. [2007], 'Numerical and experimental study of natural convection in tilted parallelepipedic cavities for large Rayleigh numbers', *Experimental Thermal and Fluid Science* **31(4)**, 309–324.

Barakos, G., Mitsoulis, E. and Assimacopoulos, D. [1994], 'Natural convection flow in a square cavity revisited: laminar and turbulent models with wall functions', *International Journal for Numerical Methods in Fluids* **18(7)**, 695–719.

Batchelor, G. K. [1954], 'Heat transfer by free convection across a closed cavity between vertical boundaries at different temperatures', *Quarterly of Applied Mathematics* **12(3)**, 209–233.

Belmonte, A., Tilgner, A. and Libchaber, A. [1994], 'Temperature and velocity boundary layers in turbulent convection', *Physical Review E* **50(1)**, 269–281.

Bénard, H. [1901], 'Les tourbillons cellulaires dans une nappe liquide transportant de la chaleur par convection en regime permanent', *Annales de Chimie et de Physique* **23**, 62–144.

Benzi, R., Toschi, F. and Tripiccione, R. [1998], 'On the heat transfer in Rayleigh-Bénard systems', *Journal of Statistical Physics* **93(3-4)**, 901–918.

Bergé, P. and Dubois, M. [1984], 'Rayleigh-Bénard convection', *Contemporary Physics* **25(6)**, 535–582.

Bohn, M. S., Kirkpatrick, A. T. and Olson, D. A. [1984], 'Experimental study of three-dimensional natural convection high-Rayleigh number', *Journal of Heat Transfer* **106(2)**, 339–345.

Brindley, J. [1967], 'Thermal convection in horizontal fluid layers', *IMA Journal of Applied Mathematics* **3(3)**, 313–343.

Brown, E. and Ahlers, G. [2006], 'Rotations and cessations of the large-scale circulation in turbulent Rayleigh-Bénard convection', *Journal of Fluid Mechanics* **568**, 351–386.

Brown, E., Nikolaenko, A., Funfschilling, D. and Ahlers, G. [2005], 'Heat transport in turbulent Rayleigh-Bénard convection: Effect of finite top- and bottom-plate conductivities', *Physics of Fluids* **17(7)**, 075108.

Brown, W. [1973], 'Heat-flux transitions at low Rayleigh number', *Journal of Fluid Mechanics* **60(3)**, 539–559.

Castaing, B., Gunaratne, G., Heslot, F., Kadanoff, L., Libchaber, A., Thomae, S., Wu, X. Z., Zaleski, S. and Zanetti, G. [1989], 'Scaling of hard thermal turbulence in Rayleigh-Bénard convection', *Journal of Fluid Mechanics* **204**, 1–30.

Catton, I. [1978], Natural convection in enclosures, in International Heat Transfer Conference Digital Library, Begel House Inc.

Chandrasekhar, S. [2013], 'Hydrodynamic and hydromagnetic stability', *Courier Corporation, Dover Publications Inc., New York* .

Chang, B. H. [2014], 'Numerical study of flow and heat transfer in differentially heated enclosures', *Thermal Science* **18(2)**, 451–463.

Chaumat, S., Castaing, B., Chilla, F., Castro, I. P., Hancock, P. E. and Thomas, T. G. [2002], 'Rayleigh-Bénard cells: influence of plate properties', *Advances in Turbulence IX (ed. IP Castro & PE Hancock), Barcelona: International Centre for Numerical Methods in Engineering, CIMNE* .

Chavanne, X., Chilla, F., Chabaud, B., Castaing, B. and Hebral, B. [2001], 'Turbulent Rayleigh-Bénard convection in gaseous and liquid He', *Physics of Fluids* **13(5)**, 1300–1320.

Chenoweth, D. R. and Paolucci, S. [1986], 'Natural convection in an enclosed vertical air layer with large horizontal temperature differences', *Journal of Fluid Mechanics* **169**, 173–210.

Chillá, F. and Schumacher, J. [2012], 'New perspectives in turbulent Rayleigh-Bénard convection', *The European Physical Journal E* **35(7)**, 58.

Chilton, T. H. and Colburn, A. P. [1934], 'Mass transfer (absorption) coefficients prediction from data on heat transfer and fluid friction', *Industrial & Engineering Chemistry* **26(11)**, 1183–1187.

Ching, E. S. C. and Tam, W. S. [2006], 'Aspect-ratio dependence of heat transport by turbulent Rayleigh-Bénard convection', *Journal of Turbulence* **(7)**, N72.

Chong, K. L. and Xia, K. Q. [2016], 'Exploring the severely confined regime in Rayleigh-Bénard convection', *Journal of Fluid Mechanics* **805**, R4–1.

Chu, T. Y. and Goldstein, R. J. [1973], 'Turbulent convection in a horizontal layer of water', *Journal of Fluid Mechanics* **60(1)**, 141–159.

Ciliberto, S., Cioni, S. and Laroche, C. [1996], 'Large-scale flow properties of turbulent thermal convection', *Physical Review E* **54(6)**, R5901–R5904.

Cioni, S., Ciliberto, S. and Sommeria, J. [1996], 'Experimental study of high-Rayleigh-number convection in mercury and water', *Dynamics of Atmospheres and Oceans* **24(1-4)**, 117–127.

Cioni, S., Ciliberto, S. and Sommeria, J. [1997], 'Strongly turbulent Rayleigh-Bénard convection in mercury: comparison with results at moderate Prandtl number', *Journal of Fluid Mechanics* **335**, 111–140.

Clever, R. M. [1973], 'Finite amplitude longitudinal convection rolls in an inclined layer', *Journal of Heat Transfer* **95(3)**, 407–408.

Coleman, H. W. and Steele, W. G. [2018], 'Experimentation, validation, and uncertainty analysis for engineers', *John Wiley & Sons* .

Deardorff, J. W. and Willis, G. E. [1965], 'The effect of two-dimensionality on the suppression of thermal turbulence', *Journal of Fluid Mechanics* **23(2)**, 337–353.

Dropkin, D. and Somerscales, E. [1965], 'Heat transfer by natural convection in liquids confined by two parallel plates which are inclined at various angles with respect to the horizontal', *Journal of Heat Transfer* **87(1)**, 77–82.

Eckert, E. R. G. and Carlson, W. O. [1961], 'Natural convection in an air layer enclosed between two vertical plates with different temperatures', *International Journal of Heat and Mass Transfer* **2(1-2)**, 106–120.

Elder, J. W. [1965a], 'Laminar free convection in a vertical slot', *Journal of Fluid Mechanics* **23(1)**, 77–98.

Elder, J. W. [1965b], 'Turbulent free convection in a vertical slot', *Journal of Fluid Mechanics* **23(1)**, 99–111.

Elsherbiny, S. M. [1996], 'Free convection in inclined air layers heated from above', *International Journal of Heat and Mass Transfer* **39(18)**, 3925–3930.

Elsherbiny, S. M., Hollands, K. G. T. and Raithby, G. D. [1982a], 'Effect of thermal boundary conditions on natural convection in vertical and inclined air layers', *Journal of Heat Transfer* **104(3)**, 515–520.

Elsherbiny, S. M., Raithby, G. D. and Hollands, K. G. T. [1982b], 'Heat transfer by natural convection across vertical and inclined air layers', *Journal of Heat Transfer* **104(1)**, 96–102.

Fellmuth, B. [2012], 'Supplementary information for the ITS-90: Introduction', *Bureau International des Poid et Measures* **68**.

Fleischer, A. S. and Goldstein, R. J. [2002], 'High-Rayleigh-number convection of pressurized gases in a horizontal enclosure', *Journal of Fluid Mechanics* **469**, 1–12.

Funfschilling, D., Brown, E., Nikolaenko, A. and Ahlers, G. [2005], 'Heat transport by turbulent Rayleigh-Bénard convection in cylindrical samples with aspect ratio one and larger', *Journal of Fluid Mechanics* **536**, 145–154.

Garon, A. M. and Goldstein, R. J. [1973], 'Velocity and heat transfer measurements in thermal convection', *Physics of Fluids* **16(11)**, 1818–1825.

Glazier, J. A., Segawa, T., Naert, A. and Sano, M. [1999], 'Evidence against 'ultrahard' thermal turbulence at very high Rayleigh numbers', *Nature* **398(6725)**, 307.

Goldstein, R. J. [2017], 'Optical systems for flow measurement: Shadowgraph, schlieren, and interferometric techniques', *Fluid Mechanics Measurements, Second Edition* pp. 475–532.

Goldstein, R. J., Chiang, H. D. and Sayer, E. [1987], Natural convection mass transfer in an inclined enclosure at high Rayleigh number, in Proceedings of the 2^{nd}

International Symposium on Transport Phenomena in Turbulent Flows, pp. 229–255.

Goldstein, R. J., Chiang, H. D. and See, D. L. [1990], 'High Rayleigh-number convection in a horizontal enclosure', *Journal of Fluid Mechanics* **213**, 111–126.

Goldstein, R. J. and Chu, T. Y. [1969], 'Thermal convection in a horizontal layer of air,', *Progress in Heat and Mass Transfer* **2**, 55–75.

Goldstein, R. J. and Tokuda, S. [1980], 'Heat transfer by thermal convection at high Rayleigh numbers', *International Journal of Heat and Mass Transfer* **23(5)**, 738–740.

Goldstein, R. J. and Wang, Q. J. [1984], 'An interferometric study of the natural convection in an inclined water layer', *International Journal of Heat and Mass Transfer* **27(9)**, 1445–1453.

Gray, D. D. and Giorgini, A. [1976], 'The validity of the Boussinesq approximation for liquids and gases', *International Journal of Heat and Mass Transfer* **19(5)**, 545–551.

Grossmann, S. and Lohse, D. [2000], 'Scaling in thermal convection: a unifying theory', *Journal of Fluid Mechanics* **407**, 27–56.

Grossmann, S. and Lohse, D. [2003], 'On geometry effects in Rayleigh-Bénard convection', *Journal of Fluid Mechanics* **486**, 105–114.

Guide to the Expression of Uncertainty in Measurement [1995], *International Organization for Standardization* .

Hamady, F. J., Lloyd, J. R., Yang, H. Q. and Yang, K. T. [1989], 'Study of local natural convection heat transfer in an inclined enclosure', *International Journal of Heat and Mass Transfer* **32(9)**, 1697–1708.

Han, S. [2004], 'The heat and mass transfer analogy factor, Nu/Sh for 2-D and 3-D boundary layers', *Ph.D. thesis, University of Minnesota* .

Hart, J. E. [1971], 'Stability of the flow in a differentially heated inclined box', *Journal of Fluid Mechanics* **47(3)**, 547–576.

He, X., Funfschilling, D., Bodenschatz, E. and Ahlers, G. [2012a], 'Heat transport

by turbulent Rayleigh-Bénard convection for $Pr \approx 0.8$ and $4 \times 10^{11} \lesssim Ra \lesssim 2 \times 10^{14}$: ultimate-state transition for aspect ratio $\gamma = 1.00$', *New Journal of Physics* **14(6)**, 063030.

He, X., Funfschilling, D., Nobach, H., Bodenschatz, E. and Ahlers, G. [2012b], 'Transition to the ultimate state of turbulent Rayleigh-Bénard convection', *Physical Review Letters* **108(2)**, p.024502.

Henkes, R. A. W. M., Van Der Vlugt, F. F. and Hoogendoorn, C. J. [1989], 'Natural-convection flow in a square cavity calculated with low-Reynolds-number turbulence models', *International Journal of Heat and Mass Transfer* **34(2)**, 377–388.

Heslot, F., Castaing, B. and Libchaber, A. [1987], 'Transitions to turbulence in helium gas', *Physical Review A* **36(12)**, 5870.

Hideo, I. [1984], 'Experimental study of natural convection in an inclined air layer', *International Journal of Heat and Mass Transfer* **27(8)**, 1127–1139.

Horanyi, S., Krebs, L. and Müller, U. [1999], 'Turbulent Rayleigh-Bénard convection in low Prandtl-number fluids', *International Journal of Heat and Mass Transfer* **42(21)**, 3983–4003.

Howell, J. R., Menguc, M. P. and Siegel, R. [2015], 'Thermal radiation heat transfer', *CRC Press* .

Hsieh, S. S. and Wang, C. Y. [1994], 'Experimental study of three-dimensional natural convection in enclosures with different working fluids', *International Journal of Heat and Mass Transfer* **37(17)**, 2687–2698.

Hunt, J. C. R., Vrieling, A. J., Nieuwstadt, F. T. M. and Fernando, H. J. S. [2003], 'The influence of the thermal diffusivity of the lower boundary on eddy motion in convection', *Journal of Fluid Mechanics* **491**, 183–205.

Jakob, M. [1946], 'Free heat convection through enclosed plane gas layers', *Journal of Heat Transfer* **68**, 189–194.

Jannot, M. and Mazeas, C. [1973], 'Etude expérimentale de la convection naturelle dans des cellules rectangulaires verticales', *International Journal of Heat and Mass Transfer* **16(1)**, 81–100.

Kerr, R. M. [1996], 'Rayleigh number scaling in numerical convection', *Journal of Fluid Mechanics* **310**, 139–179.

Kline, S. J. and Mcclintock, F. A. [1953], 'Describing uncertainties in single-sample experiments', *Mechanical Engineering* **75**, 3–8.

Kraichnan, R. [1962], 'Turbulent thermal convection at arbitrary Prandtl number', *The Physics of Fluids* **5(11)**, 1374–1389.

Krishnamurti, R. [1973], 'Some further studies on the transition to turbulent convection', *Journal of Fluid Mechanics* **60(2)**, 285–303.

Kuyper, R. A., Van Der Meer, T. H., Hoogendoorn, C. J. and Henkes, R. A. W. M. [1993], 'Numerical study of laminar and turbulent natural convection in an inclined square cavity', *International Journal of Heat and Mass Transfer* **36(11)**, 2899–2911.

Lemmon, E. W., McLinden, M. O. and Friend, D. G. [2003], *in NIST Chemistry Webbook, NIST Standard Reference Database Number 69, Linstrom, P. J., Mallard, W. G. (eds).*, National Institute of Standards and Technology: Gaithersburg, MD. **URL:** *http://webbook.nist.gov*

Linthorst, S. J. M., Schinkel, W. M. M. and Hoogendoorn, C. J. [1981], Natural convection flow in inclined air-filled enclosures of small and moderate aspect ratio, in International Symposium on Flow Visualization, Vol. 47(3), pp. 114–118.

MacGregor, R. K. and Emery, A. F. [1969], 'Free convection through vertical plane layers - moderate and high Prandtl number fluids', *Journal of Heat Transfer* **91(3)**, 391–401.

Madanan, U. and Goldstein, R. J. [2018], Prediction and correction of sidewall conductance for natural convection in horizontal enclosures, in Proceedings of the 16^{th} International Heat Transfer Conference (IHTC), Beijing, China, Aug 10-15, pp. 2731–2740.

Madanan, U. and Goldstein, R. J. [2019a], 'Thermal convection in horizontal rectangular enclosures at moderate Rayleigh numbers: Effect of sidewall conductance and aspect ratio', *International Journal of Heat and Mass Transfer* **136**, 178–185.

Madanan, U. and Goldstein, R. J. [2019b], 'Experimental investigation on very-high-Rayleigh-number thermal convection in tilted rectangular enclosures', *International Journal of Heat and Mass Transfer* **139**, 121–129.

Madanan, U. and Goldstein, R. J. [2019c], 'Effect of sidewall conductance on Nusselt number for Rayleigh-Bénard convection: A semi-analytical and experimental correction', *Journal of Heat Transfer* **(in press)**.

Magin, R. L., Mangum, B. W., Statler, J. A. and Thornton, D. D. [1981], 'Transition temperatures of the hydrates of Na_2SO_4, Na_2HPO_4, and KF as fixed points in biomedical thermometry', *Journal of Research of the National Bureau of Standards* **86(2)**.

Malkus, W. V. [1954], Discrete transitions in turbulent convection, in Proceedings of the Royal Society of London. Series A. Mathematical and Physical Sciences, Vol. 225(1161), pp. 185–195.

Markatos, N. C. and Pericleous, K. A. [1984], 'Laminar and turbulent natural convection in an enclosed cavity', *International Journal of Heat and Mass Transfer* **27(5)**, 755–772.

Naert, A., Segawa, T. and Sano, M. [1997], 'High-Reynolds-number thermal turbulence in mercury', *Physical Review E* **56(2)**, R1302.

Niemela, J. J., Skrbek, L., Sreenivasan, K. R. and Donnelly, R. J. [2000], 'Turbulent convection at very high Rayleigh numbers', *Nature* **404(6780)**, 837–840.

Niemela, J. J., Skrbek, L., Sreenivasan, K. R. and Donnelly, R. J. [2001], 'The wind in confined thermal convection', *Journal of Fluid Mechanics* **449**, 169–178.

Niemela, J. J. and Sreenivasan, K. R. [2003], 'Confined turbulent convection', *Journal of Fluid Mechanics* **481**, 355–384.

Niemela, J. J. and Sreenivasan, K. R. [2006], 'Turbulent convection at high Rayleigh numbers and aspect ratio 4', *Journal of Fluid Mechanics* **557**, 411–422.

Niemela, J. J. and Sreenivasan, K. R. [2010], 'Does confined turbulent convection ever attain the 'asymptotic scaling' with $1/2$ power?', *New Journal of Physics* **12(11)**, 115002.

Nikolaenko, A., Brown, E., Funfschilling, D. and Ahlers, G. [2005], 'Heat transport by turbulent Rayleigh-Bénard convection in cylindrical cells with aspect ratio one and less', *Journal of Fluid Mechanics* **523**, 251–260.

Nusselt, W. [1930], 'Heat transfer, diffusion, and evaporation', *Zeitschrift. für Mathematik und Mechanik* **10**, 105.

Ozoe, H., Sayama, H. and Churchill, S. W. [1975], 'Natural convection in an inclined rectangular channel at various aspect ratios and angles- experimental measurements', *International Journal of Heat and Mass Transfer* **18(12)**, 1425–1431.

Palm, E. [1975], 'Nonlinear thermal convection', *Annual Review of Fluid Mechanics* **7(1)**, 39–61.

PCC-1-2000 Edition: Guildelines for pressure boundary bolted flange joint assembnly [1999], *ASME* .

Preston-Thomas, H. [1975], 'The international practical temperature scale of 1968 amended edition of 1975', *Metrologia* **12(7)**.

Preston-Thomas, H. [1990], *The International Temperature Scale of 1990 (ITS-90), Metrologia* **27(1)**, 3.

Priestley, C. [1959], 'Turbulent transfer in the lower atmosphere', *University of Chicago Press, Chicago* .

Raithby, G. D. and Hollands, K. G. T. [1998], 'The stratification in natural convection in vertical enclosures', *Handbook of Heat Transfer Fundamentals, in: W. M. Rohsenow, J. P. Hartnett, Y. I. Cho (eds.), Vol. 3, McGraw-Hill, New York* .

Raithby, G. D., Hollands, K. G. T. and Unny, T. E. [1977], 'Analysis of heat transfer by natural convection across vertical fluid layers', *Journal of Heat Transfer* **99(2)**, 287–293.

Rayleigh, J. [1916], 'On convection currents in a horizontal layer of fluid, when the higher temperature is on the underside', *Philosophical Magazine* **32**, 529–546.

Roche, P. E., Castaing, B., Chabaud, B. and Hébral, B. [2001b], 'Observation of the $1/2$ power law in Rayleigh-Bénard convection', *Physical Review E* **63(4)**, 045303.

Roche, P. E., Castaing, B., Chabaud, B. and Hébral, B. [2002], 'Prandtl and Rayleigh numbers dependences in Rayleigh-Bénard convection', *Europhysics Letters* **58(5)**, 693.

Roche, P. E., Castaing, B., Chabaud, B., Hébral, B. and Sommeria, J. [2001a], 'Side wall effects in Rayleigh-Bénard experiments', *The European Physical Journal B* **24(3)**, 405–408.

Roche, P. E., Gauthier, F., Kaiser, R. and Salort, J. [2010], 'On the triggering of the ultimate regime of convection', *New Journal of Physics* **12(8)**, 085014.

Rossby, H. T. [1969], 'A study of Bénard convection with and without rotation', *Journal of Fluid Mechanics* **36(2)**, 309–335.

Schinkel, W. M. M. and Hoogendoorn, C. J. [1985], 'Core stratification effects on natural convection in inclined cavities', *Applied Scientific Research* **42(2)**, 109–130.

Schinkel, W. M.and Linthorst, S. J. M. and Hoogendoorn, C. J. [1983], 'The stratification in natural convection in vertical enclosures', *Journal of Heat Transfer* **105(2)**, 267–272.

Seki, N., Fukusako, S. and Inaba, H. [1978a], 'Heat transfer of natural convection in a rectangular cavity with vertical walls of different temperatures', *Bulletin of JSME* **21(152)**, 246–253.

Settles, G. S. [2012], 'Schlieren and shadowgraph techniques: visualizing phenomena in transparent media', *Springer Science & Business Media* .

Shadid, J. N. and Goldstein, R. J. [1990], 'Visualization of longitudinal convection roll instabilities in an inclined enclosure heated from below', *Journal of Fluid Mechanics* **215**, 61–84.

Shang, X. D., Qiu, X. L., Tong, P. and Xia, K. Q. [2003], 'Measured local heat transport in turbulent Rayleigh-Bénard convection', *Physical Review Letters* **90(7)**, 074501.

Shishkina, O. and Wagner, C. [2006], 'Analysis of thermal dissipation rates in turbulent Rayleigh-Bénard convection', *Journal of Fluid Mechanics* **546**, 51–60.

Shishkina, O. and Wagner, C. [2007], 'Local heat fluxes in turbulent Rayleigh-Bénard convection', *Physics of Fluids* **19(8)**, 085107.

Shishkina, O. and Wagner, C. [2008], 'Analysis of sheet-like thermal plumes in turbulent Rayleigh-Bénard convection', *Journal of Fluid Mechanics* **599**, 383–404.

Shraiman, B. I. and Siggia, E. D. [1990], 'Heat transport in high-Rayleigh-number convection', *Physical Review A* **42(6)**, 3650.

Siggia, E. D. [1994], 'High Rayleigh number convection', *Annual Review of Fluid Mechanics* **26(1)**, 137–168.

Sreenivasan, K. R., Bershadskii, A. and Niemela, J. J. [2002], 'Mean wind and its reversal in thermal convection', *Physical Review E* **65(5)**, 056306.

Srinivasan, V. [2007], 'Thermal convection at high Rayleigh numbers in compressed gases', *Ph.D. thesis, University of Minnesota* .

Stevens, R. J., Lohse, D. and Verzicco, R. [2011], 'Prandtl and Rayleigh number dependence of heat transport in high Rayleigh number thermal convection', *Journal of Fluid Mechanics* **688**, 31–43.

Sun, C., Ren, L. Y., Song, H. and Xia, K. Q. [2005], 'Heat transport by turbulent Rayleigh-Bénard convection in $1m$ diameter cylindrical cells of widely varying aspect ratio', *Journal of Fluid Mechanics* **542**, 165–174.

Urban, P., Hanzelka, P., Musilová, V., Králík, T., La Mantia, M., Srnka, A. and Skrbek, L. [2014], 'Heat transfer in cryogenic helium gas by turbulent Rayleigh-Bénard convection in a cylindrical cell of aspect ratio 1', *New Journal of Physics* **16(5)**, 053042.

Verzicco, R. [2002], 'Sidewall finite-conductivity effects in confined turbulent thermal convection', *Journal of Fluid Mechanics* **473**, 201–210.

Verzicco, R. [2004], 'Effects of nonperfect thermal sources in turbulent thermal convection', *Physics of Fluids* **16(6)**, 1965–1979.

Verzicco, R. and Camussi, R. [1997], 'Transitional regimes of low-Prandtl thermal convection in a cylindrical cell', *Physics of Fluids* **9(5)**, 1287–1295.

Verzicco, R. and Camussi, R. [2003], 'Numerical experiments on strongly turbulent

thermal convection in a slender cylindrical cell', *Journal of Fluid Mechanics* **477**, 19–49.

Waleffe, F., Boonkasame, A. and Smith, L. M. [2015], 'Heat transport by coherent Rayleigh-Bénard convection', *Physics of Fluids* **27(5)**, 051702.

Wang, Y., Lai, P. Y., Song, H. and Tong, P. [2018], 'Mechanism of large-scale flow reversals in turbulent thermal convection', *Science Advances* **4(11)**, eaat7480.

White, D. R., Ballico, M., Del Campo, D., Duris, S., Filipe, E., Ivanova, A., Dogan, A. K., Mendez-Lango, E., Meyer, C. W., Pavese, F. and Peruzzi, A. [2007], 'Uncertainties in the realization of the SPRT sub-ranges of the ITS-90', *International Journal of Thermophysics* **28(6)**, 1868–1881.

Williamson, N., Armfield, S. W., Lin, W. and Kirkpatrick, M. P. [2016], 'Stability and Nusselt number scaling for inclined differentially heated cavity flow', *International Journal of Heat and Mass Transfer* **97**, 787–793.

Willis, G. E. and Deardorff, J. W. [1967], 'Confirmation and renumbering of the discrete heat flux transitions of Malkus', *Physics of Fluids* **10(9)**, 1861–1866.

Wirtz, R. A. and Tseng, W. F. [1980], Natural convection across tilted, rectangular enclosures of small aspect ratio, in Proceedings of the 19^{th} National Heat Transfer Conference, July.

Wright, J. L. [1996], A correlation to quantify convective heat transfer between vertical window glazings, in ASHRAE Transactions, Vol. 102, pp. 940–946.

Wu, X. Z. and Libchaber, A. [1991], 'Non-Boussinesq effects in free thermal convection', *Physical Review A* **43**, 2833–2839.

Wu, X. Z. and Libchaber, A. [1992], 'Scaling relations in thermal turbulence: the aspect-ratio dependence', *Physical Review A* **45(2)**, 842.

Xi, H. D. and Xia, K. Q. [2007], 'Cessations and reversals of the large-scale circulation in turbulent thermal convection', *Physical Review E* **75(6)**, 066307.

Xia, K. Q. [2013], 'Current trends and future directions in turbulent thermal convection', *Theoretical and Applied Mechanics Letters* **3(5)**, 052001.

Xia, K. Q., Lam, S. and Zhou, S. Q. [2002], 'Heat-flux measurement in high-

Prandtl-number turbulent Rayleigh-Bénard convection', *Physical Review Letters* **88(6)**, 064501–1–064501–4.

Xu, X., Bajaj, K. M. and Ahlers, G. [2000], 'Heat transport in turbulent Rayleigh-Bénard convection', *Physical Review Letters* **84(19)**, 4357.

Yang, K. T. [1987], 'The stratification in natural convection in vertical enclosures', *Handbook of single-phase convective heat transfer, S. Kakaç, R. K. Shah, W. Aung (eds.)* .

Yedder, R. B. and Bilgen, E. [1995], 'Turbulent natural convection and conduction in enclosures bounded by a massive wall', *International Journal of Heat and Mass Transfer* **38(10)**, 1879–1891.

Zhou, Q., Liu, B. F., Li, C. M. and Zhong, B. C. [2012], 'Aspect ratio dependence of heat transport by turbulent Rayleigh-Bénard convection in rectangular cells', *Journal of Fluid Mechanics* **710**, 260–276.

Appendices

Appendix A
Data Reduction

A.1 Total heat input

The total heat input is calculated from the electrical power as:

$$q_{inp} = \sum_{heater,i=1}^{26} [V_i I_i] + [V_g I_g] \tag{A.1}$$

The heat losses are as follows: (i) guard heat loss, which is the outward heat loss from the hot plate in the direction of the guard plate (q_g); (ii) radiation heat loss from the hot surface (q_r); (iii) edge heat loss from the hot plate assembly through the balsa wood insulation that runs all around the periphery of the hot-end (q_e); (iv) surface heat loss from the sidewall outer surfaces (q_s); (v) sidewall conductance heat loss (q_{sw}).

To estimate the net heat input power from the total heat input, one needs to correct for (or, subtract) all possible heat losses, except the sidewall conductance heat loss, as shown below:

$$q_{net} = q_{inp} - q_g - q_e - q_r - q_s \tag{A.2}$$

The sidewall conductance heat loss, which is not taken into account in Equation A.2, will be included by using an empirical formula while estimating the corrected Nusselt number in the last step of data reduction.

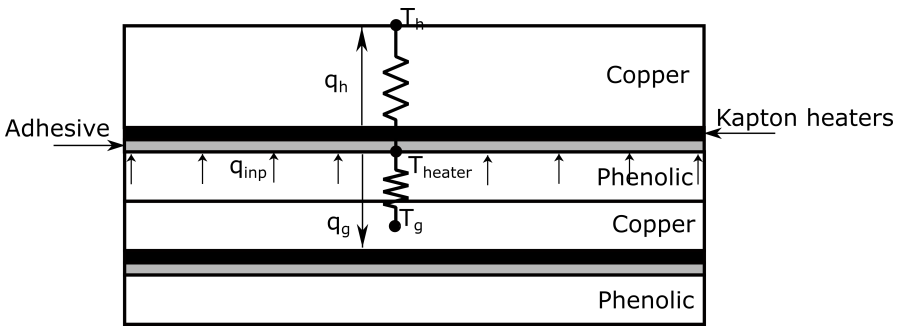

Fig. A.1 Hot plate assembly schematic for q_g calculation (not to scale)

A.2 Guard heat loss

Energy balance for the heater, considering only 1-D thermal diffusion, yields:

$$q_{inp} = q_h + q_g \tag{A.3}$$

Power supplied to the Kapton heaters = heat diffusion in the direction of the hot plate (or, the convecting fluid) + heat diffusion in the direction of the guard plate.

Heat diffusion in the direction of the hot plate can be written as:

$$q_h = \frac{T_{heater} - T_h}{R_1} \tag{A.4}$$

where the thermal diffusion resistance, R_1, is given by:

$$R_1 = \left[\frac{t_h}{k_{Cu}L^2} + \frac{t_k}{k_kL^2} + \frac{t_{ha}}{k_{ha}L^2}\right] \tag{A.5}$$

The heat diffusion in the direction of the guard-plate is:

$$q_g = \frac{T_{heater} - T_g}{R_2} \tag{A.6}$$

where the thermal diffusion resistance, R_2, is given by:

$$R_2 = \left[\frac{t_{ph}}{k_{ph}L^2} + \frac{\frac{1}{5}t_g}{k_{Cu}L^2}\right] \tag{A.7}$$

As can be seen from Equation A.7, only $\frac{1}{5}^{th}$ of the guard plate thickness is consid-

ered for the R_2 estimation. This is because the thermcouples monitoring the guard plate temperature (T_g) are embedded at an approximate depth of $\frac{t_g}{5}$.

Therefore, from Equation A.3, the total input power becomes:

$$q_{inp} = \frac{T_{heater} - T_h}{R_1} + \frac{T_{heater} - T_g}{R_2} \tag{A.8}$$

The temperature at the heater surface is calculated by re-arranging the previous equation as:

$$T_{heater} = \frac{q_{inp} + \frac{T_h}{R_1} + \frac{T_g}{R_2}}{\left[\frac{1}{R_1} + \frac{1}{R_2}\right]} \tag{A.9}$$

The diffusion heat loss in the direction of the guard plate is given by:

$$q_g = \frac{T_{heater} - T_g}{R_2} \tag{A.10}$$

Substituting Equation A.9 in Equation A.10 gives:

$$q_g = \frac{q_{inp} + \frac{(T_h - T_g)}{R_1}}{\left(1 + \frac{R_2}{R_1}\right)} \tag{A.11}$$

A.3 Radiation heat loss

Radiation heat loss from the hot surface is computed by modeling the test cell as a three body enclosure with known emissivities and temperatures (see Figure A.2).

The temperatures of the surfaces for the three-body enclosure are taken as:

$$\begin{aligned} T_1 &= T_h(K) \\ T_2 &= T_m(K) \\ T_3 &= T_c(K) \end{aligned} \tag{A.12}$$

The four sidewalls together are considered as one surface with a temperature of T_m. The resistance network for the three body enclosure is shown in Figure A.3.

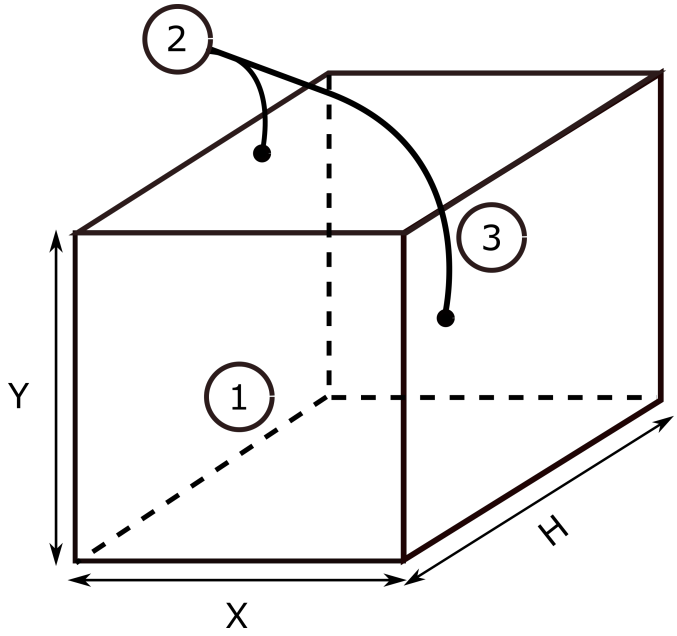

Fig. A.2 Schematic for the three body enclosure

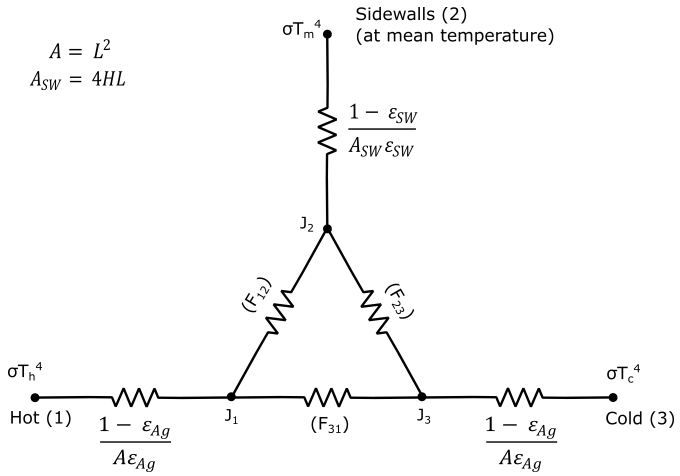

Fig. A.3 Three body enclosure radiative heat exchange: resistance network

A.3.1 View factors

The formula given by Howell et al. (2015) is used to find the view factor, F_{12}, as shown below:

$$F_{12} = \frac{2}{\pi\bar{x}\bar{y}}\left[\frac{1}{2}\ln\left(\frac{(1+\bar{x}^2)(1+\bar{y}^2)}{1+\bar{x}^2+\bar{y}^2}\right) + \bar{x}(1+\bar{y}^2)^{1/2}\tan^{-1}\left(\frac{\bar{x}}{(1+\bar{y}^2)^{1/2}}\right) + \bar{y}(1+\bar{x}^2)^{1/2}\tan^{-1}\left(\frac{\bar{y}}{(1+\bar{x}^2)^{1/2}}\right) - \bar{x}\tan^{-1}\bar{x} - \bar{y}\tan^{-1}\bar{y}\right] \quad \text{(A.13)}$$

where,

$$\bar{x} = \frac{X}{H} \qquad \bar{y} = \frac{Y}{H} \tag{A.14}$$

Given that:

$$F_{11} = 0 \tag{A.15}$$

one can determine F_{13} as:

$$F_{13} = 1 - F_{12} \tag{A.16}$$

When $X = Y = L$

$$F_{12} = F_{32} \tag{A.17}$$

$$F_{13} = F_{31}$$

A.3.2 Radiation heat exchange between the surfaces

From the radiation resistance network, one can write:

$$J_1 = \varepsilon_1 \sigma T_1^4 + (1 - \varepsilon_1)[F_{12} J_2 + F_{13} J_3] \tag{A.18}$$

$$J_2 = \varepsilon_2 \sigma T_2^4 + (1 - \varepsilon_2)[F_{23} J_2 + F_{13} J_3] \tag{A.19}$$

$$J_3 = \varepsilon_3 \sigma T_3^4 + (1 - \varepsilon_3)[F_{12} J_2 + F_{13} J_1] \tag{A.20}$$

This is a system of 3 linear equations with 3 unknowns, provided that the temperatures and the emissivities are given and the view factors are known (which is the case for the present study). By solving this set of linear equations, the values of J_i can be computed. Thus, one can find the irradiation on the hot surface using:

$$G_1 = F_{12}J_2 + F_{13}J_3 \tag{A.21}$$

Therefore, the net radiation heat loss from the hot surface is estimated as:

$$q_r = L^2(J_1 - G_1) \tag{A.22}$$

A.4 Edge heat loss

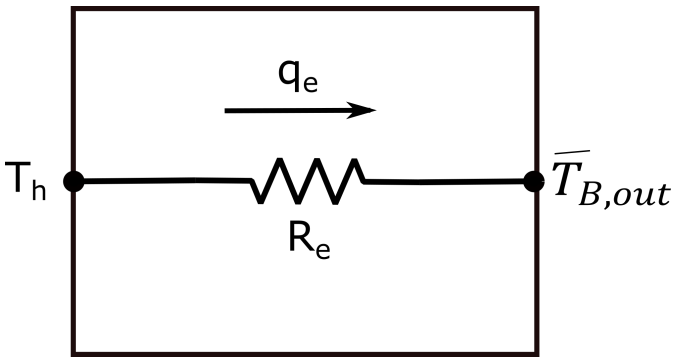

Fig. A.4 1-D thermal diffusion through the balsa wood insulation

The temperature of the hot surface and the average temperature computed from thermocouple readings at the outer balsa wood surface are used to estimate the edge heat loss. By assuming: (i) 1-D heat diffusion (i.e., the direction of heat transfer is normal to the edges), (ii) the temperature at the edge of the hot-end assembly to be equal to the surface temperature (T_h), and (iii) by not considering balsa wood as a porous material, one can write:

$$q_e = \frac{T_h - \overline{T}_{B,out}}{R_e} \tag{A.23}$$

Here, the thermal diffusion resistance, R_e, is estimated as:

$$R_e = \frac{t_B}{Lt_h k_B} \tag{A.24}$$

Thus, the edge heat loss can be computed by:

$$q_e = \frac{4k_B(T_h - \overline{T}_{B,out})Lt_h}{t_B} \tag{A.25}$$

A.5 Surface heat loss

The Styrofoam sidewalls are wrapped in a thick layer of glass wool ($\approx 7.5\,mm$ in thickness) to minimize surface heat loss toward the external fluid within the pressure vessel. Since the thermal conductivity of the glass wool is very low ($k_{gw} = 0.04\,W/mK$) and the thickness of the glass wool layer is about $7.5\,mm$, the thermal resistance to the diffusion through the glass wool layer will be much higher than that for the free convection (which removes thermal energy from the outer surface of the glass wool layer to the fluid inside the pressure vessel). Thus, it is safe to ignore the convective resistance and use only the resistance to the thermal diffusion through the glass wool layer.

Here, surface temperature of the sidewalls are assumed to be the mean temperature (T_m) and the outer surface temperature of the glass wool is taken as the measured fluid temperature inside the pressure vessel (T_{amb}). Thus, one can write:

$$q_s = \frac{T_m - T_{amb}}{R_{gw}} \tag{A.26}$$

Here, the thermal diffusion resistance, R_{gw}, is estimated as:

$$R_e = \frac{t_{gw}}{LHk_{gw}} \tag{A.27}$$

Therefore, the edge heat loss can be computed by:

$$q_s = \frac{4k_{gw}(T_m - T_{amb})LH}{t_{gw}} \tag{A.28}$$

A.6 Net input power

By knowing the total power input to the heaters and the various forms of heat losses, the net input power can be estimated using:

$$q_{net} = q_{inp} - q_g - q_r - q_e - q_s \tag{A.29}$$

It is to be noted that the sidewall conductance heat loss is not accounted for while estimating q_{net}.

A.7 Sidewall heat loss and corrected Nusselt number

From q_{net}, the uncorrected Nusselt number (Nu_{net}) is computed as:

$$Nu_{net} = \frac{q_{net} H}{L^2 \Delta T k_{f_m}}$$

To correct for the sidewall conductance heat loss, the following equation (refer to Chapter 4, Equation 4.15) is used:

$$Nu_c = \frac{Nu_{net}}{[1 + Wn^2]} \tag{A.30}$$

Here, Wn is the wall number ($= 0.18$ for the Styrofoam sidewalls) and Nu_c is the corrected Nusselt number used for the final calculations and in the development of correlations.

A.8 Rayleigh number

Rayleigh numbers are computed using fluid properties and the measured temperature difference (ΔT) between the hot and cold plates, given by:

$$Ra = \frac{g \beta \Delta T H^3}{\nu \alpha} \tag{A.31}$$

The fluid properties are estimated at the mean temperature (T_m) and are obtained from the *NIST Chemistry WebBook* (Lemmon et al., 2003)

Appendix B

Sample Calculations

Table B.1 Operating variables (Experiment no. 14, Date: 08/13/2016)

Angle of inclination, ϕ	0°
Pressure, p	$24.97\,bar$
Temperature of the hot plate, T_h	$30.97^{\circ}C$
Temperature of the cold plate, T_c	$13.01^{\circ}C$
Guard plate temperature, T_g	$31.06^{\circ}C$
Total power input, q_{inp}	$7.324\,W$
Temperature measured on the outer surface of balsa wood box, $\overline{T}_{B,out}$	$21.91^{\circ}C$
Ambient temperature, T_{amb}	$21.87^{\circ}C$

Table B.2 Thermo-physical properties (obtained from the *NIST Chemistry WebBook*)

Density at hot-end, ρ_h	$27.729\,kg/m^3$
Density at cold-end, ρ_c	$29.581\,kg/m^3$
Density at mean temperature, ρ_m	$28.623\,kg/m^3$
Dynamic viscosity at mean temperature, μ_m	$1.808 \times 10^{-5}\,Ns/m^2$
Thermal conductivity at mean temperature, k_{f_m}	$0.0265\,W/m-K$
Specific heat at mean temperature, C_{p_m}	$1081.8\,J/kg-K$

Table B.3 Constants and experimental parameters

Extent of the square active plates, L	$0.15\,m$
Spacing between the hot and cold plate, H	$0.15\,m$
Aspect ratio, A=$\frac{L}{H}$	1
Hot plate thickness, t_h	$0.0127\,m$
Thickness of guard plate, t_g	$0.00635\,m$
Thickness of glass wool insulation, t_{gw}	$0.0762\,m$
Thickness of phenolic insulation, t_{ph}	$0.00635\,m$
Thickness of Kapton layer, t_k	$5.08 \times 10^{-5}\,m$
Thickness of heater adhesive, t_{ha}	$5.08 \times 10^{-5}\,m$
Thickness of Styrofoam sidewalls, t_{st}	$0.00635\,m$
Thickness of balsa wood box, t_B	$0.0254\,m$
Thermal conductivity of balsa wood, k_B	$0.048\,W/m-K$
Thermal conductivity of copper, k_{Cu}	$400\,W/m-K$
Thermal conductivity of glass wool, k_{gw}	$0.04\,W/m-K$
Thermal conductivity of Kapton, k_k	$0.16\,W/m-K$
Thermal conductivity of adhesive, k_{ha}	$0.16\,W/m-K$
Thermal conductivity of Styrofoam, k_{st}	$0.033\,W/m-K$
Thermal conductivity of phenolic, k_{ph}	$0.07\,W/m-K$
Thermal emissivity of polished silver surface, ε_{Ag}	0.025
Thermal emissivity of Styrofoam surface, ε_{st}	0.6
Acceleration due to gravity, g	$9.806\,m/s^2$
Stefan-Boltzmann constant, σ	$5.67 \times 10^{-8}\,W/m^2-K^4$
Wall number of the Styrofoam sidewalls, Wn	0.18

B.1 Rayleigh number

The difference in temperature is estimated as follows:

$$\Delta T = T_h - T_c = 30.97 - 13.01 = 17.96\,K \tag{B.1}$$

The mean temperature of the convecting fluid is estimated by averaging the hot- and cold-plate temperatures.

$$T_m = \frac{T_h + T_c}{2} = \frac{30.97 + 13.01}{2} = 21.99\,^{\circ}C \tag{B.2}$$

Volumetric coefficient of thermal expansion is estimated using:

$$\beta = \frac{\rho_c - \rho_h}{\rho_m \Delta T} = \frac{29.581 - 27.729}{28.623 \times 17.96} = 0.003603\,K^{-1} \tag{B.3}$$

Thermal diffusivity, α, is estimated as:

$$\alpha = \frac{k_{fm}}{\rho_m c_{p_m}} = \frac{0.0265}{28.623 \times 1081.8} = 8.558 \times 10^{-7} m^2/s \tag{B.4}$$

Kinematic viscosity, ν, is calculated using the equation:

$$\nu = \frac{\mu_m}{\rho_m} = \frac{1.808 \times 10^{-5}}{28.623} = 6.316 \times 10^{-7} m^2/s \tag{B.5}$$

Finally, Rayleigh number, Ra, is computed using:

$$\begin{aligned} Ra = \frac{g\beta\Delta T H^3}{\nu\alpha} &= \frac{9.806 \times 0.003603 \times 17.96 \times (0.15)^3}{6.316 \times 10^{-7} \times 8.558 \times 10^{-7}} \\ &= 3.96 \times 10^9 \end{aligned} \tag{B.6}$$

B.2 Total input power

$$q_{inp} = \sum_{i=1}^{26} V_i I_i + V_g I_g = 7.324 W \tag{B.7}$$

B.3 Guard heat loss

Firstly, the thermal resistances R_1 and R_2 are estimated by knowing the thicknesses and the thermal conductivities of the different plates used in the hot-end sandwich design.

$$R_1 = \frac{1}{(0.15)^2}\left[\frac{0.0127}{400} + \frac{5.08 \times 10^{-5}}{0.16} + \frac{5.08 \times 10^{-5}}{0.16}\right] \tag{B.8}$$
$$= 0.0292 K/W$$

$$R_2 = \frac{1}{(0.15)^2}\left[\frac{0.00635}{0.07} + \frac{0.00635}{5 \times 400}\right] \tag{B.9}$$
$$= 4.032 K/W$$

Then, the guard heat loss can be estimated as:

$$q_g = \frac{q_{inp} + \frac{(T_h - T_g)}{R_1}}{\left(1 + \frac{R_2}{R_1}\right)} \tag{B.10}$$
$$= \frac{7.324 + \frac{(30.97 - 31.06)}{0.0292}}{\left(1 + \frac{4.032}{0.0292}\right)}$$
$$= 0.0307 W$$

B.4 Radiation heat loss

Table B.4 Three body enclosure modeling for radiation heat loss estimation

Body	Details	Temperature (K)	ε
1	Hot	304.12	0.025
2	Styrofoam sidewalls	295.14	0.60
3	Cold	286.16	0.025

B.4.1 View factors

View factors are estimated using the formula put forward by Howell et al. (2015) as:

$$\begin{aligned} F_{11} &= 0 \\ F_{13}, F_{23} &= 0.20 \\ F_{12}, F_{21} &= 0.80 \end{aligned} \tag{B.11}$$

B.4.2 Radiosity and irradiation

Once the view factors are computed, the system of 3 linear equations are solved to estimate the radiosity values. Using the values of the view factors, J_2, and J_3, the irradiation (G_1) on the hot surface is estimated. The computed values are:

$$\begin{aligned} J_1 &= 431.165 W/m^2 \\ J_2 &= 430.125 W/m^2 \\ J_3 &= 429.693 W/m^2 \\ G_1 &= 430.0387 W/m^2 \end{aligned} \tag{B.12}$$

Thus, the net radiation heat loss from the hot surface can be estimated as:

$$\begin{aligned} q_r &= L^2(J_1 - G_1) \\ &= (0.15)^2 \times (431.165 - 430.0387) \\ &= 0.0253 W \end{aligned} \tag{B.13}$$

B.5 Edge heat loss

Edge heat loss is computed using the 1-D thermal diffusion equation as:

$$\begin{aligned} q_e &= \frac{4k_B(T_h - \overline{T}_{B,out})Lt_{hot}}{t_B} \\ &= \frac{4 \times 0.048 \times (30.97 - 21.91) \times 0.15 \times 0.0127}{0.0254} \\ &= 0.131\,W \end{aligned} \tag{B.14}$$

B.6 Surface heat loss

Surface heat loss is also computed using the 1-D thermal diffusion equation as:

$$\begin{aligned} q_s &= \frac{4k_{gw}(T_m - T_{amb})LH}{t_{gw}} \\ &= \frac{4 \times 0.04 \times (21.99 - 21.87) \times 0.15 \times 0.15}{0.0762} \\ &= 5.67mW \end{aligned} \tag{B.15}$$

B.7 Net input power

The net input power, after carefully correcting for all possible heat losses except for the sidewall conductance heat loss, is calculated to be:

$$\begin{aligned} q_{net} &= q_{inp} - q_g - q_r - q_e - q_s \\ &= 7.324 - 0.0307 - 0.0253 - 0.131 - 0.00566 \\ &= 7.131\,W \end{aligned} \tag{B.16}$$

B.8 Net and corrected Nusselt number

Firstly, the sidewall-uncorrected Nusselt number, Nu_{net}, is computed as:

$$\begin{aligned} Nu_{net} &= \frac{q_{net}H}{L^2\Delta T k_{f_m}} \\ &= \frac{7.131 \times 0.15}{(0.15)^2 \times 17.96 \times 0.0265} \\ &= 99.90 \end{aligned} \tag{B.17}$$

Then, the sidewall-corrected Nusselt number (Nu_c) is estimated by using Equation 4.15 (see Chapter 4) as:

$$\begin{aligned} Nu_c &= \frac{Nu_{net}}{[1 + Wn^2]} \\ &= \frac{99.90}{[1 + (0.18)^2]} \\ &= 96.77 \end{aligned} \tag{B.18}$$

Appendix C
Uncertainty Analysis

C.1 Uncertainty in thermocouple calibration

Five representative E-type thermocouples (in the range of $4.71°C - 73.16°C$) are used for the calibration. Thirteen temperature settings are used in the selected range and 600 readings are taken per thermocouple at a particular temperature setting. This yields 3000 voltage (emf) readings for each temperature. These values are averaged to have one emf value at a particular temperature to obtain a single calibration curve for all the 5 chosen thermocouples.

C.1.1 Systematic standard uncertainty

For estimating the systematic uncertainty associated with the voltage measurements, the 40 multiplexed channels on the *Keithley 2000* Digital Multimeter (DMM) are short-circuited. This yields non-zero offset values representing the systematic error across each of the channels. The standard deviation of the distribution of these systematic errors is used to compute the systematic standard uncertainty, b, using:

$$b = \sqrt{\frac{1}{n-1}\sum_{i=1}^{n}\left(V_i - \overline{V}\right)^2} \tag{C.1}$$

where $n = 40$. This value of b is found to be $0.313\ \mu V$

C.1.2 Random uncertainty

The uncertainty associated with the measured voltage due to random errors is computed from the standard deviation of the mean, i.e.,

$$u_v = \frac{S_v}{\sqrt{N}} = \sqrt{\frac{\frac{1}{N-1}\sum_{i=1}^{N}\left(V_i - \overline{V}\right)^2}{N}} \tag{C.2}$$

Here, $N =$ number of measurements at a particular temperature $= 3000$.

Since 13 temperature settings are used for the calibration purpose, this random uncertainty can be computed for each of the 13 data points. The maximum value out of these is used as a safe guess for the random uncertainty. This value is estimated to be $0.076\,\mu V$.

C.1.3 Calibration curve and the associated uncertainty

Polynomial curves of different order are employed to fit the data points using the method of least squares. The Root Mean Square (RMS) errors of each of the polynomial fits are estimated to find the polynomial fit with the least RMS error. A 2^{nd} order polynomial fit (given by Equation C.3) is found to have the least RMS error.

$$T = 0.2288 + 16.981V - 0.2091V^2 \tag{C.3}$$

Here, T is in $[^{\circ}C]$ and V is in $[mV]$.

Coleman and Steele (2018) have suggested a method to estimate the uncertainty associated with the calibration. They have used standard error of regression, $u_{T,cal}$, defined as:

$$u_{T,cal} = \sqrt{\frac{\sum_{i=1}^{m}\left(T_{i,cal} - T_{i,meas}\right)^2}{m - o - 1}} \tag{C.4}$$

Here,

$$T_{i,cal} = \text{temperature estimated from the calibration curve}$$

$$T_{i,meas} = \text{temperature measured during the calibration procedure}$$

$$m = \text{number of data points} = 13$$

$$o = \text{order of the polynomial fit}$$

The value of $u_{T,cal}$ is estimated to be $\approx 8.93\, mK$.

C.1.4 Combined and expanded uncertainties

Total uncertainty in the voltage measurements can be computed as:

$$u_{v,total} = \sqrt{u_v^2 + b^2} \tag{C.5}$$

Using the polynomial fit function and the method of uncertainty propagation, one can estimate the uncertainty in the temperature as:

$$u_{T,p} = \sqrt{\left(\frac{\partial T}{\partial V}\right)^2 (u_{v,total})^2} \tag{C.6}$$

Therefore, the combined uncertainty $u_{T,total}$ can be computed as:

$$u_{cT} = \sqrt{\left(\frac{\partial T}{\partial V}\right)^2 (u_v^2 + b^2) + \left(U_{T,cal}^2\right)} \tag{C.7}$$

This value of u_{cT} is found to be $\approx 9.23\, mK$, which is clearly dominated by $u_{T,cal}$. Here, the value of $\left(\frac{\partial T}{\partial V}\right)$ is computed in K/V.

Coleman and Steele (2018) have recommended using a coverage factor ($k_{\%}$) to multiply and expand the combined uncertainty and get an expanded uncertainty associated with a level of confidence.

$$u_T = k_{\%} u_{cT} \tag{C.8}$$

Coleman and Steele (2018) have also proposed using the student t value (corresponding to the confidence interval ($\%$) and the number of degrees of freedom) in place of $k_{\%}$.

$$u_T = t u_{cT} \tag{C.9}$$

To find the student t value for a 95% confidence interval, the number of degrees of freedom must be known. This can be computed using Welch-Satterthwaite formula (*Guide to the Expression of Uncertainty in Measurement*, 1995) as:

$$\nu_v = \frac{\left(u_v^2 + b^2\right)^2}{\left(\frac{u_v^4}{\nu_u} + \frac{b^4}{\nu_b}\right)} \tag{C.10}$$

Here,

Number of degrees of freedom for random uncertainty calculation, $\nu_u = N - 1 = 2999$ (where $N = 3000$, number of emf readings)

Number of degrees of freedom for systematic error estimation, $\nu_b = n - 1 = 39$ (where $n = 40$, number of short-circuited multiplexed channels)

This yields a $\nu_V = 44$ and $t \simeq 2$. Therefore, the expanded uncertainty associated with the thermocouple measurements for a 95% confidence interval can be estimated by multiplying u_{cT} with 2, that is:

$$u_T = 2 \times 9.23 = 18.46\, mK \tag{C.11}$$

C.1.5 Uncertainty in the experimental Rayleigh number and Nusselt number

According to Kline and Mcclintock (1953), for a parameter (R) that depends on multiple independent variables (V_i), the associated uncertainty (U_R) is given by:

$$\delta_R = \sqrt{\sum_{i=1}^{N} \left(\frac{\partial R}{\partial V_i} \delta V_i \right)^2} \tag{C.12}$$

where U_{Vi} is the uncertainty associated with an independent variable.

If the same variable has a functional form:

$$R = \frac{A^a B^b}{C^c D^d}$$

then, the associated uncertainty is given by:

$$\frac{\delta R}{R} = \sqrt{\left(a\frac{\delta A}{A} \right)^2 + \left(b\frac{\delta B}{B} \right)^2 + \left(c\frac{\delta C}{C} \right)^2 + \left(d\frac{\delta D}{D} \right)^2} \tag{C.13}$$

C.2 Uncertainty in Rayleigh number, Ra

From Equation 3.1,

$$Ra = \frac{p^2 g C_p \Delta T H^3 (MW)^2}{\bar{R}^2 T_m^3 \mu k_f} = \frac{\rho^2 g C_p \Delta T H^3}{T_m \mu k_f} \tag{C.14}$$

And the uncertainty associated with Ra is:

$$\frac{\delta Ra}{Ra} = \sqrt{\left(2\frac{\delta \rho}{\rho} \right)^2 + \left(\frac{\delta C_p}{C_p} \right)^2 + \left(\frac{\delta \Delta T}{\Delta T} \right)^2 + \left(3\frac{\delta H}{H} \right)^2 + \left(\frac{\delta T_m}{T_m} \right)^2 + \left(\frac{\delta \mu}{\mu} \right)^2 + \left(\frac{\delta k_f}{k_f} \right)^2} \tag{C.15}$$

$$= 3.54\%$$

$$= 0.0354$$

Here, the individual uncertainties are obtained as follows:

$$\text{Pressure, } \frac{\delta p}{p} = 1\% = 1 \times 10^{-2} \tag{C.16}$$

This value, as stated in the manufacturer's manual (*PX309-3KG5V, OMEGA Engineering*), includes the systematic and calibration uncertainties. Random uncertainty is much smaller than the above stated uncertainties and is, thus, neglected.

Temperature measurements for a particular experimental run yield a random error (computed by standard deviation of the mean) of about $5.4\,mK$ ($u_{T,meas}$)

Thus, the total uncertainty associated with temperature measurement is:

$$\begin{aligned}
\delta T &= \sqrt{u_{T,meas}^2 + u_{T,thermocouple}^2} \\
&= \sqrt{\left(\frac{5.4}{1000}\right)^2 + \left(\frac{9.23}{1000}\right)^2} \\
&= 10.69\,mK \\
\frac{\delta T}{T} &\simeq 3.6 \times 10^{-3}\% \\
&= 3.6 \times 10^{-5}
\end{aligned} \tag{C.17}$$

By knowing the uncertainties associated with pressure, temperature, and the looked-up density (*NIST Chemistry Web-book*), one can estimate the uncertainty associated with the fluid density as:

$$\begin{aligned}
\text{Density, } \frac{\delta \rho}{\rho} &= \sqrt{\left(\frac{\delta p}{p}\right)^2 + \left(\frac{\delta T}{T}\right)^2 + \left(\frac{\delta \rho}{\rho}\right)_{\text{NIST}}^2} \\
&\simeq 1\% \\
&= 1 \times 10^{-2}
\end{aligned} \tag{C.18}$$

Here, the uncertainty associated with the looked-up density is taken from the *NIST Chemistry Web-Book* (*https://webbook.nist.gov/chemistry/*), that is:

$$\begin{aligned}
\left(\frac{\delta \rho}{\rho}\right)_{\text{NIST}} &= 0.01\% \\
&= 1 \times 10^{-4} \text{ (from the } \textit{NIST Chemistry Web-Book}\text{)}
\end{aligned} \tag{C.19}$$

Note that the uncertainty of the looked-up quantities is always specified as a percentage of the reported number by the *NIST Chemistry Web-Book*.

Similarly, the uncertainties associated with the specific heat, thermal conductivity, and dynamic viscosity of the fluid as stated by the *NIST Chemistry Web-Book* are:

$$\text{Specific heat, } \frac{\delta C_p}{C_p} = 0.3\% \tag{C.20}$$
$$= 3 \times 10^{-3} \text{ (from the } \textit{NIST Chemistry Web-Book}\text{)}$$

$$\text{Fluid thermal conductivity, } \frac{\delta k_f}{k_f} = 2\% \tag{C.21}$$
$$= 2 \times 10^{-2} \text{ (from the } \textit{NIST Chemistry Web-Book}\text{)}$$

$$\text{Dynamic viscousity of the fluid, } \frac{\delta \mu}{\mu} = 2\% \tag{C.22}$$
$$= 2 \times 10^{-2} \text{ (from the } \textit{NIST Chemistry Web-Book}\text{)}$$

The mean temperature (T_m) and the temperature difference (ΔT) are estimated from the temperature measurements and, thus, the uncertainty propagation needs to be considered as:

$$\text{Mean temperature, } T_m = \frac{T_b + T_c}{2} \tag{C.23}$$
$$\frac{\delta T_m}{T_m} = \sqrt{2}\frac{\delta T}{T}$$
$$= 5.1 \times 10^{-3}\%$$
$$= 5.1 \times 10^{-5}$$

$$\text{Difference in temperature, } \Delta T = T_h - T_c \tag{C.24}$$

$$\begin{aligned}\frac{\delta \Delta T}{\Delta T} &= \sqrt{2}\frac{\delta T}{T} \\ &= 5.1 \times 10^{-3}\% \\ &= 5.1 \times 10^{-5}\end{aligned}$$

$$\text{Spacing between the plates, } \frac{\delta H}{H} = \frac{1 \times 10^{-3}}{15 \times 10^{-2}} \tag{C.25}$$

$$\begin{aligned}&= 0.67\% \\ &= 6.67 \times 10^{-3}\end{aligned}$$

Here, δH is from the measurement accuracy of the ruler.

C.3 Uncertainty in the total power input, q_{inp}

The voltage and current readings from a *Keithley 193* DMM (26 Kapton heaters) and from a *HP66104A* (1 guard heater) are used for the input power calculation.

$$q_{inp} = \sum_{i=1}^{N} V_i I_i \tag{C.26}$$

$$\frac{\delta q_{inp}}{q_{inp}} = \sqrt{\sum_{i=1}^{\text{26, guard}} \left(\frac{\delta V_i}{V_i}\right)^2 + \sum_{i=1}^{\text{26, guard}} \left(\frac{\delta I_i}{I_i}\right)^2} \tag{C.27}$$

For the *Keithley 193* DMM (used for the 26 Kapton heaters controlled by the DPS), the accuracy of the voltage and current readings are specified in the manual as:

Voltage reading: $\delta V = 0.1\, mV + 0.05\%$ of reading

Current reading: $\delta I = 1\, \mu A + 0.05\%$ of reading

For the *HP66104A* power supply/voltmeter system (used for the guard heater), the accuracy of the voltage and current readings are specified in the manual as:

$$\text{Voltage reading: } \delta V = 16\, mV + 0.02\% \text{ of reading}$$

$$\text{Current reading: } \delta I = 1\, mA + 0.02\% \text{ of reading}$$

Thus, the uncertainty associated with the total input power can be estimated as:

$$\frac{\delta q_{inp}}{q_{inp}} = 2.85\%$$

and

$$\delta q_{inp} = 7.324 \times 0.0285 = 0.209\, W$$

where, the value of q_{inp} is taken from the sample calculations.

C.4 Uncertainty in radiation heat loss, q_r

The possible components for the uncertainty in radiation heat loss are the emissivities of the polished silver and the Styrofoam surface and the uncertainty in temperature measurements. The emissivity of Styrofoam has been reported to be 0.6 by all the guidebooks and manufacturers and is not expected to vary by more than a few percentage. Since the absolute temperatures (in K) are very high compared to corresponding temperature measurement uncertainties, the uncertainty associated with the temperature of the surfaces can also be ignored. Hence, the only component considered is the emissivity of the polished silver surfaces.

The mean reported value of the thermal emissivity of a polished silver surface is:

$$\overline{\varepsilon}_{Ag} = 0.025 \qquad (\textit{https://www.engineeringtoolbox.com})$$

The lowest possible value of thermal emissivity of a polished silver surface is:

$$\varepsilon_{Ag_{min}} = 0.02 \qquad (\textit{https://www.engineeringtoolbox.com})$$

The highest possible value of thermal emissivity of a polished silver surface is:

$$\varepsilon_{Ag_{max}} = 0.03 \qquad (\textit{https://www.engineeringtoolbox.com})$$

Thus, the uncertainty associated with the estimated radiation heat loss is:

$$\delta q_{rad} = q_{rad}\big|_{(\varepsilon_{Ag}=0.03)} - q_{rad}\big|_{(\varepsilon_{Ag}=0.02)} \tag{C.28}$$

$$\begin{aligned} q_{rad}\big|_{(\varepsilon_{Ag}=0.03)} &= 0.0301\,W \\ q_{rad}\big|_{(\varepsilon_{Ag}=0.02)} &= 0.0198\,W \\ \delta q_{rad} &= 0.0301 - 0.0198 \\ &= 0.0103\,W \end{aligned}$$

Although, the uncertainty in emissivity is about 40%, since q_{rad} is minimal, ε has negligible contribution in the final Nusselt number uncertainty.

C.5 Uncertainty in edge heat loss, q_e

We know,

$$q_e = \frac{4k_B(T_h - \overline{T}_{B,out})Lt_h}{t_B} \tag{C.29}$$

By using Equation C.13 one can write:

$$\frac{\delta q_e}{q_e} = \sqrt{\left(\frac{\delta k_B}{k_B}\right)^2 + \left(\frac{\delta T_h}{T_h}\right)^2 + \left(\frac{\delta \overline{T}_{B,out}}{\overline{T}_{B,out}}\right)^2 + \left(\frac{\delta t_h}{t_h}\right)^2 + \left(\frac{\delta t_B}{t_B}\right)^2 + \left(\frac{\delta L}{L}\right)^2} \tag{C.30}$$

Here, k_B is found to vary by about 50% among various balsa wood suppliers

$$\text{Thermal conductivity of balsa wood, } \frac{\delta k_B}{k_B} = 50\% \tag{C.31}$$
$$= 0.5$$

Although, the uncertainty in k_B is about 50%, since q_e is minimal, it has negligible effect on the final Nusselt number uncertainty.

$$\text{Thickness of the hot plate, } \frac{\delta t_h}{t_h} = \frac{5 \times 10^{-5}}{12.7 \times 10^{-3}} \tag{C.32}$$
$$= 3.94 \times 10^{-3}$$

(δt_h from the measurement accuracy of Vernier caliper)

$$\text{Thickness of the balsa wood insulation, } \frac{\delta t_B}{t_B} = \frac{5 \times 10^{-5}}{25.4 \times 10^{-3}} \tag{C.33}$$
$$= 1.97 \times 10^{-3}$$

(δt_B from the measurement accuracy of Vernier caliper)

$$\text{Extent of the square hot plate, } \frac{\delta L}{L} = \frac{1 \times 10^{-3}}{15 \times 10^{-2}} \tag{C.34}$$
$$= 6.67 \times 10^{-3}$$

(δL from the measurement accuracy of ruler)

$$\text{Surface temperature of the hot plate, } \frac{\delta T_h}{T_h} = 3.6 \times 10^{-5} \tag{C.35}$$

$$\text{Balsa wood outer surface temperature, } \frac{\delta \overline{T}_{B,out}}{\overline{T}_{B,out}} = 3.6 \times 10^{-5} \tag{C.36}$$

Thus, the uncertainty associated with the computed edge heat loss is found to be:

$$\frac{\delta q_e}{q_e} \simeq 0.5 \tag{C.37}$$

And, therefore:

$$\delta q_e = \left(\frac{\delta q_e}{q_e}\right) q_e = 0.065\, W \tag{C.38}$$

where, the value of q_e is taken from the sample calculations.

C.6 Uncertainty in surface heat loss, q_s

We know:

$$q_s = \frac{4k_{gw}(T_m - T_{amb})LH}{t_{gw}} \tag{C.39}$$

By using Equation C.13 one can write:

$$\frac{\delta q_s}{q_s} = \sqrt{\left(\frac{\delta k_{gw}}{k_{gw}}\right)^2 + \left(\frac{\delta T_m}{T_m}\right)^2 + \left(\frac{\delta T_{amb}}{T_{amb}}\right)^2 + \left(\frac{\delta H}{H}\right)^2 + \left(\frac{\delta t_{gw}}{t_{gw}}\right)^2 + \left(\frac{\delta L}{L}\right)^2} \tag{C.40}$$

k_{gw} depends on the $\%$ by weight of glass wool and the commonly used values have a reported variation of about 100%. Thus,

$$\text{Thermal conductivity of glass wool, } \frac{\delta k_{gw}}{k_{gw}} = 100\% \tag{C.41}$$
$$= 1$$

$$\text{Thickness of glass wool insulation, } \frac{\delta t_{gw}}{t_{gw}} = \frac{1 \times 10^{-3}}{76.2 \times 10^{-3}} = 1.31 \times 10^{-2} \tag{C.42}$$

(δt_{gw} from the measurement accuracy of ruler)

$$\text{Ambient temperature, } \frac{\delta T_{amb}}{T_{amb}} = 3.6 \times 10^{-5} \tag{C.43}$$

Thus, the uncertainty associated with the computed surface heat loss is found to be:

$$\frac{\delta q_s}{q_s} \simeq 100\% \tag{C.44}$$

Thus,

$$\delta q_s = \left(\frac{\delta q_s}{q_s}\right) q_s = 5.67\, mW \tag{C.45}$$

where, the value of q_s is taken from the sample calculations.

Note that although the uncertainty associated with k_{gw} is about 100%, since q_s is minimal, it has negligible effect on the final Nusselt number uncertainty.

C.7 Uncertainty in guard heat loss, q_g

We know from data reduction (see Appendix A, Section A.2) that,

$$R_1 = \frac{1}{L^2}\left[\frac{t_h}{k_{Cu}} + \frac{t_k}{k_k} + \frac{t_{ha}}{k_{ha}}\right] \tag{C.46}$$

$$R_2 = \frac{1}{L^2}\left[\frac{t_{ph}}{k_{ph}} + \frac{\frac{1}{5}t_g}{k_{Cu}}\right] \tag{C.47}$$

The values of R_1 and R_2 are fixed. From sample calculations (see Appendix B, Section B.3), one can realize that $R_2 \gg R_1$.

Therefore, Equation A.9 becomes:

$$T_{heater} = q_{inp}R_1 + T_h \tag{C.48}$$

And, by using Equation C.12, one can write:

$$\begin{aligned}\delta T_{heater} &= \sqrt{(R_1\delta q_{inp})^2 + (q_{inp}\delta R_1)^2 + (\delta T_h)^2} \\ &= 0.036\ K\end{aligned} \tag{C.49}$$

Here, values of all the variables are taken from the sample calculation. Furthermore, by A.10,

$$q_g = \frac{T_{heater} - T_g}{R_2} \tag{C.50}$$

and the corresponding uncertainty value,

$$\begin{aligned}\delta q_g &= \sqrt{\left(\frac{1}{R_2}\delta T_{heater}\right)^2 + \left(\frac{1}{R_2}\delta T_g\right)^2 + \left(\left(\frac{T_{heater} - T_g}{R_2^2}\right)(\delta R_2)\right)^2} \\ &= 0.011\ W\end{aligned} \tag{C.51}$$

If δR_1 and δR_2 are determined, δT_{heater} and δq_g can be computed.

By using Equation C.12, one can write:

$$\delta R_1 = \sqrt{\left(\frac{\partial R_1}{\partial t_h}\delta t_h\right)^2 + \left(\frac{\partial R_1}{\partial k_{Cu}}\delta k_{Cu}\right)^2 + ...} \tag{C.52}$$

which gives:

$$\delta R_1 = \sqrt{\left(\frac{1}{L^2 k_{Cu}}\delta t_h\right)^2 + \left(\frac{t_h}{k_{Cu}^2 L^2}\delta k_{Cu}\right)^2 + ...} \tag{C.53}$$

Knowing:

$$\delta t_h = 5 \times 10^{-5}\, m \text{ [Measurement accuracy for Vernier caliper]}$$

$$\delta k_k = 0.01\, W/mK \text{ [Supplier datasheet]}$$

$$\delta k_{Cu} = 2\, W/mK \text{ [Property datasheet]}$$

$$\delta t_k = 1 \times 10^{-5}\, m \text{ [Supplier datasheet]}$$

$$\delta t_{ha} = 1 \times 10^{-5}\, m \text{ [Supplier datasheet]}$$

$$\delta k_{ha} = 0.01\, W/mK \text{ [Supplier datasheet]}$$

We get:

$$\delta R_1 = 4.14 \times 10^{-3}\, K/W$$

Similarly,

$$\delta R_2 = \sqrt{\left(\frac{\partial R_2}{\partial t_{ph}}\delta t_{ph}\right)^2 + \left(\frac{\partial R_2}{\partial k_{ph}}\delta k_{ph}\right)^2 + ...} \tag{C.54}$$

which gives:

$$\delta R_2 = \sqrt{\left(\frac{1}{L^2 k_{ph}}\delta t_{ph}\right)^2 + \left(\frac{t_{ph}}{k_{ph}^2 L^2}\delta k_{ph}\right)^2 + ...} \tag{C.55}$$

Knowing:

$$\delta t_{ph} = 5 \times 10^{-5}\, m \text{ [Measurement accuracy for Vernier caliper]}$$

$$\delta k_{ph} = 0.01\, W/mK \text{ [Supplier datasheet]}$$

$$\delta t_g = 5 \times 10^{-5}\, m \text{ [Measurement accuracy for Vernier caliper]}$$

We get:

$$\delta R_2 = 0.576\, K/W$$

C.8 Uncertainty in net power input, q_{net}

$$q_{net} = q_{inp} - q_r - q_s - q_e - q_g \tag{C.56}$$

By using Equation C.12:

$$\begin{aligned}
\delta q_{net} =& \sqrt{(\delta q_{inp})^2 + (\delta q_r)^2 + (\delta q_s)^2 + (\delta q_e)^2 + (\delta q_g)^2} \\
=& \sqrt{(0.209)^2 + (0.0103)^2 + (0.065)^2 + \left(\frac{5.67}{1000}\right)^2 + (0.011)^2} \\
=& 0.2195\, W
\end{aligned} \tag{C.57}$$

Here, the uncertainty in q_{inp} is the major contributor.

C.9 Uncertainty in uncorrected Nusselt number, Nu_{net}

$$Nu_{net} = \frac{q_{net} H}{L^2 \Delta T k_f} \tag{C.58}$$

$$\begin{aligned}
\frac{\delta Nu_{net}}{Nu_{net}} =& \sqrt{\left(\frac{\delta q_{net}}{q_{net}}\right)^2 + \left(\frac{\delta H}{H}\right)^2 + \left(2\frac{\delta L}{L}\right)^2 + \left(\frac{\delta \Delta T}{\Delta T}\right)^2 + \left(\frac{\delta k_f}{k_f}\right)^2} \\
=& \sqrt{\left(\frac{0.2195}{7.131}\right)^2 + \left(\frac{1\times10^{-3}}{15\times10^{-2}}\right)^2 + \left(2\frac{1\times10^{-3}}{15\times10^{-2}}\right)^2 + (3.6\times10^{-5})^2 + (2\times10^{-2})^2} \\
=& 3.9\%
\end{aligned} \tag{C.59}$$

By tracing backward, one can see that the uncertainties in q_{inp} and k_f contribute the most toward the total uncertainty in Nusselt number.

C.10 Uncertainty in sidewall-corrected Nusselt number, Nu_c

We know,

$$Nu_c = \frac{Nu_{net}}{[1 + Wn^2]} \tag{C.60}$$

To estimate the uncertainty associated with Wn:

$$\begin{aligned} \frac{\delta Wn}{Wn} &= \sqrt{\left(\frac{\delta k_{st}}{k_{st}}\right)^2 + \left(\frac{\delta t_{st}}{t_{st}}\right)^2 + \left(\frac{\delta L}{L}\right)^2 + \left(\frac{\delta k_f}{k_f}\right)^2} \\ &= 10.3\% \\ &= 0.103 \end{aligned} \tag{C.61}$$

and

$$\begin{aligned} \delta Wn &= \left(\frac{\delta Wn}{Wn}\right) Wn \\ &= 0.18 \times 0.103 \\ &= 0.0185 \end{aligned} \tag{C.62}$$

The various component uncertainties are listed below:

The thermal conductivity of Styrofoam is found to vary by 10% among various property datasheets.

$$\begin{aligned} \frac{\delta k_{st}}{k_{st}} &= 10\% \\ &= 0.1 \text{ (Property datasheet)} \end{aligned}$$

Also,

$$\frac{\delta t_{st}}{t_{st}} = \frac{5 \times 10^{-5}}{6.35 \times 10^{-3}}$$
$$= 7.87 \times 10^{-3} \text{ (Measurement accuracy of vernier caliper)}$$

Now, the uncertainty associated with the sidewall-corrected Nusselt number can be estimated as:

$$\frac{\delta Nu_c}{Nu_c} = \sqrt{\left(\frac{\delta Nu_{net}}{Nu_{net}}\right)^2 + \left(\frac{2Wn\delta Wn}{1+Wn^2}\right)^2} \tag{C.63}$$
$$= \sqrt{\left(\frac{3.9}{1000}\right)^2 + \left(\frac{2 \times 0.18 \times 0.0185}{1+(0.18)^2}\right)^2}$$
$$= 3.95\% \tag{C.64}$$

The value given in Equation C.64 is the one standard deviation estimate of the uncertainty and can be multiplied with a coverage factor of two, according to Coleman and Steele (2018), for estimating the 95% confidence interval. This would yield an uncertainty of about 7.9% with a 95% confidence interval. The uncertainty estimated using this sample calculation is more or less the average value. When the Rayleigh number is increased, the value of q_{inp} increases. Thus, since uncertainty of q_{inp} is a major contributor, the associated uncertainty decreases, thereby, yielding the total uncertainty to be a lower value. The converse is true for smaller Rayleigh numbers.

Appendix D

Sample Code

Given below is an excerpt from the modified version of the code developed by Han (2004):

```
void run_pi()
{
  extern int ch;
  extern double err_old[200][100], time_old[200][100];
  extern int ph_flag, pi_flag, p_flag, t_flag, d_flag;
  extern int first_ch_h1, last_ch_h1, first_ch_h2, last_ch_h2,
     first_ch_h3, last_ch_h3, first_ch_t1, last_ch_t1;
  extern int pi_interval, count_pi, count_power, num_i;
  extern double cv_o[200], et1[200], et2[200];
  extern double sp;
  extern int sp_o, sp1, sp2, sp3;
  extern double zero1[200], zero2[200], zero3[200];
  extern double sum_power, sum_loss, p_vi[100], r_2[200],
     v_1[100], v_2[100];;
  extern double t_old, t_now;
  extern long tbegin, tnow;
  extern FILE *temp, *temp_DPS, *power, *curr, *volt,
     *heatfluxdat, *contourdat, *sumpower, *preheatdat;
  extern double pres[10], vpres[10];

  int i, j, k;

  count_pi = 0;
  count_power = 5;

  ch = 0;

  /* TC locations on surface for contour plot */

  read_xy();


  /* Initialize error for I control */
```

```
for (i = 0; i < 200; i++)
{
  for (j = 0; j < 100; j++)
    err_old[i][j] = 0;
}

/* Initialize time for I control */
for (i = 0; i < 20; i++)
{
  for (j =0 ; j < 100; j++)
    time_old[i][j] = 0;
}

/* Set cv_o for E = 0 */
if (ph_flag == 0)
  for (i = 1;i <= 150; i++)
    cv_o[i] = 0.5;

temp = fopen("Temp_all.dat","w");
temp_DPS = fopen("Temp_evl.dat","w");
volt = fopen("Voltage_all.dat","w");
curr = fopen("Current_all.dat","w");
power = fopen("Power_all.dat","w");
contourdat = fopen("T_contour.dat","w");
heatfluxdat = fopen("heat_flux.dat","w");
sumpower = fopen("Sum_power.dat","w");

open_plotwindow();


/* Open parallel port when preheating is off */
if (ph_flag == 0)
  OpenPort();

/* Open HP66100A when preheating is off */
if (ph_flag == 0)
  InitHP66100();


/* Set PI control on */
pi_flag = 1;


/* Set power measurement flag on */
p_flag = 1;


/* Put new temperature array from measured temperature for
   each heater */
for(i = first_ch_t1; i <= (first_ch_t1+28); i++)
{
```

```
  if(i != 26)
  {
    et1[i] = MeasureTemp(fabs(MeasureEmf_1(i)) - zero1[i],1);
  }
}
for(i = first_ch_t1+31; i <= first_ch_t1+35; i++)
{
  et1[i] = MeasureTemp(fabs(MeasureEmf_1(i)) -
     zero1[i],1);
}
for(i = first_ch_t1+40; i <= last_ch_t1; i++)
{
  if(i != 43)
  {
    et1[i] = MeasureTemp(fabs(MeasureEmf_1(i)) - zero1[i],1);
  }
}

assign_temp();

fprintf(temp, "%-6.2f %5.3f ",0.0,sp);
for(i = first_ch_t1; i <= (first_ch_t1+28); i++)
{
  if(i != 26 && i != 18)
  {
    fprintf(temp, "%5.3f ", et1[i]);
  }
}
for(i = first_ch_t1+31; i <= first_ch_t1+35; i++)
{
  fprintf(temp, "%5.3f ", et1[i]);

}
for(i = first_ch_t1+40; i <= last_ch_t1; i++)
{
  if(i != 43)
  {
    fprintf(temp, "%5.3f ", et1[i]);
  }
}
fprintf(temp, "\n");
fflush(temp);

fprintf(temp_DPS, "%-6.2f %5.3f ",0.0,sp);
for(i = first_ch_h1; i <= last_ch_h1; i++)
{
  fprintf(temp_DPS, "%5.3f ", et2[i]);
}
for(i = first_ch_h3; i <= last_ch_h3; i++)
{
  fprintf(temp_DPS, "%5.3f ", et2[i]);
```

```
}
fprintf(temp_DPS, "\n");
fflush(temp_DPS);

time(&tbegin);
t_old = tbegin;
t_now = tbegin;

init_keyboard();


do
{
  if(kbhit())
  {

    ch = readch();
    if (ch == 'j' || ch == 'J')
    {
      if (t_flag == 0)
      {
        t_flag = 1;
        werase(w5_3);
        wrefresh(w5_3);
        wprintw(w5_3,"Keypress detected. TEXT is ON");
        box(w5_3s, '|', '-');
        wrefresh(w5_3);
      }
      else
      {
        t_flag = 0;
        werase(w5_3);
        wrefresh(w5_3);
        wprintw(w5_3,"Keypress detected. Text is OFF");
        box(w5_3s, '|', '-');
        wrefresh(w5_3);
      }
    }

    if (ch == 'l' || ch == 'L')
    {
      if (d_flag == 0)
      {
        d_flag = 1;
        werase(w5_3);
        wrefresh(w5_3);
        wprintw(w5_3,"Keypress detected. Plot is ON");
        box(w5_3s, '|', '-');
        wrefresh(w5_3);
      }
      else
```

```
  {
    d_flag = 0;
    werase(w5_3);
    wrefresh(w5_3);
    wprintw(w5_3,"Keypress detected. Plot is OFF");
    box(w5_3s, '|', '-');
    wrefresh(w5_3);
  }
}

if (ch == 'p' || ch == 'P')
{
  if (pi_flag == 0)
  {
    pi_flag = 1;
    werase(w5_3);
    wrefresh(w5_3);
    wprintw(w5_3,"Keypress detected. PI is ON");
    box(w5_3s, '|', '-');
    wrefresh(w5_3);
  }
  else
  {
    pi_flag = 0;
    werase(w5_3);
    wrefresh(w5_3);
    wprintw(w5_3,"Keypress detected. PI is OFF");
    box(w5_3s, '|', '-');
    wrefresh(w5_3);
  }
}

if (ch == 's' || ch == 'S')
{
  if (p_flag == 0)
  {
    p_flag = 1;
    werase(w5_3);
    wrefresh(w5_3);
    wprintw(w5_3,"Keypress detected. Power Measurement
       is ON");
    box(w5_3s, '|', '-');
    wrefresh(w5_3);
  }
  else
  {
    p_flag = 0;
    werase(w5_3);
    wrefresh(w5_3);
    wprintw(w5_3,"Keypress detected. Power Measurement
       is OFF");
```

```
      box(w5_3s, '|', '-');
      wrefresh(w5_3);
    }
  }

  if (ch == 'f' || ch == 'F')
  {
    werase(w5_3);
    wrefresh(w5_3);
    wprintw(w5_3,"Keypress detected. Exiting!");
    box(w5_3s, '|', '-');
    wrefresh(w5_3);
    break;
  }
}

if (pi_flag == 1)
{
  if(count_pi % pi_interval == 0)
  {
    for(j = first_ch_h1; j <= last_ch_h1; j++)
    {
      if(j == 34 || j == 43 || j == 52|| j == 53)
        sp_o = sp1;
      else if (j == 38|| j == 47|| j == 54|| j == 55)
        sp_o = sp2;
      else
        sp_o = sp3;
      PI_code(j);
    }

    for(j=first_ch_h3;j<=last_ch_h3;j++)
    {
      PI_code_HP(j);

    }
  }

  count_power = count_power + 1;

  count_pi = count_pi + 1;

  if(count_pi % 20 == 0)
  {
    for(j = 1; j <= 29; j++)
    {
              if(j != 26 && j != 18)
                fprintf(contourdat, "%3d %5.3f %5.3f
                   %5.3f\n",j,x[j],y[j],et1[j]);
    }
    fflush(contourdat);
```

```
  }
}

preheatdat = fopen("preheat_custom.dat","w");
for(j = first_ch_h1;j <= last_ch_h1; j++)
{
  fprintf(preheatdat, "%3d %3d %f %f
     %f\n",j,sp_out[j],cv_o[j],et2[j],err_old[j][num_i]);
}
for(j = first_ch_h3; j <= last_ch_h3; j++)
{
  fprintf(preheatdat, "%3d %f %f
     %f\n",j,cv_o[j],et2[j],err_old[j][num_i]);
}
fclose(preheatdat);

t_old = t_now;

if (p_flag == 1)
{
  for(j = first_ch_h1; j <= last_ch_h1; j++)
  {
    MeasureEmf_zero3devices(j,&v1,&v2);

    v_1[j]=fabs(v1)-zero2[j];
    v_2[j]=fabs(v2)-zero3[j];

    if (t_flag == 1)
    {
      wprintw(w5_5s,"channel=%3d V1=%6.3f[V] I1=%f[A]
         P=%f[W]\n", j, v_1[j], v_2[j]/r_2[j],
         v_1[j]*v_2[j]/r_2[j]);
      wrefresh(w5_5s);
    }
  }

  v_1[j] = get_power_supply_volt(2);
  v_2[j] = get_power_supply_current(2);
  if (t_flag == 1)
  {
    wprintw(w5_5s,"channel=%3d V1=%6.3f[V] I1=%f[A]
       P=%f[W] \n",j,v_1[j],v_2[j],v_1[j]*v_2[j]);
    wrefresh(w5_5s);
  }

  werase(w5_5s);
  wrefresh(w5_5s);

  /* Measure voltage from pressure sensors */
  vpres[1] = fabs(MeasureEmf_1(55)) - zero1[55];
```

```
  /* Voltage measurement proportional to heat flux */
  pres[1] = (vpres[1] * 601.01) - 2.1401;
  pres[1] = ((pres[1] * 6894.7573)/100000) + 1.01325;
  if (t_flag == 1)
  {
    wprintw(w5_5s,"channel=55 Voltage=%lf[V], Pressure=
       %lfbar",vpres[1],pres[1]);
    wrefresh(w5_5s);
  }
}

for(i = first_ch_t1; i <= (first_ch_t1+28); i++)
{
  if(i!=26 && i!=18)
  {
    et1[i] = MeasureTemp(fabs(MeasureEmf_1(i)) -
       zero1[i],1);
    if(t_flag == 1)
    {
      wprintw(w5_3s,"channel=%3d Temperature=%6.2f[C],
         Set_T[C]=%5.2f \n",i,et1[i],sp);
      wrefresh(w5_3s);
    }
  }
}
for(i = (first_ch_t1+31); i <= (first_ch_t1+35); i++)
{
  et1[i] = MeasureTemp(fabs(MeasureEmf_1(i)) - zero1[i],1);
  if (t_flag == 1)
  {
    wprintw(w5_3s,"channel=%3d Temperature=%6.2f[C],
       Set_T[C]=%5.2f \n",i,et1[i],sp);
    wrefresh(w5_3s);
  }
}
for(i = (first_ch_t1+40); i <= last_ch_t1; i++)
{
  if(i!=43)
  {
    et1[i] = MeasureTemp(fabs(MeasureEmf_1(i)) -
       zero1[i],1);
    if (t_flag == 1)
    {
      wprintw(w5_3s,"channel=%3d Temperature=%6.2f[C],
         Set_T[C]=%5.2f \n",i,et1[i],sp);
      wrefresh(w5_3s);
    }
  }
}
```

```
/* Put new temperature array from measured temperature for
   each heater */
assign_temp();


time(&tnow);
t_now = tnow;

if (p_flag == 1)
{
 sum_power = 0.0;
 sum_loss = 0.0;

 fprintf(volt, "%-6.2f ",t_now-tbegin);
 fprintf(curr, "%-6.2f ",t_now-tbegin);
 fprintf(power, "%-6.2f ",t_now-tbegin);

 for(j = first_ch_h1; j <= last_ch_h1; j++)
 {
   p_vi[j] = v_1[j] * v_2[j] / r_2[j];
   sum_power = sum_power + p_vi[j];
   fprintf(volt, "%f ",v_1[j]);
   fprintf(curr, "%f ",v_2[j]/r_2[j]);
   fprintf(power, "%f ",p_vi[j]);
 }

 for(j = first_ch_h3; j <= last_ch_h3; j++)
 {
   p_vi[j] = v_1[j] * v_2[j];
   sum_power = sum_power + p_vi[j];
   fprintf(volt, "%f ",v_1[j]);
   fprintf(curr, "%f ",v_2[j]);
   fprintf(power, "%f ",p_vi[j]);
 }

 fprintf(volt, "\n");
 fprintf(curr, "\n");
 fprintf(power, "\n");

 fflush(volt);
 fflush(curr);
 fflush(power);

 fprintf(heatfluxdat,"%-6.2f ",t_now-tbegin);
 for(j = first_ch_h2; j <= last_ch_h2; j++)
 {
   fprintf(heatfluxdat,"%lf ",pres[1]);
 }
 fprintf(heatfluxdat,"\n");
 fflush(heatfluxdat);
```

```
 fprintf(sumpower,"%-6.2f ",t_now-tbegin);
 fprintf(sumpower,"%f\n",sum_power);
 fflush(sumpower);

 count_power = 0;
}

fprintf(temp, "%-6.2f %5.3f ",t_now-tbegin,sp);

for(i = first_ch_t1; i <= (first_ch_t1+28); i++)
{
  if(i!=26 && i!=18)
      {
        if (fabs(et1[i]) > 60.0)
          et1[i] = 0.0;
        fprintf(temp, "%5.3f ",et1[i]);
      }
}
for(i = first_ch_t1+31; i <= first_ch_t1+35; i++)
{
  if (fabs(et1[i]) > 60.0)
    et1[i] = 0.0;
  fprintf(temp, "%5.3f ",et1[i]);

}
for(i = first_ch_t1+40; i <= last_ch_t1; i++)
{
  if(i!=43)
  {
    if (fabs(et1[i]) > 60.0)
      et1[i] = 0.0;
    fprintf(temp, "%5.3f ",et1[i]);
  }
}
fprintf(temp, "\n");
fflush(temp);

fprintf(temp_DPS, "%-6.2f %5.3f ",t_now-tbegin,sp);
for(j = first_ch_h1; j <= last_ch_h1; j++)
{
  fprintf(temp_DPS, "%5.3f ",et2[j]);
}
for(j = first_ch_h3; j <= last_ch_h3; j++)
{
  fprintf(temp_DPS, "%5.3f ",et2[j]);
}

fprintf(temp_DPS, "\n");
fflush(temp_DPS);
```

```
  if (d_flag == 1)
  {
    plot_pi2();

  }

  werase(w5_5s);
  wrefresh(w5_5s);

 }while(1);

close_keyboard();


/* Reset power supply */
for (i = 1; i <= c_line; i++)
{
  Chooseline(i);
  for (j = 0; j < 16; j++)
  {
    for(k = 0; k < 4; k++)
          wwcr(j,k,0,&status);
  }
}

pclose(plot2);

fclose(temp);
fclose(temp_DPS);
fclose(volt);
fclose(curr);
fclose(power);
fclose(contourdat);
fclose(heatfluxdat);
fclose(sumpower);

/* Generate preheat data */
preheatdat = fopen("preheat_custom.dat","w");
for(j = first_ch_h1; j <= last_ch_h1; j++)
{
  fprintf(preheatdat, "%3d %3d %f %f
     %f\n",j,sp_out[j],cv_o[j],et2[j],err_old[j][num_i]);
}
for(j = first_ch_h3; j <= last_ch_h3; j++)
{
  fprintf(preheatdat, "%3d %f %f
     %f\n",j,cv_o[j],et2[j],err_old[j][num_i]);
}
fclose(preheatdat);

power_supply_close();
```

```
  ClosePort();

  p_flag=0;

  t_flag=1;

  d_flag=0;

  f_flag=0;

  ph_flag=0;

  pi_flag=0;


  return;
}
```

Appendix E
MATLAB® Code

```
a=VideoReader('16bar_30deg_cold.mov');
for img = 1:a.NumberOfFrames;
    filename=strcat('frame',num2str(img),'.tiff');
    b = read(a, img);
    imshow(b);
    imwrite(b,filename);
end
```